DOCTOR OF PHILOSOPHY

Modelling flow and pressure losses in a gasoline particulate filter

Prantoni, Marco

Award date:
2021

Awarding institution:
Coventry University

Modelling Flow and Pressure Losses in a Gasoline Particulate Filter

by

Marco Prantoni

Doctor of Philosophy

May 2021

Certificate of Ethical Approval

Applicant:

Marco Prantoni

Project Title:

Modelling flow and pressure losses in gasoline particulate filters

This is to certify that the above named applicant has completed the Coventry University Ethical Approval process and their project has been confirmed and approved as Low Risk

Date of approval:

04 August 2020

Project Reference Number:

P109503

Acknowledgements

First of all I would like to express my gratitude to my director of studies, Dr. Svetlana Aleksandrova, for guiding me throughout this work and for her endless support. My gratitude goes also to Dr. Humberto Medina and Prof. Stephen Benjamin for their precious advices and continuous feedback.

I would like to acknowledge my PhD colleagues, Dimitar, Gianluca, Sam, Abhi, Dhila and Jono, and my dear friends, Edoardo, Stefano and Kenneth for their support.

Finally, I would like to thank my entire family and in particular my parents, Paola and Mario, for believing in me, for being an example in life and for supporting me in every step of my life.

Abstract

The reduction of transport particulate matter emissions is crucial for improving air quality. Although particulate filters are efficient in removal of particulate matter, their inclusion in modern exhaust systems results in high back-pressures, which then causes higher fuel consumption as well as other problems to the engine performance. Consequently, there is an ever-increasing demand within the automotive industry for more accurate and reliable filter design tools.

This thesis investigates both numerically and experimentally different sources of the pressure losses in particulate filters in order to develop a fundamental understanding of the complex physics of the flow in wall-flow filters and to develop tools for modelling filter flows, with particular focus on Gasoline Particulate Filters (GPFs) and their operating conditions.

Although friction losses and contraction and expansion losses in laminar duct flows have been studied extensively, there are still some discrepancies in existing correlations. In some flow regimes in particulate filters, the contribution of these losses may be significant. Therefore, a numerical investigation of developing flow losses and losses due to the flow path contraction has been carried out. Improved correlations for both types of losses have been suggested, and supporting experiments for friction losses in filter channels with porous walls have been carried out. These provided useful information about filter friction factor and contraction loss coefficient, which supported the physical base of the new pressure drop models developed in this work. The results of these studies can also be used for the prediction/optimisation of the pressure drop in other applications such as catalyst filters, multi-channel systems, wind tunnels and flow meters.

In order to be able to validate the developed filter models, experimental data from a joint project with Jaguar Land Rover has been used. This data, collected as part of a team of researchers, allowed to get a better insight into the filter losses at high mass flow rates and temperatures up to $680[^{\circ}C]$. This unique data set can be used for the assessment of particulate filter models in a wide range of filter parameters and flow conditions.

From an industrial/practical point of view and with regard to the modelling of particulate filters, the main outcomes of this work include the development and assessment of two new physics-based particulate filter models.

Although a number of 1-D models exist, none of them consider turbulent flow regime which may be present in the filter under certain conditions. To address this challenge, a new 1-D particulate filter model has been developed which covers both laminar and turbulent flow regimes.

Because of the large pressure variations along the filter channel at high flow rates and temperatures, density change effects have been included in the model, which allows the model to be used at both low and high temperatures and filter back-pressures. The model predictions agree well with the experimental data and at high mass flow rates and temperatures the new model can improve the pressure drop predictions up to $30-40\%$ with respect to the original model developed by Kostandopoulos and Johnson (1989), which is often used for high Reynolds number flows despite having been developed for laminar flow regime only.

While 0-D and 1-D models of a representative filter channel are useful when it can be reasonably assumed that all filter channels have similar flow rates, this is not the case where there is considerable variation in channel properties or the upstream flow is highly non-uniform. In order to be able to account for the difference between channels, a new multi-channel particulate filter model and modelling approach, including coupling the model with CFD simulations, have been developed. This modelling approach allows to: (i) capture complex flow interactions between channels, (ii) account for density variations within individual channels, (iii) prescribe individual channel properties (i.e. wall thickness, hydraulic diameter and wall permeability) and (iv) investigate the overall

effect of a given filter configuration on the exhaust system in 3-D (i.e. upstream and downstream effects).

The potential of both models in terms of practical applications has been demonstrated by carrying out parametric studies. The results of the new 1-D particulate filter model have shown that for most of the considered filter geometries there is a range of filter sizes providing minimum losses in the given mass flow rate range, while the results of the new multi-channel modelling approach have shown that upstream flow non-uniformity may persist through the filter, which needs to be taken into account in filter design. The effect of different wall permeability between different channels has also been demonstrated. Such insights would allow filter designers to select the best filter configuration within other constraints used in the development process.

Table of contents

List of figures

List of tables

Nomenclature

Roman Letters

A	Cross-sectional area
A_1	Smaller channel cross-sectional area
A_2	Larger channel cross-sectional area
C	Constant
C_c	Contraction area ratio at the vena-contracta
C_f	Darcy Friction Factor
D	Diameter
d_c	Collision diameter
d_h	Channel hydraulic diameter
f	Fanning Friction Factor
k	Permeability
$K(\infty)$	Pressure defect asymptotic constant
$K(x)$	Pressure defect function
k_b	Boltzmann constant
Kn	Knudsen number
L	Length
L_{hy}	Hydrodynamic entrance length
L_{hy}^{+}	Dimensionless hydrodynamic entrance length
M	Molar mass
P	Pressure
p	Pressure

Q Volumetric flow rate

R Gas constant

R_{Gas} Specific gas constant

Re Reynolds number

Re^* Modified Reynolds number

Re_w Porous wall Reynolds number

s Rectangular channel height and horizontal wall thickness

T Temperature

t Vertical wall thickness

U Mean cross-sectional velocity

u_i Mean local cross-sectional velocity

u_w Mean local through wall velocity

v Mean local through wall velocity through the vertical porous wall

w Rectangular channel width and mean local through wall velocity through the horizontal porous wall

w_s Filter wall thickness

x Axial coordinate

x^+ Dimensionless axial distance

Greek Letters

β Forchheimer coefficient

ε Surface roughness

κ Hydraulic conductivity

λ Mean free path

μ Dynamic viscosity

ν Kinematic viscosity

ρ Density

σ Contraction or expansion area ratio and horizontal wall permeability

τ Vertical wall permeability

ξ Borda-Carnot coefficient

ζ Loss coefficient

$\zeta_{Contr.}$ Contraction loss coefficient

$\zeta_{Exp.}$ Expansion loss coefficient

Sub Scripts

DF Developing flow

FDF Fully developed flow

i Subscript for cell indexing

it Iteration

j Subscript for cell indexing

Abbreviations

$0-D$ Zero-dimensional

$1-D$ One-dimensional

$2-D$ Two-dimensional

$3-D$ Three-dimensional

CFD Computational fluid dynamics

DPF Diesel particulate filter

FDM Finite difference method

GDI Gasoline direct injection

GPF Gasoline particulate filter

MFR Mass flow rate

MPI Multi point injection

OFA Open frontal area

PFI Port fuel injection

PM Particulate matter

PN Particulate number

SCF Stokes-Cunningham Factor

VFM Viscous flow meter

Chapter 1

Introduction

1.1 Background

According to the World Health Organization (WHO) the transport sector has the highest energy use growth compared to any other end-use sector and it is the fastest growing contributor to climate-damaging emissions. The main transport sector responsible for such increase in energy consumption are the light-duty vehicles and freight transport.

The most relevant contributors to the climate change from the transport sector are, in order of relevance [1]:

1. The emissions of carbon dioxide CO_2, which can persists in the atmosphere for over a century and is responsible for the long-term global warming effects.

2. The emissions of black carbon, which persists in the atmosphere for only a few weeks, but has a warming effect many times more powerful than the carbon dioxide.

3. The emissions of hydrocarbon (HC) and nitrogen oxides (NO_x), which also contribute to the long-term global warming effects.

The transport sector is also one of the major responsible for the urban air pollution, which increases the risk for cardiovascular and respiratory disease, cancer and adverse birth outcomes, and is also associated with higher death rates [2]. Air pollution-related deaths and illness are linked most closely to exposures to small particulate matter (PM)

with a diameter of less than 10 or 2.5 microns (thus, named PM_{10} and $PM_{2.5}$) [3], [4] and [5]. PM is mainly composed of black carbon with added mixture of heavy metals, sulphurs, carbon compounds and carcinogens. In an internal combustion engine (ICE) these are generated from the incomplete combustion of hydrocarbons. Other harmful pollutants includes ground-level ozone (O_3), of which the NO_x is a precursor, and carbon monoxide (CO) [2].

Thus, the reduction of the emissions from the transport sector, CO_2 and PM in particular, has become a primary concern in many countries and increasingly demanding regulation have been introduced in the recent years. This prompted automotive companies to develop new technologies (e.g. engines, after-treatment systems and fuels) in order to mitigate the emissions generated by the internal combustion engines (ICE).

In terms of engines development, the refinement of the Gasoline Direct Injection (GDI) has led to higher thermal efficiency and more power output as well as lower CO_2 emissions than the traditional Port Fuel Injection (PFI) and Multi Point Injection (MPI) spark ignition engines [6], [7]. Therefore, the GDI technology has recently become of great interest for the automotive industry [8]. Despite their benefits, GDI engines produce higher particulate matter (PM) and particulate number (PN) emissions, which were previously typical of diesel engines only.

For this reason the European Union has introduced in the new Euro 6 regulation a limit for PM ($< 0.0045[g/km]$) and PN emissions ($< 6.0x10^{11}[particles/km]$) not only for diesel engines, present since the Euro 5, but also for the petrol engines which use the GDI. Regarding the limits on CO_2 emissions, instead, there are no standards for single vehicles and the European Union has only set a fleet-wide average emission target, which should be less than $95[g]$ of CO_2 per kilometre.

In order to control the particle emissions and meet the Euro 6 regulation for PN, the most effective technological solution adopted by automotive companies is the integration of the Diesel or Gasoline Particulate Filter (DPF or GPF) in the after-treatment system of the vehicles. While DPFs have been introduced to the market of road vehicles in the 1980s, GPFs have been in use only since a few years and exclusively in vehicles with GDI engines.

Although different types of filtration devices exist, most of the automotive particulate filters on the market have wall-flow monolith geometry.

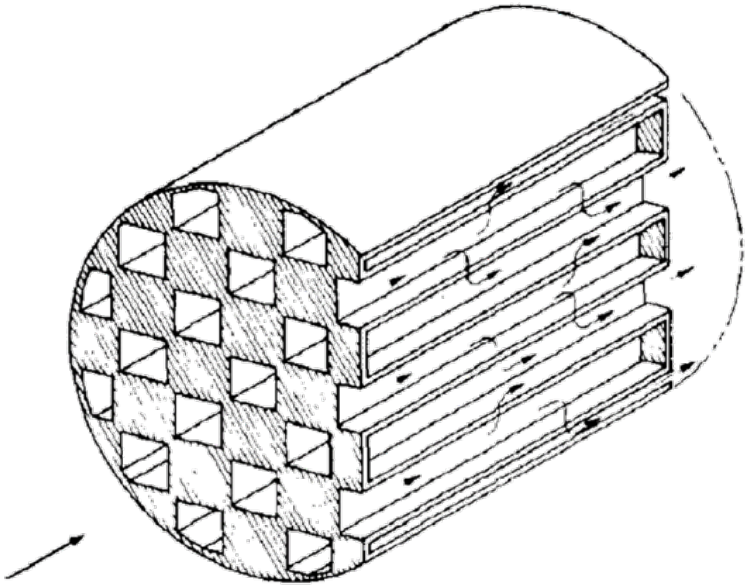

Fig. 1.1 Sketch of a wall-flow monolith Bissett (1984).

As shown in Figure 1.1, a wall-flow monolith consists of many parallel channels, typically of square cross-section with an hydraulic diameter of around $1.2[mm]$, which are alternatively blocked either at the inlet or at the outlet and are separated by a thin porous wall (around $0.2[mm]$). Thus, the exhaust gas enters firstly into the channels open at the inlet and then, since these will be blocked at the end, the flow is forced to pass through the porous walls in order to enter the adjacent channels (which are not blocked at the end) and to exit the filter. The soot are trapped in the porous wall during this process.

However, if on one side the particulate filter reduces the soot emissions, on the other side its introduction in the after-treatment system of a vehicle causes a back-pressure to the upstream components. The filter back-pressure further increases with the increasing of the soot loading, as this creates a particulate layer, commonly denominated "soot cake", along the wall surface of the inlet channels, which clogs the filter. This increase in back-pressure can have adverse effects on several components as well as on the overall vehicle performance. The most common problems are [9]:

1. Increased fuel consumption; Johnson [10] reported that for diesel engines under some conditions, a 100$[mbar]$ increase in filter back-pressure can result in a 1 to 4.5% increase in fuel consumption, which "might cost a long haul operator in the US about 600 dollars per year".

2. Increased CO_2 and NO_x emissions due to the increase of engine load.

3. Increased exhaust temperature, which can result in overheating of exhaust valves and the turbine.

4. Changes of the turbocharger operational conditions, which can cause variations in the air-to-fuel ratio (usually enrichment) affecting both emissions and engine performance.

5. Damaging of the turbocharger seals, resulting in oil leakage into the exhaust system.

6. Prevent some exhaust gases from leaving the cylinder (typically in naturally aspirated engines), creating an internal exhaust gas recirculation.

7. Scavenging problems, which affect engine performance (especially in GDI engines).

Hence, in order to avoid the back-pressure exceeding critical values, the filters undergo a process called regeneration, which consists of burning off (oxidizing) the soot accumulated in the filter. The regeneration process can be done actively, by increasing the temperature of the exhaust system on purpose, or passively (meaning no specific control action is taken), by using heat of the engine's exhaust at normal operation or, for diesel only, by using the reaction between the NO_2 and the soot [11].

Originally, particulate filters were designed with the sole purpose of decreasing the PM emissions, while the reduction of the other pollutants (CO, NO_x and HC) was entrusted to the catalytic converter. The catalytic converter is a flow-through monolith (with a similar geometry to a wall-flow filter but without the plugs). The wall of the catalyst channels are covered in washcoat which contains precious metals, such as palladium or rhodium. When these metals come into contact with the exhaust toxic

gases they convert them in to less toxic or harmless gases through a process called catalysis.

In order to decrease the installation space and overall costs, automotive companies have started using particulate filters with a catalyst washcoat applied on them, which can be placed either in series with the catalytic converter or replace it entirely.

Regarding the manufacturing, wall-flow monolith are mostly extrusions made from porous ceramic materials, typically cordierite and silicon carbide. These materials have a high melting point, a low thermal expansion and high thermal shock resistance while providing high strength and chemical durability. These characteristics are extremely important in particulate filters due to the environment in which they have to operate, which exposes them to high temperatures (as high as $1150[^{\circ}C]$ during regeneration [12]), high thermal gradients and stresses (which might crack the filter), as well as sulphuric acid corrosion and ash attack.

Since the inclusion of the particulate filters in the vehicles' after-treatment system can produce adverse effects, an extensive research effort has been carried out in order to optimize them (reduce the back-pressure without compromising the filtration efficiency). The optimization process is usually performed using mathematical/physical models, which are able to predict the flow inside a filter and its back-pressure, depending on the filter geometry, wall properties and operating conditions. With the aid of these predictive models, automotive companies are able to design more efficient filters in a quicker and cheaper way than if they were optimized through a purely experimental approach, as this would require to physically make and test a large variety of filters.

Most of the research efforts on models development have been focused on DPFs, which have been in use since several decades, and their operating conditions, while the research on GPFs is rather limited (as shown in Section 1.2.1). However, GPFs work at different operating conditions than DPFs, typically at higher flow rates and temperatures and might exhibit turbulent flow within the channels. This might also be the case in DPFs, as reported by Masoudi [13], where turbulent flow regime within the filter channels can be present in certain operating conditions. Moreover, GPFs are usually smaller than DPFs, as GDI engines produce less soot than diesel engines, and the filter channels density and wall properties also can be different. As a consequence, the models

developed for DPFs may not be suitable for predicting the flow and back-pressure of GPFs in the full operating range [14]. Hence, there is a need to further understand the flow behaviour within GPFs and to develop new predictive models suitable for their operating conditions, which provided a motivation for this study.

This chapter provides a review of the most relevant particulate filter models developed to date and a description of the flow physics underlying the pressure losses in a wall-flow monolith. Several gaps in the literature have been identified and summarised. Finally, the aims and objectives are outlined and the thesis structure is presented.

1.2 Literature review

1.2.1 Particulate filter models

Over the years many particulate filter flow models have been proposed. These can be divided in two main categories:

1. Single inlet/outlet channel models.

2. Multi-channel models.

The assumptions, advantages, disadvantages and limitations of both modelling approaches are reported in the next sections. A summary including the relevant findings is reported at the end of the section.

1.2.1.1 Single inlet/outlet channel models

The first significant particulate filter study was presented by Bissett in 1984 [15]. Although the aim of the study was primarily to gain a deeper understanding of the regeneration process in wall-flow diesel particulate filters, the model formulation laid the foundations for the development of predictive models more focused on the pressure drop characteristics of the filters. The idea behind Bissett's mathematical model was to represent the entire flow properties and thermal regeneration behaviour of a particulate filter through a single inlet and outlet channel, separated by a porous wall, in order to reduce a complex three-dimensional (3-D) problem into a simple one-dimensional (1-D)

one. The single inlet and outlet channel approach assumes that the flow in all channels is the same, and pressure and velocity are averaged over the cross-section of each inlet and outlet channel. This modelling approach offers a relatively easy implementation and fast solution of the model, when compared to the multi-channel modelling approach or full 3-D Computational Fluid Dynamics (CFD) simulations.

Bissett was the first to derive the 1-D mass, momentum and energy differential equations for the inlet and outlet channels and coupled these equations for the two channels through Darcy's Law (see section 1.2.2.3), which represents the pressure drop due to the porous wall. The model equations can be solved numerically using an appropriate set of boundary conditions. Bissett's model was intended to give only an insight into the regeneration process and the predicted pressure drop was not validated against experimental data. This model accounts for the variation of the density and viscosity along the channel using the ideal gas law and the Sutherland's law, respectively, and thus is often called compressible.

Note that in most of the work reviewed here the term "compressible" is used to describe models which account for the density variation due to the variations in pressure. Although this is not, strictly speaking, a fully compressible flow model, and the Mach number is well below 0.3 in most cases, the term "compressible" will be used throughout this thesis to indicate that the density variation has been taken into account. In the formulation of Bissett the variation of the density along the channel is a function only of the local temperature but not of the local pressure.

A few years later, in 1989, Kostandopoulos and Johnson [16] proposed a simple 1-D flow model for DPF flow and pressure losses and assessed it against the available experimental pressure drop data of typical wall-flow monoliths used at the time. The intent of the authors was to provide a tool for the rational engineering design and optimization of DPFs. The principal assumptions on which the model is based are:

1. The model is based on the single inlet and outlet approach, so that all inlet channels and all outlet channels can be described by the behaviour of a single representative, inlet or outlet, channel.

2. The flow is in steady state.

3. The flow within the channels is laminar.
4. The temperatures of the flow entering and leaving the filter are approximately equal (isothermal flow).
5. The gas properties are spatially uniform (incompressible flow, meaning that the density and viscosity variation along the channel are not accounted for).
6. The flow distribution at the entrance of the monolith is uniform.
7. The flow profile in the channels is unaffected by the suction/injection from the porous wall (described in section 1.2.2.1) and it is fully developed.
8. The slip effects (described in section 1.2.2.3) are neglected.
9. The irreversible losses due to contraction and expansion at the entrance and exit of the filter (described in section 1.2.2.2) are neglected.
10. There is no axial momentum transfer in the wall normal direction at the porous wall surface.
11. The Forchheimer losses (described in section 1.2.2.3) are negligible.

Similarly to Bissett's formulation [15], the model by Konstandopoulos and Johnson [16] includes the 1-D mass and momentum balance in the inlet and outlet channels and Darcy's Law but, because of the isothermal flow assumption, the energy equation is not needed. For this reason, the Konstandopoulos and Johnson model is effectively a subset of equations of Bissett's model and, thus, sometimes it will be referred to as the **Bissett-Konstandopoulos model** throughout this thesis.

The main advantage of this model is that the model equations can be solved analytically. Therefore, the filter pressure drop can be expressed through a single analytical equation. The model equations require several parameters, such as the filter geometry and gas properties, most of which are usually known. However, the wall permeability required for the Darcy equation, is often difficult to determine for extruded monoliths, especially in catalysed applications, and thus is usually obtained via a model calibration

procedure. The calibration of the permeability was performed by the authors by fitting their analytical equation to the experimental pressure drop.

A full description of the Bissett-Konstandopoulos model, its limitations and permeability calibration method is given later in this thesis (see section 6.4.1) as the 1-D model proposed in Chapter 6 is an extension of this model.

The pressure drop predictions of the Bissett-Konstandopoulos model have been assessed against the experimental data of Mogaka et al. [17], who performed measurements on a cold flow test rig, and the data of Miller et al. [18] and Kostandopoulos and Johnson [16], who performed their experiments at high temperatures, varying from $260[^{\circ}C]$ to $632[^{\circ}C]$, with the flow provided by the exhaust gases of a diesel engine. Kostandopoulos and Johnson [16] showed that the predictions of their model agree well with both of these cold and hot flow measurements up to a channel Reynolds number of $Re_{d_h} \sim 1000$, while the predictions worsen for higher Reynolds number values. The channel Reynolds number in [16] was defined as $Re_{d_h} = \frac{\rho U d_h}{\mu}$, where ρ is the gas density, U is the mean axial cross-sectional velocity at the entrance of the inlet channel, d_h is the hydraulic diameter of the channels and μ is the dynamic viscosity of the gas. The authors also stated that a better agreement with the high temperatures data points could be achieved by including a slip-flow correction factor.

In addition to the 1-D model, Kostandopoulos and Johnson [16] proposed a 0-D model, also referred to as "lumped" model in the literature. This 0-D model was derived by simplifying the analytical solution of their 1-D model using an approximation which allowed to separate/uncouple the pressure drop contribution of the friction losses along the channels from the losses through the porous wall. With a 0-D model the flow variables are not calculated locally along the filter axial direction but the total filter pressure drop is expressed by an analytical formula. Thus, the 0-D model does not provide information about the flow and pressure distribution inside the channels.

As stated by Kostandopoulos and Johnson [16], this was the "first comprehensive relation that expresses explicitly the pressure drop of clean wall-flow monoliths in terms of their manufacturing parameters and exhaust properties," and it was a breakthrough in the understanding the flow physics within particulate filters and a useful tool for their design optimization.

The assumption allowing to uncouple the friction and through wall losses introduced in the 0-D model was shown to be valid for the range of parameters considered by Kostandopoulos and Johnson [16]. For these parameters, the 0-D model predictions are nearly identical to their 1-D model. However, these might deviate if the filter parameters or flow are different (e.g. if the walls have higher permeability), even in laminar flow. This can be seen in Figure 1.2, which illustrates the difference between the pressure drop predicted with the Kostandopoulos and Johnson [16] 1-D and 0-D models for different channel Reynolds numbers. Figure 1.2 (a) shows that the two models perform almost identically (within the laminar regime) for a filter with a low permeability ($k = 1.9 \times 10^{-13}$), typical for catalyst coated filters. Figure 1.2 (b) shows that, for a filter with a high permeability ($k = 5.5 \times 10^{-12}$), characteristic for a bare filter, there is a deviation between the two predictions for $Re_{d_h} > 1000$, and the 0-D model under-predicts the pressure drop compared to the 1-D model. The filter parameters (e.g. cell density, diameter, length, etc.) and permeabilities for this comparison have been taken from Prantoni et al. [14], cores #2 and #1 respectively, with a gas temperature of $T = 680[^{\circ}C]$.

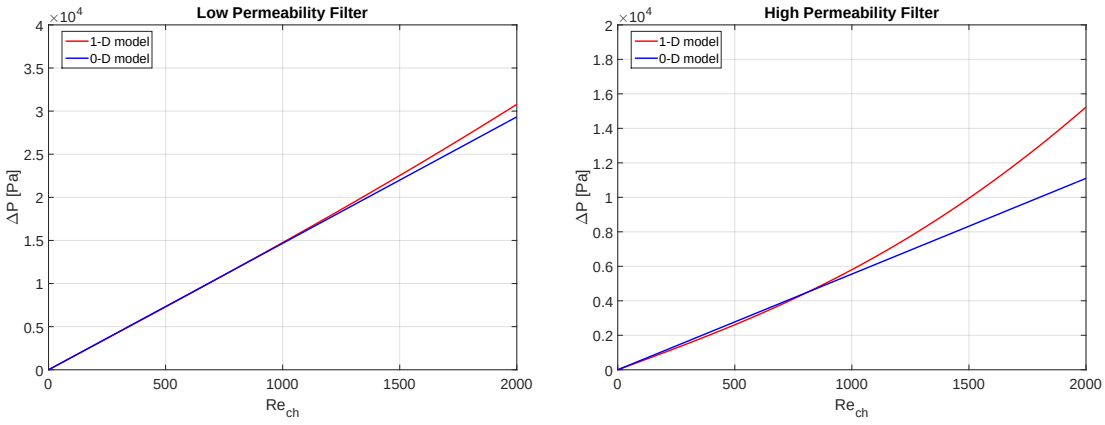

(a) (b)

Fig. 1.2 Comparison between the Kostandopoulos and Johnson (1989) 1-D and 0-D models predictions: (a) Catalyst coated filter with low permeability ($k = 1.9 \times 10^{-13}$) and (b) Bare filter with high permeability ($k = 5.5 \times 10^{-12}$). Filter parameters for cores #2 and #1 from Prantoni et al. (2019) have been used for calculations.

Therefore, since 1-D models make fewer assumptions about the flow physics compared to 0-D models, they are more likely to perform well over a wider range of

parameters. They also provide information about the flow distribution inside the channels, which is important for soot and ash accumulation analysis.

Ten years later, in 1999, Konstandopoulos et al. [19] extended the 1-D model of Kostandopoulos and Johnson [16] to account for the non-Darcian flow through the porous walls (see Darcy-Fochheimer Law in section 1.2.2.3), which may become relevant at high mass flow rates. However, the inclusion of this non-linear term means that the model equations cannot be solved analytically any more and they have to solved numerically instead. The authors used a "shooting" method for the numerical solution. The model predictions were then assessed using 3-D CFD analysis and experimental results for the pressure drop of four filters obtained at Johnson Matthey Sweden in the laminar flow regime on a cold flow rig. Note that the 3-D CFD analysis was performed on a simplified domain, which included a quarter of four neighbouring channels and the porous walls that separate them. The simplified domain was used as it would be too computationally expensive to use a full 3-D CFD approach to simulate the flow within all the channels of a particulate filter, and to the best of the author's knowledge this has never been done so far. The channels and through wall velocities were found to be in good agreement with the 3-D CFD results, and the pressure drop agreed well with the experimental data.

In 2000, Masoudi et al. [20] further extended the analytical solution of the 1-D model of Kostandopoulos and Johnson [16] by adding the pressure drop due to the channel plugs, the contraction and expansion losses due to the flow entering and exiting the particulate filter, and the non-Darcian effects. These extra pressure losses have been accounted for by adding them in series to the analytical solution of Kostandopoulos and Johnson [16]. However, the contraction and expansion loss coefficients and the Forchheimer term for the non-Darcian effects have been incorporated in a unique coefficient (not reported in the paper), which has to be determined empirically through experiments. This means that, in addition to the permeability, an extra coefficient has to be calibrated. The model was then validated against experimental data of the pressure drop of a filter tested at ambient temperature in laminar regime. Several filter lengths have been considered and a good agreement between the model predictions and the experimental data has been found.

Since the most common approach for calibrating the filter permeability is to fit the model equations to the experimental pressure drop, the choice of the model will have an effect on the value of the estimated permeability. For example, using a model that accounts for the pressure losses due to contraction and expansion will result in a higher permeability value estimate. Although a small difference in the value of the permeability might not affect significantly the estimated pressure drop at low mass flow rates, it might become important at high mass flow rates, for which the contribution of the through wall losses will increase.

In the same year (2000), Konstandopoulos et al. [21] extended the 0-D model of Kostandopoulos and Johnson [16] by adding a slip-flow correction to be used at high temperature. The model predictions were assessed with the experimental data of Kwetkus and Egli [22], and showed a good agreement. The authors also reported that the contraction and expansion losses were not included as they were found to be negligible.

In 2001, Konstandopoulos et al. [23] further extended the 0-D model of Kostandopoulos and Johnson [16] to account for the contraction and expansion losses and non-Darcian effects. Several formulae taken from other studies ([24], [17], [25], [26]) for the contraction and expansion loss coefficients were assessed. The model predictions agreed well with the experimental data of Masoudi et al. [20] at the lower mass flow rates, however they deviate for the higher values, under-predicting the pressure drop. The authors attributed this behaviour to the fact that the contraction and expansion loss coefficients used were mostly derived for single openings or perforated plates, and that these were "not adequate to quantify similar losses taking place in a DPF entrance and exit" [23]. The effect of the Forchheimer term was found to be negligible.

Hashimoto et al. [27] developed a new empirical 0-D model in 2002. The authors assumed that the total pressure losses of a particulate filter can be estimated by adding in series the pressure losses from five different sources, uncoupled from each other: 1) filter contraction and expansion, 2) channel friction, 3) through wall losses in the porous medium, 4) through wall losses in the soot layer and 5) inlet and outlet duct conical expansion and contraction (before and after the filter) losses. Filter contraction and expansion losses were investigated experimentally. The authors cut out the edges

of several filters, in the proximity of the plugs, and tested theses short plugged samples at different flow rates. The experimental results were then used to derive an empirical correlation for the sum of the contraction and expansion losses. Due to the nature of the experiments the resulting correlation is more suitable for the pressure losses in a perforated plate rather than the contraction and expansion losses in a filter. The channel friction losses were investigated in a similar manner, by testing several unplugged filters, and an empirical correlation to describe them was proposed. However, both proposed correlations do not have the dimensions of pressure, as they are $\left[\frac{kg}{m^3}\frac{m^{2.2063}}{s^{2.2063}}\right]$ and $\left[\frac{kg}{ms^2}m^{0.0814}\right]$, for the contraction/expansion and friction losses expressions respectively. Thus, this model cannot be considered strictly physical.

In 2003, Konstandopoulos [28] further extended the 0-D model of Kostandopoulos and Johnson [16] to account for the contraction and expansion losses, non-Darcian effects and change in density (compressibility effects). The author stated that "all developments so far have been based on the assumption of constant (at most temperature dependent) physical properties" and that "it may happen though that DPFs are flow tested at such high values of filter pressure drop where gas compressibility effects may become important" [28]. This was a considerable step forward, as accounting for the density changes due to the high back-pressure in the filter can greatly improve the performance of a model at high values of the back-pressure, as discussed in Chapter 6 of this thesis.

In the same paper Konstandopoulos investigated the effect of the contraction and expansion losses in particulate filters. This was done by fitting the new model to the experimental data for the pressure drop of four filters with different properties to calibrate both the permeability and the inertial loss coefficient (the sum of the contraction and expansion loss coefficients). Although the resulting values of the permeabilities are in agreement with the values reported in the literature for similar filters, the estimated inertial loss coefficients (ranging from 2.4 to 8.3) are considerably higher than any other value reported so far, as reported in section 1.2.2.2.

In 2004, Haralampous et al. [29] proposed a new compressible 1-D model similar to Bissett's model [15]. In this model, which requires a numerical solution, the gas density along the channel axis depends on the local pressure but not on the local temperature.

The contraction and expansion losses are also accounted for. For the contraction losses the authors proposed a correlation to fit the data of Kays [24] for the contraction loss coefficient in laminar flow, while the expansion loss coefficient is derived from the Borda-Carnot equation. The authors also performed hot flow experiments, where the flow to the filter was provided from the exhaust gases of a diesel engine. The pressure drop predictions of the 1-D model were shown to agree well with the experimental data. As in the paper of Kostandopoulos and Johnson [16], Haralampous et al. [29] proposed a 0-D approximation of their model, which was shown to agree well with the predictions of the 1-D model in the range of parameters considered in their study.

In 2017, Watling et al. [30] also proposed a 1-D compressible model based on Bissett's model [15]. A momentum correction coefficient has been added into the momentum equations for the inlet and outlet channel to reflect the fact that the flow profile within the channels is not flat. The authors used the momentum correction coefficient that corresponds to a fully developed laminar flow profile in a square channel. However, the flow within the channels is not likely to be fully developed as it will be affected by the deceleration and acceleration of the flow in the inlet and outlet channel, respectively, due to the mass flow passing from one channel to another.

The contraction and expansion losses in [30] have been calculated using the coefficients proposed by Kays [24], with the momentum correction coefficient also included. In contrast with all previously reviewed models, Watling et al. [30] used the static pressure losses, rather than the irreversible mechanical energy losses. Thus, in their formulation, the expansion results in a pressure rise. Nevertheless, the authors stated that "while the expansion results in a pressure rise, mechanical energy is still lost in the process" [30]. The model was assessed with cold flow experimental data for two filters tested on a SuperFlow rig, and a good agreement was shown.

In 2018 Depick et al. [31] proposed a revised single equation pressure drop model derived for both dynamically incompressible and compressible flow. According to the authors the compressible model accounts for the effect of both temperature and pressure on the density. However, the energy equation is not included in the model formulation to calculate the temperature along the filter, and the temperature profile has to be assumed a priori. Moreover, in order to be used, this model requires the

knowledge of the pressure upstream the filter (the filter back-pressure) to calculate the density at the entrance of the inlet channels, which usually is (or should be) an output of the model. When comparing their model with the model of Kostandopoulos and Johnson [16], the authors report that "for the simulation efforts, the inlet pressure was adjusted in order to achieve an inlet density of $0.54[kg/m^3]$ as indicated in the paper of Kostandopoulos and Johnson [16]" [31]. It is not reported how this operation was carried out. The models of Depick et al. [31] do not include the contribution to the total pressure drop due to contraction and expansion losses.

It is worth mentioning that a few other single inlet/outlet channel models exist, such as the 2-D models of Opris and Johnson [32] and Oxarango et al. [33], the model of Basu et al. [34], which includes the effects of the soot loading (these were also included in [29], [30] and [31]), and the models of Piscaglia and Ferrari [35] and Torregrosa et al. [36], which account for the unsteady effects. The 2-D studies have not been included in the present literature review as they are more complex and provide relatively little to no advantages compared to the 0-D and 1-D models, as reported by Yang et al. [37], while the other models have not been included as they focus on aspects which are outside the scope of the present thesis.

1.2.1.2 Multi-channel models

All the models reviewed until this point are based on a scaling approach through which the pressure drop of the filter can be modelled by considering a simplified geometry including only one inlet and one outlet channel. As reported by Bissett [15], the approximation introduced through such scaling approach can be justified when the velocity profile entering the filter is flat, so that the mass flow rate is the same in all channels, and when the ratio between the cell hydraulic diameter and the filter diameter is very small ($d_h/D_{Filter} \ll 1$), so that the full coupling between open and closed channels is negligible on the scale of the entire filter. The applicability of the scaling approach is also limited to filters with homogeneous properties (e.g. all the channels have the same hydraulic diameter, all the porous walls have the same permeability, and soot is distributed homogeneously).

However, in most of the applications the velocity profile upstream the filter is likely to be non-uniform. This can be due to a combination of different factors such as: a) the concentric or eccentric expansion upstream the filter, present in most after-treatment systems because of the different diameter between the exhaust pipeline and the filter, b) a non-uniform soot loading , c) a non-uniform wall permeability, often present in catalyst coated filters due to the non-homogeneous deposit of catalyst coating material in different channels, d) a swirling flow upstream the filter, which might be present in turbo- or super-charged systems. In such cases, accurate modelling of the particulate filter flow is much more challenging, not only because of the flow exchange between neighbouring channels, which should be taken into account, but also, and most importantly, because the flow profile upstream the filter cannot be known a priori.

The formulation of the first multi-channel model was proposed by Konstandopoulos et al. [38] in 2001. The model includes a system of coupled differential equations describing mass, momentum and energy balance for each channel of the filter. The authors state that "the mathematical problem can be solved in principle". However, due to a lack of adequate computational resources (in 2001), Konstandopoulos et al. [38] did not solve the full problem but proposed a simplified version instead. The simplified version of the model involved a series of single inlet/outlet channels placed along the radius of the filter but uncoupled between each other. This simplification, named "homogenization method" by the authors, requires again that $d_h/D_{Filter} \ll 1$, so that "the coupling between open channels or between closed channels is insignificant on the scale of the entire filter" [38]. The simplified model was applied to an axisymmetric, so that ultimately only one line of channels was simulated. The velocity distribution upstream the filter has to be assumed a priori and the density is assumed constant along the filter (incompressible flow).

The same or similar a approach was used in the studies of Haralampous et al. [39], Kostoglou et al. [40], Koltsakis et al. [41], Torregrosa et al. [36] and Pozzato et al. [42]. Among these models, it is worth mentioning the effort of Koltsakis et al. [41], as in contrast with the other studies they tried to calculate the velocity profile upstream of the filter instead of prescribing it a priori. This was done by assuming that the pressure drop of each channel is equal and adjusting the flow rate entering into each channel

with an iterative method. However, this assumption limits the flow configuration as the pressure distribution upstream of after-treatment devices with an expansion can be highly non-uniform due to the high velocity central flow impinging onto the middle part of the monolith, as shown in Chapter 7.

An alternative to modelling filter flow is using 3-D CFD simulations where the filter is modelled as a porous medium, as shown in the recent study of Cirstea et al. [43]. However, the flow within each channel is not considered with this approach and thus a lot of useful information is lost. For example, similar to the 0-D models, this approach cannot be used for soot and ash accumulation analysis.

1.2.1.3 Summary

To summarise, the literature review of particulate filter models has shown that although an extensive research effort has been carried out in order to model accurately the flow behaviour in a particulate filter, several gaps still need to be filled.

Firstly, there is a lack of experimental data of the pressure drop for clean filter at high flow rates and temperatures. The knowledge of the filter pressure drop under these conditions would be useful in order to validate models and ensure that their derivation is based on the physics of the flow. Most of the reviewed models have been validated only against one or two sets of data, either at ambient temperature or at high temperature but with the presence of soot and ash. This might results in a model which agrees well with the experimental data it was calibrated with, but might differ considerably from experimental data collected under different flow conditions.

Secondly, all of the reviewed models are limited to laminar flow conditions, even though several of them are compared with experimental data where the Reynolds number is higher than the critical value based on the channel parameters. The flow in particulate filters might be turbulent under some of the engine operational conditions and thus this is a limitation.

Filling both these gaps would be especially relevant for improving models prediction capabilities and models validation under GPFs operational conditions (higher flow regimes and temperatures).

There is also an uncertainty in the estimation of the contraction and expansion losses (in particular the contraction losses in laminar flow as discussed in section 1.2.2.2). Most of the authors use different equations or methods to calculate the contraction and expansion loss coefficients. The inclusion of inaccurate contraction and expansion losses in a particulate filter model might affect the calibration of the permeability. These inertial losses become even more important for higher velocities characteristic to GPFs operating regime.

Finally, the multi-channel models currently available require the knowledge of the velocity or pressure profile upstream of the filter (which is not known a priori) and do not take into account the full cross-flow between the channels, instead modelling the filter as a collection of identical inlet/outlet channel pairs. These shortcomings might greatly affect the models performance.

Despite the gaps reported above, it can be safely stated that the majority of the researchers who investigated the flow in particulate filters agree that the friction along the channels, the passage of the flow through the porous wall, the contraction and expansion at the inlet and outlet of the filter and the density change effects (at high values of the back-pressure) are the main mechanisms through which pressure (and thus energy) is lost in a particulate filter. The models developed under these assumptions agree reasonably well with existing experimental data. Thus, the next section will examine these contributions and review the available methodology for their estimation.

1.2.2 Pressure losses

This section reviews the most relevant characteristics of the friction losses, the contraction and expansion losses, and the through wall losses, in the contest of particulate filters modelling. A summary including the relevant findings is reported at the end of the section.

1.2.2.1 Friction losses

Flows in pipeline and duct systems are encountered in many hydraulic applications and for this reason the pressure losses associated with them have been extensively

investigated over the years. Friction losses in particular attracted a lot of attention as they are often the main source of pressure losses in such systems and thus are often referred to as "major losses".

A brief explanation of the physical mechanism through which friction losses are generated is given below, while a more detailed discussion can be found in most of the books on the fundamentals of fluid mechanics (e.g. Munson et al. [44] or Cengel and Cimbala [45]). When a viscous fluid moves along a solid boundary the no-slip condition dictates that the speed of the fluid at the boundary is zero, while at a certain distance away from the boundary, the speed of the fluid is that of the bulk flow. Due to the viscosity of the fluid and the velocity gradient between the boundary and the bulk flow shear stress is generated, and thus a shear force (or viscous shear force), which opposes the motion of the fluid. Thus, in order to move a fluid within a pipeline with no acceleration, a pressure force (in the direction of the flow) has to be supplied to balance the viscous shear force (in the direction opposite to the flow). The overall losses of pressure along a pipeline caused by the viscous shear forces are called friction losses.

The magnitude of the friction losses depends on the flow characteristics, i.e. whether this is in the laminar, transitional or turbulent regime and/or the flow is fully developed or developing. Friction losses also depend on the characteristics of the walls, e.g. whether they are smooth or rough and/or solid (meaning that the flow can not pass through them) or porous (meaning that material has a certain permeability and the flow can pass through them). Due to the relevance of the topic for this thesis, the following sections describe the most relevant features of the friction losses under different conditions, while a more detailed discussion can be found in fluid mechanics textbooks such as Munson et al. [44] or Cengel and Cimbala [45].

Friction losses in channels with solid walls - Fully developed flow

In a pressure-driven flow within a horizontal pipe of constant diameter, when the **fully developed flow** is established and under steady state conditions, the pressure losses due to friction per unit length are constant. These losses can be expressed by an empirical

equation, namely the Darcy-Weisbach equation:

$$\Delta P_{F.D.F.} = C_f \frac{L}{D} \frac{\rho U^2}{2}, \tag{1.1}$$

where, $\Delta P_{F.D.F.}$ is the pressure drop for fully developed flows, C_f is the Darcy friction factor, L and D are the length and hydraulic diameter of the pipe, ρ is the density of the fluid and U is the mean cross-sectional axial velocity.

The Darcy friction factor is an empirical dimensionless coefficient that depends on the roughness of the surface and the flow regime (i.e. on the density and viscosity of the fluid). The Moody chart (Figure 1.3) shows the graphical representation of the Darcy friction factor and its functional dependence on the pipe Reynolds number Re and the surface relative roughness ε/D, where ε is a measure of the surface roughness. Note that this chart is valid only for circular pipes with steady, fully developed and incompressible flow, as it was derived from the experimental data of Nikuradse [46] that was collected under these conditions.

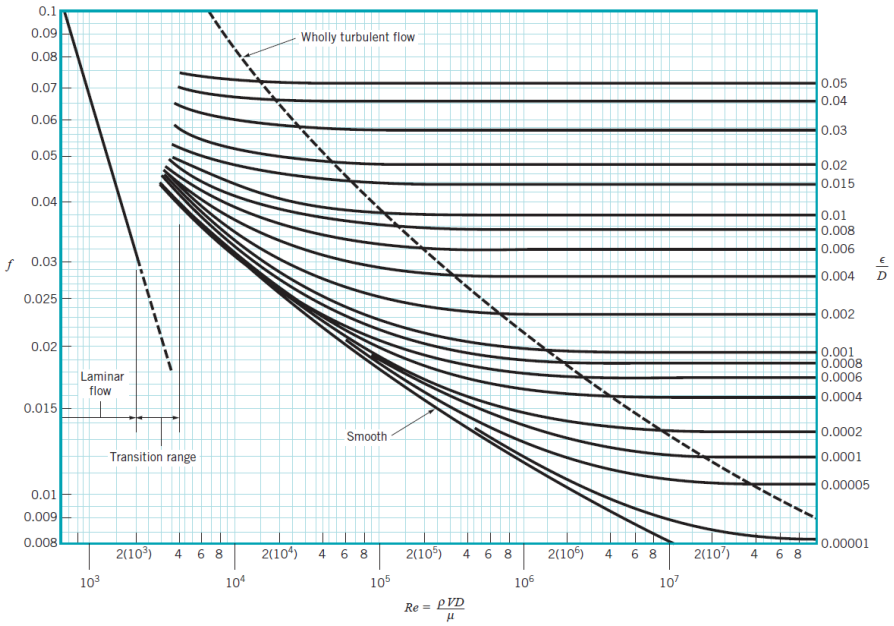

Fig. 1.3 Moody Chart Munson (2009).

Figure 1.3 shows that **the friction factor in laminar flows** is independent from the surface relative roughness, and that it varies linearly with the Reynolds number. In a circular pipe under laminar flow conditions the Darcy friction factor can be expressed as

$C_f = 64/Re$. The transitional regime has not been properly characterised and predicting friction losses in transitional flows is still a challenge. **The friction factor in turbulent flows** varies with the surface relative roughness and its dependence on the Reynolds number is not linear. Colebrook [47] was the first to propose a correlation, known as Colebrook equation, for the Darcy friction factor in turbulent flow:

$$\frac{1}{\sqrt{C_f}} = -2\log\left(\frac{\frac{\varepsilon}{D}}{3.7} + \frac{2.51}{Re\sqrt{C_f}}\right). \tag{1.2}$$

However, the Colebrook equation does not provide an explicit expression of C_f for given Reynolds numbers and surface roughness and it is not possible to solve Eq. 1.2, for the friction factor, analytically. For this reason many authors tried to approximate the Colebrook equation in order to have an explicit analytical formula. Most of the available approximations have been reviewed and reported by Brkić [48].

Among all the correlations reported by Brkić [48], only the correlation proposed by Churchill [49] (1977) can be used in the laminar, transitional and turbulent regime, while all the others can be used only in the turbulent flow regime.

Since the Colebrook equation has been derived from the experiments of Nikuradse [46] on pipes with circular cross-section, all the approximations of the Colebrook equation are limited to pipes with circular cross-section. This means that these approximations would not be adequate to describe the friction factor coefficient in the channels of a particulate filter, since they are typically of square cross-section.

A comprehensive review on the friction losses in pipes of rectangular and square cross-section has been performed by Jones [50]. Jones observed that the friction factor for both the circular and rectangular ducts varies with the Reynolds number with a similar trend and that the two can be correlated by means of a modified Reynolds number defined as:

$$Re^* = \frac{64}{C\left(\frac{w}{s}\right)} Re, \tag{1.3}$$

where, C is a constant that can be determined experimentally and depends on the geometry, w and s are the width and hight of the channel and Re is the standard Reynolds number based on the hydraulic diameter. For a square channel the constant $C = 56.908$, while the ratio between the width and hight is $w/s = 1$. Hence, the modified

Reynolds number for square channels is $Re^*_{Square} = \frac{64}{56.908} Re$. This means, for example, that in laminar flow the Darcy friction factor for a duct with square cross-section is $C_f = 56.908/Re$.

Friction losses in channels with solid walls - Developing flow

In the entrance region of a pipe the flow is termed **developing flow** and it reaches the fully developed stage only after a certain distance downstream the entrance. The most relevant feature of these flows is an increased pressure loss with respect to fully developed flow, caused by the development of the boundary layer.

The pressure losses in **laminar developing flows** ($\Delta P_{D.F.}$), are usually estimated by adding two components: 1) the pressure losses for fully developed flow ($\Delta P_{F.D.F.}$), and 2) the additional pressure losses due to momentum change and accumulated wall shear difference between developing and developed flow [51]:

$$\Delta P_{D.F.} = \Delta P_{F.D.F.} + K(x)\frac{\rho U^2}{2}, \tag{1.4}$$

where, $K(x)$ is a dimensionless coefficient, often referred to as incremental pressure drop number or pressure defect, ρ is the density of the fluid and U is the cross-sectional mean velocity. $K(x)$ increases monotonically from zero at the location in which the velocity profile, typically assumed as flat, starts to develop (e.g. at the entrance of a duct) to a constant value $K(\infty)$ in the fully developed region. The length of the transitional region in which the velocity profile is developing is called hydrodynamic entrance length L_{hy}, and is commonly defined as the distance from the inlet to the cross-section where the centreline velocity reaches the 99% of the fully developed centreline velocity. Therefore, when the pipe length $L \gg L_{hy}$, Eq. 1.4 can be rewritten in the following form:

$$\Delta P_{D.F.} = \Delta P_{F.D.F.} + K(\infty)\frac{\rho U^2}{2}. \tag{1.5}$$

While the pressure losses in a fully developed flow can be estimated through the established Darcy-Weisbach equation, there is no agreement on the value of $K(\infty)$ (derived experimentally or numerically) and, to the authors' knowledge, there is only one established correlation for $K(x)$.

Hagenbach [52] was the first to attempt to define a correction factor (the constant $K(\infty)$ in Eq. 1.5) to account for the additional losses due to boundary layer development. Other notable experiment-based studies have been performed by Knibbs [53] (who performed an analysis of Poiseuille's [54] and of Jacobson's [55] experiments), Schiller [56], Dorsey [57], Rieman [58], Weltmann and Keller [59] and Beavers et al. [60]. A summary of the corresponding values of $K(\infty)$ is shown in Table 1.1. The maximum variation between different results exceeds 20%. The values of the standard deviation of $K(\infty)$ in the experiments conducted by each author is also quite high. In most of these studies, the details of the experimental set-up are not reported in full, making the assessment of the results difficult. In the studies of Dorsey [57] and Poiseuille [54], in which the apparatus is described in some detail, the test sections (the ducts) used for the experiments are preceded, respectively, by a sharp-edged contraction and a round-edged contraction (details of the rounding radius are not given). As a consequence, it is likely that in these experiments the flow velocity profile entering in the duct was not uniform. Moreover, in the case with sharp-edged contraction a recirculation region might form right after the contraction, causing a constriction of the main flow cross-section known as "vena-contracta" and increasing the pressure losses. These two factors have not been accounted for in these studies, influencing the values of $K(\infty)$.

Table 1.1 Experimental values of $K(\infty)$.

Author	$K(\infty)$	Standard Deviation	Range
Hagenbach [52]	0.5800	-	-
Knibbs[1] [53]	1.2509	0.1860	1.040 - 1.660
Knibbs[2] [53]	1.2812	0.4390	0.580 - 2.100
Schiller [56]	1.3188	0.1431	1.115 - 1.450
Dorsey[3] [57]	1.0673	0.1033	0.820 - 1.180
Rieman [58]	1.2483	0.0161	1.220 - 1.268
Weltmann and Keller [59]	-	-	1.080 - 1.320

[1] From Poiseuille [54] experiments
[2] From Jacobson [55] experiments
[3] From Poiseuille [54] experiments

Numerical studies to determine the value of $K(\infty)$ also present a wide range of values, as summarised in Table 1.2. These investigations employ principally four different methods, as documented by Shah and London [51] axially matched solutions, integral solutions, solutions by linearising momentum equations, and solutions using a finite difference method.

Table 1.2 Theoretical/numerical values of $K(\infty)$.

Author	$K(\infty)$	Method
Atkinson and Goldstein [61]	1.410	Matched
Schiller [56]	1.160	Integral
Langhaar [62]	1.280	Linearisation
Hornback [63]	1.269	FDM
Schmidt and Zeldin [64]	1.314 - 1.397[4]	FDM
Bender [65]	1.25	FDM

The first attempt to derive an expression for the pressure loss accumulation in the developing part of the pipe flow was made by Shapiro et al. [66] who derived a theoretical correlation for the local pressure losses in the entry region of a pipe in laminar flow:

$$\Delta P^*_{D.F.} = 13.74\sqrt{x^+}, \tag{1.6}$$

where, x^+ is the dimensionless axial distance from the entrance in the flow direction, defined as $x^+ = x/(DRe)$, x is the axial distance from the entrance in the flow direction and $\Delta P^*_{D.F.}$ is the dimensionless pressure drop, defined as $\Delta P^*_{D.F.} = \Delta P_{D.F.}/\frac{\rho U^2}{2}$. This correlation was found to be in good agreement with the experimental results of Kline and Shapiro [67]. However, the applicability of this correlation is limited to $x^+ \leq 10^{-3}$ and, therefore, it can be used only in a very limited number of applications.

Bender [65] was the first to derive a correlation for the full range of x^+:

$$\Delta P^*_{D.F.} = 13.74\sqrt{x^+} + \frac{1.25 + 64/x^+ - 13.74\sqrt{x^+}}{1 + 0.00018(x^+)^{-2}}. \tag{1.7}$$

[4]Depends on the Reynolds number

Eq. 1.7 was derived combining Eq. 1.6 for small x^+ with Eq. 1.5 for $x^+ \to \infty$ with $K(\infty) = 1.25$, which is the constant found by Bender through his study. The matching was done using Bender's finite difference modelling results [68], which are often misquoted as being an "exact" solution. The main limitation of Bender's correlation is that it can be applied exclusively to pipes of circular cross-section.

Bender's correlation was later expanded by Shah [69], who generalised it so that it could also be used for square, rectangular and concentric annular ducts:

$$\Delta P^*_{D.F.} = 13.76\sqrt{x^+} + \frac{K(\infty) + (fRe)(4x^+) - 13.76\sqrt{x^+}}{1 + C(x^+)^{-2}}, \tag{1.8}$$

where $K(\infty)$, f (Fanning friction factor $f = C_f/4$) and C are coefficients which depend on the duct cross-section. According to Shah and London [51], Eq. 1.8 and the value of the coefficient C were computed in such a way that the $\Delta P^*_{D.F.}$ provided the least rms error when compared with the data of Liu [70]. However, in the same text, the authors reported that the data used for the fitting/validation were only tabulated by Liu, who interpolated them from a graph published in the earlier numerical work of Shah and Farnia [71].

Comparing Shah's correlation with the data of Liu (reported by Shah and London [51]) and of Bender shows that the values of $K(x)$ accurately match only for $x^+ \leq 0.02$ (Figure 1.4).

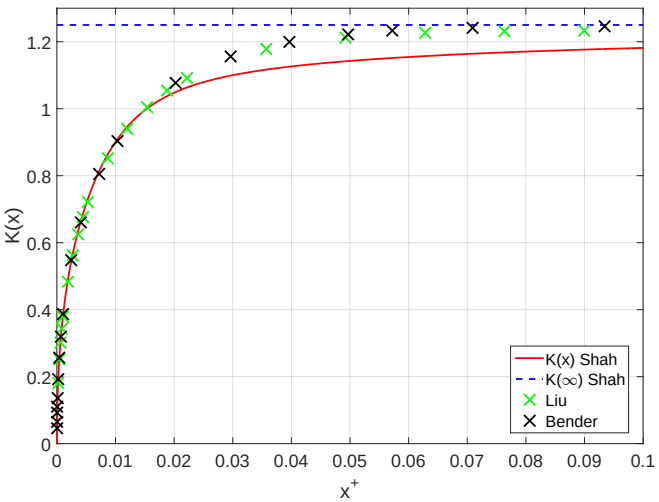

Fig. 1.4 $K(x)$ in Shah's Correlation vs data of Liu and Bender.

Thus, to the best of the authors' knowledge, Eq. 1.8 has not been truly assessed against experimental data prior or after the publication.

Finally, Su et al. [72] proposed a correlation derived by fitting CFD results for elliptical channels:

$$\Delta P^*_{D.F.} = (4x^+)\left[\left(C(x^+)^n\right)^N + \left(20.11 + 18.93e^{-2.44\varepsilon} - \frac{19.3}{1+2.35\varepsilon}\right)^N\right]^{1/N}, \quad (1.9)$$

where, C, n and N have been derived through curve fitting and ε is the cross-section aspect ratio.

Similar correlations have been developed by Yilmaz [73] and Muzychka and Yovanovich [74] for ducts of arbitrary cross-section without the need of tabulated data for each pipe type that Shah's correlation requires. They are all based on the Shah's correlation and therefore do not offer an improvement in the accuracy of the predictions.

Another parameter relevant for practical applications is the hydrodynamic entrance length, as this determines the distance after which the flow becomes fully developed. The hydrodynamic entrance length L_{hy} is commonly defined as the distance from the inlet where the centreline velocity reaches the 99% of the fully developed centreline velocity and is usually expressed through a dimensionless hydrodynamic entrance length L^+_{hy}:

$$L_{hy} = L^+_{hy} DRe. \quad (1.10)$$

Table 1.3 reports the theoretical/numerical values of L^+_{hy} proposed by different authors for laminar developing flows in pipes of circular cross-section.

Table 1.3 Theoretical/numerical values of L^+_{hy}.

Author	L^+_{hy}	Method
Atkinson and Goldstein [61]	0.0650	Matched
Schiller [56]	0.0288	Integral
Langhaar [62]	0.0575	Linearisation
Bender [65]	0.0566	Theoretical

So far the **turbulent developing flows** have received less attention than the laminar ones, and they are generally considered more complex. The pressure losses in turbulent developing flows are usually estimated with Eq. 1.5. Schetz and Fuhs [75] reported $k(\infty) = 0.04$ for smooth pipe with well rounded inlet and $Re > 10^5$, while for fully rough pipe this value can increase up to two or three times higher. Regarding the hydrodynamic entrance length textbooks such as Munson et al. [44] or Cengel and Cimbala [45] report $L_{hy} = 4.4DRe^{1/6}$, which is considerably shorter than the laminar one.

Friction losses in channels with passive porous walls

The two previous sections focused on the discussion of the friction losses in channels with solid walls. However, the channels of the wall-flow monoliths used for particulate filters are made of permeable porous materials and the friction losses in these types of channels can present different characteristics than those in solid walls. The friction losses in channels with permeable porous walls also depend on whether the walls are passive, meaning that there is no mass flow incoming or outgoing through the porous walls, as in catalytic converters, or active, meaning that there is a mass flow incoming or outgoing through the porous walls, as in particulate filters. This section provides some details about the friction losses in channels with passive porous walls, while the next section discusses those with active porous walls.

Flows in channels with passive porous walls are typically encountered in engineering applications such as catalytic converters and fuel cells as they provide a larger contact area with the fluid when compared to solid walls. This characteristic is usually exploited to promote chemical reactions or heat and mass transfer [76].

In these types of channels part of the fluid flows within the porous wall, as shown in Figure 1.5, and the velocity of the flow at the interface with the porous wall is not zero (the no-slip condition does not apply). This effect is called slip flow and it causes an alteration of the characteristics of the friction losses. Note that, as shown later in section 1.2.2.3, the slip flow can occur also at high temperature due to the fluid rarefaction effects.

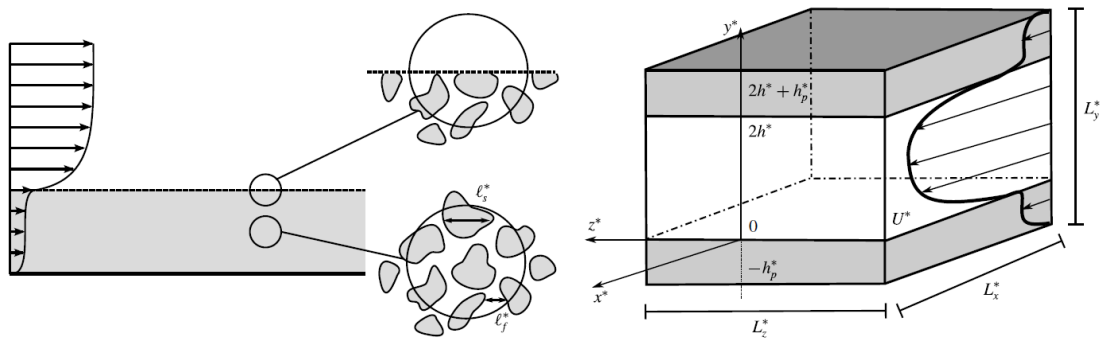

(a) (b)

Fig. 1.5 Sketch of the flow velocity profile along a porous wall: (a) Flat porous plate and (b) Infinitely wide channel with two porous walls Rosti et al. (2015).

Jimenez et al. [77] performed a DNS (Direct Numerical Simulation) analysis of an infinitely wide channel with one porous wall and reported an increase of the friction factor, which can reach values up to 40% higher than in solid walls. Breugem and Boersma [78] performed a similar study and reported an increase of the friction factor of almost 50%. Hahn et al. [79] performed a DNS analysis of an infinitely wide channel with two porous walls and reported a significant reduction (up to almost 30%) of the friction factor. Breugem et al. [80] performed a DNS analysis of and infinitely wide channel with two porous walls and reported an increase of the friction factor up to three times higher than that for a channel with solid walls. They also explained that in the study of Hahn et al. [79] the decrease in the friction factor was attributed to the fact that they "assumed that the flow near the permeable wall is essentially laminar, and, because wall permeability causes a decrease in the viscous wall shear stress, they therefore found a decrease in the friction factor" [80]. The authors argued that in turbulent flow, the wall permeability causes an increase of the Reynolds shear stresses and thus an increase of the friction factor. Rosti et al. [81] also performed a DNS analysis of and infinitely wide channel with two porous walls and reported an increase of the friction factor. Suga et al. [76] performed a PIV (Particle Image Velocimetry) study on a very wide channel (almost 2-D) with one porous wall. Their experimental investigation also showed/confirmed that the turbulent shear stresses increase, resulting in a higher friction factor compared to solid walls. Additionally, they observed that the flow tends to transition from laminar to turbulent at lower Reynolds numbers than the flow in a

channel with solid walls. This effect was found to be highly influenced by the porous wall permeability. The authors reported that the laminar flow starts to transition at Reynolds number as low as $Re \sim 1000$ for highly permeable porous walls, while it transitions at $Re \sim 2000$ for porous walls with low permeability.

Although these studies seem to report consistent results, which show that with the introduction of passive porous walls the friction factor decreases for laminar flows and increases for turbulent flows, and that the transition from laminar to turbulent flow is shifted, a comprehensive correlation for the estimation of the friction factor with respect to the Reynolds number and porous wall permeability has never been proposed.

Friction losses in channels with active porous walls - Injection and extraction effect

The friction losses in channels with active porous walls exhibit different characteristics than those in passive porous walls. These changes depend on whether the mass flow is injected or extracted through the porous walls.

The first investigation on the topic is reported in the pioneering work of Berman in 1953 [82], which investigates the effects of flow extraction (or suction) on the velocity and pressure distributions in porous channels. The problem was approached theoretically considering the mass and momentum balance in a 2-D geometry with two parallel porous plates, with the flow assumed to be fully developed, laminar and in steady state. The fluid was treated as incompressible and the extraction of mass was imposed as uniform. The problem was reduced to a third-order non-linear ordinary differential equation with the aid of a stream function and solved through a perturbation technique that uses the wall Reynolds number as perturbation parameter. The wall Reynolds number is usually defined as $Re_w = \frac{\rho u_w D}{\mu}$, where u_w is the velocity through the wall and D is the channel hydraulic diameter. The author reported that the extraction of the flow from the channel decreased the friction losses. Nevertheless, Berman [82] pointed out that the method used for the solution of the model is valid only at low values of the wall Reynolds number.

A similar theoretical study was published by Yuan and Finkelstein in 1955 [83], who investigated the effects of both injection and extraction on the flow through porous

channels with circular cross-section. The channel was considered axisymmetric, and the same assumptions on the fluid and flow made by Berman [82] were applied. The problem was simplified in the same way as in the study of Berman [82]. However, in contrast to their predecessor, Yuan and Finkelstein further exploited the perturbation method, developing two different solutions for their model, one for small wall Reynolds number values and one for large ones. The authors then proposed two correlations to estimate the friction factor at low and high wall Reynolds numbers. These correlations showed that the friction factor decreases when the flow is extracted from the porous wall and increases when the flow is injected.

One year later, in 1956, Yuan [84] extended Berman's investigation of the 2-D channel flow to high values of the Reynolds number, using the perturbation method developed with Finkelstein in the previous paper. The author also proposed a correlation for the friction factor in this geometry, which showed a similar trend to the channel with circular cross-section.

Further relevant studies on the friction losses in channels with porous walls have been published by Kinney in 1968 [85] and Raithby in 1970 [86].

The study conducted by Kinney [85] considers a fluid flowing in an axisymmetric straight porous tube, of circular cross section, in the same conditions as the previous studies (e.g. fully developed laminar flow, etc…). The novelty of this investigation consists in the fact that the third-order non-linear ordinary differential equation, obtained in the same fashion as Yuan and Finkelstein [83], is solved numerically without the aid of a perturbation technique. The author states that the result of primary importance of his investigation is the functional relationship between the product of the Fanning friction factor and the channel Reynolds number fRe and the wall Reynolds number Re_w, which was termed the universal law of friction. However, in contrast with the previous work, the explicit formula relating fRe and Re_w, for the case under study, was not reported in the paper and the results are only presented through a plot.

The investigation conducted by Raithby [86] considered both a fluid flowing in an axisymmetric straight porous tube, of circular cross section, and in a two-dimensional straight porous duct (two parallel porous plates). Again, the same assumptions on the fluid and flow made by Berman [82] were applied in this study The third-order

non-linear ordinary differential equation, describing the motion of the flow, was solved numerically and the equations expressing the dependence of fRe on Re_w are given explicitly for both the geometries.

More investigations have been, carried out in the nineties. The most relevant are those of Cheng and Hwang, who published two papers, one with a theoretical approach [87] in 1992 and one with an experimental approach [88] in 1995. Both studies consider a channel with square cross section and only one porous wall, through which mass injection or extraction is applied.

In the first study [87], a 3-D model was used to describe the flow and the temperature fields in a square duct with one wall subjected to uniform fluid injection or extraction and heat transfer with constant heat flux. In contrast with the previous investigations, the flow was assumed laminar but developing and in steady state. Other assumptions were the constant thermophysical properties of the fluid, and a uniform wall mass transfer. Novel was also the solution approach, in which the three-dimensional Navier-Stokes equations were solved numerically with a velocity-vorticity method. However, an explicit correlation between fRe and Re_w was given only for the case of fully developed flow with injection.

In the second study [88] an experimental system was built for measuring the axial velocity distribution, pressure variation, wall temperature variation, as well as the bulk mean fluid temperatures at the inlet and outlet of a one porous wall square duct with various fluid injection rates. The explicit correlation between fRe and Re_w was reported.

The most relevant study of the friction losses in porous channel flows, with regard to the particulate filters application, has been published by Bisset et al. [89] in 2012. They considered a 3-D square channel with four porous walls. The conditions imposed on the fluid and flow are the same as Berman's [82]. The 3-D Navier-Stokes equations describing the flow are solved numerically with the velocity-vorticity method. An explicit correlation between fRe and Re_w is given for both the case of extraction and injection, which in a particulate filter would correspond respectively to the inlet and outlet channels.

In order to compare and summarise the study reviewed here, the correlations of fRe versus Re_w proposed by Kinney [85], Raithby [86], Cheng and Hwang [88] and

Bisset et al. [89] are plotted in Figure 1.6. The Fanning friction factor for square cross-section channels with solid walls has been added to the plot for comparison. All of these correlations are valid only in laminar flow and no studies were found in the turbulent flow regime.

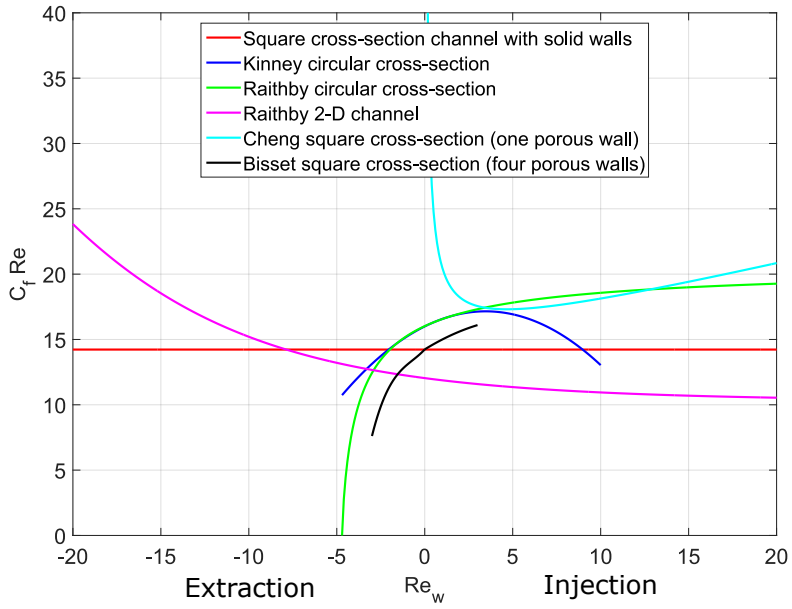

Fig. 1.6 Effect of mass flow extraction and injection on the friction factor.

Although the studies reviewed in this section show that the extraction and the injection of mass flow through porous walls can change the value of the friction factor, these effects are usually neglected in particulate filters models and it is standard practice to use the Darcy friction factor for a channel with solid walls for the estimation of the friction losses. Only the model developed by Watling et al. [30] included the correlations proposed by Bisset et al. [89] to account for the effects of the extraction and the injection, but the authors concluded that the effect of the inclusion of these terms was negligible for the range of parameters which were investigated.

1.2.2.2 Contraction and expansion losses

As discussed in the previous section, the pressure losses due to friction in long straight sections of a pipe can be calculated by using the friction factor. Most pipe systems, however, employ diverse types of fittings, valves, bends and/or sudden enlargements

and reduction of the cross section. In these systems, the additional components and change in geometry cause the flow to accelerate or decelerate and/or to increase the turbulence in the form of eddies causing additional losses, often referred to as "minor losses".

The complexity of most of the components makes a theoretical analysis extremely difficult to perform and therefore the estimation of these losses is usually performed through experimental techniques [44]. The most common method used to express these pressure losses is through a non-dimensional loss coefficient ζ, so that:

$$\Delta P = \zeta \frac{1}{2} \rho U^2. \tag{1.11}$$

Thus, the losses due to contraction and expansion are usually expressed as:

$$\Delta P_{Contr.} = \zeta_{Contr.} \frac{\rho U^2}{2}, \tag{1.12}$$

$$\Delta P_{Exp.} = \zeta_{Exp.} \frac{\rho U^2}{2}, \tag{1.13}$$

where, $\zeta_{Contr.}$ is the contraction loss coefficient, $\zeta_{Exp.}$ is the expansion loss coefficient and U is the mean cross section velocity in the smaller duct.

As a fluid flows in a pipeline system, a certain amount of mechanical energy is always lost irreversibly and can not be regained. This is in contrast to the static pressure, which can be either lost (e.g in a pipe with a flow path contraction) or gained (e.g in a pipe with a flow path expansion). The contraction and expansion loss coefficients can be defined to include either the static pressure change or the irreversible losses. Unless differently specified, in this thesis the contraction and expansion loss coefficients are used to estimate the irreversible losses.

Figure 1.7 illustrates where energy is dissipated in pipes with sudden expansion and contraction of the cross-section. Note that the situation is slightly different when the fluid is entering/exiting from a reservoir.

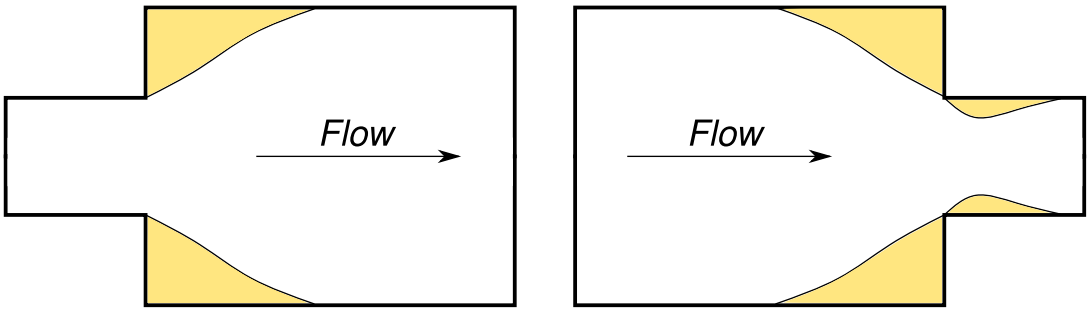

(a) (b)

Fig. 1.7 Energy dissipation regions in pipes with sudden expansion or contraction of the cross-section.

In a sudden expansion the flow decelerates as it enters the larger pipe. A part of the kinetic energy of the flow in the smaller pipe is lost due to viscous effects because the flow separates from the walls after the expansion, forming a recirculation region. The kinetic energy that is not dissipated is converted into static pressure. If the flow is discharged into a reservoir all the kinetic energy is dissipated.

A theoretical formula for the estimation of the expansion loss coefficient (Eq. 1.14) exists, and can be derived from the Borda-Carnot equation [44]:

$$\zeta_{Exp.} = \xi \left(1 - \frac{A_1}{A_2}\right)^2, \tag{1.14}$$

where A_1 and A_2 are the areas of the smaller and larger cross-section, respectively, and ξ is a coefficient that can vary between 0 and 1 and depends on the geometry. If the expansion is sudden, then $\xi = 1$, while if the expansion is gradual (e.g. if the pipe expands through a cone), then ξ has to be determined experimentally and its value will depend on how gradual is the change in section. Figure 1.8 shows how the expansion loss coefficient calculated from Eq. 1.14 varies with the expansion area ratio for a sudden expansion.

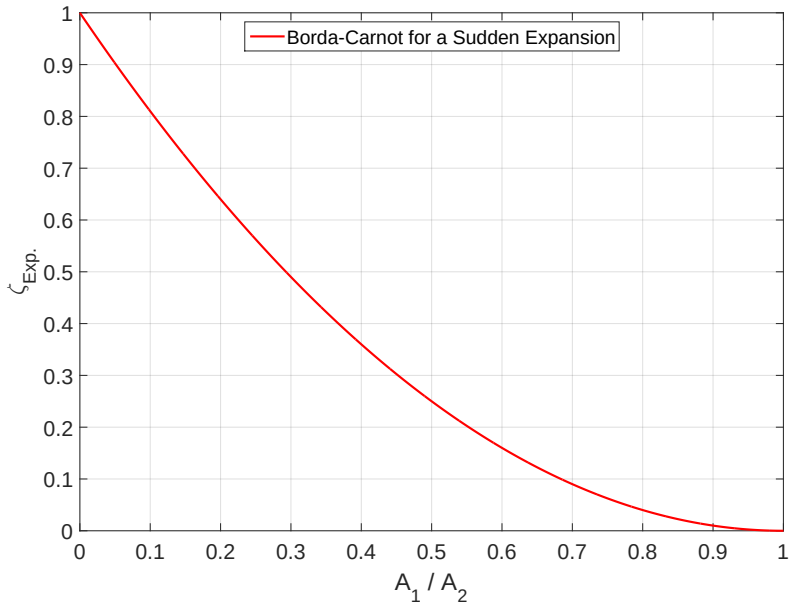

Fig. 1.8 Expansion loss coefficient versus contraction area ratio.

The maximum value of the losses due to flow path expansion equals the maximum value of the kinetic energy of the fluid in the smaller pipe. Since the Borda-Carnot equation for a sudden expansion is based on the assumption that the velocity profile approaching the expansion and the one some distances away from it are flat, and the kinetic energy for a flat profile is $\rho U^2/2$, then the maximum value of the expansion loss coefficient is 1. As shown by Kays [24], if the velocity profile approaching the contraction and the one after it are not flat, it should be taken into account. This can be done by using the kinetic energy correction coefficient, which relates the kinetic energy of the flow in a pipe cross-section to the velocity profile.

In the case of a sudden contraction the flow accelerates as it enters the smaller pipe. Here, part of the static pressure is converted into dynamic pressure, while another part is dissipated.

If the flow is entering the smaller pipe from a reservoir, the flow can only separate after the contraction, in the smaller pipe (Figure 1.7 (b)). As a result, the cross-section available for the fluid to advance is reduced with respect to the nominal hydraulic diameter of the smaller pipe and as a consequence the flow velocity is increased. This region is known as vena-contracta. Once the separation region starts to reduce in size, the fluid expands gradually (generating irreversible losses) until it can finally occupy the

whole pipe cross-section. The flow profile after the vena-contracta is not fully developed and thus additional pressure is lost after the contraction due to the flow development. As reported by Munson et al. "an obvious way to reduce the contraction losses is to round the entrance region, thereby reducing or eliminating the vena-contracta effect" [44].

If the flow enters the smaller pipe from a larger pipe, then, in addition to the vena-contracta, another separation region is formed upstream the contraction (Figure 1.7 (b)). This was shown in a PIV study performed by Durst and Loy [90] on laminar flows through a sudden contraction. This separation region also contributes to the generation of irreversible losses.

For the contraction loss coefficient various definitions can be found in the literature, which are all empirical and based on experimental data. The correlations proposed by Brightmore [91] (Eq.1.15), Merriman [92] (Eq.1.16), Weisbach [93] (Eq.1.17), Sullivan [94] (Eq.1.18) and Kays [24] (Eq.1.19 for turbulent flow and Eq.1.20 for laminar flow) are:

$$\zeta_{Contr.} = 0.7\left(1-\frac{A_1}{A_2}\right)^2, \tag{1.15}$$

$$\zeta_{Contr.} = \left(\frac{1}{C_c}-1\right)^2, \quad C_c = 0.582+\frac{0.0418}{1.1-\sqrt{\frac{A_1}{A_2}}}, \tag{1.16}$$

$$\zeta_{Contr.} = \left(\frac{1}{C_c}-1\right)^2, \quad C_c = 0.63+0.37\left(\frac{A_1}{A_2}\right)^3, \tag{1.17}$$

$$\zeta_{Contr.} = 0.5\left(1-\frac{A_1}{A_2}\right), \tag{1.18}$$

$$\zeta_{Contr.} = 0.5-0.4\frac{A_1}{A_2}, \tag{1.19}$$

$$\zeta_{Contr.} = 1.1-0.4\frac{A_1}{A_2}. \tag{1.20}$$

where A_1 and A_2 are the areas of the smaller and larger cross-section, respectively, and C_c is a coefficient that expresses the area ratio between the smallest cross-section at the vena-contracta and the smaller pipe hydraulic diameter.

Figure 1.9 shows how the contraction loss coefficient, calculated with these formulae, varies with the contraction area ratio.

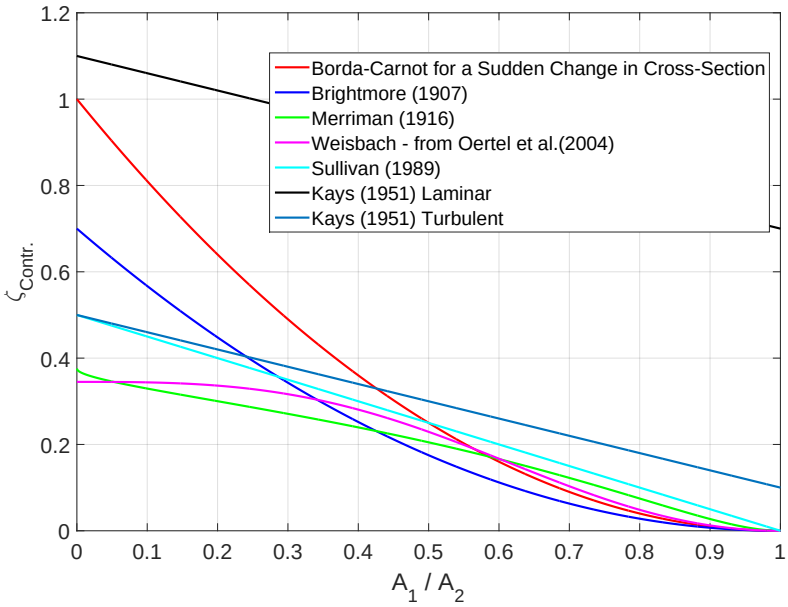

Fig. 1.9 Contraction loss coefficient versus contraction area ratio.

Note that very few details of the experiments performed by Brightmore [91] and used to derive Eq. 1.15 have been reported and that those used to derive Eq. 1.16 - 1.20 have not been reported at all.

Brightmore [91] investigated the losses due to contraction and expansion for two contraction and expansion area ratios ($A_1/A_2 = 0.25$ and $0.\bar{4}$). In this configuration, both the vena-contracta and the flow separation upstream should have been accounted for in the pressure losses. However, the location where the pressure was measured is not reported, and thus it is not clear whether the measured pressure drop included both loss sources. It is interesting to notice that in the study of Brightmore [91] the experimental data have been compared to the Borda-Carnot equation (Eq. 1.14) for a sudden expansion, which was also referred to as the "theoretical" expression for the estimation of the contraction loss coefficient. To the author knowledge, Brightmore is the only author who suggests using the Borda-Carnot equation as a theoretical expression for estimation of both the contraction and expansion loss coefficients for sudden change in cross-section. Also, Eq. 1.15 is the same as the Borda-Carnot equation (Eq. 1.14) for a sudden expansion multiplied by 0.7.

The correlations of Merriman [92] and Weisbach [93] (Eq. 1.16 and Eq. 1.17) only account for the losses due to the vena-contracta (it can be seen from the fact

that they use the coefficient C_c). The correlation reported by Sullivan [94] (Eq. 1.18) is an approximation of Weisbach's coefficient (as reported by Crane [95]), and no experiments were carried out. As reported by Brater [96], Eq. 1.16 and Eq. 1.17 have been shown to agree well with experiments for the turbulent flow regime, while the agreement in the laminar regime is not mentioned. The correlations proposed by Kays [24] (Eq. 1.19 and Eq. 1.20) only account for the losses due to enlargement after the vena-contracta, and use the cross-section restriction ratio C_c from Rouse [97], which was derived for orifice plate. Moreover, Eq. 1.20 does not seem to be well validated against the experimental data of Kays [24] for low Reynolds numbers, in multiple channel geometries, as shown by Aleksandrova et al. [98].

To the author knowledge, apart from the experiments of Kays [24], only Konstandopoulos [28] investigated experimentally the effect of the contraction and expansion losses in particulate filters while no other experiments on contraction and expansion losses in multi-channel geometry have been reported. As mentioned in section 1.2.1.1, Konstandopoulos [28] investigated the effect of the contraction and expansion losses in particulate filters by fitting a 0-D particulate filter model to the experimental data for the pressure drop of four filters with different properties to calibrate both the permeability and the inertial loss coefficient (the sum of the contraction and expansion loss coefficients). However, although the resulting values of the permeabilities are in agreement with the values reported in the literature for similar filters, the estimated inertial loss coefficients, ranging from 2.4 to 8.3, are considerably higher than any other value reported by other authors (e.g. Brightmore [91], Merriman [92], Weisbach [93], Sullivan [94] and Kays [24]).

Therefore, while a unanimous consensus on the value of the contraction loss coefficient to be used in particulate filter models has not been reached yet, and further research is required, in absence of more reliable data any equation among Eqs. 1.15 - 1.20 can been considered as good approximation for contraction losses in particulate filter geometries, as reported by Konstandopoulos et al. [23] and Haralampous et al. [29].

1.2.2.3 Through wall losses

Flows through porous media are encountered in many engineering applications (e.g. filtration systems) as well as in nature (e.g. lungs, river beds), and have been extensively investigated over the years. The through wall losses depend on several parameters, such as the flow rate, the fluid temperature and the characteristics of the porous media (e.g. porosity, tortuosity, pore size). Due to the relevance of the topic for this thesis, the following sections describe the most relevant features of these losses under different conditions.

Darcy's law

The first significant study on the flow through porous media has been conducted by Darcy in 1856 [99], who performed several experiments on the filtration of water through a packed column of sand.

The most important result derived from these experiments is the functional relation between the flow rate through the porous media and the pressure drop:

$$Q = -\kappa A \left(\frac{\Delta P}{\rho L} \right), \tag{1.21}$$

where Q is the volumetric flow rate through the porous medium, ΔP is the pressure drop, κ is the hydraulic conductivity of the porous medium, A is the cross-sectional area of the porous medium in the direction perpendicular to the flow, ρ is the fluid density and L is the length of the porous medium.

This original equation was then modified by replacing the hydraulic conductivity $\kappa = k/\nu$, which depends on the kinematic viscosity ν of the fluid, with the permeability k, which depends only on the material structure of the packed bed:

$$Q = -kA \left(\frac{\Delta P}{\mu L} \right). \tag{1.22}$$

Eq. 1.22 is commonly denominated Darcy's Law.

As reviewed in the book of Dullien [100], several models have been proposed to estimate the permeability of a porous medium using its mean porosity and pore diameter.

However, as pointed out by Dullien [100], the permeability is also affected by other parameters, such as the tortuosity, the pore shape and distribution, which are difficult to account for in a model. Therefore, the permeability of porous media is often determined empirically, by fitting the Darcy's Law to the experimental data of the pressure drop.

The Darcy's Law has been later supported by a theoretical study published by Whitaker [101]. The author showed that Darcy's Law can be derived from applying a volume-averaging technique to the Stokes equations for the macroscopic flow. This volume-averaging technique consists of averaging the microscopic flow field over a small spatial volume in order to obtain a macroscopic volume-averaged flow field. Using the same technique applied to the full Navier-Stokes equations, Whitaker [102] derived the so called Volume-Averaged Navier-Stokes equations (VANS), which can be considered as a generalisation of Darcy's Law.

Darcy-Forchheimer law

The accuracy and limitations of Darcy's Law have been discussed by several authors over the years [103]. Because the linear equation proposed by Darcy was not appropriate for describing pressure losses at high Reynolds numbers. The linear relationship between the pressure gradient, dp/dx, and the flow velocity, U, is more evident rewriting Darcy's Law (Eq. 1.22) in the following differential form:

$$\frac{dp}{dx} = -\frac{\mu}{k}U. \tag{1.23}$$

In 1901 Forchheimer [104] proposed a non-linear equation in order to extend the validity of Darcy's Law to high Reynolds numbers:

$$\frac{dp}{dx} = -\frac{\mu}{k}U - \beta\rho U^2. \tag{1.24}$$

This equation, commonly denominated Darcy-Forchheimer Law, adds a term that accounts for the kinetic energy of the fluid, which increases non-linearly with the velocity (and therefore the Reynolds number). The author justification was in fact that with the increasing of the Reynolds number the inertial effects become more important

and not negligible. The additional term is commonly referred to as the Forchheimer term, while the parameter β as the Forchheimer constant [105].

Although the Darcy-Forchheimer Law improves the accuracy of the predictions for high Reynolds number, it introduces an additional level of complexity related to the determination of the Forchheimer constant. From a dimensional analysis it can be understood that the constant β must have a dimension which is the inverse of a length. Nevertheless, multiple length scales are involved in fluid flow through a porous medium. Consequently, a theoretical determination of the Forchheimer constant is not an easy task. Similar to the permeability the Forchheimer term is usually determined empirically by fitting the Darcy-Forchheimer Law to the pressure drop measurements [105].

The Forchheimer term is typically not included in particulate filters models, as its effect was found negligible [23].

Slip flow permeability

The pressure drop through porous media can also be influenced by the temperature and pressure of the flow due to slip flow effects associated with gas rarefaction. At high temperatures and low pressures the mean free molecule path λ, defined as the average distance travelled by a molecule before colliding with another one in the equilibrium state [106], becomes higher. Several mathematical formulations of the mean free path can be found in the literature, as reported by Zhang et al. [106], and one should be careful when comparing equations from different authors. A formula for the mean free path can be expressed as:

$$\lambda = \frac{k_b T}{\sqrt{2}\pi d_c^2 P}, \tag{1.25}$$

where $k_b = 1.3806 \times 10^{-23}[J/K]$ is the Boltzmann constant, T and P are the fluid temperature and pressure, respectively, and d_c is the collision diameter. The collision diameter is often assumed to be equal to the molecule diameter [107].

As the mean free path increases, slip flow may occur and the molecules collisions with the wall surface should be taken into account [108]. In the case of gases, a common method to model this kind of flow is through the rarefied gas dynamics.

A key dimensionless parameter for considering the rarefaction effect is the Knudsen number:

$$Kn = \frac{\lambda}{D}, \tag{1.26}$$

where, λ is the mean free path and D is the flow conduit characteristic length [108], which in porous media is often taken as the pore diameter.

The influence of the rarefaction effect increases with the increasing of the Knudsen number [108] and four different flow regimes can be distinguished depending on the range of the latter [106], as shown in Table 1.4.

Table 1.4 Knudsen number range and flow regime description Zhang et al. (2012).

Knudsen number range	Flow regime description
$Kn < 10^{-2}$	**Continuum regime**: the continuum and thermodynamic equilibrium assumptions are appropriate, and the flow can be described by the Navier–Stokes equations with conventional no-slip boundary conditions.
$10^{-2} < Kn < 10^{-1}$	**Slip flow regime**: the non-equilibrium effects dominate near the walls. The no-slip boundary condition fails to provide agreement between theoretical predictions and experimental results, although continuum conservation equations can still be used to describe the bulk flow. However, the gas micro flow can still be analysed by solving the Navier–Stokes equations with slip velocity and temperature jump boundary conditions.
$10^{-1} < Kn < 10$	**Transition regime**: the rarefaction effects dominate and the continuum and thermodynamic equilibrium assumptions of the Navier–Stokes equations begin to break down. The slip models become more complex, and alternative solution methods, such as direct simulation Monte Carlo (DSMC), should be taken into account.
$Kn > 10$	**Free molecular regime**: the intermolecular collisions are negligible as compared with the collisions between the gas molecules and wall surfaces.

The classification of the flow regimes is indispensable for the selection of the technique used to model the flow, because the equations governing the flow, and consequently their solution method, change depending on the Knudsen number range, as shown in Table 1.4.

Since particulate filters operate at high temperatures and, as reported by Konstandopoulos and Johnson [16], the estimated Knudsen numbers could reach values close to

0.01 or higher, slip flow may occur. Under such condition, the most appropriate methods to predict the flow dynamics are the molecular dynamic (MD), direct simulation Monte Carlo (DSMC) or solution of linearized Boltzmann equation (LBE), which describe the flow at the molecular level. However, simulating a gas flow in a large scale system using these methods is still impractical due to the excessive amount of time required for the solutions.

Therefore, in particulate filters models, the effect of the slip flow is generally accounted for by using a modified expression of the permeability, called apparent permeability or slip permeability. Several authors, such as Maxwell [109], Beskok and Karniadakis [110], Konstandopoulos and Johnson [16], Konstandopoulos et al. [21] and Haralampous et al. [29], proposed different formulae for the apparent permeability, which is usually correlated to the standard permeability k_{Non_Slip} and the Knudsen number Kn. Among these formulae it is worth reporting the correlation proposed and used by Konstandopoulos et al. [21]:

$$k_{Slip} = k_{Non\_Slip} SCF, \tag{1.27}$$

where $SCF = 1 + Kn\left(1.257 + 0.4e^{-1.1/Kn}\right)$ is the Stokes-Cunningham Factor. This correlation was validated by Konstandopoulos et al. [21] using the experimental data of Kwetkus and Egli [22], and a good agreement was demonstrated.

1.2.2.4 Summary

To summarise, the literature review of the relevant contributions to the pressure losses in particulate filters has shown that although an extensive research effort has been carried out in order to model the friction losses, contraction and expansion losses, and through wall losses, several gaps still need to be filled.

Firstly, although the different types of friction losses are generally well understood, the losses due to developing flow and the losses in channels with porous walls are still not entirely or properly characterised. Regarding the developing flow losses, none of the proposed correlations for the pressure defect $K(x)$ estimation has been validated with experimental data or up to date RANS CFD analysis. Additionally, different

experimental and numerical studies reported different values for the pressure defect asymptotic value $K(\infty)$ as well as for the hydrodynamic entrance length L_{hy}. Regarding the friction losses in channels with porous walls, the transition from laminar to turbulent flow appears to occur at lower Reynolds numbers than in solid walls but it is not well characterised.

Secondly, while the expansion loss coefficient for a sudden expansion can be estimated with the Borda-Carnot equation, different experimental studies reported different values for the contraction loss coefficient for a sudden contraction and its variation with the contraction area ratio. Additionally, as reported by Brater [96], several equations to estimate the contraction loss coefficient (i.e. Eq. 1.16 and Eq. 1.17) have been shown to agree well with experiments for the turbulent flow regime, while the agreement in the laminar regime is not mentioned.

Since both friction and contraction losses are used for modelling particulate filters (as well as other multi-channels devices), a further understanding and characterisation of these losses would be useful in order to improve the accuracy of particulate filter models.

1.3 Aims and objectives

The aim of this project was to develop a fundamental understanding of the complex physics of the flow in wall-flow filters and to develop tools for modelling filter flows, with particular focus on Gasoline Particulate Filters (GPFs) and their operating conditions. In order to achieve this aim, the following objectives were set:

1. Collection of experimental data for a variety of plugged filter samples for model validation and assessment at different flow regimes and temperatures.

2. Collection of experimental data for a variety of unplugged filter samples for establishing flow transition parameters in particulate filter channels.

3. Establish validity and limitations of existing correlations for friction and contraction/expansion losses through experiments and CFD analysis.

4. Development of a new 1-D pressure drop model and assessment of its prediction capabilities using the collected experimental data.

5. Development of a new approach for modelling wall-flow filters to overcome the limitations of the traditional 0-D and 1-D modelling approaches.

Although the work is focused more on the high temperature/high flow rates regimes characteristic to GPFs, most of the project findings and models are also applicable to DPFs, provided the appropriate flow regime and geometry properties are taken into account.

1.4 Thesis outline

Chapter 2 describes the experimental apparatus and methodology, and provides the main details about the two numerical methodologies used throughout the thesis. Chapter 3 presents the numerical investigation regarding the developing flow losses in channels with circular and square cross-section, while Chapter 4 presents the numerical investigation regarding the contraction losses in channels with circular and square cross-section. Chapter 5 discusses the experimental results of the unplugged and plugged filters. In Chapter 6 a new 1-D particulate filter model is presented and assessed against experimental data. Chapter 7 presents a new multi-channel modelling approach for particulate filters. Finally, Chapter 8 includes a summary of the main conclusions and recommendations for future work.

Chapter 2

Methodology

2.1 Introduction

This chapter presents the experimental and numerical methodologies used throughout this thesis. The experimental methodology section includes a description of the apparatus (rig and instrumentation) used to conduct the experiments, the filter samples and the experimental procedure, while the numerical methodology includes an overview of the two commercial software packages used for the modelling, namely Star-CCM+ and MATLAB, along with a description of their main features used in this project. More details about the numerical methodology procedure will be discussed in Chapter 3, Chapter 4, Chapter 6 and Chapter 7, where relevant.

2.2 Experimental methodology

The literature review has shown that there is a lack of experimental data for particulate filter pressure drop at high mass flow rates and temperatures, which are required for models assessment. Hence, an experimental apparatus has been designed to measure the pressure drop of several particulate filter cores under these conditions. The data collected in these experiments has then been used to assess the two numerical models developed during this project.

The same apparatus has been used to measure the pressure losses of several unplugged filters of different length. The data collected in these experiments has been

used to investigate and establish the validity of existing correlation for friction losses (in particular the transition from laminar to turbulent in channels with porous walls).

2.2.1 Experimental apparatus: Rig and instrumentation

The flow measurements were performed in the Flow Laboratory at the Engineering, Environment and Computing Building at Coventry University. The experimental apparatus used for the experiments (Figure 2.1) was designed in 2015 for a commercial project with Jaguar Land Rover and was already available.

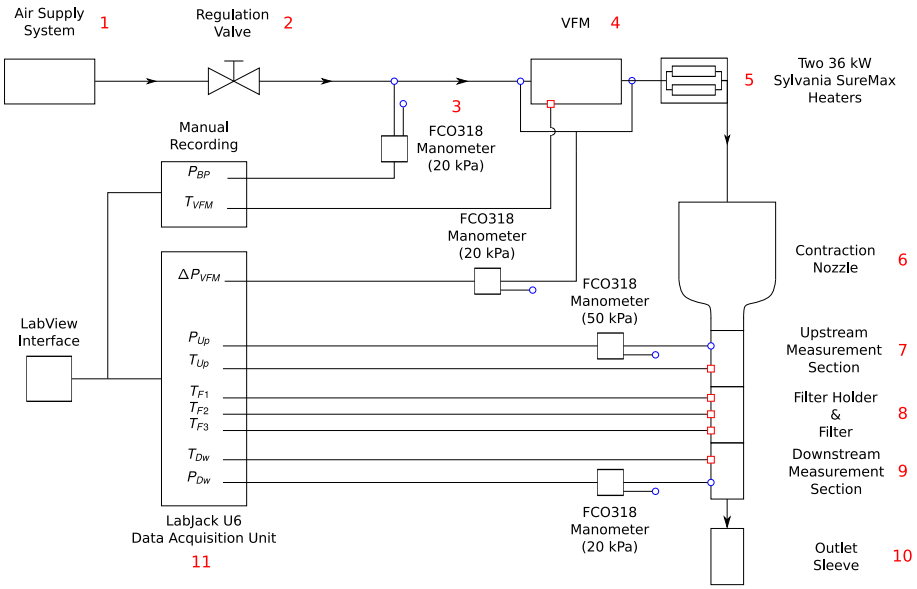

Fig. 2.1 Schematic of the experimental apparatus.

Dry air at room temperature was used as fluid medium for all experiments. The air is supplied into the rig through a 2000 litre receiver (Air Supply System (1) in Figure 2.1) at 11 bar (gauge pressure) fed by a 55 kW compressor.

The mass flow rate is measured through a calibrated custom made viscous flow meter (VFM (3) in Figure 2.1) placed upstream of the test rig along with a manual valve (Regulation Valve (2) in Figure 2.1) that allows to adjust the amount of air which can enter the rig.

The VFM is a differential pressure flow meter, which incorporates two sections of pipes separated by a metal honeycomb monolith, two pressure tappings to measure the pressure upstream and downstream the monolith and a thermocouple to measure

the temperature of the fluid. The VFM pressure drop depends on the mass flow rate, temperature and back-pressure in the pipe [111]. The VFM calibration consists in correlating these parameters, so that from the measurement of the VFM pressure drop, fluid temperature and pipe back-pressure it is possible to estimate the mass flow rate. The calibration equation is reported in Appendix A.

Thus, three measurements are needed to establish the mass flow through the VFM: the differential pressure drop, air temperature and back pressure (absolute pressure upstream of the VFM). The pressure drop across the VFM was measured through two pressure tappings, placed before and after the VFM, connected to a differential pressure transmitter, the FCO318 by Furness Controls ($\pm 20[kPa]$ range and accuracy within $\pm 0.25\%$ of the read). The air temperature at the VFM was monitored using a Type K thermocouple (accuracy within $\pm 2.5[^{\circ}C]$) by TC Direct connected to the Digitron 2038T digital thermometer ($-200-1350[^{\circ}C]$ range and accuracy within $\pm 0.1\%$ of the read). The back-pressure in the pipeline (upstream the VFM) was measured either with a pressure gauge ($0-2.5[bar]$ range and accuracy within $\pm 0.01[bar]$) or with the FCO318 pressure transmitter by Furness Controls ($\pm 20[kPa]$ range and accuracy within $\pm 0.25\%$ of the riding). The overall accuracy of the mass flow rate measurements with the VFM was estimated in [112] and was found to be within $\pm 5\%$.

Downstream of the VFM, the pipeline then splits in two lines and the flow passes through the two $36[kW]$ Sylvania SureMax heaters ((5) in Figure 2.1), which can heat the air up to $750[^{\circ}C]$. The heaters have a minimum mass flow rate safety limit of $6[g/s]$ each. The desired temperature of each heater can be selected manually and a PID controller ensures that the temperature stays constant at the selected value.

From the heaters, the hot air enters a double-skinned contraction nozzle ((6) in Figure 2.1) designed to provide a uniform flow profile at the inlet of the test section and to mix the hot air from the heaters.

The nozzle directs the air into an upstream measurement section, the test section and a downstream measurement section, ((7), (8) and (9) in Figure 2.1).

The upstream measurement section ((7) in Figure 2.1) includes a thermocouple and four pressure tappings. The Type K thermocouple by TC Direct was located $25[mm]$ upstream of the test section to measure the temperature of the flow entering into the

test section. The thermocouple was positioned in the centre of the pipe cross-section to measure the temperature at that location. The pressure tappings, located at $30[mm]$ upstream of the test section, were spaced equally around the circumference of the pipe and were connected to a single differential pressure transmitter, the FCO318 by Furness Controls ($\pm 50[kPa]$ range and accuracy within $\pm 0.25\%$ of the riding) to improve accuracy of the results and eliminate the effect of any asymmetry.

The test section ((8) in Figure 2.1) includes the filter holder (shown in Figure 2.2) and three Type K thermocouples. The filter holder was made from a stainless steel pipe with an inner diameter of $58[mm]$ and was welded to two flanges at its top and bottom. The holder inner diameter was chosen to match the outer diameter of the plugged filters cores used for the testing.

The bottom flange had an inner diameter of $50[mm]$, so that once a filter is inserted from the top of the holder this sits on the flange. A stainless steel ring with inner diameter of $50[mm]$ was placed over the top of the filter, as shown in Figure 2.2, to prevent any flow to enter the channels outside the $50[mm]$ cross-section. Thus, although the inner diameter of the holder was $58[mm]$, the effective diameter available for the flow to pass through was $50[mm]$ only.

The thermocouples were placed at a quarter, half and three-quarter of the holder length and their tips were in contact with the filter outer surface. These measurements were used introduced to ensure that the filter temperature was stable during the experiments.

Fig. 2.2 Filter core holder.

The downstream measurement section ((9) in Figure 2.1) contained a thermocouple and four pressure tappings. The Type K thermocouple by TC Direct was located at $75[mm]$ downstream of the test section to measure the temperature of the flow leaving the test section positioned at the centre of the pipe cross-section. The pressure tappings, located at $95[mm]$ downstream of the test section, were spaced equally around the circumference of the pipe and are connected to a differential pressure transmitter, the FCO318 by Furness Controls ($\pm 20[kPa]$ range and accuracy within $\pm 0.25\%$ of the read).

An outlet sleeve ((10) in Figure 2.1) made of stainless steel was connected to the downstream measurement section along with an adjustable duct attached to its end to direct the air flow outside the building through an extractor duct.

All the components from the nozzle to the outlet sleeve were connected through flanges bolted together and with gaskets in between them to provide a seal and avoid leakages. These components have been covered by several layers of Vitcas ceramic fibre blanket, each $25[mm]$ thick, secured with exhaust tape to provide thermal insulation. Nevertheless, due to the size and the complexity of the rig, heat losses could not be prevented altogether. The highest temperature achieved in the test section was around $680[^{\circ}C]$ (with air temperature of $750[^{\circ}C]$ at the exit from the heaters).

Fig. 2.3 Experimental hot flow rig (shown without insulation).

The ambient pressure within the laboratory was continuously monitored using a GE PACE1000 High Precision Pressure Indicator ($0-1150[mbar]$ range and accuracy of 0.005% of the full scale).

All measurements were recorded using a custom LabView interface with an acquisition unit, the LabJack U6-PRO (14 channels), except the pressure gauge before the VFM and the VFM thermocouple. The measurements from the two latter instruments were recorded manually and did not vary considerably during the experiments. All digitally recorded readings were continuously logged with intervals of approximately $0.5[s]$. The final data point recording was triggered manually when the rig was considered in thermal equilibrium. An average of 10 logged data points was recorded. The variation between these 10 readings was low, within $\pm 1\%$ on average.

Table 2.1 shows a summary of the instruments used for the measurements and their manufacturing details.

Table 2.1 Instruments and manufacturing details.

Measurement	Instrument	Range	Accuracy
LAb pressure	GE PACE 1000	$0-1150[mbar]$	$\pm 0.005\%$ FS
Pipeline back-pressure	FCO318	$\pm 20[kPa]$	$\pm 0.25\%$ rdg
Pipeline back-pressure	Pressure gauge	$0-2.5[bar]$	$\pm 0.01[bar]$
VFM temperature	Digitron 2038T	$-200-1350[^{\circ}C]$	$\pm 0.1\%$ rdg
VFM differential pressure	FCO318	$\pm 20[kPa]$	$\pm 0.25\%$ rdg
Upstream pressure	FCO318	$\pm 50[kPa]$	$\pm 0.25\%$ rdg
Upstream pressure ($> 50[kPa]$)	Testo525	$0-70[kPa]$	$\pm 0.05\%$ FS
Downstream pressure	FCO318	$\pm 20[kPa]$	$\pm 0.25\%$ rdg

2.2.2 Filter core samples

The test section was designed to have a circular opening of $50[mm]$ in diameter available to the flow at both ends. The diameter of filters for automotive applications is larger (around $120-140[mm]$), therefore a scaling approach was adopted, so that the mass flow rates used in the experiments would be representative for the typical operational ranges of a real size filter.

Two types of filter samples have been used for the testing: (a) unplugged filter cores and (b) plugged filter cores. These are described in the next sections.

Unplugged filters samples

The testing was performed with a $300/8[Cpsi]$ unplugged filter core sample, shown in Figure 2.4, which was cut from a cordierite monolith. The same core has been tested and then cut at different lengths, from $100[mm]$ to $40[mm]$ with steps of $10[mm]$, to investigate the effect of the filter length on the pressure drop.

The filter effective diameter was $50[mm]$, while the total outer diameter was $54[mm]$. This is because the outer perimeter of the filter was covered with a $2[mm]$ layer of cement to avoid air flow through the sides of the filter

Since the unplugged filters were tested only at ambient temperature, a custom made filter holder that included two flanges which relative distance can be regulated through a screw was used during the experiments and the samples were taped to the flanges to avoid any leak. A spray leak detector was used to ensure that the taping was placed correctly and no leakage was present.

As some of the channels were partially closed by the outer layer of cement coating, the estimation of the open frontal area with the nominal parameters is subject to minor variations [98]. The open frontal area was calculated as $\frac{\pi D_{Filter}^2}{4}\frac{d_h^2}{(d_h+w_s)^2}$, where D_{Filter} is the filter diameter, d_h is the cell hydraulic diameter and w_s is the wall thickness.

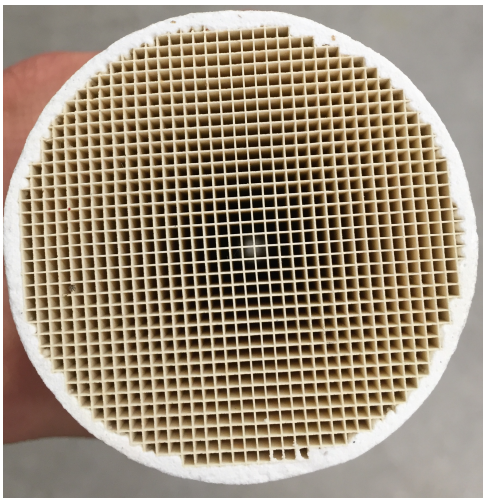

Fig. 2.4 Unplugged filter sample.

Table 2.2 Unplugged filters samples manufacturing details.

Property	Unit	Core
Cell density	*Cpsi*	300
Bare wall thickness	*mil*	8
Bare wall thickness	*mm*	0.203
Length	*mm*	100 - 40
Filter effective diameter	*mm*	50
Cell hydraulic diameter	*mm*	1.26
Coated	–	No
Median pore size	μm	17.5
Median porosity	–	0.64

Plugged filters samples

The testing was performed on four different filter core samples cut from a cordierite monolith. One of the samples is shown in Figure 2.5.

The filter effective diameter was $54[mm]$, while the total outer diameter was $58[mm]$.

Since both cold (ambient temperature) and hot flow (up to $680[^{\circ}C]$) testing was performed, the core samples were enclosed in a steel sample holder (described in the previous section and shown in Figure 2.2) with effective diameter of $50[mm]$.

The manufacturing details of the four samples used for the experiments are reported in Table 2.3. Core #1 is uncoated, while cores #2, #3 and #4 have a catalyst coating applied. The monolith wall thickness and hydraulic diameter were estimated using the data provided by the manufacturer. Measurements performed on several randomly selected channels using a Mitutoyo Vision measurement system showed hydraulic diameter values within 5% of the nominal values for all filters.

As some of the channels were partially closed by the outer layer of cement coating, the estimation of the open frontal area with the nominal parameters is subject to minor variations [98]. The open frontal area was calculated as $\frac{\pi D_{Filter}^2}{4} 0.5 \frac{d_h^2}{(d_h+w_s)^2}$, where D_{Filter} is the filter diameter, d_h is the cell hydraulic diameter and w_s is the wall thickness (including the washcoat thickness).

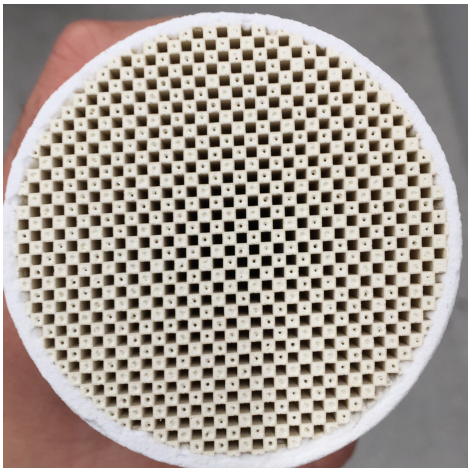

Fig. 2.5 Plugged filter sample.

Table 2.3 Plugged filters samples manufacturing details.

Property	Unit	Core #1	Core #2	Core #3	Core #4
Cell density	*Cpsi*	300	300	300	300
Bare wall thickness	*mil*	8	8	8	12
Bare wall thickness	*mm*	0.203	0.203	0.203	0.305
Length	*mm*	125	125	100	125
Filter effective diameter	*mm*	50	50	50	50
Cell hydraulic diameter	*mm*	1.26	1.22	1.22	1.13
Coated	–	No	Yes	Yes	Yes
Coating thickness	*mm*	0.000	0.035	0.035	0.022
Total wall thickness	*mm*	0.203	0.238	0.238	0.327
Median pore size	μm	17.5	10.3	10.3	12.3
Median porosity	–	0.64	0.59	0.59	0.55

2.2.3 Experimental procedure

The following test procedure was used for the hot flow experiments:

1. Set all pressure transmitters to zero.

2. Open the air line valve and ensure air flow rate is above $12[g/s]$ (minimum required for the safe heater operation). A high mass flow is initially used to heat the whole rig up to the required temperature quickly.

3. Start data logging.

4. Start the heaters and set the temperature to a value above the desired filter temperature to compensate for the heat losses between the heaters and the test section. For high temperatures this has been done in several stages by increasing the temperature of $100-200[^{\circ}C]$ at a time, to avoid a sharp temperature increase that can cause the heaters to locally overheat and shut down.

5. Monitor temperatures upstream and downstream of the test section and on the core surface, and adjust the heater temperature as required to reach the desired gas temperature. This stage can take around 2 hours.

6. Once the core temperature is nearly stabilised set the mass flow rate to the lowest test value and adjust the heater temperature if necessary.

7. Wait for the temperatures to stabilise again and take the first measurement.

8. Increase mass flow rate to the next testing value and adjust the heater temperature, if required, to ensure that the gas temperature does not change.

9. Wait for the temperatures to stabilise again and take the next measurement.

10. Repeat steps 8-9 till the maximum mass flow rate is reached.

This procedure was adopted after initial trial and error to ensure that the rig heats up to the temperature quickly (hence higher mass flow rate is used initially) and that the temperature inside the core is reasonably stabilised (after initial testing it was established that the thermal equilibrium is reached after around 2 hours, when the core surface temperature changes by around $1-2[^{\circ}C]$ in $10-15$ minutes).

Because the mass flow rate in the air line depends on several parameters (VFM differential pressure, air temperature in the VFM and pipeline backpressure), and two of those are recorded manually, the mass flow rate during testing was known only

approximately. Therefore, the change in VFM differential pressure was used as indicator for changing the mass flow rate, which was then calculated after the testing. Steps of $100[Pa]$ were used for lower differential pressures while steps of $50[Pa]$ were used for the higher differential pressures, as the mass flow rate increases non-linearly with the VFM differential pressure at high values of the pipeline backpressure.

The same procedure was used for the cold flow experiments with the exception of the temperature changes.

2.3 Numerical methodology

Two commercial software packages have been used for numerical modelling to gain further understanding of the flow physics in particulate filters and to develop predictive tools.

The CFD package Star-CCM+ has been used to simulate/predict the flow behaviour in a variety of geometrical configurations, namely:

1. The developing laminar flow in a straight section of pipe in Chapter 3.

2. The flow in a pipe with a sudden contraction, in order to estimate contraction losses due to abrupt change in cross-section under laminar flow conditions in Chapter 4.

3. The flow in a simplified automotive filter configuration used for demonstration of the multi-channel model in Chapter 7.

Since the computational domains and simulations set-up are different for all cases, only a broad overview of their modelling with Star-CCM+ is given in this Chapter, while the full details are reported in Chapter 3, Chapter 4 and Chapter 7.

The second software package is MATLAB, which has been used for all the data analysis and plotting of data, as well as for the derivation of the correlations proposed in Chapter 3 and for the implementation and solution of the two 1-D models presented in Chapter 6 and Chapter 7. Thus, a top level description of the non-linear curve fittings and boundary value problems and their solutions with MATLAB is reported below, while more specific details are reported in Chapter 3, Chapter 6 and Chapter 7.

2.3.1 Numerical modelling with Star-CCM+

Star-CCM+ is a Computational Aided Engineering (CAE) solution for solving multidisciplinary problems in both fluid and solid continuum mechanics.

The Star-CCM+ solver uses the finite volume method to obtain an approximate solution to the underlying equations of fluid flow. This requires a mesh to be created, which represents the fluid volume as a collection of much smaller volumes known as cells. A mesh with trimmed hexahedral cells and prism layers near the walls has been used for the modelling of the developing flow losses and contraction losses because the flow is mainly unidirectional, while a mesh with polyhedral cells and prism layers near the walls has been used for the modelling of the flow redistribution in the upstream section of a wall-flow filter, since in the case with a sudden expansion the flow is not unidirectional. A mesh dependency study has been carried for all cases, as reported in the relative sections.

A laminar flow solver has been used for the modelling of the developing flow losses and contraction losses, while the turbulent model v^2f has been used for the modelling of the flow redistribution in the upstream section of a wall-flow filter. Turbulence model v^2f has been chosen as it has been shown to perform reasonably well in separated flows [113].

The residuals and stability of the CFD simulations have been monitored to ensure convergence of the results. For the developing flow study, presented in Chapter 3, all the simulations reached a stable solution with residuals' magnitude in the order of 10^{-13}, while for the sudden contraction and flow redistribution upstream the filter, presented in Chapter 4 and Chapter 7, the simulations reached a stable solution with residuals' magnitude in the order of 10^{-8}. The term stable solution used above means that the residuals do not show any significant change for at least 500 iterations.

More details about the computational domains and simulation set-up are given in Chapter 3, Chapter 4 and Chapter 7.

2.3.2 Numerical modelling with MATLAB

MATLAB is a programming language developed by MathWorks and designed specifically for engineers and scientists. MATLAB allows matrix manipulations, plotting of functions and data, implementation of algorithms, creation of user interfaces, and interfacing with programs written in other languages [114].

In Chapter 3 and Chapter 4 several correlations are proposed, derived by fitting curves to the numerical data of the CFD simulations. Since these data points presented a non-linear trend, the **non-linear least-squares** method is used for the fitting. MATLAB offers a solver for these types of fitting problems, namely the *lsqcurvefit*. The *lsqcurvefit*, which implements the Trust-Region-Reflective iterative algorithm, finds the set of coefficients x that solve the problem:

$$\min_x \|F(x,x_{data}) - y_{data}\|_2^2 = \min_x \sum_i \left(F(x,x_{data_i}) - y_{data_i}\right)^2, \tag{2.1}$$

given input data x_{data}, and the observed output y_{data}, where x_{data} and y_{data} are matrices or vectors, and $F(x,x_{data})$ is a matrix-valued or vector-valued function of the same size as y_{data} [115]. The function $F(x,x_{data})$ has to be guessed by the user and it is not proposed by the solver.

In Chapter 6 and Chapter 7 two particulate filter models are proposed, and the model equations are solved with a **boundary value problem** solver.

Boundary value problems (BVPs) are differential equations combined with a set of boundary conditions. Unlike initial value problems, a BVP can have a finite solution, no solution, or infinitely many solutions. Thus, in order to be useful in practice, a boundary value problem has to be well posed, meaning that given the input to the problem there exists a unique solution, which depends continuously on the input. The initial guess of the solution is an integral part of solving a BVP, and the quality of the guess can be critical for the solver performance or even for a successful computation [116].

In the two models developed in this thesis, the differential equations to be solved are the mass and momentum balance equations in the inlet and outlet channels of a wall-flow monolith, while the boundary conditions are Dirichlet conditions for either the velocity or the pressure at the entrance or exit of the channels.

MATLAB offers two solvers to solve boundary value problems, namely *bvp4c* and *bvp5c*. Although the two solvers are very similar, *bvp5c* has been chosen over *bvp4c* since the former implements a fifth-order method and solves the algebraic equations directly, while the latter implements a fourth-order method and uses analytical condensation.

The main limitation of both solvers is that their current implementation in MATLAB does not allow a solution in parallel (parallelisation), and the software uses only one CPU to solve the problem. This can greatly affect the time required to solve a boundary value problem, as for the case of the multi-channel model presented in Chapter 7 due to the great number of differential equations involved. An alternative boundary value problem solver code for MATLAB that allows parallelisation and uses the GPU has been developed in 2014 by Antony [117] at Purdue University, and was shown to be able to decrease considerably the time required to solve boundary value problems. However, this code was not accessible and thus it could not be used.

More specific details about the use of the non-linear least-squares and the boundary value problems are given in Chapter 3, Chapter 4, Chapter 6 and Chapter 7.

Chapter 3

Modelling of developing flow losses in laminar flow

3.1 Introduction

The literature review has shown that there are still several discrepancies between studies of the pressure losses in laminar developing flow. In particular, different experimental and numerical studies reported different values for the pressure defect asymptotic value $K(\infty)$ as well as for the hydrodynamic entrance length L_{hy} and none of the proposed correlations for the pressure defect $K(x)$ estimation has been validated with experimental data or up to date RANS CFD analysis.

Therefore, this chapter examines the source of the discrepancies found in the literature, and demonstrates that the inlet configuration is critical for the correct assessment of the developing flow losses in a straight pipe. Both circular and square cross-sectional channels have been investigated.

Since no universal correlation for the friction factor can be derived for all practical applications with realistic inlet conditions, an approximation is offered which is shown to be suitable for a well-designed uniform inlet flow configuration. For circular cross-sectional channels two additional correlations for the kinetic energy correction factor $\alpha(x)$ and momentum correction factor $\beta(x)$ are derived, which can be useful for the determination of the contraction and expansion coefficients in flows with abrupt cross-

sectional changes as shown by Kays [24], Sadri and Floryan [118] and Chalfi and Ghiaasiaan [119].

The ability to correctly separate friction losses associated with the flow development from the contraction and expansion losses is crucial for predicting losses in complex flow devices such as automotive catalyst and filter systems or heat exchangers, as pointed out by Konstandopoulos [28] and Shah and London [51].

3.2 Channels with circular cross-section

3.2.1 Simulations set-up

In absence of reliable experimental data, numerical solutions of Navier-Stokes equations are a good approximation for laminar incompressible continuum flows of Newtonian fluids. Therefore, CFD modelling of developing pipe flow is used here in order to improve existing correlations for developing flow losses in laminar flow regime. Several laminar flow simulations have been performed using the commercial CFD package Star-CCM+. Four 2-D axisymmetric computational domains have been investigated to assess both idealised and more practical configurations:

1. **Computational Domain 1** (Figure 3.1): consists only of a pipe. In this case the inlet boundary condition, which is a constant/flat inlet velocity profile, is applied at the exact entrance of the pipe ($x^+ = 0$). Thus, this configuration represents an ideal case, as in practical applications it would be unrealistic to achieve a completely flat inlet velocity profile, as shown in Figure 3.5.

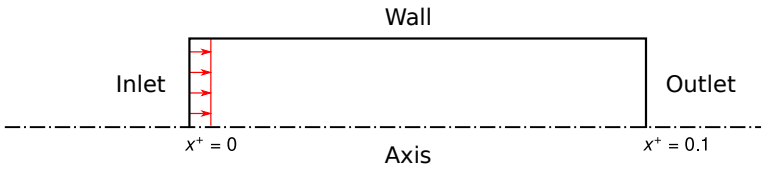

Fig. 3.1 Computational Domain 1.

2. **Computational Domain 2** (Figure 3.2): consists of a pipe and an extra inlet section of one hydraulic diameter in length. Because of the elliptical nature of the incompressible Navier-Stokes equations, the flow at the entrance to the

duct is affected by both upstream and downstream conditions. Thus, imposing a uniform profile at $x^+ = 0$ distorts the flow and pressure distributions in the vicinity of the duct entry. Using a short inlet section before the duct mitigates this problem. In this case the inlet boundary condition (a constant/flat inlet velocity profile) is applied some distance upstream of the pipe entrance. A symmetry plane boundary condition ($\partial/\partial r = 0$) is used at $r/R = 1$ in the inlet section ($x^+ < 0$) so that a uniform velocity profile can be maintained up to the duct entrance, as shown in Figure 3.5. The velocity profile entering the channel can be considered more representative for practical applications, but is still somewhat idealised assuming an "infinitely thin" channel wall. In practical applications, some flow path contraction would be expected due to the finite wall thickness. This domain geometry is similar to the one suggested by Schmidt and Zeldin [64].

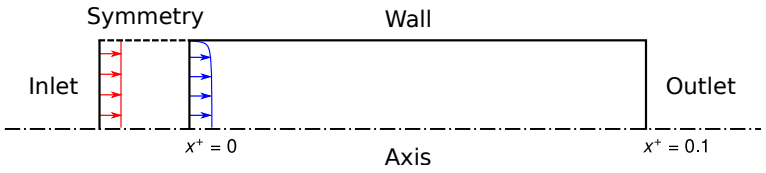

Fig. 3.2 Computational Domain 2.

3. **Computational Domain 3** (Figure 3.3): consists of a pipe with a bell-mouth contraction nozzle placed upstream. The contraction nozzle (with contraction area ratio $C_c = 8.6$) used for this computational domain follows the 3rd order polynomial proposed by Bell and Metha [120]. Bell and Metha [120] optimized this shape for the design of small low-speed wind tunnels in order to have the lowest boundary layer thickness at the contraction exit, and thus a mostly flat velocity profile. This configuration is representative of geometries used in practical application. In contrast with the two previous cases, the inlet velocity profile entering the pipe is Reynolds number dependent, as shown in Figure 3.3. This effect is attributed to the shape of the contraction. Figure 3.5 shows how the velocity profile for this case, at $Re = 500$, compares with the profiles of the other computational domains.

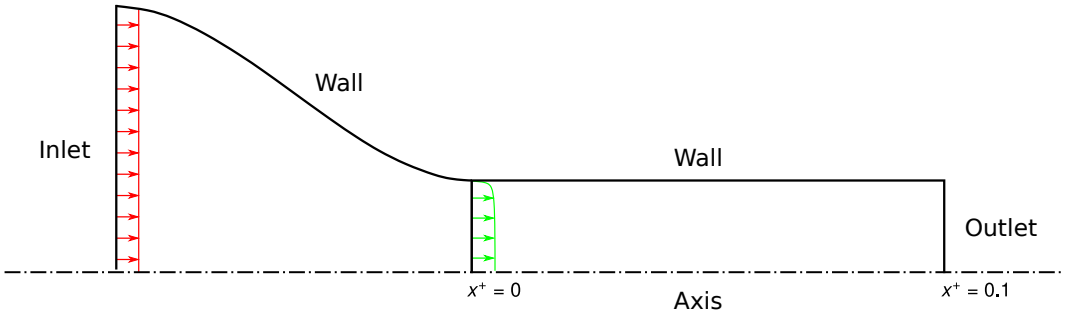

Fig. 3.3 Computational Domain 3.

4. **Computational Domain 4** (Figure 3.4): is the same as the previous one but the bell-mouth contraction nozzle shape follows the 5th order polynomial proposed by Bell and Metha [120]. The inlet velocity profile entering the pipe is Reynolds number dependent, as shown in Figure 3.4. Figure 3.5 shows how the inlet velocity profile for this case, at $Re = 500$, compares with the profiles of the other computational domains.

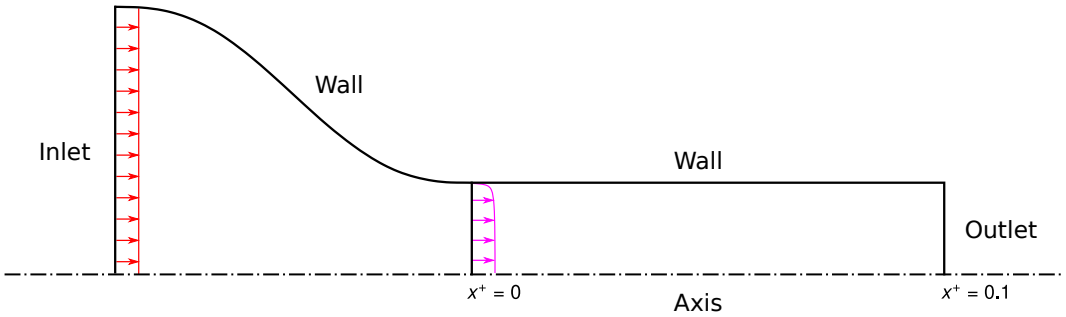

Fig. 3.4 Computational Domain 4.

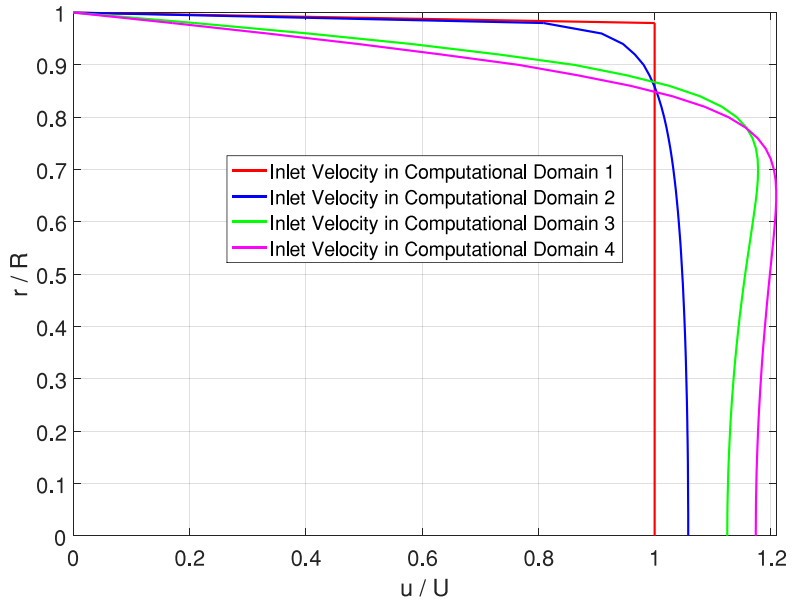

Fig. 3.5 Normalized inlet velocity profile at $x^+ = 0$: Computational Domain 1 vs. Computational Domain 2 vs. Computational Domain 3 at $Re = 500$ vs. Computational Domain 4 at $Re = 500$.

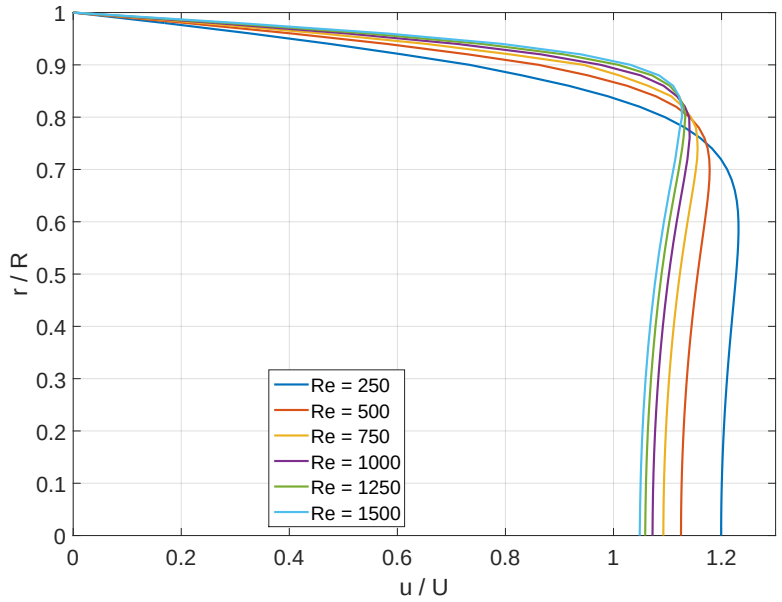

Fig. 3.6 Normalized inlet velocity profile at $x^+ = 0$: Computational Domain 3.

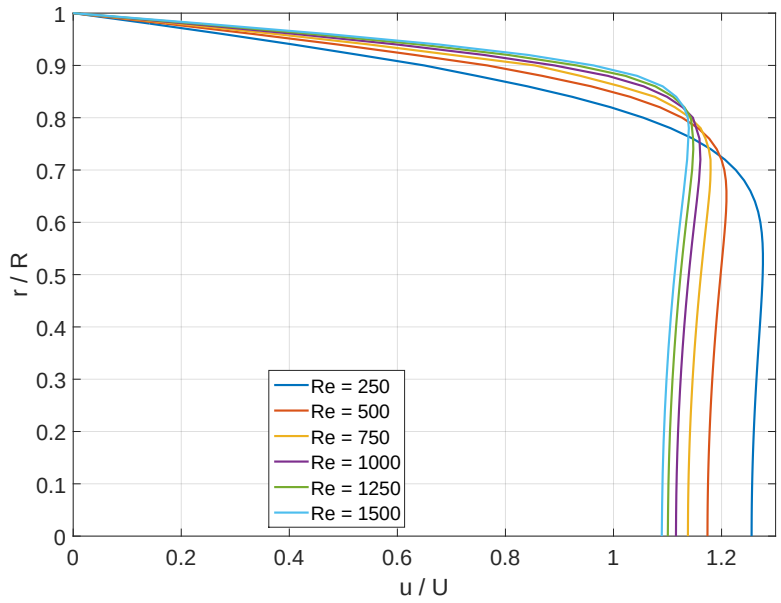

Fig. 3.7 Normalized inlet velocity profile at $x^+ = 0$: Computational Domain 4.

The boundary conditions are shown in Table 3.1. The Reynolds number definition $Re = \frac{\rho UD}{\mu}$ is based on the mean velocity U and channel hydraulic diameter D, with μ being the dynamic viscosity and ρ being air density. Six values of the Reynolds number from $Re = 250$ to $Re = 1500$ (in steps of 250) have been chosen in order to ensure a fully laminar regime. The length L of the pipe was varied for each Reynolds number in order to maintain the dimensionless length of the domain $x^+ = \frac{L}{DRe} = 0.1$. Other parameters and assumptions for the CFD modelling are reported in Table 3.2.

Table 3.1 Developing flow in channels with circular cross-section: Boundary Conditions.

Boundary	Boundary Condition
Inlet	Constant Velocity
Outlet	Ambient Static Pressure ($P_{Amb.} = 101325[Pa]$)
Wall	No Slip
Axis	Axis
Symmetry	Symmetry Plane ($\partial/\partial r = 0$)

Table 3.2 Developing flow in channels with circular cross-section: Star-CCM+ Models.

Parameter	Model
Geometry/Domain	2-D Axisymmetric
Viscous Regime	Laminar
Time Dependence	Steady State
Flow Solver	Segregated Flow
Solution Algorithm	SIMPLE
Convection Scheme	Second-Order
Equation of State	Constant Density
Fluid Density	$\rho = 1.2041\,[Kg/m^3]$
Fluid Dynamic Viscosity	$\mu = 1.8133 \times 10^{-5}\,[Pa\,s]$

A mesh with trimmed hexahedral cells and 10 prism layers near the walls has been used and a mesh dependency study has been carried out in order to ensure that the simulations results are independent from the mesh size. Three values of the cell base size, $0.3[mm]$, $0.25[mm]$ and $0.2[mm]$ have been investigated (for an hydraulic diameter of $10[mm]$). It was found that the cell sizes $0.25[mm]$ and $0.2[mm]$ provide nearly identical results, with a difference in the total pressure drop below 1%. Therefore, the cell base size was set at $0.25[mm]$ for all simulations.

3.2.2 Results

To assess the static pressure loss along the pipe, the average cross-section static pressure ($P_{D.F.-CFD}$) was calculated from the CFD results as:

$$P_{D.F.-CFD} = \frac{1}{A}\int_0^A P dA, \tag{3.1}$$

where A is the cross-sectional area of the pipe. The dimensionless local static pressure $\left(P^*_{D.F.-CFD} = P_{D.F.-CFD}/\frac{\rho U^2}{2}\right)$ and cumulative static pressure drop $\left(\Delta P^*_{D.F.-CFD} = \Delta P_{D.F.-CFD}/\frac{\rho U^2}{2}\right)$ were also calculated along the pipe. A typical pressure distribution for one of the cases at $Re = 500$ is shown in Figure 3.8, along with the respective

trend of the same parameters calculated with the Darcy-Weisbach equation for fully developed flow ($P^*_{F.D.F.}$ and $\Delta P^*_{F.D.F.}$) expressed in terms of x^+ as:

$$\Delta P_{F.D.F.} = 4fRex^+. \tag{3.2}$$

Here that the Fanning friction factor is $f = 16/Re$, since the cross-section is circular.

Figure 3.8 shows that sufficiently far from the pipe entrance the non-dimensional static pressure reaches the asymptotic gradient characteristic for fully developed flow. The contribution of the flow development losses to the total pressure drop compared with the losses due to fully developed flow is more important for shorter pipes with lower x^+. When $x^+ = 0.1$, the loss due to flow development is about 16% of the total loss. This relative contribution increases as x^+ decreases. Thus, not accounting for the losses due to flow development can lead to considerable errors in applications such as heat exchangers (e.g. [51]) or automotive catalyst systems (e.g. [121] and [113]), where the flow is often laminar and the aspect ratio of the duct (L/D) is low, and hence x^+ is small.

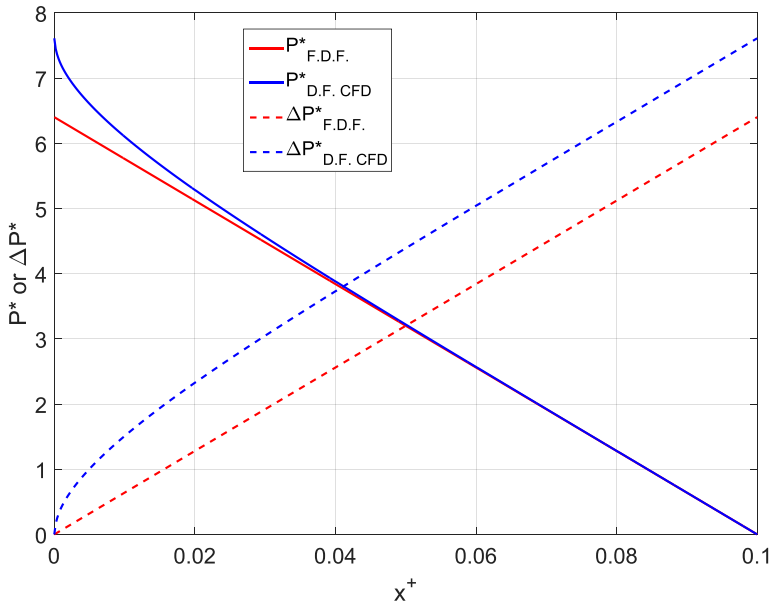

Fig. 3.8 Dimensionless local static pressure and cumulative static pressure drop.

The pressure defect function $K(x)$ has been calculated subtracting the dimensionless cumulative pressure drop for fully developed flow from the cumulative pressure drop

evaluated from the CFD results, which takes into account the additional losses due to flow development:

$$K(x) = \Delta P^*_{D.F.-CFD} - \Delta P^*_{F.D.F.}. \tag{3.3}$$

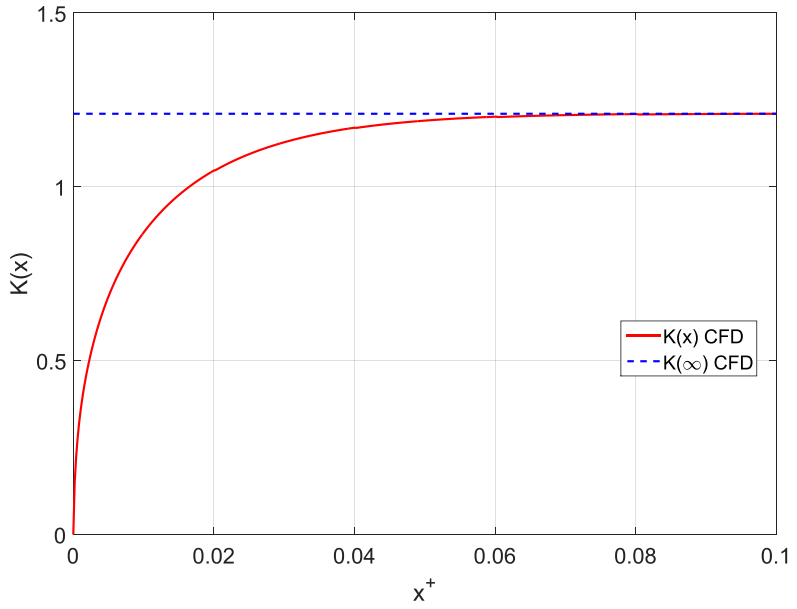

Fig. 3.9 $K(x)$ and $K(\infty)$ from CFD.

Figures 3.10 - 3.13 shows the CFD results for $K(x)$ for the four computational domains at different Reynolds numbers, compared with $K(x)$ and $K(\infty)$ evaluated with the correlation of Shah [69].

In the **Computational Domain 1** $K(x)$ depends on the Reynolds number and the pressure defect decreases with increasing Reynolds number (Figure 3.10). These results are consistent with the findings of Schmidt and Zeldin [64] and Su et al. [72], while they are considerably higher than those of Shah [69].

The dependence of $K(x)$ and $K(\infty)$ on the Reynolds number might be caused by the inlet boundary condition, which constrains the profile of the velocity to be constant/flat along the radius while being zero at the wall due to the no-slip condition. As a consequence, an unrealistically sharp velocity gradient is formed right at the pipe inlet, as shown in Figure 3.5, which then causes the transverse pressure gradients across the entry sections of the pipe to become non negligible, as hypothesised by Shah and London [51] and Bender [65], and to increase the cumulative pressure losses.

As mentioned previously, a completely flat inlet velocity profile is an idealised condition and, therefore, the trends of $K(x)$ and the values of $K(\infty)$ obtained from the Computational Domain 1 are not suitable for practical applications.

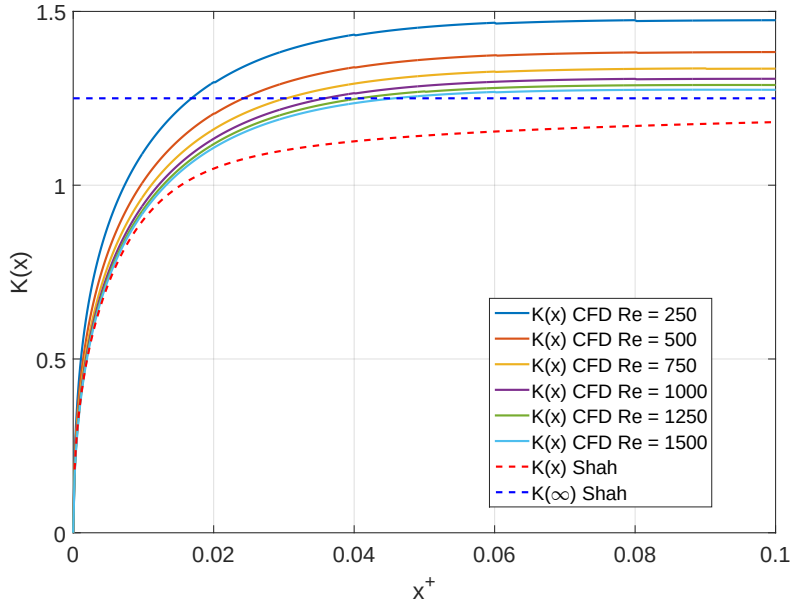

Fig. 3.10 $K(x)$ from Computational Domain 1.

In the **Computational Domain 2** $K(x)$ is independent of the Reynolds number and so is $K(\infty)$ (Figure 3.11). This confirms that $K(x)$ is extremely sensitive to the inlet conditions and with the boundary conditions used in the Computational Domain 2, the effect of the Reynolds number is almost completely eliminated. Hence, for the more realistic inlet velocity profile shown in Figure 3.5 for the Computational Domain 2, $K(x)$ and $K(\infty)$ are independent of the Reynolds number. Figure 3.11 shows a good agreement between the pressure defect $K(x)$ derived from CFD and the correlation of Shah [69]. The main difference lies in the fact that $K(x)$ reaches the constant value of $K(\infty)$ at a shorter distance (at $x^+ = 0.069$ instead of $x^+ = 0.858$) from the entrance, and that the value of $K(\infty)$ is 3.6% lower ($K(\infty) = 1.205$ in CFD results instead of $K(\infty) = 1.25$ used by Shah [69]).

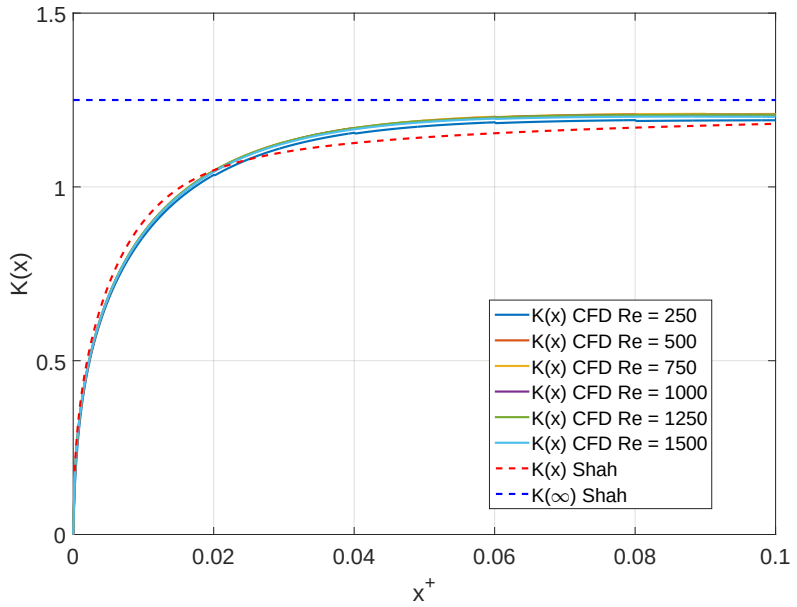

Fig. 3.11 $K(x)$ from Computational Domain 2.

In the **Computational Domain 3** and **Computational Domain 4** $K(x)$ depends on the Reynolds number (Figures 3.12 - Figure 3.13) and, in contrast with the results of the Computational Domain 1 and those reported by Su et al. [72], the pressure defect increases with the increasing of the Reynolds number. The pressure defect is, in both cases, lower than that predicted by Shah [69]. Overall, values of $K(x)$ for the Computational Domain 3 are about 3 to 10% higher than those obtained for the Computational Domain 4.

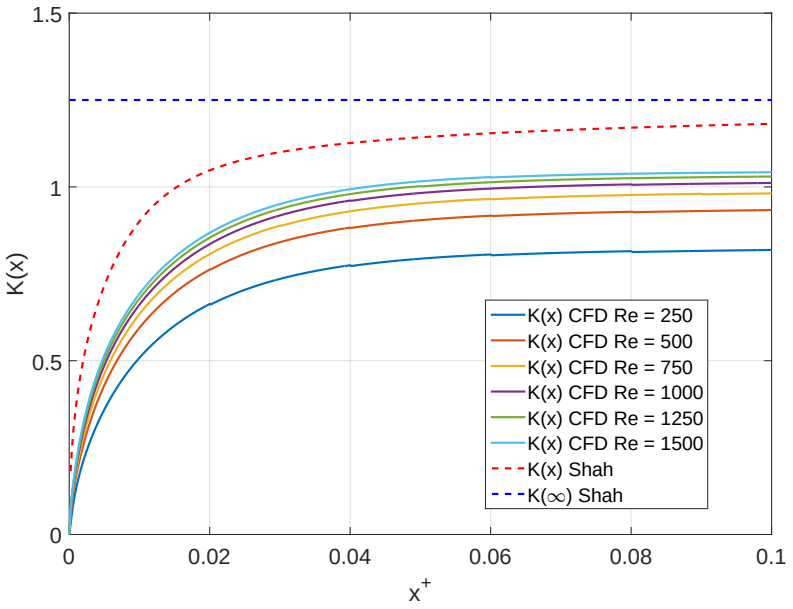

Fig. 3.12 $K(x)$ from Computational Domain 3.

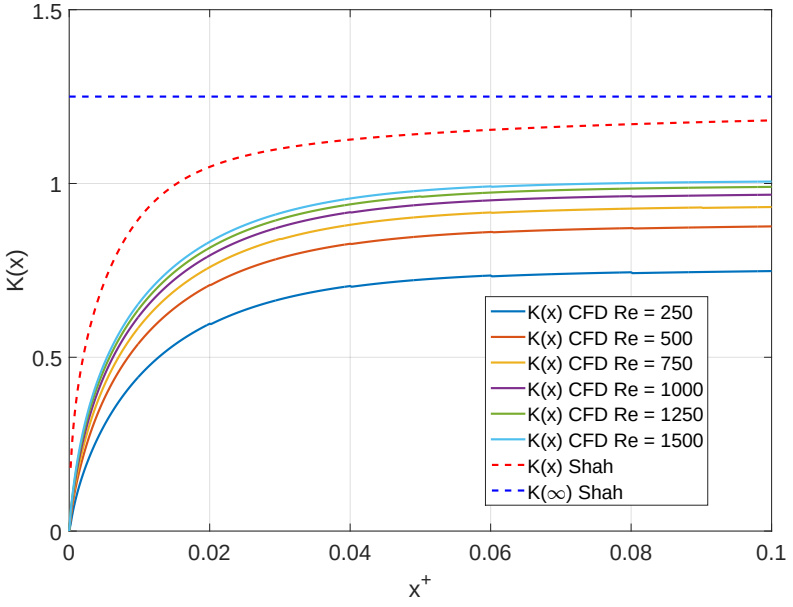

Fig. 3.13 $K(x)$ from Computational Domain 4.

Thus, the results presented for the four different inlet configurations show that imposing a fully flat velocity profile at the pipe inlet produces non-physical results, which explains some of the discrepancies observed in the literature between the numerical and experimental results for $K(\infty)$. This is attributed to the singularity introduced at the wall at the pipe entrance, where the prescribed non-zero entrance velocity profile has to

satisfy the non-slip condition. With the more robust inlet conditions used in Computational Domain 2, the pressure defect becomes Reynolds number independent. However, this domain is not completely representative of the experimental configurations, where the uniform inlet flow is usually achieved by using a carefully designed contraction nozzle.

For the two contraction nozzles considered here, which are based on an optimised design, the pressure defect is not Reynolds independent and increases with the Reynolds number. Moreover, the total pressure loss is considerably lower than that predicted by Shah [69]. The Reynolds number dependence and the difference between the results for the Computational Domain 3 and the Computational Domain 4 can be attributed to the different inlet velocity profile entering the pipe after the contraction. As shown in Figures 3.6 - 3.7, the velocity gradient at the wall increases with the increasing of the Reynolds number. The steeper velocity gradient at the wall increases the wall shear at the entrance of the channel causing higher pressure losses and, hence, higher values of $K(x)$.

3.2.3 Proposed correlations

It has been shown that in practical applications there will be some dependence of the pressure loss on Reynolds number, and this dependence is sensitive to the inlet configuration. It is impractical to provide a correlation for every possible upstream geometry, thus to a first approximation a solution independent of the Reynolds number can be used. Therefore, the **Computational Domain 2** has been chosen as a "standard case" for the derivation of the following correlations:

1. Pressure defect $K(x)$.
2. Hydrodynamic entrance length L_{hy}^{+}.
3. Kinetic energy correction factor $\alpha(x)$.
4. Momentum correction factor $\beta(x)$.

However, the pressure defect has been shown to be lower for well-designed bell-mouth contraction nozzles. Therefore, a second correlation for $K(x)$, specifically

designed for bell-mouth contractions, is proposed as well. These correlations have been derived by fitting a suitable model function to the CFD results using the lest-squares fitting method.

Pressure defect $K(x)$ and hydrodynamic entrance length L_{hy}

The following exponential function has been chosen for the derivation of the pressure defect correlation:

$$K(x) = K(\infty)\left(1 - e^{-C_2\left(x^+\right)^{C_3}}\right). \tag{3.4}$$

Here C_2 and C_3 are the coefficients which have to be found by fitting Eq. 3.4 to the CFD results. This exponential function ensures that $K(x) = 0$ at $x^+ = 0$ and that $K(x)$ reaches an asymptotic value, $K(\infty)$, as $x^+ \to \infty$. The constants calculated using the non-linear least squares method in MATLAB are: $K(\infty) = 1.205$, $C_2 = 26.1728$ and $C_3 = 0.65$. Figure 3.14 shows the quality of the fit, where the difference between the CFD results and Eq. 3.4 is under 2% for $x^+ < 0.01$ and under 0.1% for $x^+ > 0.01$.

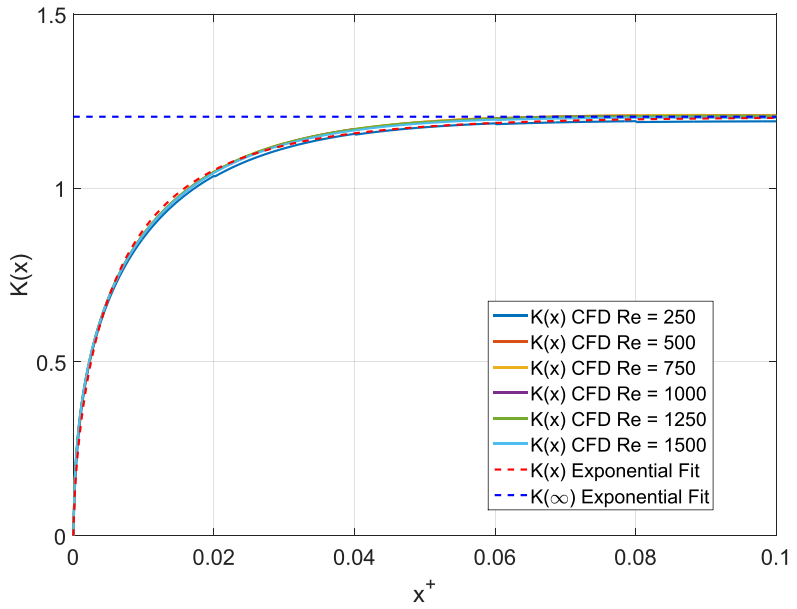

Fig. 3.14 $K(x)$ exponential fit.

The dimensionless hydrodynamic entrance length L_{hy}^+, defined as $L_{hy}^+ = L_{hy}/(DRe)$, can be found by calculating the dimensionless axial distance in which the centreline velocity reaches the 99% of the fully developed centreline velocity. This condition

gives $L_{hy}^{+} = 0.0544$, which is consistent with other studies reported in the literature (e.g. [61],[62], [65], [74] and [44]) as shown in Table 1.3. Note here that the correlation of Shah [69] cannot be used to derive the hydrodynamic entrance length based on the centreline velocity, as the author did not investigate the velocity trend in the duct. However, the hydrodynamic entrance length is an important parameter for the design of flow meters (e.g. [122], [123] and EN ISO 5167-1:2003 section 7.2.1), wind tunnels (e.g. [45]) and micro-channels where the boundary layer development region is used for enhancing the heat transfer for cooling applications (e.g. [124]). Moreover, Shah's correlation for the pressure defect does not reach the 99% of its asymptotic value of $K(\infty) = 1.25$ until $x^{+} = 0.858$ which is an order of magnitude higher than the entrance length based on the centreline velocity (see Table 1.3), while in the correlation 3.4 the 99% of the asymptotic value is reached at $x^{+} = 0.069$ which is comparable to the entrance length based on the centreline velocity. For the Computational Domain 3 and Computational Domain 4 the pressure drop results are Reynolds number dependent, and thus a Reynolds number dependent correlations for both $K(x)$ and $K(\infty)$ has to be found. $K(\infty)$ can be obtained by fitting the CFD results of both Computational Domain 3 and Computational Domain 4 with the following equation:

$$K(\infty) = C_4 \left(1 - e^{-C_5 (Re)^{C_6}}\right). \tag{3.5}$$

The constants calculated using the non-linear least squares method in MATLAB are: $C_4 = 1.0639$, $C_5 = 0.0843$ and $C_6 = 0.5$, and the deviation of the fitting from the CFD results of the two domains is within $\pm 5\%$.

Then, by using the same exponential function as Eq. 3.4, with Eq. 3.5 for the calculation of $K(\infty)$, a new correlation of $K(x)$ specifically for bell-mouth contractions can be found. The constants calculated using the non-linear least squares method in Matlab are: $C_2 = 32.5169$ and $C_3 = 0.7572$.

Figures 3.15 - 3.16 shows a comparison of the two proposed correlations (the Reynolds independent and the Reynolds dependent) against the other correlations reported in the literature. The results are plotted up to $x^{+} = 0.5$ to illustrate when the different correlations for $K(x)$ reach their asymptotic values.

Figure 3.15 shows the Reynolds independent correlations. All the correlations provide nearly identical values of $K(x)$ up until $x^+ < 10^{-3}$, while they start to deviate after this value. The correlations of Bender [65] and Shah [69] are almost equal in the full range of x^+ and, as mentioned previously, $K(x)$ is still increasing even after $x^+ = 0.5$. The correlation of Yilmaz [73] provides marginally higher results than Shah's correlation, while the correlation of Muzychka and Yovanovich [74] shows much higher results. Note that the correlation by Muzychka and Yovanovich [74] is not derived as a sum of the fully developed and developing flow losses, therefore the value at $x^+ \to \infty$ has been subtracted from it to deduce the developing flow contribution. The correlation proposed here shows similar results to the correlation of Shah, with slightly higher values of $K(x)$ in the range between $0.04 < x^+ < 0.1$ and a slightly lower value of $K(\infty)$ which is still consistent with some of the available experimental measurements listed in 1.1. In contrast with all the previous correlations, $K(x)$ reaches the constant value of $K(\infty)$ at a much shorter distance from the entrance (at $x^+ = 0.069$).

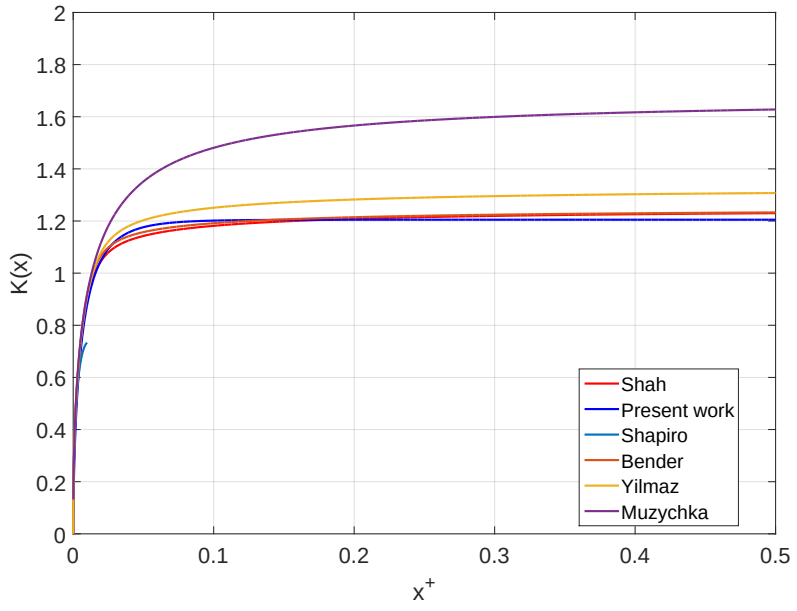

Fig. 3.15 Reynolds independent correlations for $K(x)$.

Figure 3.16 shows the Reynolds dependent correlations plotted with the present Reynolds independent correlation for comparison purposes. In the correlation of Su et al. [72] $K(x)$ decreases with the increasing of the Reynolds number and its values are much higher than those of the Reynolds independent correlation. This trend is consistent with

the results obtained for the Computational Domain 1 investigated in the present study (see Figure 3.10), which, as explained previously, has been considered not representative of the practical applications as a completely flat inlet velocity profile is idealised and uses the same inlet condition as Su et al. [72]. Moreover, the pressure defect calculated by Su et al. [72] is still increasing after $x^+ = 0.5$, while the authors stated that the hydrodynamic entrance length based on the centreline velocity is around $L_{hy}^+ \sim 0.06$ for Reynolds number higher than $Re = 250$. The present correlation for bell-mouth contraction shows the opposite trend, with $K(x)$ increasing with the increasing Reynolds number and values lower than those of the Reynolds independent correlation. $K(x)$ reaches the constant value of $K(\infty)$ in the same manner as the Reynolds independent solution.

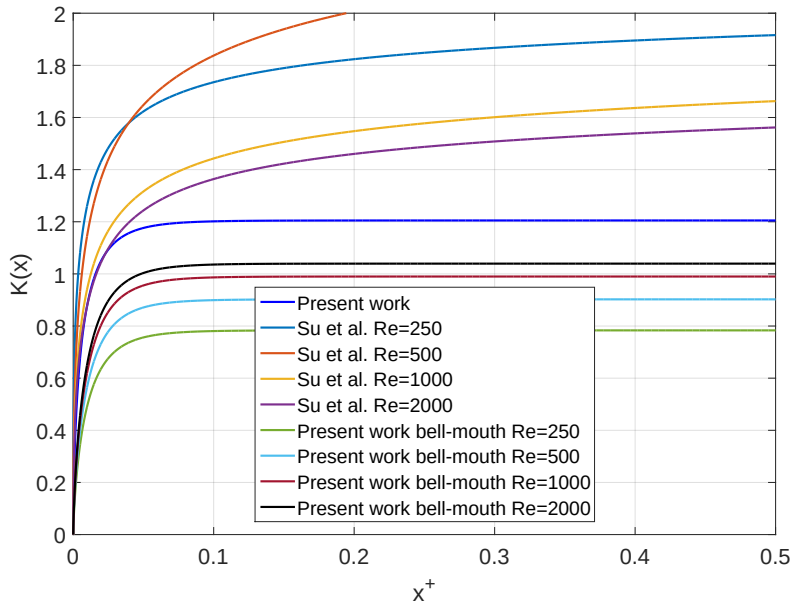

Fig. 3.16 Reynolds dependent correlations for $K(x)$.

The two correlations presented here have been derived for a semi-ideal inlet configuration and a well-designed inlet nozzle, which limits their application. As reported at the beginning of this section, it is evident that in practical applications there will be some dependence of the pressure loss on the Reynolds number. This dependence is caused by the fact that the inlet velocity profile in any non-idealised geometry is Reynolds-dependent. Since it would be impractical to provide a correlation for every possible upstream geometry, the Reynolds independent correlation Eq. 3.4 can be used as a first

approximation for flows where the inlet velocity profile is close to being uniform. The Reynolds-dependent effect of the extra inlet losses due to flow non-uniformity can then be accounted for by adding such losses if these can be estimated using measurements or known correlations.

For example, to estimate the pressure losses in a single or multiple tube system configuration with abrupt changes in the cross section, the developing flow losses calculated with the Reynolds independent correlation Eq. 3.4 can be added to the contraction losses calculated from correlations available in the literature (e.g. [24]).

Kinetic energy correction factor $\alpha(x)$

The change in kinetic energy between two sections associated with going from a uniform velocity profile to a parabolic one can be accounted for through the kinetic energy correction factor, defined as [51]:

$$\alpha = \frac{\int_A \rho u^3 dA}{\rho U^3 A}, \tag{3.6}$$

where u is the local velocity along the cross-section and U is the mean cross-sectional velocity. For a flat velocity profile $u_{Flat} = U$ and $\alpha_{Flat} = 1$, while in fully developed laminar flow $u_(F.D.F.) = 2U\left[1-(r/R)^2\right]$ and $\alpha_{F.D.F.} = 2$. The value of α along the axial direction, $\alpha(x)$, can be computed using Eq. 3.6 by extracting the velocity field from the CFD results.

The following exponential function has been chosen for the derivation of the kinetic energy correction factor:

$$\alpha(x) = 2 - e^{-C_2\left(x^+\right)^{C_3}}, \tag{3.7}$$

so that $\alpha(x) = 1$ at $x^+ = 0$ and $\alpha(x) = 2$, as $x^+ \to \infty$. The constants calculated using the non-linear least squares method in MATLAB are: $C_2 = 26.1728$ and $C_3 = 0.65$. Note here that the value of $\alpha(x)$ at $x^+ = 0$ has been approximated to 1, which would correspond to a perfectly flat velocity profile, to simplify the correlation.

Figure 3.17 shows show the quality of the fit, where the difference between the CFD results and Eq. 3.7 is under 4% for $x^+ < 0.01$ and under 0.1% for $x^+ > 0.01$.

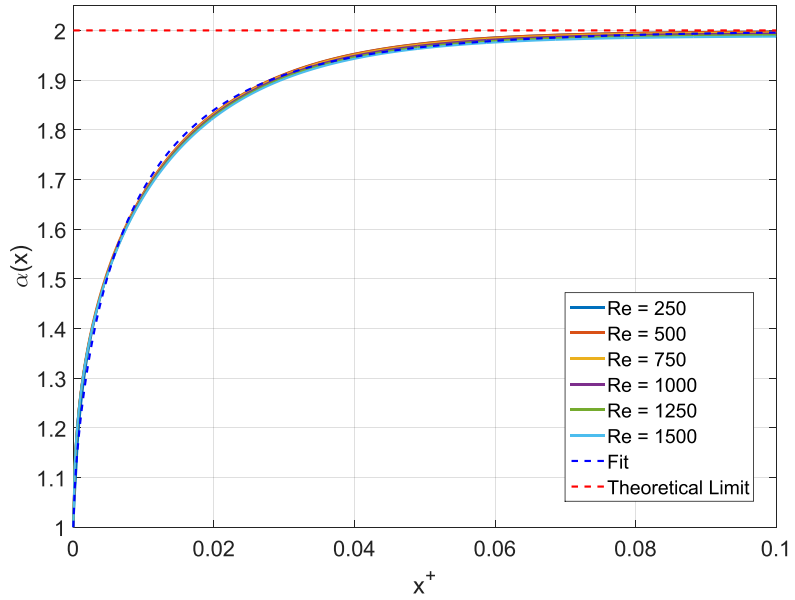

Fig. 3.17 Kinetic energy correction factor.

Momentum correction factor $\beta(x)$

Similarly to the change in kinetic energy, the change in total flow momentum between two cross-sections associated with going from a uniform velocity profile to a parabolic one can be accounted for through the momentum correction factor, defined as [51]:

$$\beta = \frac{\int_A \rho u^2 dA}{\rho U^2 A}, \tag{3.8}$$

where, u is the local velocity along the cross-section and U is the mean cross-sectional velocity. When the velocity profile is flat $\beta_{Flat} = 1$, while for fully developed laminar flow $\beta_{F.D.F.} = 4/3$. The value of β along the axial direction, $\beta(x)$, can be computed through Eq. 3.8 by extracting the velocity field from the CFD results.

The following exponential function has been chosen for the derivation of the momentum correction factor:

$$\beta(x) = \frac{1}{3}\left(4 - e^{-C_2(x^+)^{C_3}}\right), \tag{3.9}$$

so that $\beta(x) = 1$ at $x^+ = 0$ and $\beta(x) = 4/3$, as $x^+ \to \infty$. The constants calculated using the non-linear least squares method in MATLAB are: $C_2 = 26.1728$ and $C_3 = 0.65$.

Note here that the value of $\beta(x)$ at $x^+ = 0$ has been approximated to 1, which would correspond to a perfectly flat velocity profile, to simplify the correlation.

Figure 3.18 shows show the quality of the fit, where the difference between the CFD results and Eq. 3.10 is under 2% for $x^+ < 0.01$ and under 0.1% for $x^+ > 0.01$.

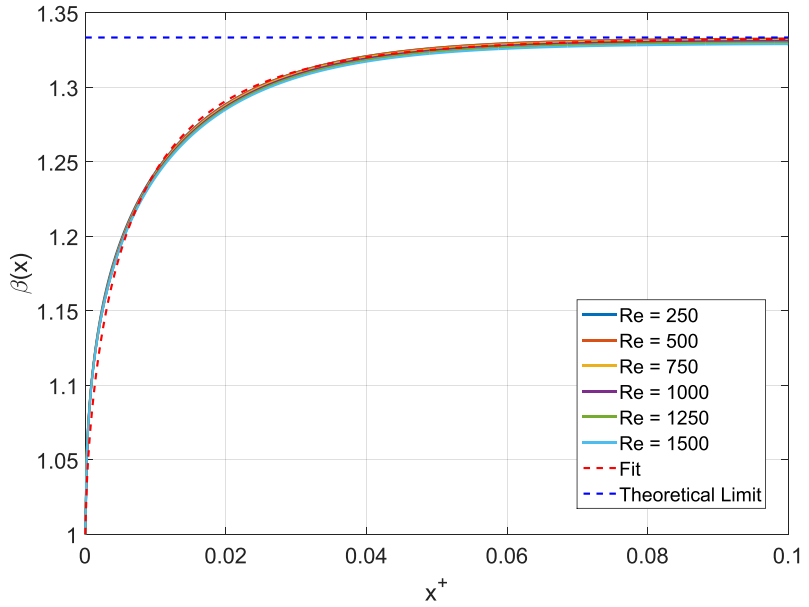

Fig. 3.18 Momentum correction factor.

Apart from being useful in some fluid dynamics applications, such as for the investigation of the contraction and expansion coefficients (e.g. [24], [118] and [119]), the knowledge of the momentum correction factor can be used to verify the physical interpretation of the pressure defect. As reported in the literature review, the pressure losses in developing flows are usually estimated adding two components: 1) the pressure losses for fully developed flow and 2) the additional pressure losses due to momentum change and accumulated wall shear difference between developing and developed flow [51]. Hence, according to Eq. 1.4, the term $K(x)$ represents the dimensionless losses due to momentum change and accumulated wall shear difference between developing and developed flow.

The momentum change losses along the channel can be calculated as:

$$\Delta P_{MomentumChange}(x) = [\beta(x) - \beta(0)]\,\rho U^2 = \left[\frac{1}{3}\left(4 - e^{-C_2\left(x^+\right)^{C_3}}\right) - 1\right]\rho U^2. \quad (3.10)$$

The losses due to accumulated wall shear difference between developing and developed flow can be calculated by subtracting the cumulative losses due to wall shear calculated with the wall shear from the CFD results, $\tau_{w,D.F.-CFD}$, from the cumulative losses due to wall shear calculated with the fully developed wall shear.

Figure 3.19 shows that adding the dimensionless losses due to fully developed flow to the accumulated wall shear difference and momentum change exactly matches the dimensionless losses extracted from the CFD results, or in other words the dimensionless losses calculated through Eq. 1.4 and Eq. 3.4. This confirms the physical interpretation of the pressure defect given by Shah and London [51].

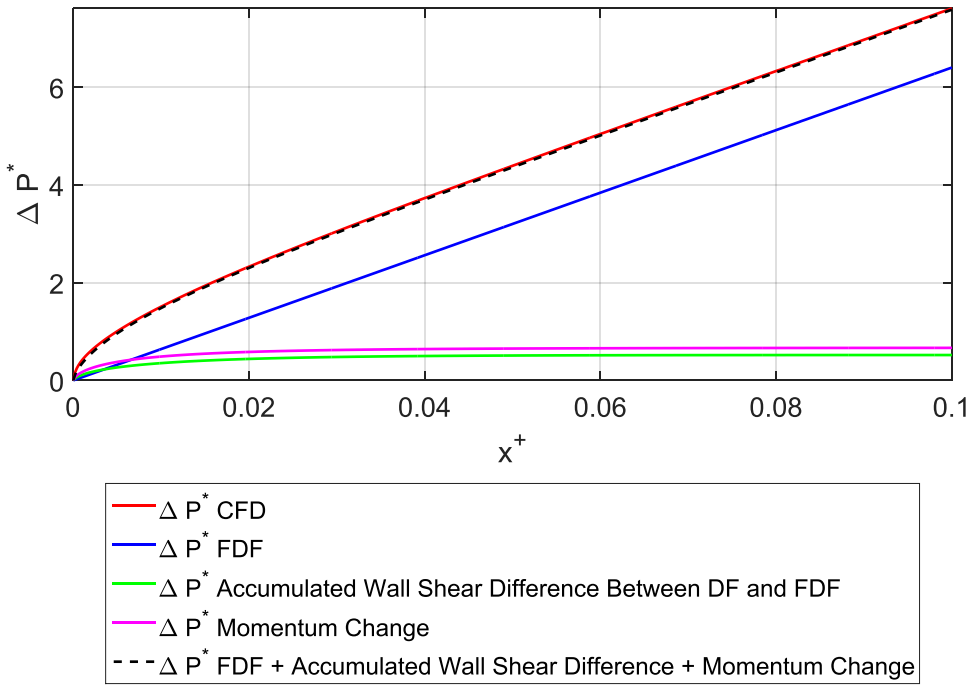

Fig. 3.19 Pressure losses due to fully developed flow friction, accumulated wall shear difference between developing flow and fully developed flow and momentum change.

3.3 Channels with square cross-section

3.3.1 Simulations set-up

The previous section has shown that in practical applications there will be some dependence of the pressure loss on Reynolds number, and that this dependence is sensitive to the inlet configuration. However, as it would be impractical to provide a correlation for every possible upstream geometry, a computational domain similar to the **Computational Domain 2**, which provided Reynolds independent results, has been chosen for the analysis of the developing flow losses of channels with square cross-section.

Figure 3.20 shows the Computational Domain. Since the geometry is not axisymmetric, a full 3-D CFD approach is used. In order to decrease the computational effort, only a quarter of a channel was used due to the symmetry properties of the geometry. A no-slip condition is used at the walls, while a symmetry plane boundary condition has been used for the other two surfaces (mid planes of the channel).

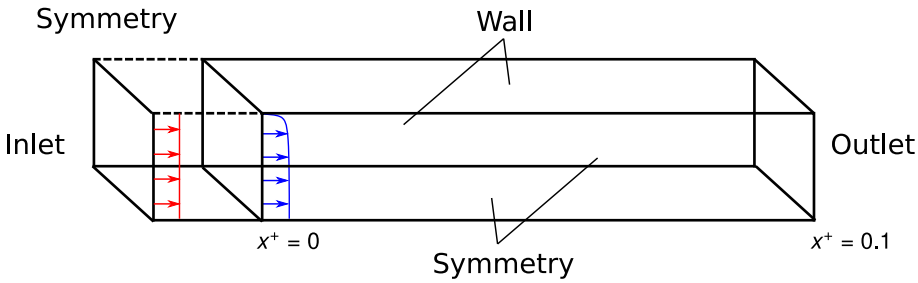

Fig. 3.20 Computational domain for the square channel.

The boundary conditions for the regions, defined as in Figure 3.20, are shown in Table 3.3. The Reynolds number definition $Re = \frac{\rho U D}{\mu}$ is based on the mean velocity U and channel hydraulic diameter D, with μ being the dynamic viscosity and ρ being air density. Six values of the Reynolds number from $Re = 250$ to $Re = 1500$ (in steps of 250) have been chosen in order to ensure a fully laminar regime. The length L of the pipe was varied for each Reynolds number in order to maintain the dimensionless length of the domain $x^+ = \frac{L}{DRe} = 0.1$. Other parameters and assumptions for the CFD modelling are reported in Table 3.4.

Table 3.3 Developing flow in channels with square cross-section: Boundary Conditions.

Boundary	Boundary Condition
Inlet	Constant Velocity
Outlet	Ambient Static Pressure ($P_{Amb.} = 101325[Pa]$)
Wall	No Slip
Symmetry	Symmetry Plane ($\partial/\partial h = 0$)

Table 3.4 Developing flow in channels with square cross-section: Star-CCM+ Models.

Parameter	Model
Geometry/Domain	3-D
Viscous Regime	Laminar
Time Dependence	Steady State
Flow Solver	Segregated Flow
Solution Algorithm	SIMPLE
Convection Scheme	Second-Order
Equation of State	Constant Density
Fluid Density	$\rho = 1.2041\ [Kg/m^3]$
Fluid Dynamic Viscosity	$\mu = 1.8133 \times 10^{-5}\ [Pa\,s]$

3.3.2 Results

The average cross-sectional static pressure, fully developed flow losses and pressure defect have been calculated using Eq. 3.1, Eq. 3.2 and Eq. 3.3. Note here that in Eq. 3.2 the Fanning friction factor is $f = 14.227/Re$, since the cross-section is square.

Figure 3.21 shows the CFD results of $K(x)$ compared with $K(x)$ and $K(\infty)$ evaluated with the correlation of Shah [69] for square cross-section. Similar to the circular pipe case, $K(x)$ is independent of the Reynolds number and so is $K(\infty)$. A good agreement between the pressure defect $K(x)$ derived from CFD and the correlation of Shah [69] is shown. The main difference lies in the fact that $K(x)$ reaches the constant value of $K(\infty)$ at a shorter distance (at $x^+ = 0.0915$ instead of $x^+ = 0.8906$) from the entrance, and that

the value of $K(\infty)$ is 2.8% lower ($K(\infty) = 1.39$ in CFD results instead of $K(\infty) = 1.43$ used by Shah [69]).

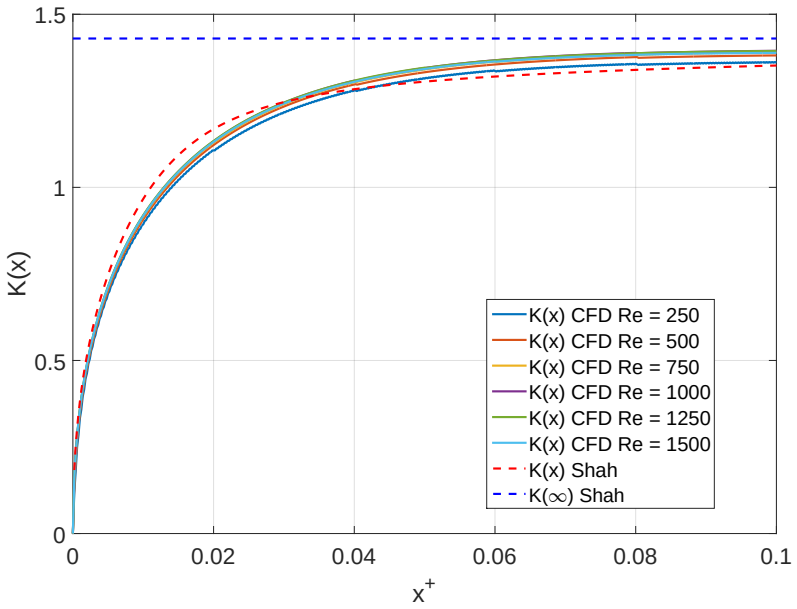

Fig. 3.21 $K(x)$ from the square computational domain.

3.3.3 Proposed correlation

The same exponential function used for fitting the CFD results of the Computational Domain 2 (Eq. 3.4) has been chosen for the derivation of the pressure defect correlation for the square cross-section. The constants calculated using the non-linear least squares method in MATLAB are: $K(\infty) = 1.39$, $C_2 = 21.7992$ and $C_3 = 0.65$. Figure 3.22 shows the quality of the fit, where the difference between the CFD results and Eq. 3.4 is under 2% for $x^+ < 0.01$ and under 0.1% for $x^+ > 0.01$.

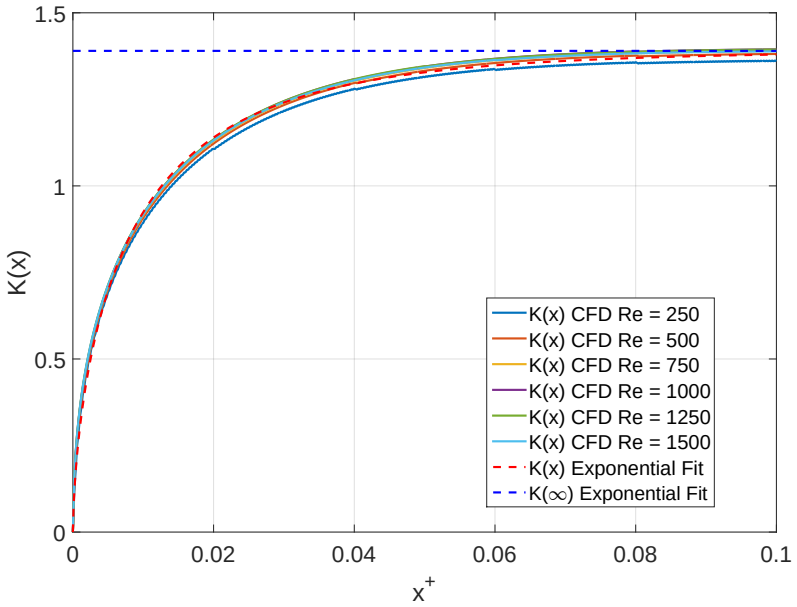

Fig. 3.22 $K(x)$ square exponential fit.

The dimensionless hydrodynamic entrance length L_{hy}^{+}, defined as $L_{hy}^{+} = L_{hy}/(DRe)$, can be found by calculating the dimensionless axial distance in which the centreline velocity reaches the 99% of the fully developed centreline velocity. This condition gives $L_{hy}^{+} = 0.0674$. As for the circular cross-section results, Shah's correlation for the pressure defect does not reach the 99% of its asymptotic value of $K(\infty) = 1.43$ until $x^{+} = 0.89$ which is an order of magnitude higher than the entrance length based on the centreline velocity (see Table 1.3), while in the correlation 3.4 the 99% of the asymptotic value is reached at $x^{+} = 0.094$ which is comparable to the entrance length based on the centreline velocity.

3.4 Chapter summary

In order to address some discrepancies in the previous studies, a numerical investigation of laminar developing flows in circular and square cross-sectional ducts has been conducted. In particular, the effect of the inlet conditions on the pressure loss due to the development of the boundary layer has been investigated.

For the circular cross-section channels four types of inlet conditions have been used to study the effect of idealised (flat profile at the pipe inlet) and semi-idealised (flat

profile provided upstream of the pipe inlet) inlet conditions, as well as two more realistic bell-mouth contraction nozzle inlet configurations. The results show that only the semi-idealised configuration provides Reynolds number independent solutions, suggesting that in real applications the pressure losses due to laminar developing flows can be influenced by the duct Reynolds number. In configurations with a contraction nozzle upstream of the pipe, the velocity profiles entering the pipe are not completely flat, with Reynolds-dependent velocity gradients present near the pipe walls. This Reynolds number dependence is related to the shape of the contraction upstream the pipe, as this determines the shape of the velocity profile entering the pipe.

The results presented here clearly demonstrate that for different inlet configurations the pressure defect can be Reynolds-independent, or change with the Reynolds number. This would explain the scatter in the experimental results found in the literature.

For the square cross-section channels only one inlet condition has been used, which matches the semi-idealised (flat profile provided upstream of the pipe inlet) inlet condition used also for circular cross-section channels. The results of this analysis show that the pressure defect is Reynolds number independent.

New correlations for the pressure defect and hydrodynamic entrance length, based on the fitting of the numerical solutions, have been proposed and compared with previous studies for the Reynolds-independent semi-idealised configuration. The trend of the pressure defect $K(x)$ derived from these analyses is in reasonable agreement with the classical correlation of Shah [69]. The main difference between the CFD results and the correlation of Shah [69] lies in the fact that $K(x)$ reaches the constant value of $K(\infty)$ at a shorter distance from the entrance (lower hydrodynamic entrance length) and that the value of $K(\infty)$ is lower. Since the original correlation by Shah [69] appears to be based on the now outdated numerical results by Shah and Farnia [71] tabulated by Liu [70], it is expected that the current correlation, derived using robust modern numerical methods with high grid resolution, is more accurate. The resulting 3.6% and 2.8% improvement in prediction of $K(\infty)$ for the circular and square cross-section ducts, respectively, might be non-negligible in the design of components such as automotive catalysts and filters or compact heat exchangers, where the extra pressure loss will result in increased fuel and/or energy consumption.

Another new correlation has been developed to approximate losses for a convergent nozzle inlet geometry (with circular cross-section), which is more relevant for practical applications, and shown to be Reynolds number-dependent. Losses for pipes with sharp edged contraction entry and other less efficient inlet configurations will be different, and would need a further investigation.

For both correlations, the dimensionless hydrodynamic entrance length based on the centreline velocity is in good agreement with the values reported in the previously published studies (e.g. [56], [61], [62], [65], [74] and [44]). As discussed in the introduction, an accurate prediction of the hydrodynamic entrance length is important for the design of flow meters (e.g. [122], [123] and EN ISO 5167-1:2003 section 7.2.1), wind tunnels (e.g. [45]) and microchannels where the boundary layer development region is used for enhancing the heat transfer for cooling applications (e.g. [124]). The present correlation for the pressure defect, in both circular and square cross-section channels, reaches its asymptotic value at an x^+ comparable to the hydrodynamic entrance length based on the centreline velocity, while in all the previous correlations the asymptotic value is reached at an x^+ one order of magnitude higher.

Finally, for circular cross-section ducts, a correlation for the momentum correction factor and kinetic energy correction factor, as a function of the axial position from the duct entrance, has been proposed for the first time (to the authors' knowledge). These are routinely used for calculation of flow contraction and expansion losses in heat exchangers (e.g. [24]) and other applications such as particulate filters, and no reliable analytical expressions for these correction factors exist.

Thus, along with a better understanding of the sources of the developing flow losses, this study offers two improved correlations for pressure loss calculations for pipes with two different representative inlet geometries, which can be easily adapted for other inlet configurations. Better prediction of developing flow losses is particularly important for the design of multi-channel flow devices, such as laminar flow meters and micro-channel heat exchangers, and development of accurate 1-D flow models for these devices.

Chapter 4

Modelling of contraction losses in laminar flow

4.1 Introduction

The literature review has shown that there are still several discrepancies between studies regarding the estimation of the contraction losses in laminar flow in single and multi-channels configurations. In particular, different experimental studies reported different values for the contraction loss coefficient for sudden contractions and its variation with the contraction area ratio.

Therefore, this chapter examines the contraction losses using an up to date RANS CFD numerical approach. Both circular and square cross-sectional channels have been investigated. A new method has been proposed to derive the contraction loss coefficient and to separate the contribution of the contraction losses from the friction and developing flow losses upstream and downstream the contraction location. In the case of particulate filters this is particularly important since after the contraction the flow is likely not to re-develop as in other multi-channel systems, due to the mass flow passing from one channel to another.

4.2 Channels with circular cross-section

4.2.1 Simulations set-up

In absence of reliable experimental data, numerical solutions of Navier-Stokes equations are a good approximation for laminar incompressible continuum flows of Newtonian fluids. Therefore, CFD modelling of the flow in a sudden contraction is used here in order to improve existing correlations for the contraction losses in laminar flow regime.

Several laminar flow simulations have been performed using the commercial CFD package Star-CCM+. Two 2-D axisymmetric computational domains have been investigated to assess the effect of the flow profile approaching the contraction:

1. **Contraction Computational Domain 1** (Figure 4.1): consists of two pipes with different diameter connected through a sudden contraction. The upstream pipe has a length of $x^+ = \frac{L}{DRe} = 0.005$ so that when the flow approaches the contraction the velocity profile is still developing (and it is almost flat). The downstream pipe has a length of $x^+ = \frac{L}{DRe} = 0.1$ so that at the end of the pipe the flow profile is fully developed.

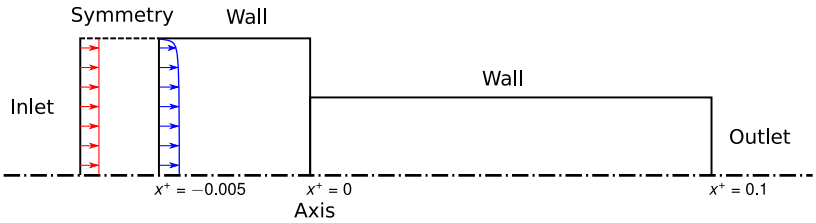

Fig. 4.1 Contraction Computational Domain 1.

2. **Contraction Computational Domain 2** (Figure 4.2): consists of two pipes with different diameter connected through a sudden contraction. The upstream pipe has a length of $x^+ = \frac{L}{DRe} = 0.1$ so that when the flow approaches the contraction the velocity profile is fully developed. The downstream pipe has a length of $x^+ = \frac{L}{DRe} = 0.1$ so that at the end of the pipe the flow profile is fully developed.

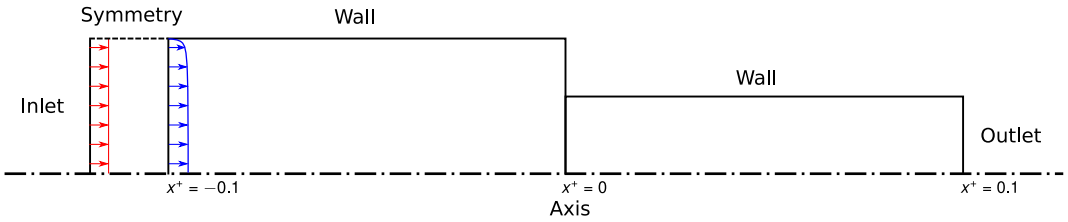

Fig. 4.2 Contraction Computational Domain 2.

Both domains include an inlet section (as in the Computational Domain 2 in Chapter 3) to avoid the high velocity gradient and pressure distortion in the vicinity of the duct entry. The boundary conditions are shown in Table 4.1.

The Reynolds number definition $Re = \frac{\rho UD}{\mu}$ is based on the mean velocity U and channel hydraulic diameter D, with μ being the dynamic viscosity and ρ being air density. Three values of the Reynolds number in the downstream (smaller) pipe $Re = 500$, $Re = 1000$ and $Re = 1500$ have been chosen in order to ensure a fully laminar regime. Four contraction area ratios, defined as the ratio between the area of the pipe downstream A_1 and the area of the pipe upstream A_2, $\sigma = A_1/A_2 = 0.2$, 0.4, 0.6 and 0.8 have been investigated . The length L of the upstream and downstream pipes was varied for each Reynolds number in order to maintain the dimensionless length of the domain x^+. Other parameters and assumptions for the CFD modelling are reported in Table 4.2.

Table 4.1 Contraction losses in channels with circular cross-section: Boundary Conditions.

Boundary	Boundary Condition
Inlet	Constant Velocity
Outlet	Ambient Static Pressure ($P_{Amb.} = 101325[Pa]$)
Wall	No Slip
Axis	Axis
Symmetry	Symmetry Plane

Table 4.2 Contraction losses in channels with circular cross-section: Star-CCM+ Models.

Parameter	Model
Geometry/Domain	2-D Axisymmetric
Viscous Regime	Laminar
Time	Steady State
Flow Solver	Segregated Flow
Solution Algorithm	SIMPLE
Convection Scheme	Second-Order
Equation of State	Constant Density
Fluid Density	$\rho = 1.2041 \left[Kg/m^3\right]$
Fluid Dynamic Viscosity	$\mu = 1.8133 \times 10^{-5} \left[Pa\,s\right]$

4.2.2 Pressure calculation

Looking at Figure 4.1 and 4.2 from left to right the pressure losses can be divided in:

1. Losses due to friction and flow development upstream of the contraction.
2. The contraction losses in the proximity of the contraction location.
3. The gain in dynamic pressure after the contraction.
4. Losses due to friction and flow development downstream of the contraction.

To assess the mechanical energy losses (total pressure losses) due to a sudden contraction both static and dynamic pressure have to be considered. By definition, the total pressure along a streamline can be calculated by adding the local streamline values of the static and dynamic pressure. However, in most of the practical applications, the the local streamline values of the static and dynamic pressure are not known, and only the mean cross-sectional static and dynamic pressure are available. For this reason, in the present study the total pressure losses due to a sudden contraction and the contraction loss coefficient have been calculated using the mean cross-sectional static and dynamic pressure, so that they could be used in a wider range of practical applications.

The mean dimensional and dimensionless cross-sectional total pressure (P_{Total} and P^*_{Total}) along the pipe can be calculated by adding the average cross-sectional static and dynamic pressures as:

$$P_{Total} = P_{Static} + P_{Dynamic}, \tag{4.1}$$

$$P^*_{Total} = P^*_{Static} + P^*_{Dynamic}. \tag{4.2}$$

Here, the mean dimensional and dimensionless cross-sectional static and dynamic pressure (P_{Static}, P^*_{Static}, $P_{Dynamic}$ and $P^*_{Dynamic}$) along the pipe were calculated at every $x^+ = 2.1 \times 10^{-4}$ from the CFD results as:

$$P_{Static} = \frac{1}{A}\int_0^A P dA, \tag{4.3}$$

$$P^*_{Static} = P_{Static} / \frac{\rho U^2}{2}, \tag{4.4}$$

$$P_{Dynamic} = \frac{\rho u^2}{2}, \tag{4.5}$$

$$P^*_{Dynamic} = P_{Dynamic} / \frac{\rho U^2}{2}, \tag{4.6}$$

where A is the cross-sectional area of the pipe, U is the mean cross-sectional velocity in the downstream pipe and u is the local mean cross-sectional velocity.

4.2.3 Results

The data presented in this section has been obtained by sampling respective variable values from CFD results with step of $x^+ = 2.1 \times 10^{-4}$, and interpolating between these points (at every $x^+ = 5.25 \times 10^{-5}$) using cubic interpolation to facilitate analysis. It was found that the effect of the interpolation on the accuracy of the results is minimal, and, as shown later in this section, a sensitivity study has been performed to ensure that small variations in data point positions do not affect the conclusions significantly.

Figure 4.3 shows the dimensionless mean cross-sectional static pressure versus x^+ for the **Contraction Computational Domain 1** and contraction area ratio $\sigma = 0.2$. The sudden contraction is located at $x^+ = 0$. The pressure losses for fully developed flow (Darcy-Weisbach Eq. 3.2 and labelled F.D.F. in the legend) and developing flow

(Eq. 1.4 and Eq. 3.4 and labelled D.F. in the legend) in the downstream pipe are also plotted for comparison purposes.

Figure 4.3 (a) shows that after the contraction the static pressure trend is well captured (less than 1% difference) by the trend of the developing flow losses calculated with Eq. 1.4 and Eq. 3.4, except in the proximity of the contraction ($0 < x^+ < 0.005$). Figure 4.3 (b), which is a zoomed version of Figure 4.3 (a) for $-0.005 < x^+ < 0.005$, shows that the overall static pressure losses are almost Reynolds number independent. This is valid also for the other contraction area ratios, although not shown here, and $\sigma = 0.2$ was chosen only for demonstration purposes. However, a small difference in the local pressure for different Reynolds numbers can be seen in the region $0 < x^+ < 0.001$. This behaviour is attributed to the presence of the vena-contracta in this location, the size of which varies with the Reynolds number.

At Reynolds number $Re = 500$ the size of the vena-contracta is very small and it is characterised by a thickening of the boundary layer without flow recirculation. The thickening of the boundary layer in this region causes the shear stresses at the wall to be lower than for an ideal developing flow, thus producing less pressure losses. This could explain why the developing flow losses calculated with Eq. 1.4 and Eq. 3.4 show a higher pressure loss for $0 < x^+ < 0.005$, at the smaller pipe entrance.

At Reynolds number $Re = 1000$ and 1500 the size of the vena-contracta increases and it is characterised by a thickening of the boundary layer with a flow recirculation zone formed immediately after the contraction location. For these two Reynolds numbers the presence of the vena-contracta has a clear effect on the local pressure, which is characterised by a sudden decrease followed by a pressure recovery once the flow re-expands in the cross-section.

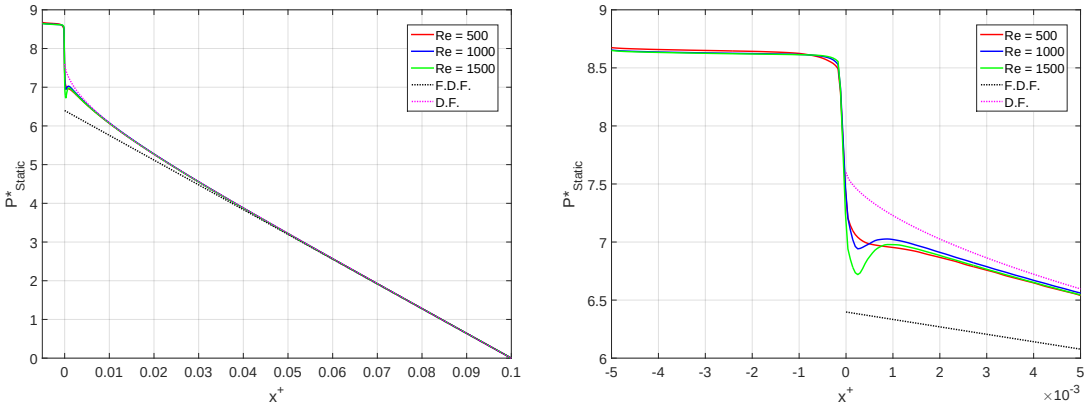

(a) (b)

Fig. 4.3 Contraction Computational Domain 1: Dimensionless static pressure for $\sigma = 0.2$ and $Re = 500$, 1000 and 1500: (a) full domain and (b) zoom in the proximity of the contraction. F.D.F. abbreviates fully developed flow while D.F. abbreviates developing flow.

Figure 4.4 shows the dimensionless mean cross-sectional static pressure versus x^+ for all the contraction area ratios investigated ($\sigma = 0.2$, 0.4, 0.6 and 0.8) at Reynolds number $Re = 500$, while Figure 4.5 shows the same graph but for the dimensionless mean cross-sectional total pressure. From these figures it can be seen that the overall pressure losses depend on the contraction area ratio and that after the contraction and vena-contracta (after the pressure recovery) the flow re-develops with the same trend for all the contraction area ratios. This is the case also for all the other Reynolds numbers, although not shown here, and $Re = 500$ was chosen only for demonstration purposes.

Figure 4.4 (a) shows also the dimensionless mean cross-sectional dynamic pressure versus x^+ for all the contraction area ratios investigated ($\sigma = 0.2$, 0.4, 0.6 and 0.8) at Reynolds number $Re = 500$. In contrast with the static pressure, which is decreasing from the left to right in the domains considered here, the dynamic pressure increases when the flow passes from the larger pipe to the smaller one, as the mean cross-sectional velocity increases.

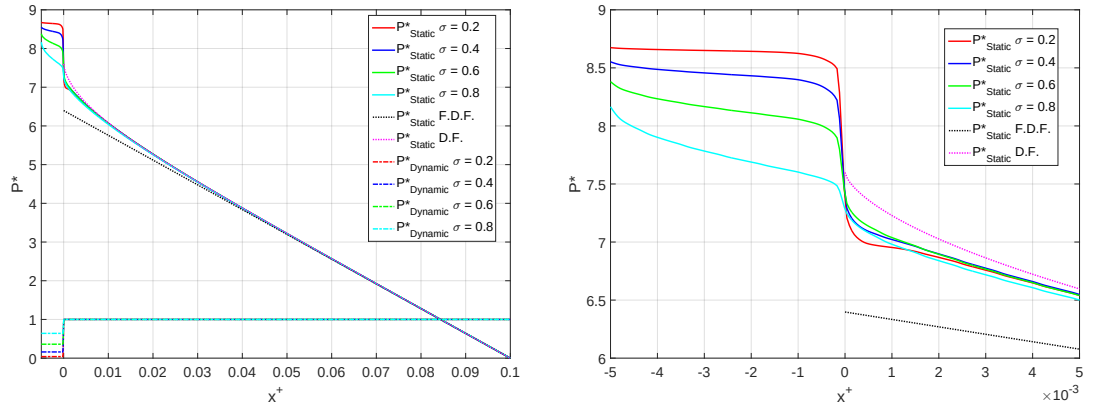

(a) (b)

Fig. 4.4 Contraction Computational Domain 1: Dimensionless static and dynamic pressure for $\sigma = 0.2$, 0.4, 0.6 and 0.8 and $Re = 500$: (a) full domain and (b) zoom in the proximity of the contraction. F.D.F. abbreviates fully developed flow while D.F. abbreviates developing flow.

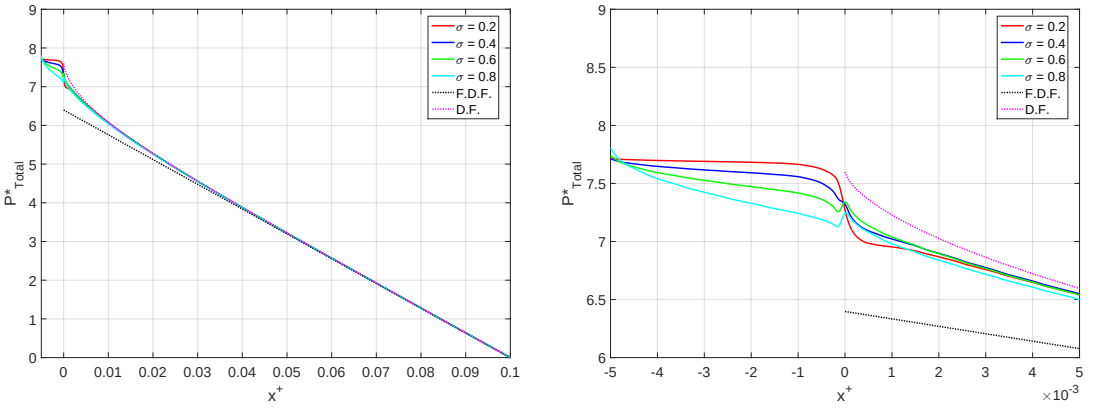

(a) (b)

Fig. 4.5 Contraction Computational Domain 1: Dimensionless total pressure for $\sigma = 0.2$, 0.4, 0.6 and 0.8 and $Re = 500$: (a) full domain and (b) zoom in the proximity of the contraction. F.D.F. abbreviates fully developed flow while D.F. abbreviates developing flow.

Figure 4.5 (b) shows how calculating the total pressure with the mean cross-sectional static and dynamic pressure, instead of along the flow streamlines, affects the local values of the total pressure in the proximity of the contraction. As the total pressure represents the irreversible losses, this should be always decreasing (or in other words

the total pressure drop should be always increasing) from left to right in the domains considered here.

However, this is not the case for the two smaller contractions ($\sigma = 0.6$ and 0.8) where a small increase in the mean cross-sectional total pressure can be observed between $0 < x^+ < 5 \times 10^{-4}$.

This behaviour is caused by the definition of the "total pressure" here, which is taken as an average of the total pressure values across the cross-section of the pipe. If the total pressure was calculated along a streamtube as it should be, this increase would not be observed. However, it is difficult to do in practical applications as the size of the vena-contracta is not known a priori. Downstream, where the main flow expands to the whole cross-section, the monotonic decrease of the "total pressure" used here is recovered. This does not invalidate the calculation of the contraction coefficient, as these are performed bearing in mind the definitions, and using the pressure drop between cross-sections outside the vena-contracta.

Since the total pressure losses measured between an upstream and downstream position of the sudden contraction incorporate the coupled contribution of the changes in the dynamic pressure, the friction losses associated with fully developed and developing flow and the irreversible losses caused by the contraction, defining and separating these losses quantitatively can be done in different ways. To the author knowledge, this is the first study that investigates the contraction losses in laminar flow with CFD and the reviewed experimental studies reported in the literature do not clearly specify the method used to separate the contraction losses from the friction and development losses.

The method proposed here, which aims to identify an upstream and downstream location of the sudden contraction where the pressure deviates from the developed/developing flow pattern so that the extra losses due to the presence of the contraction is not negligible, is based on the knowledge of the fully developed and developing flow losses (Chapter 3) and the investigation of the gradient of the static and total pressure.

Figure 4.6 (a) shows the dimensionless total pressure in the proximity of the contraction for the contraction area ratios $\sigma = 0.2$ and 0.6 at Reynolds number $Re = 500$. These have been plotted together with the dimensionless developing flow losses upstream ($\sigma = 0.2$ D.F. and $\sigma = 0.6$ D.F.) and downstream (D.F.) the contraction, calculated

using Eq. 1.4 and Eq. 3.4, and the dimensionless fully developed flow losses, calculated using Eq. 3.2. This plot allows to identify the axial location where the developing flow upstream of the contraction deviates from its ideal trend due to the effect of the contraction.

Similar to one of the definitions of the developing flow, where the flow is considered fully developed when the centreline velocity is within 1% of its "ideal" fully developed value, one can introduce a criterion for identifying the point where the contracting flow behaviour deviates from the flow in a pipe without contraction. Here the flow will be considered to be unaffected by the downstream contraction up to the location where the CFD solution of the cross-sectional mean total pressure deviates less than $\pm 1\%$ from the developing flow trend upstream. Hence, the location where the total pressure deviates from the developing flow pressure profile by 1% (black marks in the plot) was selected as the location that denotes the separation between the friction losses upstream and the beginning of the contraction losses.

Figure 4.6 (b) shows the axial gradient of the dimensionless static pressure in the proximity of the contraction for the contraction area ratios $\sigma = 0.2$ and 0.6 at Reynolds number $Re = 500$, together with the gradient of the dimensionless developing flow losses and the fully developed flow losses downstream of the contraction. This plot allows to identify the approximate location where the re-developing flow downstream of the contraction starts following the trend of an ideal developing flow, which will be used as indication of the separation between the end of the contribution of the contraction losses and the beginning of the friction and developing flow losses downstream.

The pressure gradient was used here rather than the actual pressure because, due to the different velocity profile at the inlet of the downstream pipe between the ideal developing flow and the case with a sudden contraction, the pressure development in the proximity of the contraction is slightly different for different contraction ratios, while the gradient/rate of change remains almost identical.

Thus, the location downstream the contraction, which denotes the end of the contribution of the contraction losses and the beginning of the re-developing flow losses, has been selected as the first location after the contraction and after the location of the pressure recovery, if present, (marked with a circle in Figure 4.6) where the gradient

of the total pressure falls in between the fully developed flow and developing flow gradient.

This criterion has been selected because when the gradient of the total pressure is lower (or higher if taken in absolute value) than the developing flow gradient for the same location it means that an higher pressure is lost compared to the only ideal developing flow losses, and hence the contribution of the contraction losses is still non negligible. As for the top value, the gradient of the fully developed flow was used as this is the asymptotic value to which the gradient should converge.

Since the total pressure is non dimensionalised with the dynamic pressure in the outlet channel, the difference in the dimensionless pressure between the two location selected (one upstream and one downstream the contraction) corresponds to the contraction loss coefficients, as defined in Eq. 1.12.

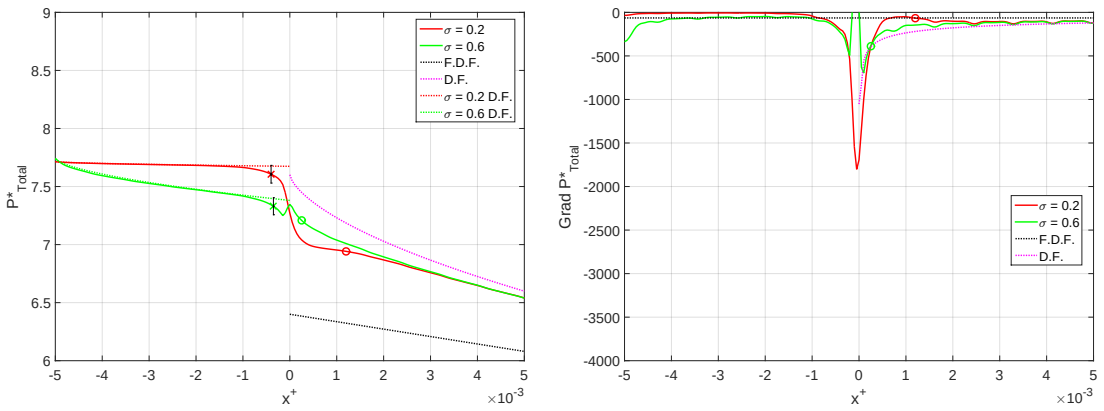

(a) (b)

Fig. 4.6 Dimensionless total pressure and gradient of the total pressure for $\sigma = 0.2$ and 0.6 and $Re = 500$: (a) total pressure (b) gradient of the total pressure. F.D.F. abbreviates fully developed flow while D.F. abbreviates developing flow.

Figure 4.7 shows that the contraction loss coefficient for the cases with Reynolds number $Re = 500$ derived with the present method agrees well with the contraction loss coefficient derived from the Borda-Carnot equation (Eq. 1.14) for a sudden change in cross-section. Two additional contraction area ratios $\sigma = 0.05$ and 0.95 have been simulated as well at Reynolds number $Re = 500$ to capture the full trend.

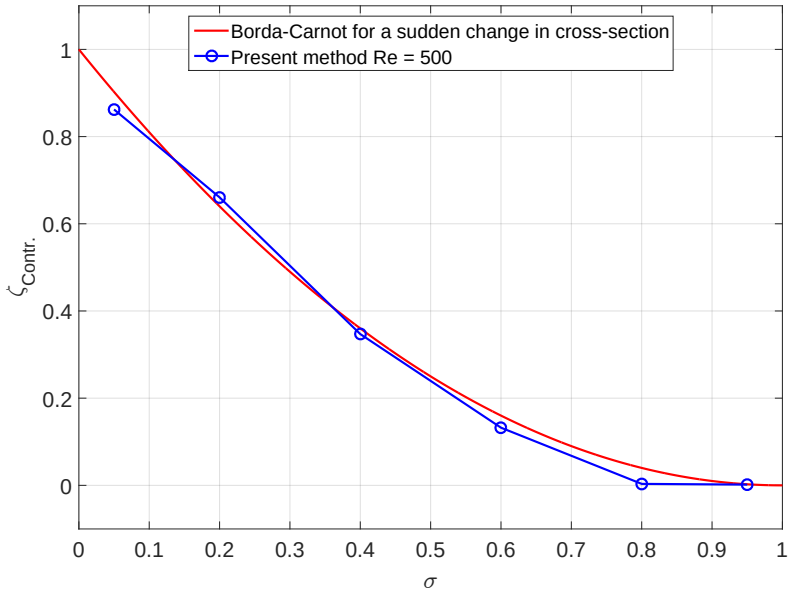

Fig. 4.7 Contraction loss coefficient for the contraction area ratios $\sigma = 0.05$, 0.2, 0.4, 0.6, 0.8 and 0.95 cases with Reynolds number $Re = 500$.

The method proposed here relies on the establishing the interval where the contraction losses are believed to change the pressure distribution in comparison with a fully developed/developing flow. In order to further asses the method, a sensitivity analysis was performed to evaluate how much the contraction loss coefficient would change if a different x^+ location upstream and downstream the contraction was used for the calculations. Thus, the contraction loss coefficient was also calculated using the total pressure at a $|\Delta x^+| = 1.575 \times 10^{-4}$ further upstream and downstream from the previously selected location.

Figure 4.8 shows the values of the contraction loss coefficient for all the contraction area ratios and Reynolds numbers investigated, as well as the values calculated using the further upstream and downstream locations (marked with a square and cross respectively) from the previously selected location (marked with a circle). It can be seen here that the contraction loss coefficient calculated with the present method agrees well with the contraction loss coefficient derived from the Borda-Carnot equation (Eq. 1.14) for a sudden change in cross-section with a maximum deviation of 0.1, regardless of the contraction area ratio, Reynolds number and chosen downstream location.

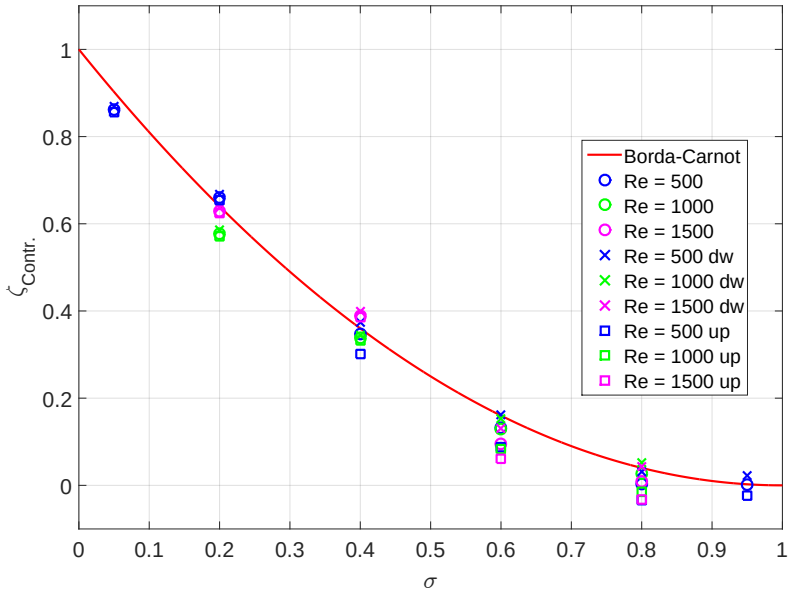

Fig. 4.8 Contraction Computational Domain 1: Contraction loss coefficient for all the contraction area ratios and Reynolds number calculated using different downstream locations.

Applying the same method to calculate the contraction loss coefficient for the **Contraction Computational Domain 2** gives similar results, as shown in Figure 4.9.

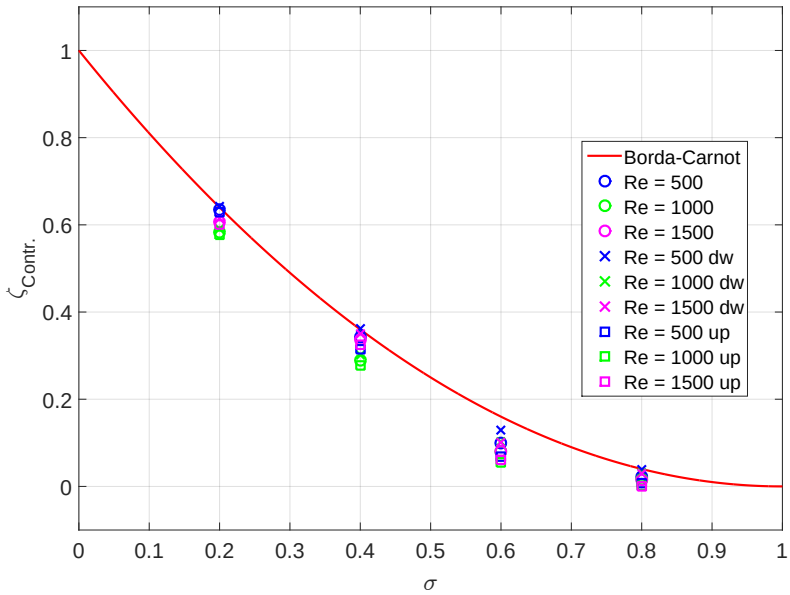

Fig. 4.9 Contraction Computational Domain 2: Contraction loss coefficient for all the contraction area ratios and Reynolds number calculated using different downstream locations.

Comparing these results with the empirical correlations reported in the literature (Eqs. 1.15 - 1.20, plotted in Figure 1.9) suggests that the contraction loss coefficient and its variation with the contraction area ratio is affected considerably by the pipe configuration/type of contraction and it cannot be generalised. In the configuration investigated in this section (Figure 4.1 and Figure 4.2) as well as in the experimental study of Brightmore [91], where both the vena-contracta and the flow separation upstream are present, the contraction loss coefficient follows the trend of the Borda-Carnot equation (Eq. 1.14). Therefore, the present results further give credit to Brightmore's suggestion to use the Borda-Carnot equation as a theoretical expression for estimation of both the contraction and expansion loss coefficients for sudden change in cross-section.

However, in different configurations, where the flow separation upstream is not present (or possibly not included in the contraction loss coefficient calculations), the contraction loss coefficient shows a different trend. The latter effect has been further investigated as shown in the next section.

4.3 Channels with square cross-section

The previous section has shown that the contraction loss coefficient in channels with circular cross-section are well approximated by the contraction loss coefficient derived from the Borda-Carnot equation.

However, in GPFs and other multi-channel systems the cross-section of the channels is often square. Therefore, a new computational domain with square cross-section and upstream flow bounded by solid walls and one without upstream flow bounded by solid walls have been investigated in the following sections.

4.3.1 Single channel contraction simulations set-up

Figure 4.10 shows the computational domain, named **Single Channel Contraction Square Computational Domain**, where the upstream flow is bounded by solid walls.

Since the geometry is not axisymmetric, a full 3-D CFD approach is used. In order to decrease the computational effort, only a quarter of a channel was used due to the symmetry properties of the geometry. A no-slip condition is used at the walls, while

a symmetry plane boundary condition has been used for the other two surfaces (mid planes of the channel).

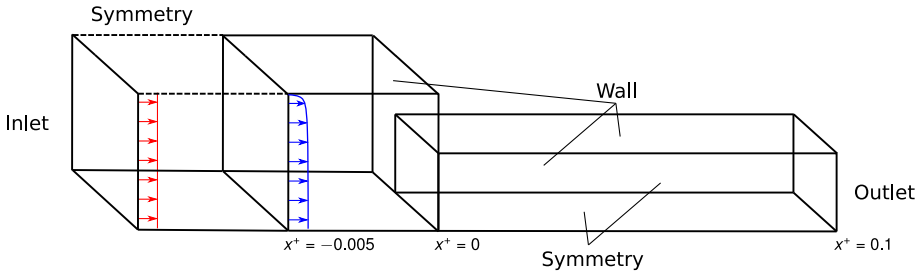

Fig. 4.10 Single Channel Contraction Square Computational Domain.

The domain includes an inlet section (as in the Computational Domain 2 in Chapter 3) to avoid the high velocity gradient and pressure distortion in the vicinity of the duct entry.

The boundary conditions are shown in Table 4.3.

The Reynolds number definition $Re = \frac{\rho UD}{\mu}$ is based on the mean velocity U and channel hydraulic diameter D, with μ being the dynamic viscosity and ρ being air density. Three values of the Reynolds number in the downstream (smaller) pipe $Re = 500$, $Re = 1000$ and $Re = 1500$ have been chosen in order to ensure a fully laminar regime. Four contraction area ratios, defined as the ratio between the area of the pipe downstream A_1 and the area of the pipe upstream A_2, $\sigma = A_1/A_2 = 0.2, 0.4, 0.6$ and 0.8 have been investigated . The length of the upstream and downstream pipes was varied for each Reynolds number in order to maintain the dimensionless length of the domain, $x^+ = -0.005$ upstream and $x^+ = 0.1$ downstream the contraction. Other parameters and assumptions for the CFD modelling are reported in Table 4.4.

Table 4.3 Contraction losses in channels with square cross-section: Boundary Conditions.

Boundary	Boundary Condition
Inlet	Constant Velocity
Outlet	Ambient Static Pressure ($P_{Amb.} = 101325[Pa]$)
Wall	No Slip
Symmetry	Symmetry Plane ($\partial/\partial h = 0$)

Table 4.4 Contraction losses in channels with square cross-section: Star-CCM+ Models.

Parameter	Model
Geometry/Domain	3-D
Viscous Regime	Laminar
Time Dependence	Steady State
Flow Solver	Segregated Flow
Solution Algorithm	SIMPLE
Convection Scheme	Second-Order
Equation of State	Constant Density
Fluid Density	$\rho = 1.2041 \left[Kg/m^3\right]$
Fluid Dynamic Viscosity	$\mu = 1.8133 \times 10^{-5} \left[Pa\,s\right]$

4.3.2 Single channel contraction results

Figure 4.11 shows the dimensionless mean cross-sectional static pressure versus x^+ for the **Single Channel Contraction Square Computational Domain** and contraction area ratio $\sigma = 0.2$. The sudden contraction is located at $x^+ = 0$. The pressure losses for fully developed flow (Darcy-Weisbach Eq. 3.2 and labelled F.D.F. in the legend) and developing flow (Eq. 1.4 and Eq. 3.4 and labelled D.F. in the legend) in the downstream pipe are also plotted for comparison purposes.

Figure 4.11 presents nearly identical features to Figure 4.3, discussed in the previous section, and in particular it shows that the contraction losses in channels with circular and square cross-section are both nearly Reynolds number independent. This is valid also for the other contraction area ratios, although not shown here, and $\sigma = 0.2$ was chosen only for demonstration purposes.

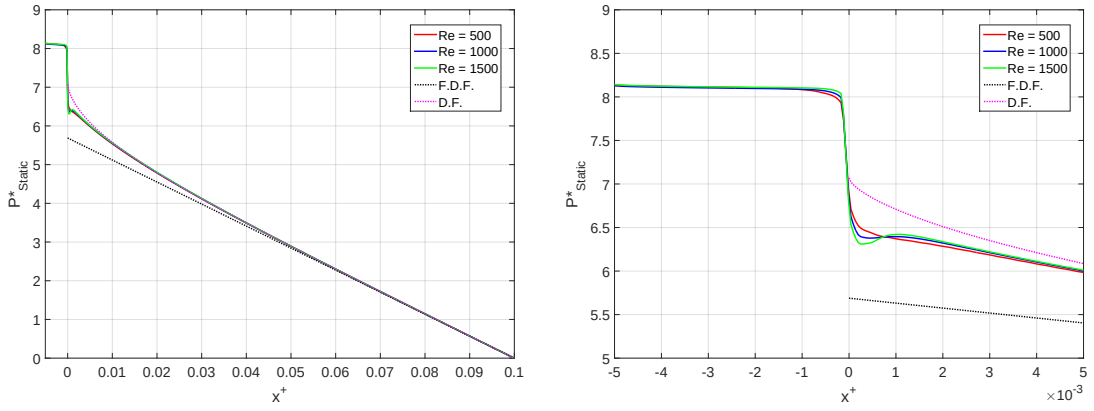

(a) (b)

Fig. 4.11 Single Channel Contraction Square Computational Domain: Dimensionless static pressure for $\sigma = 0.2$ and $Re = 500$, 1000 and 1500: (a) full domain and (b) zoom in the proximity of the contraction. F.D.F. abbreviates fully developed flow while D.F. abbreviates developing flow.

Figure 4.12 shows the dimensionless mean cross-sectional static pressure versus x^+ for all the contraction area ratios investigated ($\sigma = 0.2$, 0.4, 0.6 and 0.8) at Reynolds number $Re = 500$, while Figure 4.13 shows the same graph but for the dimensionless mean cross-sectional total pressure. From these figures it can be seen that the overall pressure losses depend on the contraction area ratio and that after the contraction the flow re-develops with a similar trend for all the contraction area ratios. This is the case also for all the other Reynolds numbers, although not shown here, and $Re = 500$ was chosen only for demonstration purposes.

Figure 4.12 (b) and Figure 4.13 (b) also show that, as expected, for the present configuration (Figure 4.10), there is a pressure loss between $x^+ = -0.005$ and the contraction ($x^+ = 0.$).

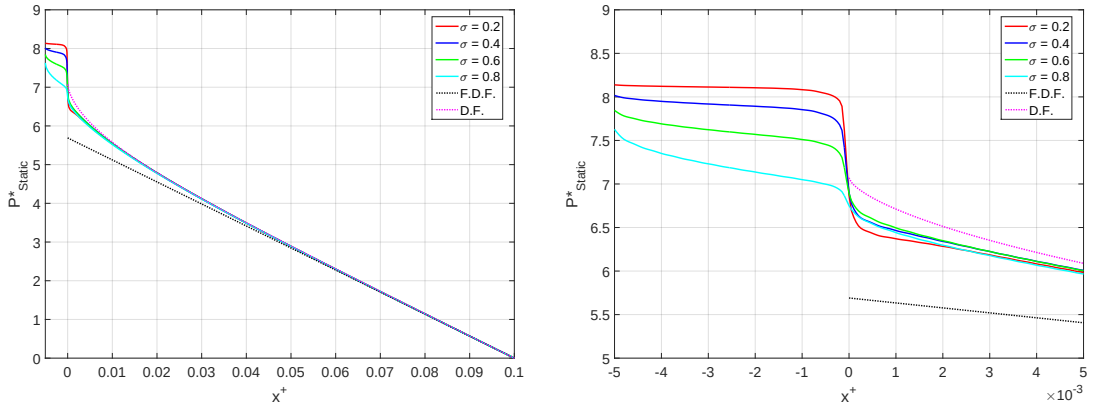

(a) (b)

Fig. 4.12 Single Channel Contraction Square Computational Domain: Dimensionless static and dynamic pressure for $\sigma = 0.2$, 0.4, 0.6 and 0.8 and $Re = 500$: (a) full domain and (b) zoom in the proximity of the contraction. F.D.F. abbreviates fully developed flow while D.F. abbreviates developing flow.

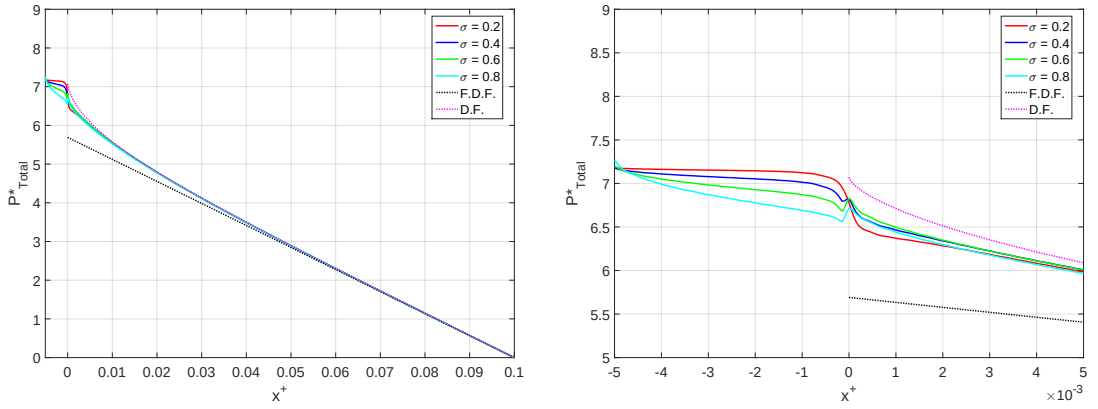

(a) (b)

Fig. 4.13 Single Channel Contraction Square Computational Domain: Dimensionless total pressure for $\sigma = 0.2$, 0.4, 0.6 and 0.8 and $Re = 500$: (a) full domain and (b) zoom in the proximity of the contraction. F.D.F. abbreviates fully developed flow while D.F. abbreviates developing flow.

The method presented in section 4.2, and used to calculate the contraction loss coefficient in single channels contraction with circular cross-section, was also used for the present configuration.

Figure 4.14 shows the dimensionless total pressure and gradient of the total pressure in the proximity of the contraction for the contraction area ratios $\sigma = 0.2$ and 0.6 at

Reynolds number $Re = 500$. Here the location downstream the contraction, which denotes the end of the contribution of the contraction losses and the beginning of the re-developing flow losses, has been selected as the first location after the contraction (marked with a circle in Figure 4.14) where the gradient of the total pressure falls in between the fully developed flow and developing flow gradient and after the location of the pressure recovery (if present).

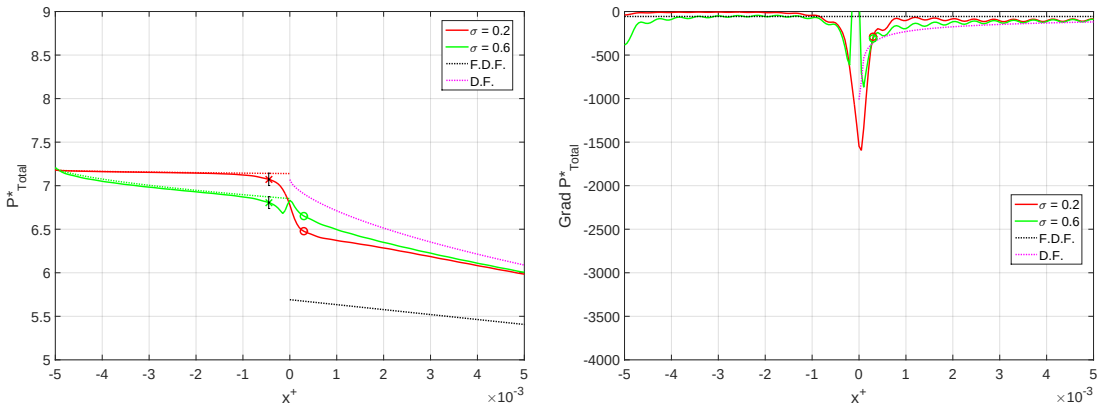

(a) (b)

Fig. 4.14 Single Channel Contraction Square Computational Domain: Dimensionless total pressure and gradient of the total pressure for $\sigma = 0.2$ and 0.6 and $Re = 500$: (a) total pressure (b) gradient of the total pressure. F.D.F. abbreviates fully developed flow while D.F. abbreviates developing flow.

Figure 4.14 (b) shows a slight oscillation for the gradients of the CFD pressure results, which is not a physical behaviour but rather a numerical artefact as discussed in the previous section.

A sensitivity analysis was performed to evaluate how much the contraction loss coefficient would change if a different x^+ location upstream and downstream the contraction was used for the calculations. Thus, the contraction loss coefficient was also calculated using the total pressure at a $|\Delta x^+| = 1.575 \times 10^{-4}$ further upstream and downstream from the previously selected location. Two additional contraction area ratios $\sigma = 0.05$ and 0.95 have been simulated as well at Reynolds number $Re = 500$ to capture the full trend.

Figure 4.15 shows the values of the contraction loss coefficient for all the contraction area ratios and Reynolds numbers investigated, as well as the values calculated

using the further upstream and downstream locations (marked with a square and cross respectively) from the previously selected location (marked with a circle).

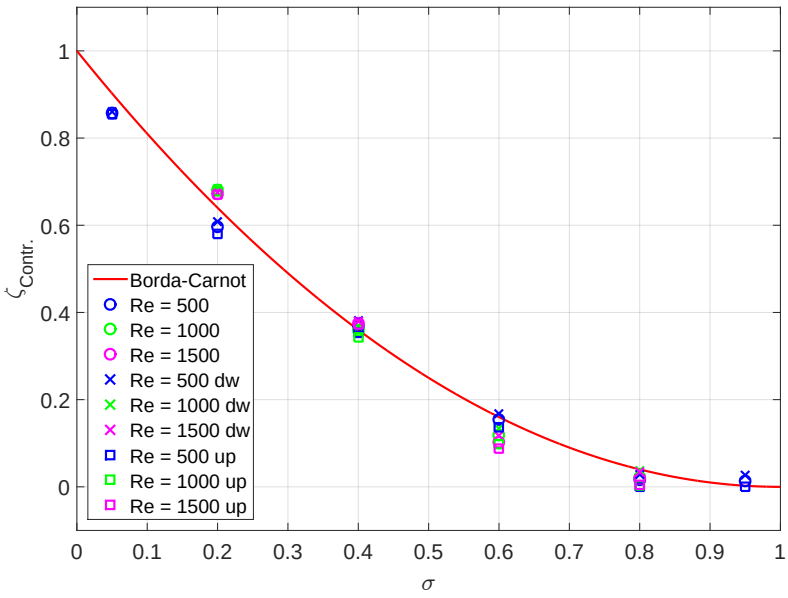

Fig. 4.15 Single Channel Contraction Square Computational Domain: Contraction loss coefficient for all the contraction area ratios and Reynolds number calculated using different downstream locations.

These results show that the square cross-section does not have a significant effect on the contraction losses and that the contraction loss coefficient can be approximated using the Borda-Carnot equation as for the circular cross-section contraction.

4.3.3 Multi-channel contraction simulations set-up

All the previous contraction losses results have shown that in laminar flows through pipes with sudden contractions and upstream flow bounded by solid walls the contraction loss coefficient appears to follow the Borda-Carnot equation. However, in GPFs the upstream flow is not bounded by solid walls and thus the flow separation upstream the contraction is not present. This also means that the flow profile is different (more uniform, without the wall boundary layers) before entering the contraction, which will affect the contraction losses. To study the effect of this different upstream flow on the contraction losses, a configuration without side wall upstream is considered here.

Figure 4.16 shows the computational domain, named **Multi-Channel Contraction Square Computational Domain**, used for the CFD analysis. Since the geometry is not axisymmetric, a 3-D domain is used. In order to decrease the computational effort, only a quarter of a channel was used due to the symmetry properties of the geometry. A no-slip condition is used at the walls, while a symmetry plane boundary condition has been used for the other surfaces. Using a symmetry boundary condition on the sides of the upstream section implies that the channel is surrounded by an infinite number of channels on each side, hence the name **Multi-Channel Contraction Square Computational Domain**.

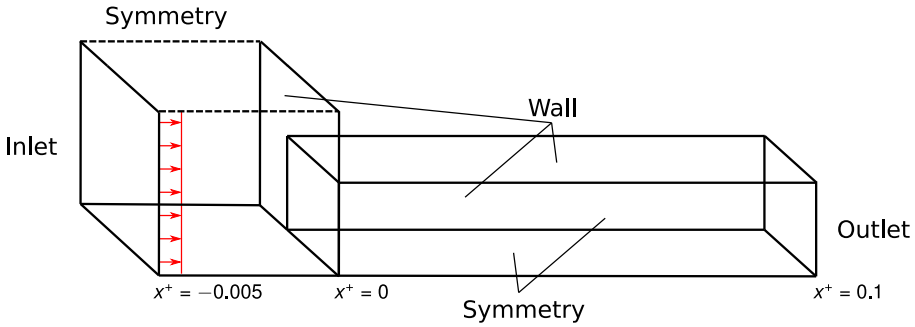

Fig. 4.16 Multi-Channel Contraction Square Computational Domain.

The boundary conditions are shown in Table 4.5.

The Reynolds number definition $Re = \frac{\rho UD}{\mu}$ is based on the mean velocity U and channel hydraulic diameter D, with μ being the dynamic viscosity and ρ being air density. Three values of the Reynolds number in the downstream (smaller) pipe $Re = 500$, $Re = 1000$ and $Re = 1500$ have been chosen in order to ensure a fully laminar regime. Four contraction area ratios, defined as the ratio between the area of the pipe downstream A_1 and the area of the pipe upstream A_2, $\sigma = A_1/A_2 = 0.2, 0.4, 0.6$ and 0.8 have been investigated . The length of the upstream and downstream pipes was varied for each Reynolds number in order to maintain the dimensionless length of the domain, $x^+ = -0.005$ upstream and $x^+ = 0.1$ downstream the contraction. Other parameters and assumptions for the CFD modelling are reported in Table 4.6.

Table 4.5 Contraction losses in channels with square cross-section: Boundary Conditions.

Boundary	Boundary Condition
Inlet	Constant Velocity
Outlet	Ambient Static Pressure ($P_{Amb.} = 101325[Pa]$)
Wall	No Slip
Symmetry	Symmetry Plane ($\partial/\partial h = 0$)

Table 4.6 Contraction losses in channels with square cross-section: Star-CCM+ Models.

Parameter	Model
Geometry/Domain	3-D
Viscous Regime	Laminar
Time Dependence	Steady State
Flow Solver	Segregated Flow
Solution Algorithm	SIMPLE
Convection Scheme	Second-Order
Equation of State	Constant Density
Fluid Density	$\rho = 1.2041\,[Kg/m^3]$
Fluid Dynamic Viscosity	$\mu = 1.8133 \times 10^{-5}\,[Pa\,s]$

4.3.4 Multi-channel contraction results

Figure 4.17 shows the dimensionless mean cross-sectional static pressure versus x^+ for the contraction area ratio $\sigma = 0.2$. The sudden contraction is located at $x^+ = 0$. The pressure losses for fully developed flow (Darcy-Weisbach Eq. 3.2 and labelled F.D.F. in the legend) and developing flow (Eq. 1.4 and Eq. 3.4 and labelled D.F. in the legend) in the downstream pipe are also plotted for comparison purposes.

Figure 4.17 presents nearly identical features to Figure 4.3 and in particular it shows that the contraction losses in channels with circular and square cross-section are both nearly Reynolds number independent. This is valid also for the other contraction

area ratios, although not shown here, and $\sigma = 0.2$ was chosen only for demonstration purposes.

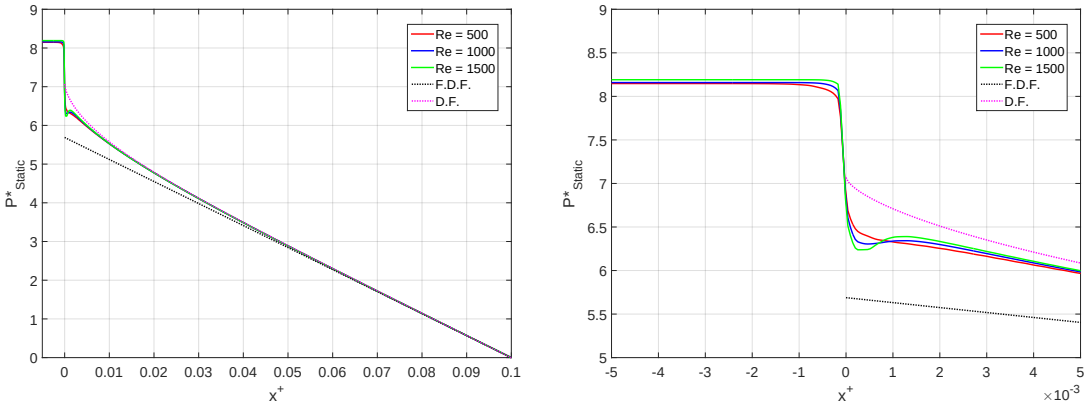

(a) (b)

Fig. 4.17 Multi-Channel Contraction Square Computational Domain: Dimensionless static pressure for $\sigma = 0.2$ and $Re = 500$, 1000 and 1500: (a) full domain and (b) zoom in the proximity of the contraction. F.D.F. abbreviates fully developed flow while D.F. abbreviates developing flow.

Figure 4.18 shows the dimensionless mean cross-sectional static pressure versus x^+ for all the contraction area ratios investigated ($\sigma = 0.2$, 0.4, 0.6 and 0.8) at Reynolds number $Re = 500$, while Figure 4.19 shows the same graph but for the dimensionless mean cross-sectional total pressure. From these figures it can be seen that the overall pressure losses depend on the contraction area ratio and that after the contraction the flow re-develops with a similar trend for all the contraction area ratios. This is the case also for all the other Reynolds numbers, although not shown here, and $Re = 500$ was chosen only for demonstration purposes.

Figure 4.18 (b) and Figure 4.19 (b) also show that, for the present configuration (Figure 4.16), there isn't any pressure loss until $x^+ \sim -5 \times 10^{-4}$ upstream the contraction, in contrast with the circular and square cross-section cases shown in the previous sections. This behaviour is not attributed to the square cross-section but rather to the fact that the section upstream the contraction is not bounded by solid walls and hence there isn't any pressure lost due to friction.

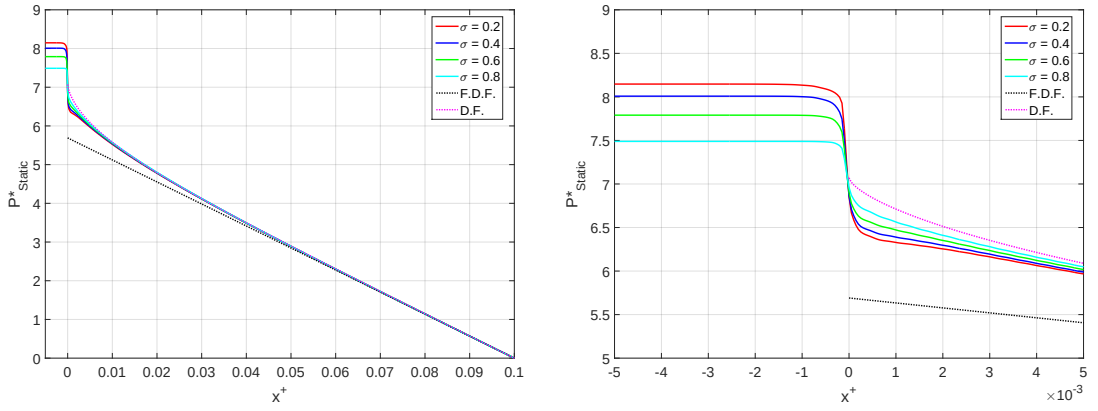

(a) (b)

Fig. 4.18 Multi-Channel Contraction Square Computational Domain: Dimensionless static and dynamic pressure for $\sigma = 0.2$, 0.4, 0.6 and 0.8 and $Re = 500$: (a) full domain and (b) zoom in the proximity of the contraction. F.D.F. abbreviates fully developed flow while D.F. abbreviates developing flow.

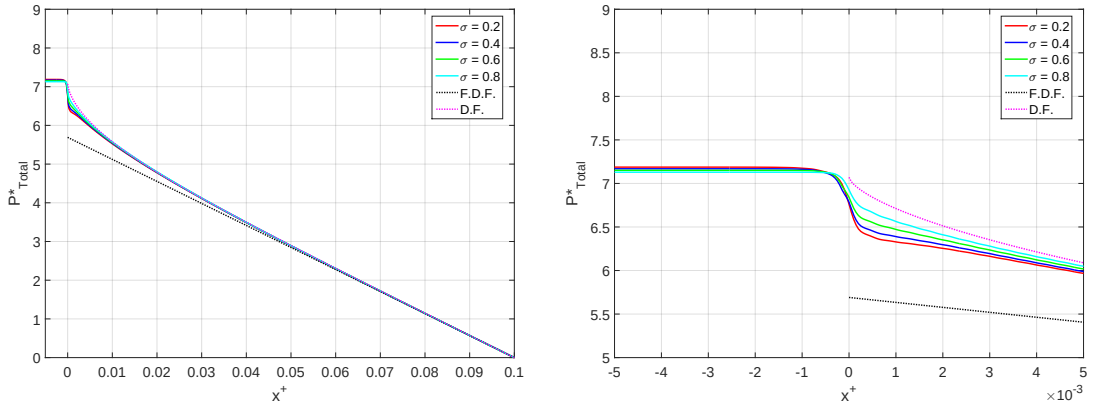

(a) (b)

Fig. 4.19 Multi-Channel Contraction Square Computational Domain: Dimensionless total pressure for $\sigma = 0.2$, 0.4, 0.6 and 0.8 and $Re = 500$: (a) full domain and (b) zoom in the proximity of the contraction. F.D.F. abbreviates fully developed flow while D.F. abbreviates developing flow.

The same method presented in the previous sections was used here to calculate the contraction loss coefficient, except for the determination of the axial location upstream the contraction that identifies the beginning of the contraction losses. In fact, as in the present configuration there isn't any pressure lost due to friction upstream the contraction, all the losses before the contraction are attributed to and included in the

contraction losses. Thus, only the location downstream the contraction had to be determined, while the total pressure at the beginning of the Multi-Channel Contraction Computational Domain Square ($x^+ = -0.005$) was used for the calculations.

Figure 4.20 shows the dimensionless total pressure and gradient of the total pressure in the proximity of the contraction for the contraction area ratios $\sigma = 0.2$ and 0.6 at Reynolds number $Re = 500$. Here, as in the previous sections, the location downstream the contraction, which denotes the end of the contribution of the contraction losses and the beginning of the re-developing flow losses, has been selected as the first location after the contraction (marked with a circle in Figure 4.20) where the gradient of the total pressure falls in between the fully developed flow and developing flow gradient and after the location of the pressure recovery (if present).

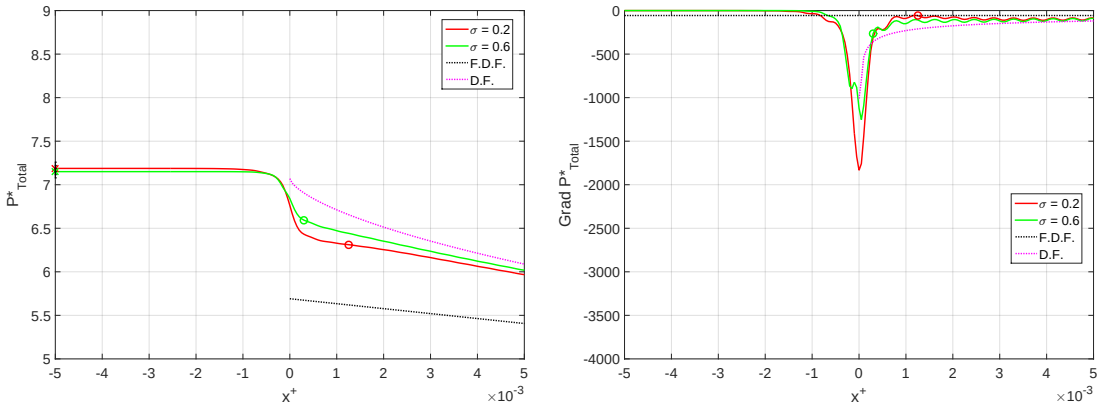

(a) (b)

Fig. 4.20 Multi-Channel Contraction Square Computational Domain: Dimensionless total pressure and gradient of the total pressure for $\sigma = 0.2$ and 0.6 and $Re = 500$: (a) total pressure (b) gradient of the total pressure. F.D.F. abbreviates fully developed flow while D.F. abbreviates developing flow.

Figure 4.20 (b) shows a slight oscillation for the gradients of the CFD pressure results, which is not a physical behaviour but rather a numerical artefact. Several methods exist to filter or smooth such oscillations/noise in the data (e.g. moving average). However, due to the marginal effect of these oscillations, it has been preferred not to apply any filter to the data.

A sensitivity analysis was performed to evaluate how much the contraction loss coefficient would change if a different x^+ location downstream the contraction was used

for the calculations. Thus, the contraction loss coefficient was also calculated using the total pressure at a $|\Delta x^+| = 1.575 \times 10^{-4}$ further upstream and downstream from the previously selected location. Two additional contraction area ratios $\sigma = 0.05$ and 0.95 have been used as well at Reynolds number $Re = 500$ to capture the full trend.

Figure 4.21 shows the values of the contraction loss coefficient for all the contraction area ratios and Reynolds numbers investigated, as well as the values calculated using the further upstream and downstream locations (marked with a square and cross respectively) from the previously selected location (marked with a circle). It can be seen here that, in contrast with the previous results, the contraction loss coefficient calculated with the present method differs significantly from the contraction loss coefficient derived from the Borda-Carnot equation for a sudden change in cross-section.

Thus, the non-linear least squares method was used to derive a correlation (Eq. 4.7) which provides a good fit for the contraction loss coefficient data:

$$\zeta_{Contr.\,Square} = 0.92\left(1-\sigma^2\right). \tag{4.7}$$

Eq. 4.7 provides a maximum deviation of 0.1 from the calculated contraction loss coefficient, regardless of the contraction area ratio, Reynolds number or chosen downstream location.

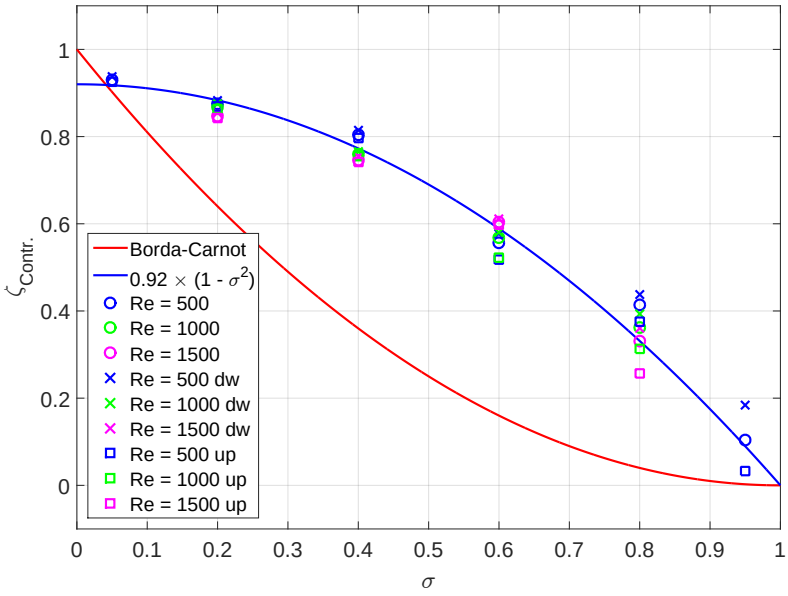

Fig. 4.21 Multi-Channel Contraction Square Computational Domain: Contraction loss coefficient for all the contraction area ratios and Reynolds number calculated using different downstream locations.

These results, along with the empirical correlations reported in the literature (Eqs. 1.15 - 1.20, plotted in Figure 1.9), show that in a configuration where the flow separation upstream is not present (i.e. Figure 4.16) the contraction loss coefficient presents a trend significantly different from the Borda-Carnot equation and thus cannot be estimated with Eq. 1.14.

Eq. 4.7 is a concave function and, although with a different magnitude, presents a trend similar to Merriman [92] and Weisbach [93] empirical correlations (Eq. 1.16 and Eq. 1.17), which are mostly concave functions, in contrast with the Borda-Carnot equation which is a convex function. Note that Merriman [92] and Weisbach [93] empirical correlations include only the effect of the vena-contracta and not the flow separation upstream the contraction. Due to the lack of information on the experimental set-up, range of Reynolds numbers and method used by Merriman [92] and Weisbach [93] to calculate the contraction loss coefficients it is difficult to properly identify the source of the discrepancy in the magnitude between the values estimated with Eq. 4.7 and Eqs. 1.16 - 1.17.

4.4 Chapter summary

In order to address some discrepancies in the previous studies, a numerical investigation of the contraction losses in laminar flows in circular and square cross-sectional ducts with a sudden contraction has been conducted. In particular, a new method has been proposed to derive the contraction loss coefficient and to separate the contribution of the contraction losses from the friction and developing flow losses upstream and downstream the contraction location. This means that the contraction loss coefficient derived through this method can be used to estimate the losses due to the contraction regardless of the fact that the flow may or may not re-develop downstream the contraction.

For the circular cross-section two configurations have been studied to investigate the impact of the velocity profile approaching the contraction on the contraction loss coefficient. The results show that there isn't a significant difference between these two cases and that the Borda-Carnot equation for a sudden change in cross-section provides a good fit for the the contraction loss coefficient, with a maximum deviation below 0.1.

For the square cross-section two configurations have been studied. One with bounding walls upstream, to match a standard single contraction with square cross-section, and one without bounded walls upstream the contraction, to match the conditions at the entrance of a GPF or other similar multi-channel systems.

In the first configuration the results show a good agreement with the Borda-Carnot equation for a sudden change in cross-section, with a maximum deviation below 0.1. In the second configuration (multi-channel system), instead, the contraction loss coefficient results show a significant difference from those derived from the Borda-Carnot equation for a sudden change in cross-section, while they present a similar trend to the empirical correlations of Merriman [92] and Weisbach [93]. A new correlation, Eq. 4.7, has been proposed and provides a good fit for the the contraction loss coefficient, with a maximum deviation below 0.1. Due to the lack of information on the experimental set-up, range of Reynolds numbers and method used by Merriman [92] and Weisbach [93] to calculate the contraction loss coefficients it is difficult to properly identify the source of the discrepancy in the magnitude between the values estimated with Eq. 4.7 and Eqs. 1.16 - 1.17, and further experimental data is required for validation.

The CFD predictions presented in this chapter and the method used to calculate the contraction loss coefficient can be exploited to design an experimental set-up to estimate and compare the contraction losses. In particular, the present analysis might be of help for the determination of the location in which the pressure measurements should be taken in the close proximity of the contraction, so that both the upstream and downstream energy dissipation regions are accounted for. Also, for comparison purposes, it would be useful to correlate the results in terms of x^+, which accounts for both the channel aspect ratio and the Reynold number.

Finally, the results presented in this chapter further suggest that the inertial loss coefficients estimated by Konstandopoulos [28], ranging from 2.4 to 8.3, are too high and might be non-physical.

Chapter 5

Experimental study of pressure losses in filter cores

5.1 Introduction

The literature review has shown that the friction losses in channels with porous walls may differ considerably from those in channels with solid walls. Therefore, using existing correlations derived for solid walls for particulate filter models needs to be justified. Moreover, the presence of porous walls may change the Reynolds number which correspond to the transition from laminar to turbulent flow regime. In this chapter, an experimental study is carried out with filter cores with and without the plugs in order to characterise the friction factor in filter channels with porous walls, which will be used in the particulate filter models, and to collect pressure drop data, which will be used for the assessment of the models.

In order to fill these gaps an experimental apparatus and methodology have been developed, as described in Chapter 2, and in this chapter the experimental results of both the unplugged and plugged filter cores testing are presented and discussed.

5.2 Pressure losses in unplugged filter cores

The testing was performed with a $300/8[Cpsi]$ unplugged filter core sample, shown in Figure 2.4, which was cut from a cordierite monolith. The same core has been tested

and then cut at different lengths, from 100[*mm*] to 40[*mm*] with steps of 10[*mm*], to investigate the effect of the filter length on the pressure drop. This allowed to investigate the friction losses and to identify the Reynolds numbers for which the flow is laminar, transitional or turbulent in channels with passive porous walls.

5.2.1 Pressure loss sources in unplugged filters

Note that the unplugged filter cores tested are made of the same material and have the same porosity of typical uncoated GPFs. Since, as shown by Watling et al. [30], the effect of injection and extraction of flow through porous walls was found negligible on the overall pressure losses in particulate filters, the friction factor investigated through these experiments should be similar to the friction factor in particulate filters with similar wall properties.

The overall pressure losses of an unplugged filter, where the flow does not pass through the porous medium, can be decomposed in four main contributions, as shown in Figure 5.1:

1. Pressure losses due to contraction ($\Delta P_{Contr.}$).
2. Pressure losses due to friction, which can be represented as a combination of flow development losses and fully developed flow losses ($\Delta P_{Friction}$).
3. Pressure losses due to expansion ($\Delta P_{Exp.}$).

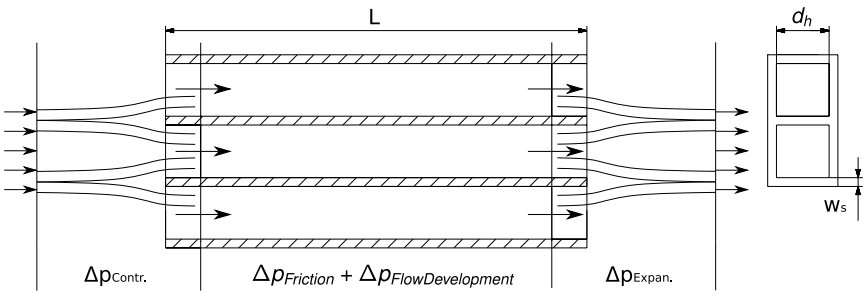

Fig. 5.1 Unplugged channels schematic.

Therefore, the total pressure loss of an unplugged filter can be approximated as follows:

$$\Delta P_{UnpluggedFilter} = \Delta P_{Contr.} + \Delta P_{Friction} + \Delta P_{Exp.}, \tag{5.1}$$

where $\Delta P_{Contr.}$ and $\Delta P_{Exp.}$ can be calculated from Eq. 1.12 and Eq. 1.13, respectively, while $\Delta P_{Friction}$ is usually calculated using Eq. 1.1 (neglecting the effect of the porous walls) plus the developing flow losses which can be calculated using Eq. 1.4 and Eq. 3.4.

5.2.2 Experimental results of the unplugged filters

Figure 5.2 shows the experimental results of the pressure drop versus mass flow rate for the seven different core lengths considered. The mass flow rate uncertainty is also plotted and it was calculated as shown in Appendix A.

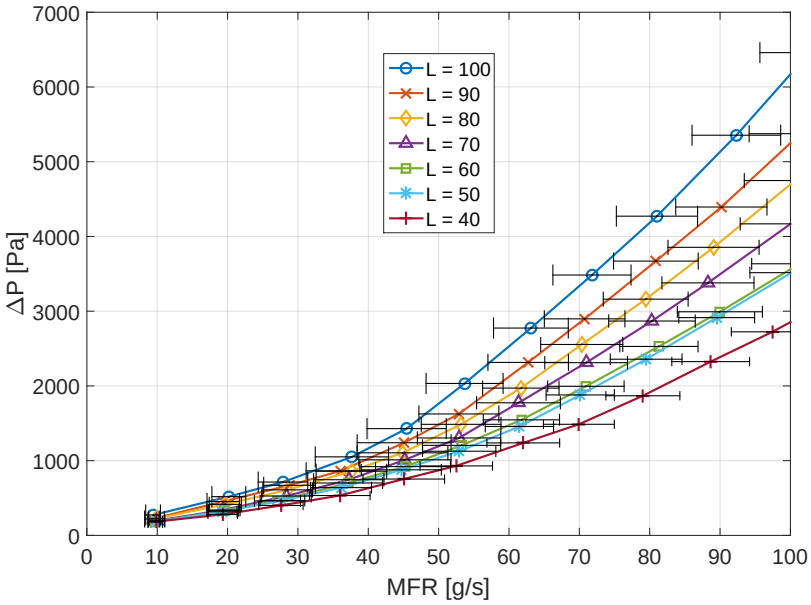

Fig. 5.2 Unplugged filters experimental data.

As all experiments were performed with the same filter core, with only the filter length changing, the degree of flow path contraction and expansion is the same. Therefore, the associated contraction and expansion losses are expected to be very similar in all experiments, and only friction losses will account for the differences in the total pressure loss. Thus, the pressure losses due to friction can be separated from the others assuming that the contraction and expansion losses and flow development losses are the same for different filter lengths and that the friction factor f is the same for filters with a different length. A similar procedure to estimate the friction losses and friction

factor in unplugged filters has been recently used by Aleksandrova et al. [98]. Thus, the pressure losses of two filters with different length $L_1 \neq L_2$ can be expressed by the following formulae:

$$\Delta P_{L_1} = \Delta P_{Contr.,L_1} + \Delta P_{Friction,L_1} + \Delta P_{Exp.,L_1}, \tag{5.2}$$

$$\Delta P_{L_2} = \Delta P_{Contr.,L_2} + \Delta P_{Friction,L_2} + \Delta P_{Exp.,L_2}, \tag{5.3}$$

where, due to the previously defined assumptions:

$$\Delta P_{Contr.,L_1} = \Delta P_{Contr.,L_2}, \tag{5.4}$$

$$\Delta P_{Exp.,L_1} = \Delta P_{Exp.,L_2}. \tag{5.5}$$

As a consequence, the friction losses can be established from the experimental data (ΔP_{L_1} and ΔP_{L_2}) by subtracting the pressure losses of two filters with different length ($\Delta P_{L_1-L_2} = \Delta P_{L_1} - \Delta P_{L_2}$). Using Eqs. 5.2 - 5.5 and the Darcy-Weibach equation (Eq. 1.1) yields:

$$\Delta P_{L_1-L_2} = \Delta P_{Friction,L_1} - \Delta P_{Friction,L_2} = 4f\frac{L_1 - L_2}{d_h}\frac{\rho U^2}{2}. \tag{5.6}$$

Dividing both sides by $\frac{\rho U^2}{2}$ the non-dimensional form of Eq. 5.6 can be obtained:

$$f = \frac{\Delta P^*_{L_1-L_2}}{4\frac{L_1-L_2}{d_h}}. \tag{5.7}$$

Experimental results shown in Figure 5.2 have been used to calculate the friction factor using expression Eq. 5.7. Since the measurement points in different experiments were performed at different mass flow rates, the data was first interpolated at the same mass flow rate values using linear interpolation.

The Darcy Friction Factor C_f ($C_f = 4f$) derived from the experiments is plotted in Figure 5.3 versus channel Reynolds number.

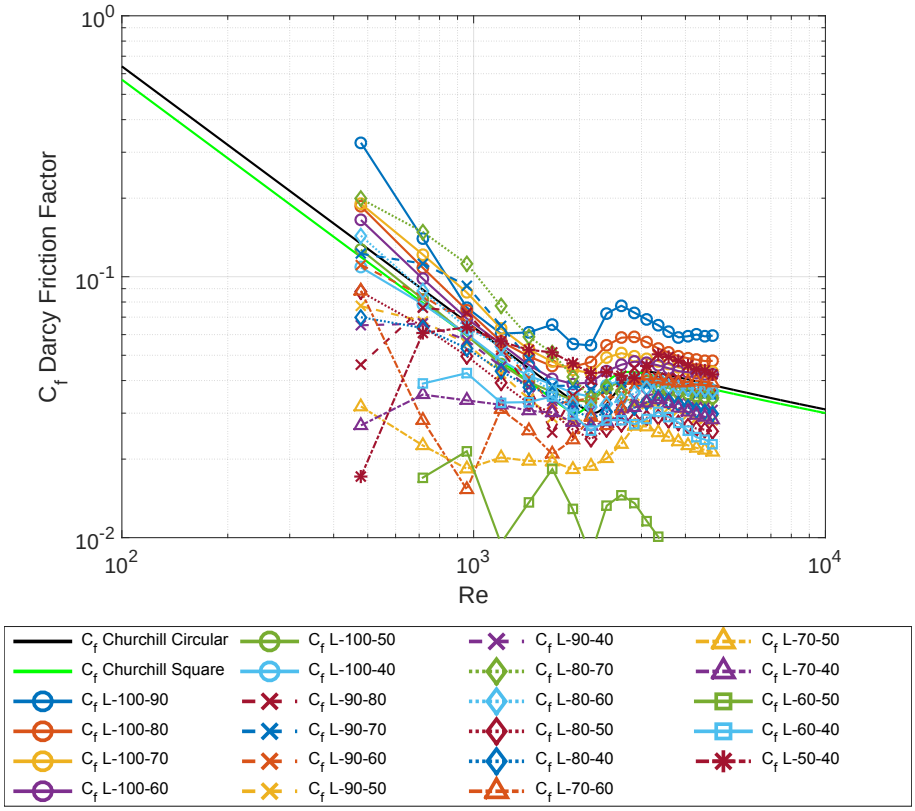

Fig. 5.3 C_f Darcy Friction Factor.

In the legend of Figure 5.3 the term $C_f L-100-90$ means that the friction factor was calculated using Eq. 5.7 with $L_1 = 100[mm]$ and $L_2 = 90[mm]$ and the same notation was used for the other lengths.

It can be seen here that the trend of the experimental friction factor is in reasonably good agreement with the existing theoretical expression for the friction factor (Eq. 5.8) proposed by Churchill [49] which covers laminar, transitional and turbulent flow ranges:

$$f_{Churchill} = 2\left[\left(\frac{8}{Re}\right)^{12} + \left[\left[-2.457ln\left(\left(\frac{7}{Re}\right)^{0.9} + 0.27\frac{\varepsilon}{d_h}\right)\right]^{16} + \left(\frac{37530}{Re}\right)^{16}\right]^{-1.5}\right]^{1/12}. \quad (5.8)$$

However, Eq. 5.8 was derived for channels of circular cross-section, and a correction factor is required to account for the square cross-section used here. As reported in the literature review, Jones [50] investigated the friction factor in ducts with different cross-

sections and proposed a simple empirical correction factor, derived from experimental data, based on a modified Reynolds number (Eq. 1.3) to correlate the friction factor of circular cross-section ducts to other shapes. Jones [50] introduced the modified Reynolds number, Re^*_{Square}, that allows to correlate circular cross-section and square cross-section friction losses:

$$Re^*_{Square} = \frac{64}{56.908} Re. \tag{5.9}$$

Here Re is the Reynolds number for ducts of circular cross-section.

Using Re^*_{Square} instead of Re in Eq. 5.8 gives an expression for the friction factor in ducts of square cross-section:

$$f_{Churchill\,Square} = 2\left[\left(\frac{8}{Re^*_{Square}}\right)^{12} + \left[\left[-2.457ln\left(\left(\frac{7}{Re^*_{Square}}\right)^{0.9} + 0.27\frac{\varepsilon}{d_h}\right)\right]^{16} + \left(\frac{37530}{Re^*_{Square}}\right)^{16}\right]^{-1.5}\right]^{1/12}. \tag{5.10}$$

Because of the scatter of the results in Figure 5.3 it is difficult to see how well the results agree with Eq. 5.10. To get a better insight into the overall trend, the mean value of all experimental results for each Reynolds number has been calculated. The results are shown in Figure 5.4 along with the standard deviation calculated for each Reynolds number considered.

Figure 5.4 shows that the filter friction factor estimated from the experiments agrees well with the friction factor in ducts of square cross-section calculated with Eq. 5.8.

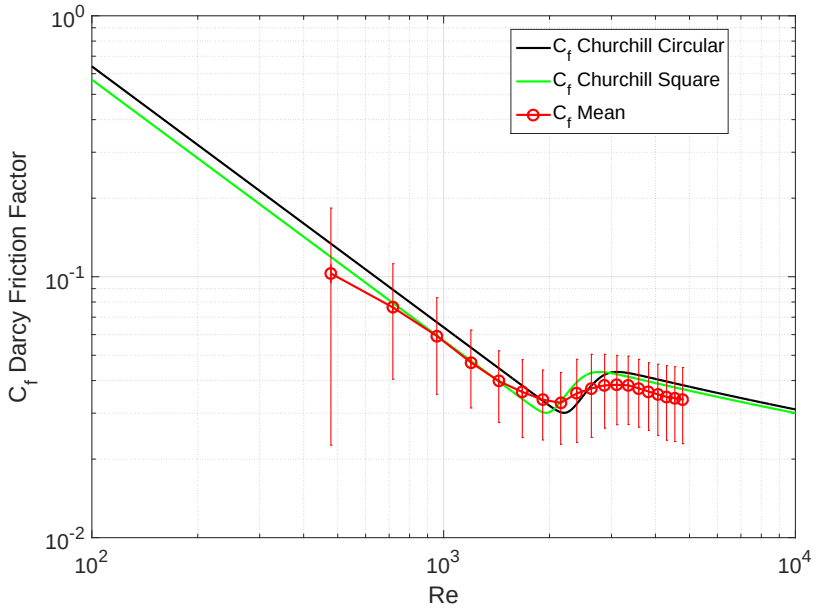

Fig. 5.4 Mean C_f Darcy Friction Factor.

Thus, it has been established that the friction factor in both laminar and turbulent regimes and the onset of transition in filter channels are comparable to those in channels with solid walls. These results are consistent with the findings reported by Aleksandrova et al. [98].

5.3 Pressure losses in plugged filter cores

The hot flow experiments were carried out by a team of researchers as part of a project with Jaguar Land Rover. The testing was performed on four different filter core samples cut from a cordierite monolith, as described in Chapter 2. This testing provided experimental data for a range of mass flow rates and temperatures that will be used for the development and assessment of the models (presented in Chapter 6 and Chapter 7) and to show that there is experimental evidence of laminar to turbulent flow regime change in a particulate filter.

The cold flow (ambient temperature) test results are shown in Figure 5.5. As expected, the uncoated filter core #1 shows the lowest pressure drop, while the filter core #4, which has the thickest coating layer, shows the highest pressure drop. The catalyst coating not only increases the wall thickness, but also has smaller pore size and

therefore lower permeability, as discussed in [107]. Cores #2 and #3 have a different length but identical coating parameters and nominal geometry.

Core #2 shows a lower pressure drop than core #3, although this is 25$[mm]$ longer. This counterintuitive result is in agreement with the study of Masoudi et al. [20] on the effect of the filter length on the pressure drop. This effect is further discussed in a parametric study shown in Chapter 6.

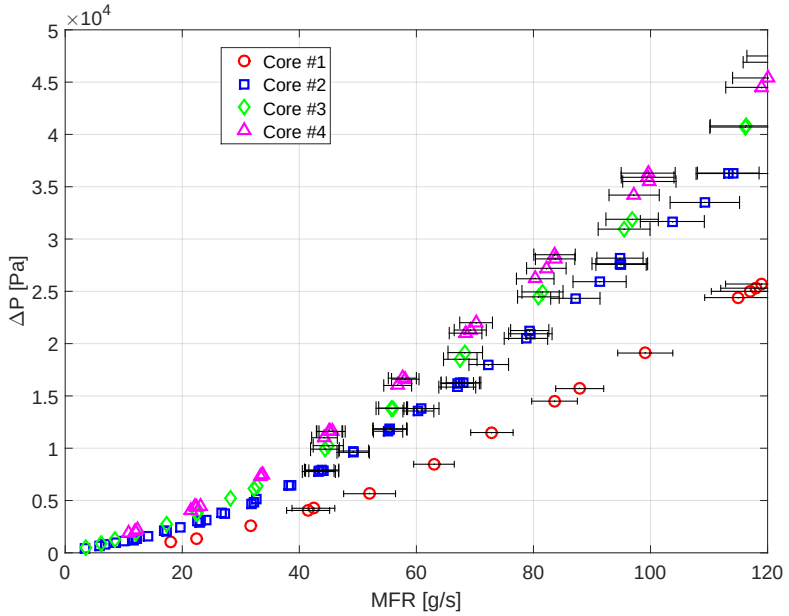

Fig. 5.5 Plugged cold flow results.

The mass flow rate uncertainty has been calculated as in Appendix Appendix A.

Figure 5.6 shows the change of the filter non-dimensional pressure drop $\left(\Delta P^* = \frac{\Delta P}{\frac{\rho U^2}{2}}\right)$, with the Reynolds number calculated at the entrance of the inlet channel,

$$Re = \frac{\rho U d_h}{\mu}. \tag{5.11}$$

Here, the velocity at the entrance of the inlet channel is defined as:

$$U = \frac{MFR}{\rho OFA}, \tag{5.12}$$

with MFR being the experimental mass flow rate, OFA the filter open frontal area, d_h the channel hydraulic diameter, while ρ and μ are the density and dynamic viscosity of the air upstream the core.

Figure 5.6 shows that, although other non-dimensional groups (which will depend on the filter properties such as permeability, length, etc.) play an important role, the non-dimensional pressure losses in all cores present similar trends. A change in the slope between lower and higher values of the Reynolds number is clearly visible. The friction loss slope typical for laminar (Re^{-1}) and turbulent $(Re^{-1/4}$ [44]) flow regimes have been plotted along with the experimental data. C_1 and C_2 are coefficients which have been selected arbitrarily to display the slope lines next to the test data. Up to $Re < 1800$ the experimental data follow the slope characteristic for laminar flows, while for $Re > 3000$ the data coincide with the turbulent slope line. These results are consistent with Jones's investigation [50] who observed that in ducts with square cross-section the laminar regime ends earlier than in ducts with circular cross-section. Hence, a clear change of the pressure drop trend corresponding to the transition from the laminar to turbulent regime has been demonstrate through the present experimental data.

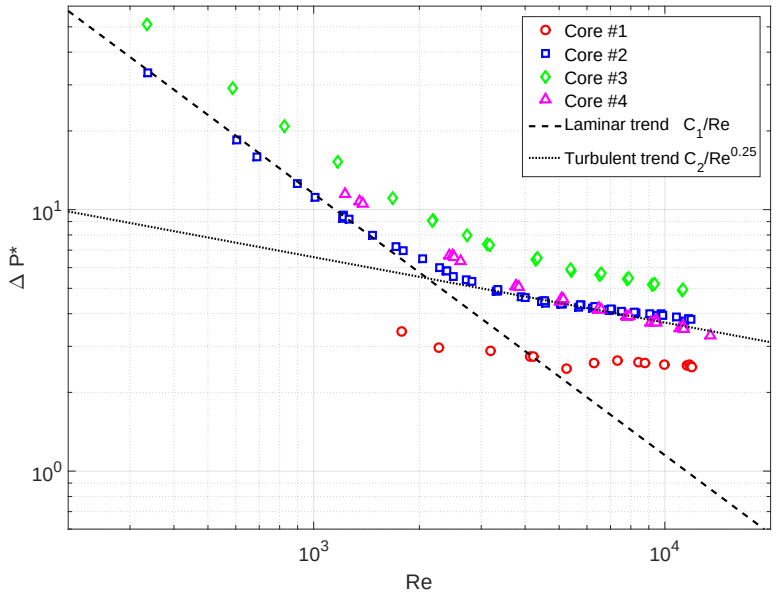

Fig. 5.6 Dimensionless plugged cold flow results.

Figure 5.7 shows the pressure drop of the four cores at $T = 20$, 200, 400 and 680$[^{\circ}C]$, which are the temperatures chosen to assess the models presented in Chapter 6 and Chapter 7. Although not presented here, the pressure drop data for all four filters have been collected also at $T = 50$, 100, 150, 250, 300, 350, 450, 500, 550, 600 and 650$[^{\circ}C]$, and the full set of results is shown in [98].

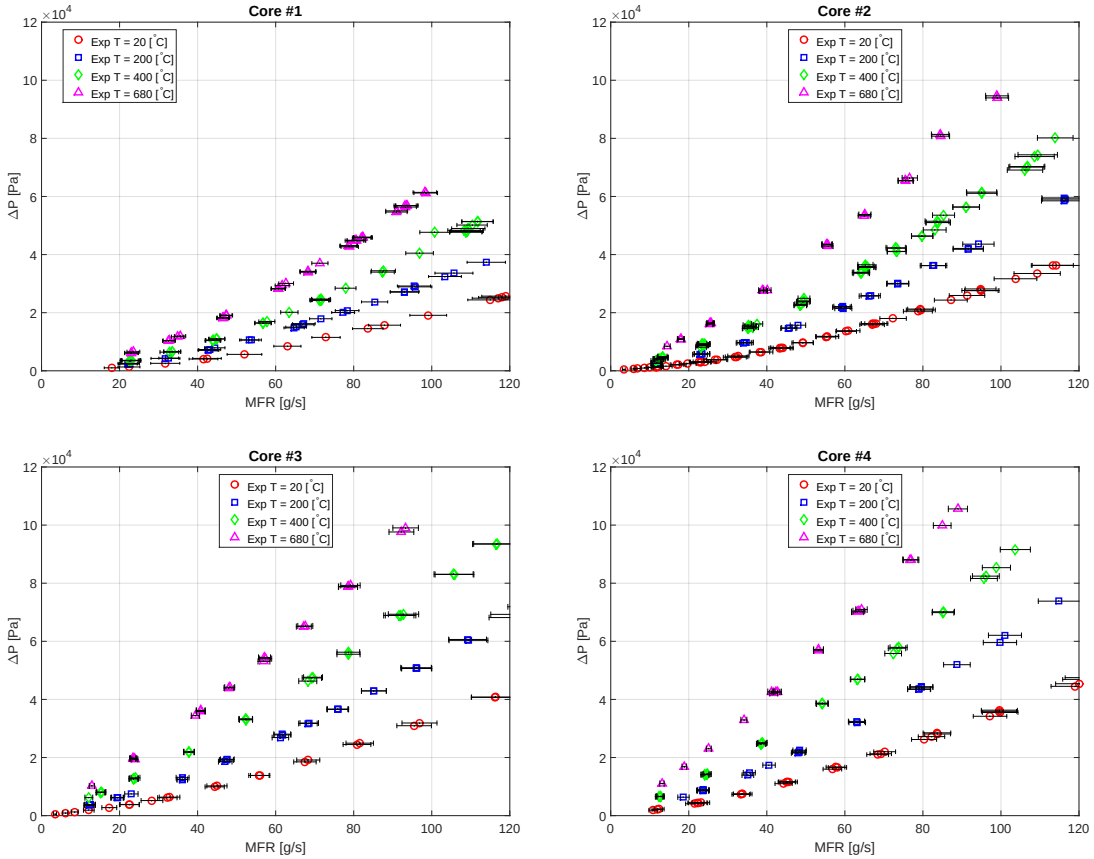

Fig. 5.7 Plugged filter cores experimental pressure drop.

The results show that the pressure losses increase with temperature for a fixed mass flow rate. This is the consequence of the increased volumetric flow rate which results in higher channel velocities, and therefore higher total losses for all pressure contributions. More detailed analysis of the experimental results will be presented in the next chapter when they are compared with the new 1-D particulate filter model predictions.

5.4 Chapter summary

An experimental investigation on unplugged and plugged filter cores has been conducted to characterise the friction factor in channels with porous walls and to fill the lack of experimental data for particulate filter pressure drop at high mass flow rates and temperatures.

The unplugged filter cores results show that the friction factor and the transitional regime in filter channels with porous walls are comparable to those in channels with solid walls. For channels of square cross-section the friction factor trend and its variation with the Reynolds number can be approximated by Eq. 5.10, which is a modified version of Churchill's correlation, Eq. 5.8, derived for the square cross-section.

Experimental data of the pressure drop of four plugged particulate filter cores with different properties has been collected for a large range of mass flow rates and temperatures. This data, as shown in the next chapter, can be used to validate particulate filter predictive models for a wide range of flow conditions and filter properties. Assessing a predictive model with a great variety of experimental data can ensure that the model is based on physical principles rather than on empirically derived fitting coefficients, and thus that the model can be used independently from the flow conditions or filter properties. Additionally, the analysis of the results has shown that there is experimental evidence of laminar to turbulent transition regime in particulate filters, which should be accounted for in particulate filter predictive models.

Chapter 6

New 1-D particulate filter model

6.1 Introduction

The the literature review of particulate filter models has shown that all of the existing 1-D models are limited to laminar flow conditions. However, the flow in particulate filters might be turbulent under some of the engine operational conditions. Additionally, the experimental data used for validation of the reviewed models is usually limited and does not cover both low and high flow regimes and temperatures.

This chapter presents a new 1-D model for particulate filter pressure losses, which has been published in [14]. The proposed model is an extension of the Bissett-Konstandopoulos model [16] to turbulent flow regime and high temperatures.

In the following sections the Bissett-Konstandopoulos model's formulation and its limitations are described in details first and successively the new model is presented and assessed against the experimental data presented in the previous chapter.

6.2 Bissett-Konstandopoulos model

In 1989 Kostandopoulos and Johnson [16] proposed a simple single inlet/outlet channels 1-D flow model (Figure 6.1). This model, which provided the first tool for the rational engineering design and optimization of DPFs, was validated with the experimental pressure drop data of wall-flow monoliths available at the time.

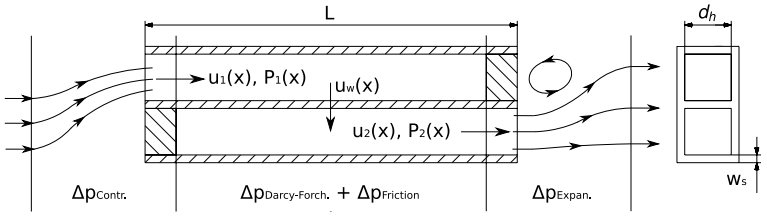

Fig. 6.1 Single inlet/outlet channels schematic.

Because of the model assumptions, reported in section 1.2.1.1, the flow within the particulate filter can be described by a 1-D model, which includes four differential equations, describing the mass and momentum balance in the inlet and outlet channels, and an algebraic one, describing the wall pressure drop:

Mass balance:

$$\frac{d}{dx}(\rho u_1) = -\frac{4}{d_h}\rho u_w, \tag{6.1}$$

$$\frac{d}{dx}(\rho u_2) = +\frac{4}{d_h}\rho u_w, \tag{6.2}$$

Momentum balance:

$$\frac{d}{dx}\left(\rho u_1^2\right) = -\frac{d}{dx}(P_1) - \frac{2}{d_h} f_1 \rho u_1^2, \tag{6.3}$$

$$\frac{d}{dx}\left(\rho u_2^2\right) = -\frac{d}{dx}(P_2) - \frac{2}{d_h} f_2 \rho u_2^2, \tag{6.4}$$

Wall pressure drop:

$$P_1 - P_2 = \frac{\mu}{k} u_w w_s, \tag{6.5}$$

where:

- $u_1(x)$ and $u_2(x)$ are the local mean cross-sectional axial velocities along the inlet and outlet channels and $u_w(x)$ is the local mean velocity in the porous wall.
- $P_1(x)$ and $P_2(x)$ are the local mean cross-sectional pressures along the inlet and outlet channels.
- $f_1(x)$ and $f_2(x)$ are the local Fanning friction factors along the inlet and outlet channels.
- d_h is the cell hydraulic diameter.

- w_s is the porous wall thickness.
- ρ is the gas density.
- μ is the gas dynamic viscosity.
- k is the filter permeability.
- x is the axial coordinate, varying from 0 at the entrance of the filter to L at the exit of the filter.

The model formulation is then completed through the following boundary conditions:

$$u_1(0) = U, \tag{6.6}$$

$$u_2(0) = 0, \tag{6.7}$$

$$P_2(L) = P_{Atm.}. \tag{6.8}$$

where:

- U is the mean flow velocity at the entrance of the inlet channel (at $x = 0$).
- $P_{Atm.}$ is the atmospheric pressure (which can be replaced with pressure at the outlet of the filter).

These boundary conditions (Eqs. 6.6 - 6.8) reflect the fact that: (i) the velocity at the entrance of the inlet channel is known, (ii) the velocity at the entrance of the outlet channel is zero (as the plug blocks the flow), and (iii) the pressure at the exit of the outlet cell is known (and equal to the atmospheric pressure in this case).

As this formulation only accounts for laminar flow, the Fanning friction factor can be defined as:

$$f_i = \frac{14.227}{Re_i} \quad \text{or} \quad f_i Re_i = 14.227, \tag{6.9}$$

where $Re_i = \frac{\rho d_h u_i}{\mu} \quad (i = 1,2)$ is the local Reynolds number along the channel.

As shown in Eq. 6.9, the product of $f_i Re_i$ is a constant. This assumption, valid only in laminar flow, simplifies the model considerably, so that it can be solved analytically.

The total pressure drop of the filter is then given by:

$$\Delta P_{Konst.} = \left[A_1 + A_2\left[\frac{1}{2} + \frac{c_1}{g_1}\left(e^{g_1} - 1\right) + \frac{c_2}{g_2}\left(e^{g_2} - 1\right)\right] + c_1 g_1 + c_2 g_2\right]\frac{\mu U a w_s}{4Lk}. \tag{6.10}$$

with:

$$A_1 = \frac{k}{d_h w_s}\frac{4L}{d_h}Re, \tag{6.11}$$

$$A_2 = 8C_f Re\frac{k}{d_h w_s}\left(\frac{L}{d_h},\right)^2 \tag{6.12}$$

$$g_1 = A_1 - \sqrt{A_1^2 + 2A_2}, \tag{6.13}$$

$$g_2 = A_1 + \sqrt{A_1^2 + 2A_2}, \tag{6.14}$$

$$c_1 = \frac{1}{2} - c_2, \tag{6.15}$$

$$c_2 = \frac{1}{2}\left(\frac{e^{g_1} + 1}{e^{g_2} - e^{g_1}}\right). \tag{6.16}$$

Kostandopoulos and Johnson [16] reported that this was the "first comprehensive relation that expresses explicitly the pressure drop of clean wall-flow monoliths in terms of their manufacturing parameters and exhaust properties," and it was a breakthrough towards the advancement of understanding the flow physics within the particulate filters and a useful tool for their design optimization.

However, the limitations of this model need to be considered carefully, as the Bisset-Kostandopoulos model has been often used for high Reynolds number flow despite having been developed for laminar flow regime only. In fact, the Eq. 6.9 is only valid for laminar flow, and outside this range $f_i Re_i$ is not a constant. Moreover, the density change of the exhaust gas along the channels has not been account for in this model and the contraction and expansion losses have been neglected. As shown later in this chapter, the effect of both density change and contraction and expansion losses need to be accounted for, as their contribution becomes non negligible at high flow rates and back-pressures.

Turbulent flow regimes within the filter channels can be present in some DPFs operating conditions, as reported in the study of Masoudi et al. [13]. Although high

local Reynolds numbers do not necessarily mean that transition to turbulent regime is present, the experiments conducted in this thesis, as presented in Chapter 5, show that there is evidence of turbulent flow. Therefore, considering that GPFs have different geometry and wall properties (i.e. thicker walls and/or lower cell density) than DPFs and generally work at different operating conditions, including higher flow rates, the turbulent flow losses may become even more relevant in GPFs.

The model proposed by Konstandopoulos and Johnson [16] as well as all other 1-D models based on their formulation do not consider turbulent flow losses and only some models include the pressure loss contribution of the density change and contraction and expansion losses. Hence, the model proposed here aims to fill these gaps.

6.3 Model development

The model presented in the following sections is based on the same equations (Eqs. 6.1 - 6.5) and the same assumptions as the Bissett-Kostandopoulos [16] model, with the exception of the laminar flow assumption and the definition of the gas density. The irreversible pressure losses due to contraction and expansion are added to the total pressure loss to complete the model. Here, pressure loss contributions from different sources are discussed in detail.

6.3.1 Coupled friction and through wall losses

The fully developed flow friction factor for a duct with circular cross-section can be estimated with the Colebrook equation [47], which is an implicit equation with no closed solution. Many approximate solutions of this equation exists (see [48]), including the correlation of Churchill [49], which compared to other approximations has the advantage of covering all flow regimes (laminar, transitional and turbulent) in an explicit formula. Churchill's correlation as been shown previously in Eq. 5.8 and is

reported below to facilitate the reading:

$$f_i = 2\left[\left(\frac{8}{Re_i}\right)^{12} + \frac{1}{\left[2.457ln\left(\frac{1}{\left(\frac{7}{Re_i}\right)^{0.9}+0.27\frac{\varepsilon}{D}}\right)\right]^{16} + \left(\frac{37530}{Re_i}\right)^{16}}\right]^{\frac{1}{12}}, \tag{6.17}$$

where $Re_i = \frac{\rho d_h u_i}{\mu}$ with $(i = 1,2)$ is the local Reynolds number along the channel and ε is the surface roughness.

Thus, in order to account for turbulent flow losses, Churchill's correlation (Eq. 6.17) is implemented for the friction factor. Consequently, the model uses the appropriate friction factor based on the local Reynolds number value. Note that strictly speaking Eq. 6.17 was proposed only for fully developed flow in channels with non-porous walls. However, the experimental results of the unplugged filters presented in the previous chapter show that this equation can be used to approximate the friction factor also in channels with porous walls and porosity typical of particulate filters.

Since Eq. 6.17 has been derived for channels of circular cross-section, a correction factor is required to account for the square cross-section used here, as discussed in section 5.2.2. The friction factor in circular cross-section and square cross-section can be correlated through the following equation (reported also in section 1.2.2.1 and shown here to facilitate the reading):

$$Re_{Square,i} = \frac{16}{14.227} Re_{Circular,i} = \frac{16}{14.227}\frac{\rho d_h u_i}{\mu}, \tag{6.18}$$

where $Re_{Circular,i}$ is the local Reynolds number along the channel for ducts of circular cross-section, while $Re_{Square,i}$ is the local Reynolds number along the channel for ducts of square cross-section.

Thus, using $Re_{Square,i}$ instead of Re_i in Eq. 6.17 gives an expression for the friction factor in ducts of square cross section.

Following the same procedure as Kostandopoulos and Johnson [16] (but without assuming $fRe = const.$), to reduce the system of equations (Eqs. 6.1 - 6.5) to a single

one, leads to the following second order non-linear differential equation:

$$\frac{\mu}{k} w_s \frac{d_h}{4} \frac{d^2}{dx^2}(u_2) - 2\rho U \frac{d}{dx}(u_2) + \frac{2}{d_h} f_1 \rho \left(U^2 + u_2^2 - 2u_2 U\right) - \frac{2}{d_h} f_2 \rho u_2^2. \tag{6.19}$$

Here f_1 and f_2 can be derived by substituting Eq. 6.18 into Eq. 6.17.

Eq. 6.19 can be solved numerically for u_2 with the following boundary conditions:

$$u_2(0) = 0, \tag{6.20}$$

$$u_2(L) = U. \tag{6.21}$$

Once u_2 is known, the other variables can be calculated numerically from the system of equations (Eqs. 6.1 - 6.5). In order, u_w is calculated from Eq. 6.2, u_1 is calculated from Eq. 6.1, P_2 is calculated from Eq. 6.4 with Eq. 6.8 as boundary condition and finally P_1 is calculated from Eq. 6.5. Once P_1 and P_2 are known, the filter pressure drop due to coupled friction and through wall losses can be calculated as:

$$\Delta P_{Friction+ThroughWall} = P_1(0) - P_2(L). \tag{6.22}$$

Similar to the original laminar flow solution presented by Kostandopoulos and Johnson [16], the through wall losses and the losses due to friction are coupled. As a result, varying some filter parameters (i.e. the permeability, the channels hydraulic diameter, others) affects at the same time the velocity within the channels, and thus the losses due to friction, and the the velocity within the porous wall, and thus the through wall losses. As shown in Figure 1.2, uncoupling the friction and through wall losses may lead to considerable errors for some parameter ranges.

6.3.2 Contraction and expansion losses

In the present model, the losses due to contraction and expansion, which can be estimated by Eq. 6.23 and Eq. 6.24 respectively, are added in series to the pressure drop

resulting from the solution of the model (Eq. 6.22):

$$\Delta P_{Contr.} = \zeta_{Contr.} \frac{\rho_{Inlet} U^2}{2}, \tag{6.23}$$

$$\Delta P_{Exp.} = \zeta_{Exp.} \frac{\rho_{Outlet} U^2}{2}, \tag{6.24}$$

where the contraction and expansion loss coefficients are defined by Eq. 1.15 and Eq. 1.14 and ρ_{Inlet} and ρ_{Outlet}, the densities at the inlet and outlet, are discussed in the following section.

Note that the equation derived in Chapter 4 (Eq. 4.7) for the contraction loss coefficient was ultimately not implemented as it was not possible to properly validate it with experimental data. Nevertheless, the study presented in Chapter 4 was useful in order to determine that the inertial loss coefficients estimated by Konstandopoulos [28] are not physical and should not be used.

6.3.3 Density variation effects

At high filter back-pressure and absolute local pressure within the channels the effect of the density change becomes more relevant and has to be accounted for [28]. According to the ideal gas law, the density is defined as:

$$\rho = \frac{M}{RT} P, \tag{6.25}$$

where M is the molar mass of the gas, P its local pressure, T its local temperature and R is the universal gas constant.

In the present model, the density of the gas has been assumed to be spatially constant, which allowed to simplify the implementation and solution of the equations. The effect of the density change caused by the back-pressure has been accounted for by defining the density of the gas as the mean density value based on the average local pressure between the inlet and outlet channel [28]. Thus, the density is defined as:

$$\rho = \frac{M}{RT} \frac{1}{L} \int_0^L \frac{P_1 + P_2}{2} dx, \tag{6.26}$$

where P_1 is the local pressure along the inlet channel and P_2 is the local pressure along the outlet channel.

Introducing this new definition of the density requires knowledge of the pressure distribution inside the channels and thus the proposed model requires an iterative solution, which is summarized in the next section.

6.3.4 Model summary

The proposed predictive 1-D model takes into account the coupled effect of the friction (including turbulent regime) and through wall losses, the effect of the density change and the losses due to contraction and expansion.

The pressure drop due to friction and through wall losses is given by Eq. 6.22, as described earlier, while the losses due to contraction and expansion are given by Eq. 6.23 and Eq. 6.24. The effect of the density change is accounted for through an iterative process, as the local pressure in the inlet and outlet channels used in Eq. 6.26 are not known a priori.

Thus, the iterative solution process consists of the following steps:

1. At the first iteration step, Eq. 6.22 is solved using a density based on the outlet pressure $\rho_{it=1} = \frac{M}{RT} P_2(L)$.

2. The contraction and expansion losses, as defined in Eq. 6.23 and Eq. 6.24, are added to Eq. 6.22. As after the first step the local pressure in the inlet and outlet channel are known, the inlet and outlet density used in Eq. 6.23 and Eq. 6.24 can be defined as $\rho_{Inlet,it=1} = \frac{M}{RT} P_1(0)$ and $\rho_{Outlet,it=1} = \frac{M}{RT} P_2(L)$, respectively.

3. The mean density within the channels is recalculated using Eq. 6.26 and it used as input density for the successive iteration.

4. Steps 1) to 3) are repeated n times, until $|\frac{\Delta P_{it=n-1} - \Delta P_{it=n}}{\Delta P_{it=n-1}} 100 < 0.005|$, which is the criterion selected for the convergence here.

6.4 Assessment of the model

The new 1-D model is assessed here against the experimental data presented in Chapter 5 and is compared with the Bissett-Konstandopoulos [16] model (with and without added contraction and expansion losses).

Before the assessment, the permeability calibration, required for calculation of the through wall losses, is presented.

6.4.1 Permeability calibration

One of the main advantages of the model is the fact that only one parameter needs to be calibrated through experimental testing, namely the porous wall permeability.

Since at ambient temperature and in laminar regime the proposed model is nearly identical to the Bissett-Kostandopoulos [16] model, their explicit expression (Eq. 6.10) along with the losses due to contraction and expansion (Eqs. 6.23 - 6.24) can be used to find the permeability value that results in fittings the experimental pressure drop in the laminar flow regime. This method can be justified as at low mass flow rates and temperatures, the density changes along the channels due to back-pressure are negligible and the turbulent friction losses are not present. Note that it is suggested to only use the experimental data in the laminar regime at ambient temperature for the estimation of the permeability, as under these conditions the pressure losses are well understood and, thus, better accuracy can be achieved. A different method could also be considered, which would involve estimating the permeability by using the new 1-D model instead of the Bissett-Kostandopoulos [16] model. However, as the new model requires a numerical solution while the laminar flow model can be solved analytically, it was more efficient to use the laminar flow model analytical solution.

For the Bissett-Kostandopoulos [16] model, the pressure drop is expressed by Eqs. 6.10, 1.12 and 1.13, and thus the permeability can be estimated using the least square fit. The resulting values of the permeability for cores #1, #2, #3 and #4 are $k = 5.5 \times 10^{-12}[m^2]$, $k = 1.9 \times 10^{-13}[m^2]$, $k = 1.4 \times 10^{-13}[m^2]$ and $k = 1.7 \times 10^{-13}[m^2]$, respectively. In order to further support the validity of the present method for the permeability estimation, the permeability obtained from core #1 was compared with the

one estimated by Aleksandrova et al. [107], which was derived experimentally through wafer samples testing of the same core. The fact that the permeability estimated with both method are similar, further confirms the validity of the method used here. The permeability values reported above were used in the final model validation.

6.4.2 Model validation and comparison with the Bissett- Konstandopoulos model

In the present study, the new 1-D model has been implemented in MATLAB and the boundary value problem solver bvp5c has been used to solve the ordinary differential equations (Eq. 6.19, with boundary conditions Eq. 6.20 and 6.21, and Eq. 6.4, with boundary condition Eq. 6.8). bvp5c is a finite difference code that uses the four-stage Lobatto Illa formula, which is implemented as an implicit Runge-Kutta formula. Since bvp5c is a finite difference code this requires a mesh of points to be created along the channel axis. Thus, several mesh densities have been investigated in order to achieve mesh independent solutions. It was found that 31 mesh points for the bare filter and 11 mesh points for the coated one are sufficient to reach independence of the solutions. However, since the computational requirements to solve the model equations is minimal, a mesh of 101 points has been used for all cases to increase the results definition. The script takes between 1 to 20 seconds to converge for each single pressure drop prediction, depending on the flow conditions. Note that the number of mesh points required to achieve mesh independent solutions might be different if a solver other than bvp5c is used and that bvp5c was set to use a mesh with equally spaced points along the channels axis.

In order to validate the new 1-D model, its predictions at different flow rates and temperatures have been compared to the experimental data of all four cores reported in Chapter 5 (Figure 6.2). Additionally, the new model has been compared to the Bissett-Kostandopoulos [16] model with added contraction and expansion losses (see Figure 6.2 (a)) and with the Bissett-Kostandopoulos [16] model with added contraction and expansion losses and "corrected" to account for the density change effects (see Figure 6.2 (b)). The contraction and expansion losses (expressed by Eqs. 6.23 - 6.24)

and the iterative process to account for the density change effects have been included in the Bissett-Kostandopoulos [16] model following the same procedure used for the proposed model (see section 6.3.4). These two comparison have been included so that the effect of the change in density and the turbulent friction losses could be evaluate separately.

The effect of the density change "correction" can be evaluated by comparing the Bissett-Kostandopoulos [16] model (Figure 6.2 (a)) with the corresponding density "corrected" version (Figure 6.2 (b)). At low mass flow rates and temperatures, when the filter back-pressure is small with respect to the filter outlet pressure, the effect of the density change is negligible and both models show nearly identical results. However, with increasing flow rate and temperature, and hence back-pressure, this effect becomes increasingly significant and the model that does not account for the density change effects clearly overpredicts the pressure drop (Figure 6.2 (a)).

The effect of the inclusion of the turbulent friction losses alone can be evaluated by comparing the density "corrected" version of the Bissett-Kostandopoulos [16] model with the new 1-D model (Figure 6.2 (b)), as both models include the density change "correction" and differs only in the definition of the friction factor. Note that the laminar flow model predictions have been plotted with dotted lines in the laminar flow regime and dashed lines in the transitional and turbulent regime to facilitate the interpretation of the results. Figure 6.2 (b) clearly show that the density "corrected" version of the Bissett-Kostandopoulos [16] model deviates from the experimental data immediately outside of the laminar flow regime, while the new model performs well even in the turbulent flow regime. For all cores, the difference between the new model predictions and experimental measurements is within $\pm 10\%$, with exception of a few data points. This means that a great part of the predictions lay within the experimental uncertainty.

Thus, Figure 6.2 (a) and Figure 6.2 (b) show that by including the generalized friction factor (Eq. 6.17) and the density variation (Eq. 6.26) good predictions of pressure loss for all temperatures and flow regimes can be made. In particular, at high mass flow rates and temperatures the new model can improve the pressure drop predictions up to $30-40\%$ with respect to the Bissett-Kostandopoulos [16] model.

Note that the maximum mass flow rate considered here is 120 $[g/s]$ for a filter core with diameter 50 $[mm]$. This is equivalent to 690 $[g/s]$ (or 2500 $[kg/h]$) for a filter with diameter 120 $[mm]$, which is a common size for GPFs. Although this mass flow rate is much higher than the mean mass flow rate in most of the engines operating conditions, turbulent flow regime can occur in some applications as discussed earlier.

Considering high mass flow rates ensures that the model's prediction of the flow physics is valid for different operational regimes. For example, when considering pulsating flows the instantaneous mass flow rate can be twice as high as the mean and, thus, being able to model turbulent flows would be even more relevant/necessary for accurate predictions if such condition is to be simulated.

Of course, the current model was not designed to cope with pulsating flows or transient effects as this was outside the scope of the present project. As shown by Piscaglia and Ferrari [35] and Torregrosa et al. [36], unsteady effects can be accounted for in a particulate filter model by using the time dependent mass and momentum balance equations (which include the term $\frac{d}{dt}(\rho u)$) and the local density (as done for the model presented in Chapter 7), and can be solved using a shock-capturing numerical method. Such modifications to the model presented here are possible, and could be considered in the future.

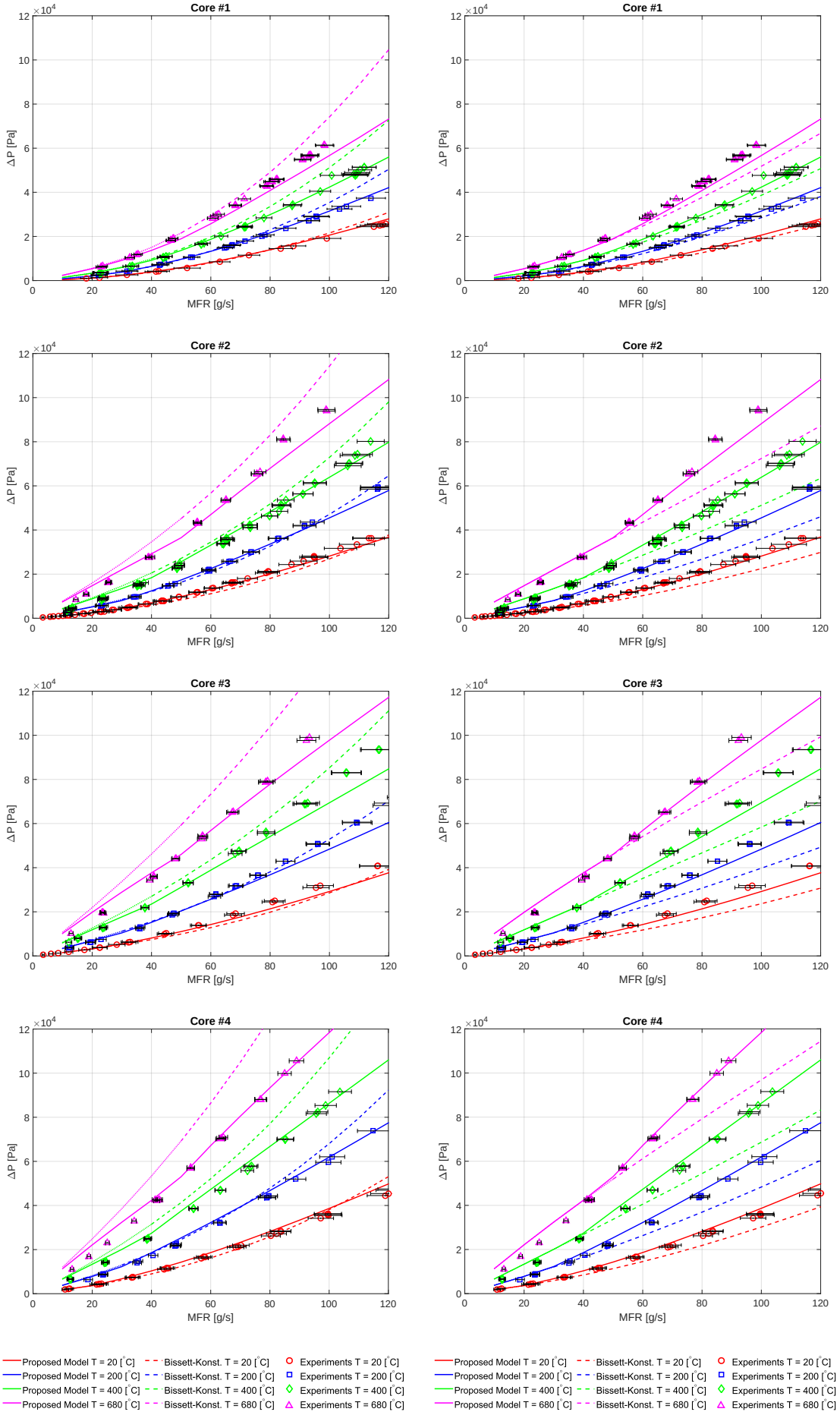
Core #1
Core #2
Core #3
Core #4
ΔP [Pa]
MFR [g/s]
×10^4
Proposed Model T = 20 [°C]
Proposed Model T = 200 [°C]
Proposed Model T = 400 [°C]
Proposed Model T = 680 [°C]
Bissett-Konst. T = 20 [°C]
Bissett-Konst. T = 200 [°C]
Bissett-Konst. T = 400 [°C]
Bissett-Konst. T = 680 [°C]
Experiments T = 20 [°C]
Experiments T = 200 [°C]
Experiments T = 400 [°C]
Experiments T = 680 [°C]

(a) (b)

Fig. 6.2 Comparison of the proposed model with experiments and (a) the Bissett-Konstandopoulos model with contraction and expansion losses and (b) the Bissett-Konstandopoulos model with contraction and expansion losses and density change effects. Dotted part of the lines indicates laminar regime.

6.4.3 Flow distribution in the filter channels

Compared to 0-D models, an additional advantage of 1-D models is the fact that they can provide information about flow and pressure distribution in the channels. These can be used to give a physical interpretation of the change in trend of the pressure drop for different filters.

Combining the pressure drop predictions with the analysis of flow distribution along the axis of the filter can also provide a guidance on the choice of the filter sizes. For example, if a portion of the filter is not utilized for filtration, a shorter filter may be considered. To demonstrate this process, two parametric study varying filter length or volume have been carried out and are presented below.

Figure 6.3 (a) shows how the pressure drop for cores #1, #2 and #4 would vary with the filter length and mass flow rate, while keeping all the other parameters constant. The length, and thus volume, corresponding to the lowest pressure drop ("optimal length" and "optimal volume" for a fixed diameter), for a given mass flow rate, is marked with a black circle. In a filter with constant diameter, the variation of the length has a double effect on the overall pressure drop. The total loss is the sum of friction and through wall losses, which have opposite trends with respect to the length. The friction losses increase with the increasing of the length, while the through wall losses decrease with the increasing of the length, and vice versa.

The length for which the minimum total loss is achieved is also strongly affected by the permeability, as this changes the contribution of the through wall losses with respect to the friction ones. High values of the permeability decrease the through wall losses (and thus their contribution) and vice versa. This is clearly visible in Figure 6.3 (a), where for core #1 (high permeability) the "optimal length" is shorter than for core #2 and #4 (low permeability). Since coated filters are also used as catalytic converters, this might be beneficial in terms of promoting the chemical reactions, as a bigger volume

would increase the residence time. Moreover, for coated filters, the variation of the pressure loss is very small for a large range of filter lengths, which means that from the design point of view there is certain degree of freedom in choosing the filter length.

Figure 6.3 (b) shows how the predicted pressure drop would change keeping the volume constant ($V = 1.9635 \times 10^5 [mm^3]$, which is the original volume of cores #1, #2 and #4) and varying the filter length and diameter ("optimal length to diameter ratio" for a fixed volume), which is a common design procedure in sizing the after-treatment devices. Here it can be seen that the pressure drop increases with the increasing of the length to diameter ratio. However, the coated cores exhibit very little pressure loss change at low length to diameter ratio, which again allows the manufacturers to combine pressure loss considerations with other constraints (i.e. packaging requirements and cost).

For coated filters, a comparison of Figure 6.3 (a) and (b) shows that, if the filter diameter is kept constant, increasing the length would be beneficial for reducing pressure loss, while if it is the volume to be kept constant, it would be more beneficial to increase the diameter at the expenses of the length, provided that this does not adversely affect the flow distribution across the filter.

However, the total pressure loss is not the only optimization parameter that needs to be considered. The primary function of the particulate filters is the filtration of the PM and the filtration efficiency is largely affected by other parameters, such as the pore size and the volume of the porous media. Thus, for example, the shorter filters presented in Figure 6.3 (a) and (b) would be unpractical for real applications, and they have been plotted here only to illustrate the full trend of the pressure drop and location of the minimum. Additionally, filtration efficiency is linked to the wall flow, and uneven wall flow distribution along the channel axis will affect the soot and ash accumulation patterns.

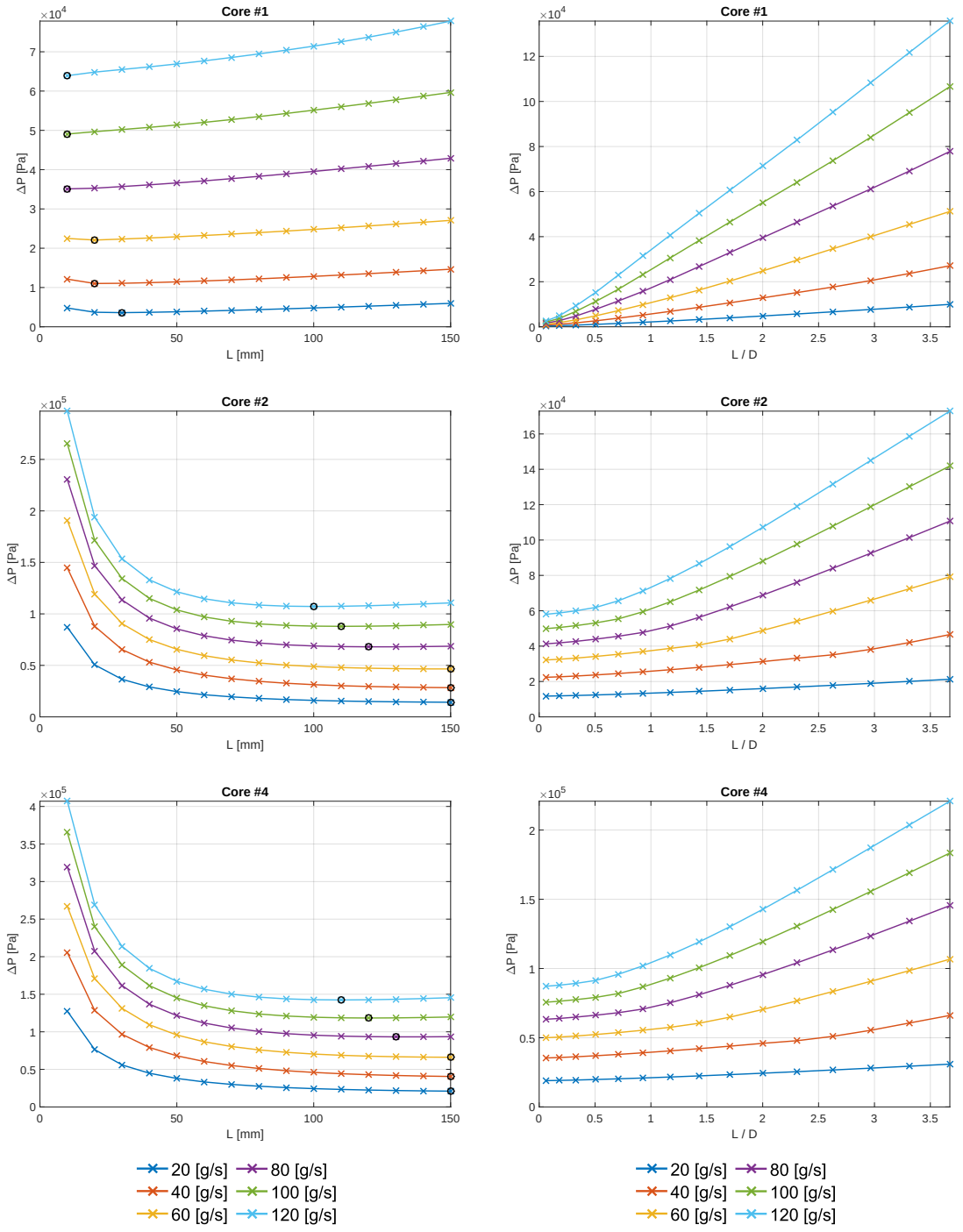

(a) (b)

Fig. 6.3 Predicted pressure drop vs (a) filter length with constant filter diameter and different mass flow rate and (b) filter length to diameter ratio with constant filter volume and different mass flow rate.

Figure 6.4, Figure 6.5 and Figure 6.6 show the predicted dimensional and normalized velocities within the channels and in the porous wall, for three different length $L1 = 50$

$[mm]$, $L2 = 100$ $[mm]$ and $L3 = 150$ $[mm]$, tested at $MFR = 60$ $[g/s]$ and $T = 680$ $[°C]$ for three filter core specifications.

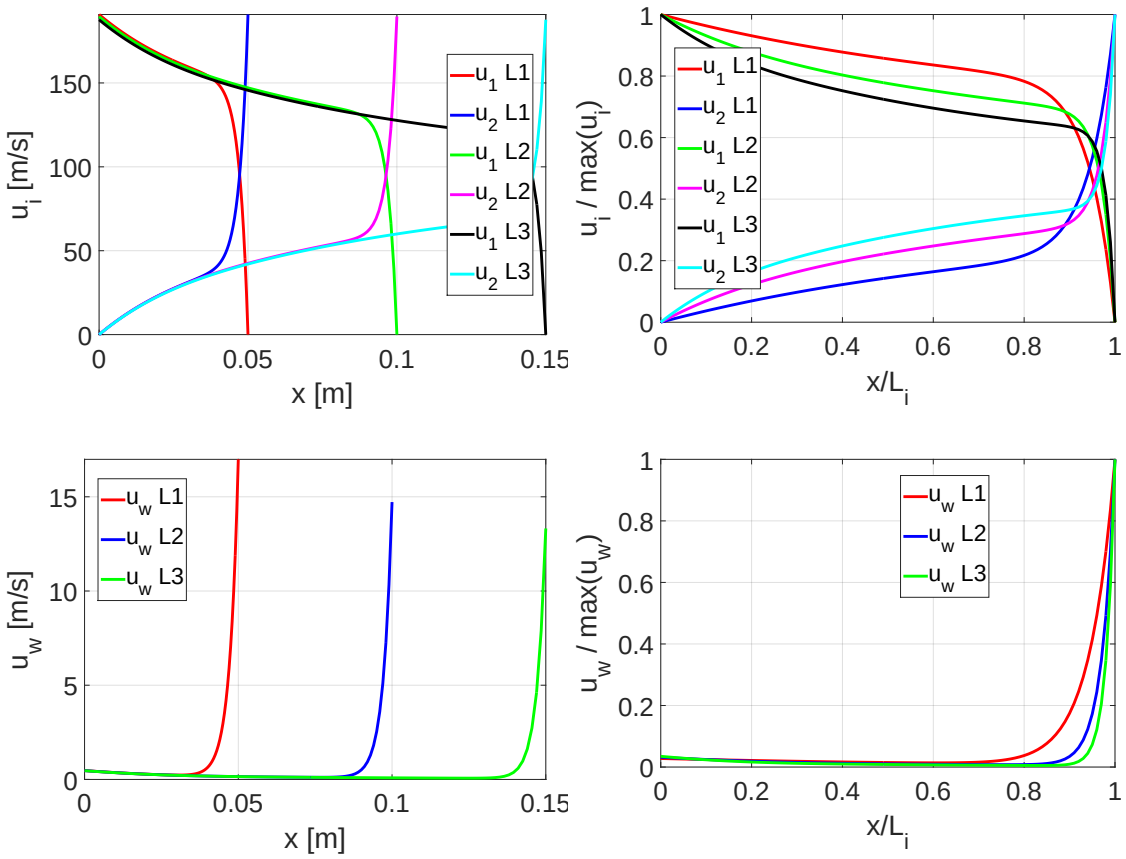

Fig. 6.4 Core #1: Predicted channels and through wall velocities with varying filter length (dimensional values on the left and normalized values on the right).

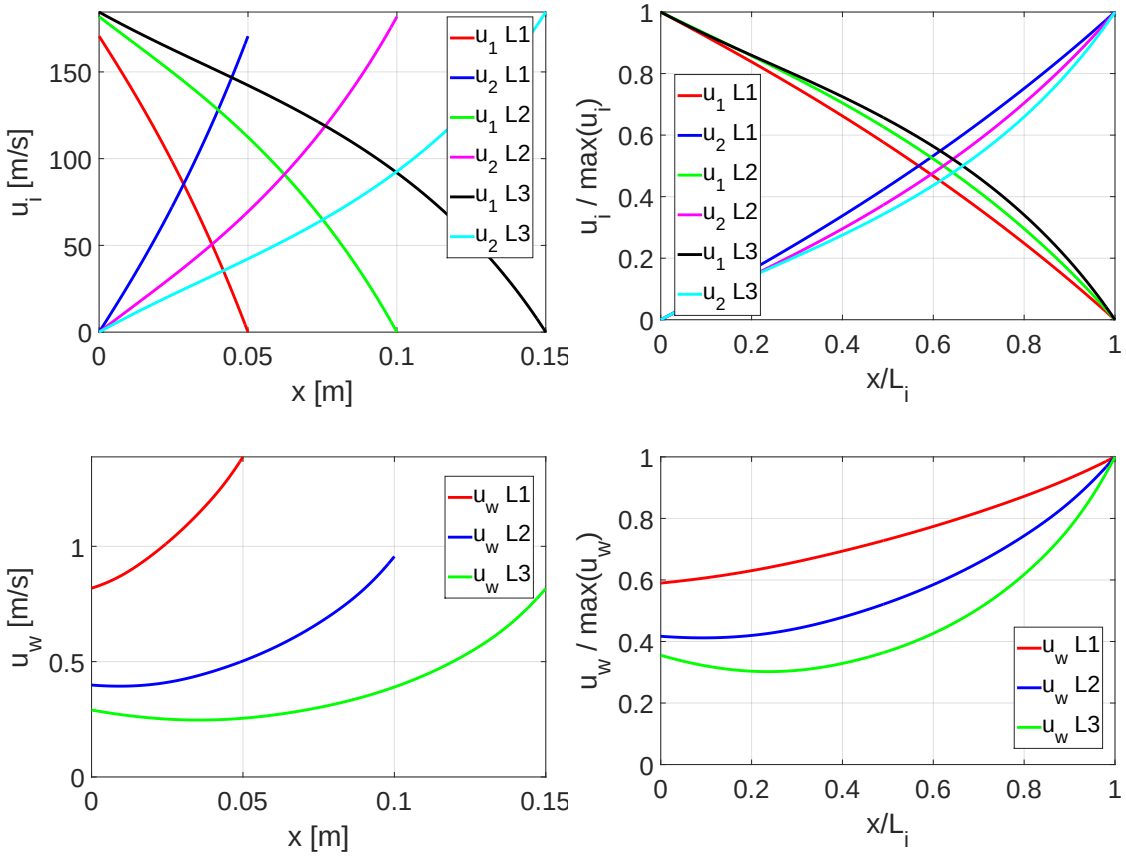

Fig. 6.5 Core #2: Predicted channels and through wall velocities with varying filter length (dimensional values on the left and normalized values on the right).

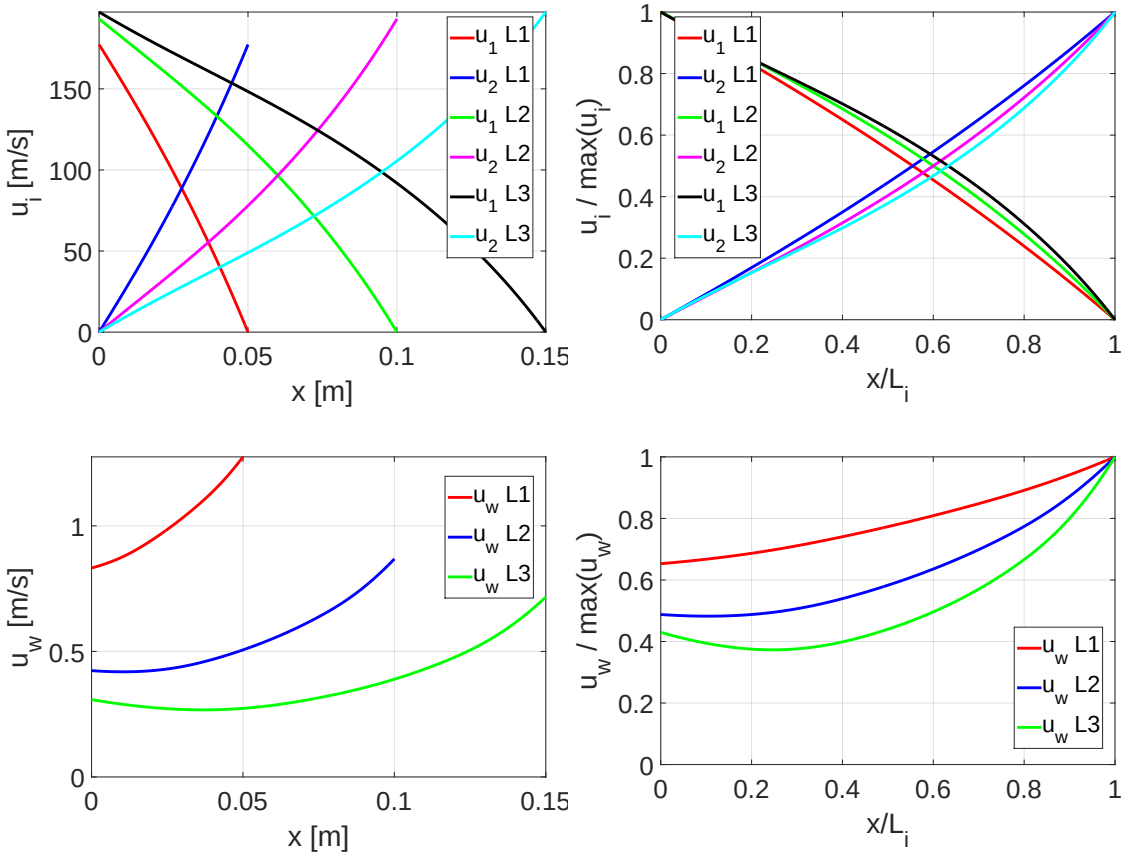

Fig. 6.6 Core #4: Predicted channels and through wall velocities with varying filter length (dimensional values on the left and normalized values on the right).

Figure 6.4 shows that for the uncoated core the through wall velocities are highly non-uniform, with low values for most of the filter length and a steep increase towards the end. Also, the shortest core shows a slightly less steep velocity increase towards the end, but with a peak of higher magnitude. Instead, for the coated filters, as shown in Figure 6.5 and Figure 6.6, the through wall velocities are much more evenly distributed along the channel length and in the shortest filters the velocity is the most uniform.

Although the model indicates that higher wall velocities are expected in the end part of the filter, resulting in more soot accumulated here, the transient nature of soot and ash accumulation means that no definitive conclusions can be made unless the model is modified to account for transient soot layer thickness effects.

The pressure difference $(P_1 - P_2)$ across the wall reflects the distribution of the through wall velocities, u_w, shown in Figure 6.4, Figure 6.5 and Figure 6.6.

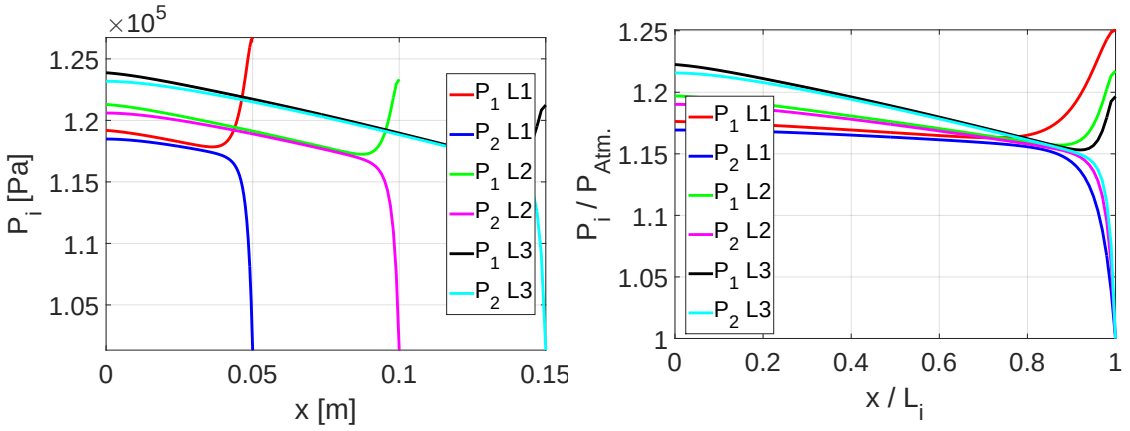

Fig. 6.7 Core #1: Predicted channels pressure with varying filter length (dimensional values on the left and normalized values on the right).

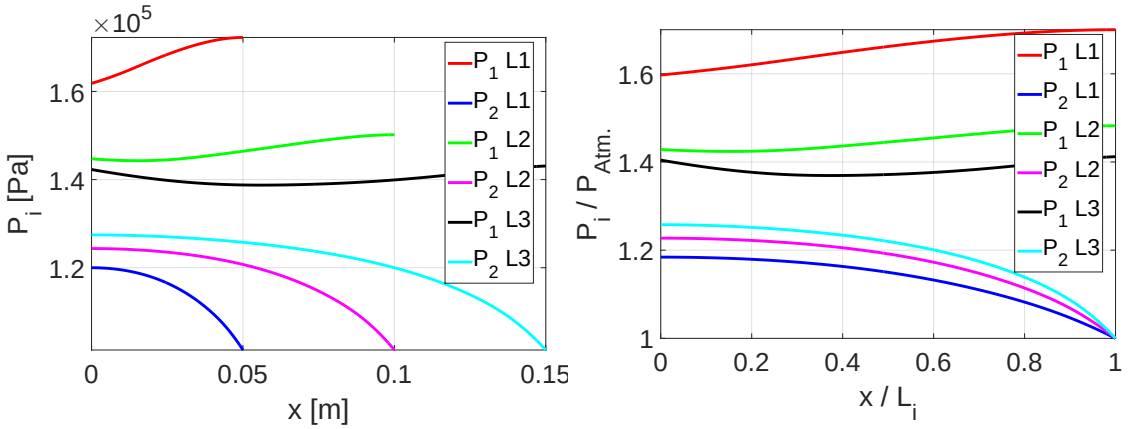

Fig. 6.8 Core #2: Predicted channels pressure with varying filter length (dimensional values on the left and normalized values on the right).

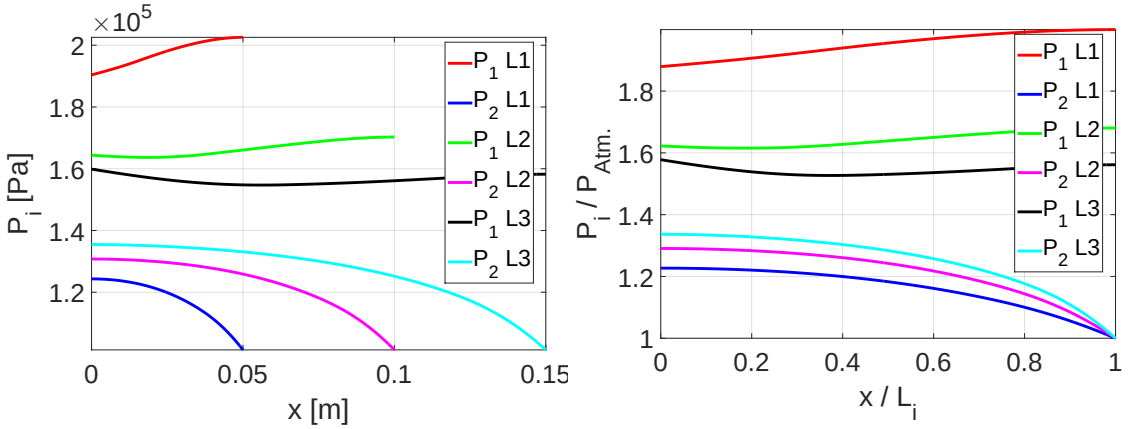

Fig. 6.9 Core #4: Predicted channels pressure with varying filter length (dimensional values on the left and normalized values on the right).

For the uncoated filter (Figure 6.7) the pressure is highly non-uniform in both channels and slowly decreases for most of the filter length; the pressure difference across the wall is small. Towards the end of the filter, the pressures change rapidly producing a relatively large pressure difference and high through wall velocities. In the coated filters (Figure 6.8 and Figure 6.9), the pressure is more evenly distributed along the length of the filter, resulting in a more uniform through wall velocity as a consequence of their lower wall permeability. The larger pressure drop for the coated filters means that accounting for the density variation in the model will be more relevant.

6.5 Chapter summary

A new 1-D model has been proposed, which covers both laminar and turbulent flow regimes. The new model requires solving a non-linear ordinary differential equation, which is the case for most of the filter flow models based on the Bisset-Konstandopoulos [16] model. The density variation effect has also been accounted for and requires an iterative solution. It has been shown how the model can be implemented in MATLAB, although any other commercial or open source boundary value problem solver can be used. With the current implementation the model requires between 1 to 20 seconds to be solved, and thus it can be considered efficient. In contrast to some other laminar flow models that require the calibration of both wall permeability and inertial loss coefficient, the present model requires the calibration of the wall permeability only. This can be performed by fitting the model to the pressure drop experimental data of the filter at ambient temperature and in laminar flow.

Unlike most of the reviewed models, which have only been validate against one or two data sets, the predictions of the proposed model have been validated against the pressure drop experimental data of four different filter cores (with varying cell density, length and permeability) tested in both laminar and turbulent regime and at high temperatures (up to $T = 680\ [^{\circ}C]$). It has been demonstrated that the model predictions agree well with the experimental data and that at high mass flow rates and temperatures the new model can improve the pressure drop predictions up to $30-40\%$ with respect to the Bissett-Kostandopoulos [16] model. Thus, the proposed model

effectively extends the Bissett-Kostandopoulos [16] model to the turbulent flow regime and to high temperatures.

A parametric study has been carried out to look at the effect of the filter geometry on the flow distribution and pressure losses. These studies show how the model could be potentially used as a partial tool (as the pressure drop is not the only relevant parameter) for filter selection or optimization.

A deeper knowledge of the contraction and expansion loss coefficients in the laminar flow regime and the effects that the slip flow have on the friction losses may further help in improving the model predictions and strengthen its physical base. Additionally, the effect of the density change can be improved by using the channel local density instead of assuming it as spatially constant.

Finally, the model is subject to the same limitations of the other single inlet/outlet models and can be used for the prediction of the pressure drop and flow of clean filters only. Predictions of loaded filters could be achieved through a deeper understanding of the soot transport and accumulation, and accounting for transient effects.

Chapter 7

New multi-channel particulate filter model

7.1 Introduction

The the literature review of particulate filter models has shown that although an extensive research effort has been carried out in order to model accurately the flow behaviour in a particulate filter, several gaps still need to be filled. In particular, regarding the multi-channel models, all of the reviewed models require the knowledge of the velocity or pressure profile upstream of the filter (which is not known a priori) and do not account for the full cross-flow between the channels, instead modelling the filter as a collection of identical inlet/outlet channel pairs. These shortcomings might greatly affect the models predictions.

This chapter presents a new multi-channel model, which has been published in [125]. This model is based on the 1-D model formulation proposed by Konstandopoulos and Johnson [16], and it is coupled with a 3-D CFD simulation.

The new multi-channel model accounts for the full channel-to-channel cross-flow and the uneven flow velocity and pressure profile upstream of the filter. The 3-D flow upstream of the filter is coupled to the model, so that no prior knowledge of the upstream flow is required. This is particularly relevant as it allows to avoid making assumptions on the flow profile upstream the filter, which is generally not known. Density variation in each individual channel is also taken into account, and uneven channel properties

(along the channel and between different channels) can be accounted for. Apart from the total pressure drop, the new model gives information about the flow and pressure distribution in each individual filter channel. These details are highly valuable for particulate filter optimisation.

7.2 Multi-channel model development and coupling with CFD

7.2.1 Multi-channel model formulation

The wall-flow filter channel geometry considered here is the same as the one discussed in previous works such as [16] or [14]. A filter with circular cross-section has been used here for demonstration purposes. However, since particulate filters can have other cross-sectional shapes (e.g. oval), the present model formulation and implementation have been developed to allow the assignment of any given cross-section to the filter. A sketch of a typical filter frontal area is shown in Figure 7.1. A 2-D indexing system (i, j) is used to refer to the filter channels. The indexing notation (Figure 7.2) reflects that every open channel (in white) has an even sum of indices and every closed channel (in grey) has an odd sum of indices.

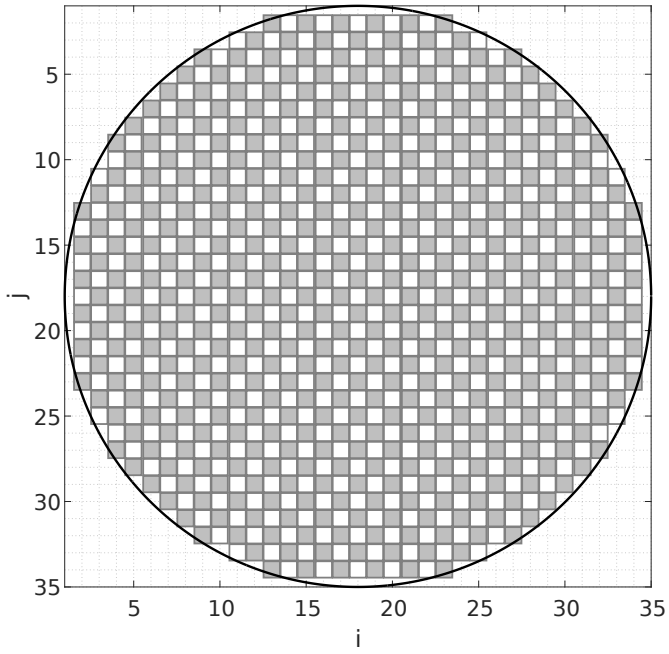

Fig. 7.1 Cell indexing schematic.

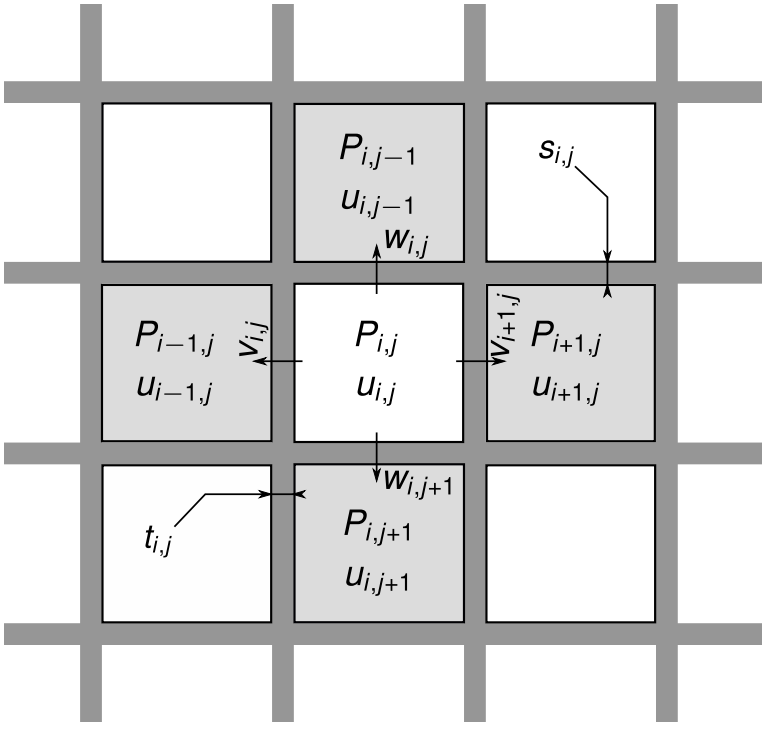

Fig. 7.2 Notation of the multi-channel flow variables.

The equations governing the flow in the (i, j) channel can be written as follows, in accordance with the notation shown in Figure 7.2:

Inlet channels ($i+j=$ even) and outlet channels ($i+j=$ odd)

Mass balance:

$$\frac{d}{dx}\left(\rho_{i,j}u_{i,j}\right) = -\xi\frac{1}{d_h}\rho_{i,j}\left(v_{i,j}+w_{i,j}+v_{i+1,j}.+w_{i,j+1}\right), \tag{7.1}$$

Momentum balance:

$$\frac{d}{dx}\left(\rho_{i,j}u_{i,j}^2\right) = \frac{d}{dx}\left(P_{i,j}\right) - 2fRe\frac{\mu}{d_h^2}u_{i,j}, \tag{7.2}$$

Wall pressure drop:

$$P_{i,j}-P_{i-1,j} = \xi P_{i,j}\left(\frac{2}{P_{i,j}-P_{i-1,j}}\right)\frac{\mu}{\tau_{i,j}}t_{i,j}v_{i,j}, \tag{7.3}$$

$$P_{i,j}-P_{i,j-1} = \xi P_{i,j}\left(\frac{2}{P_{i,j}-P_{i,j-1}}\right)\frac{\mu}{\sigma_{i,j}}s_{i,j}w_{i,j}, \tag{7.4}$$

$$P_{i,j}-P_{i+1,j} = \xi P_{i,j}\left(\frac{2}{P_{i,j}-P_{i+1,j}}\right)\frac{\mu}{\tau_{i+1,j}}t_{i+1,j}v_{i+1,j}, \tag{7.5}$$

$$P_{i,j}-P_{i,j+1} = \xi P_{i,j}\left(\frac{2}{P_{i,j}-P_{i,j+1}}\right)\frac{\mu}{\sigma_{i,j+1}}s_{i,j+1}w_{i,j+1}. \tag{7.6}$$

Here:

- $u_{i,j}$ is the mean cross-sectional axial velocity in the (i,j) channel.
- $P_{i,j}$ is the mean cross-sectional pressure in the (i,j) channel.
- $v_{i,j}$ and $w_{i,j}$ are the superficial velocities through the "vertical" and "horizontal" walls respectively as shown in Figure 7.2.
- $\rho_{i,j}$ is the mean cross-sectional density in the (i,j) channel.
- μ is the gas dynamic viscosity.
- $t_{i,j}$ and $s_{i,j}$ are the thicknesses of the "vertical" and "horizontal" walls respectively as sown in Figure 7.2.
- $\tau_{i,j}$ and $\sigma_{i,j}$ are the permeabilities of the vertical and horizontal walls respectively.

- ξ is a coefficient equal to $\xi = 1$ for the inlet channels and $\xi = -1$ for the outlet channels, and can be expressed as $\xi = (-1)^{i+j}$.
- d_h is the cell hydraulic diameter.
- f is the Fanning friction factor.
- Re is the channel Reynolds number (defined as $Re = (\rho U d_h)/\mu$).
- x is the axial coordinate, varying from 0 at the entrance of the filter to L at the exit of the filter.

The proposed formulation allows to prescribe individual channel properties. To demonstrate this a filter with different permeability in the central part and in the outer part of the filter have been simulated later in this chapter. Eqs. 7.3 - 7.6 come from solving the differential form of Darcy's law to allow for the change in gas density through the filter wall as suggested by Konstandopoulos [28]. The hydraulic diameter of selected cells could also be prescribed individually, although for correctness this would require a different form of Darcy's law to account for the trapezoidal cross-section of the walls, which has not been accounted for at this stage of the study. Nevertheless, Darcy's law for a trapezoidal cross-section has been derived before and it can be incorporated in the model with minor changes.

The local density can be calculated according to the ideal gas law as:

$$\rho_{i,j} = \frac{P_{i,j}}{R_{Gas} T}, \tag{7.7}$$

where R_{Gas} is the specific gas constant.

Eqs. 7.1 - 7.6 can be rearranged to give the following differential equations for mass and momentum balance:

$$\frac{d}{dx}\left(u_{i,j}\right) = \frac{1}{\left(1-\frac{1}{1+\frac{1}{R_{Gas}T}u_{i,j}^2}\frac{2}{R_{Gas}T}u_{i,j}^2\right)}\left[\frac{1}{P_{i,j}}\left(\frac{1}{1+\frac{1}{R_{Gas}T}u_{i,j}^2}\right)2fRe\frac{\mu}{d_h^2}u_{i,j}^2 - \frac{1}{P_{i,j}}\frac{1}{d_h}\frac{1}{2\mu}\left(\frac{\tau_{i,j}}{t_{i,j}}\left(P_{i,j}^2-P_{i-1,j}^2\right)+\frac{\sigma_{i,j}}{s_{i,j}}\left(P_{i,j}^2-P_{i,j-1}^2\right)+ \frac{\tau_{i+1,j}}{t_{i+1,j}}\left(P_{i,j}^2-P_{i+1,j}^2\right)+\frac{\sigma_{i,j+1}}{t_{i,j+1}}\left(P_{i,j}^2-P_{i,j+1}^2\right)\right)\right], \quad (7.8)$$

$$\frac{d}{dx}\left(P_{i,j}\right) = \frac{1}{1+\frac{1}{R_{Gas}T}u_{i,j}^2}\left[-\frac{2}{R_{Gas}T}P_{i,j}u_{i,j} \left[\frac{1}{\left(1-\frac{1}{1+\frac{1}{R_{Gas}T}u_{i,j}^2}\frac{2}{R_{Gas}T}u_{i,j}^2\right)}\left[\frac{1}{P_{i,j}}\left(\frac{1}{1+\frac{1}{R_{Gas}T}u_{i,j}^2}\right)2fRe\frac{\mu}{d_h^2}u_{i,j}^2 - \frac{1}{P_{i,j}}\frac{1}{d_h}\frac{1}{2\mu}\left(\frac{\tau_{i,j}}{t_{i,j}}\left(P_{i,j}^2-P_{i-1,j}^2\right)+\frac{\sigma_{i,j}}{s_{i,j}}\left(P_{i,j}^2-P_{i,j-1}^2\right)+ \frac{\tau_{i+1,j}}{t_{i+1,j}}\left(P_{i,j}^2-P_{i+1,j}^2\right)+\frac{\sigma_{i,j+1}}{t_{i,j+1}}\left(P_{i,j}^2-P_{i,j+1}^2\right)\right)\right]\right] - 2fRe\frac{\mu}{d_h^2}u_{i,j}\right]. \quad (7.9)$$

Thus, for each individual channel the two unknowns $u_{i,j}$ and $P_{i,j}$ satisfy first order non-linear differential equations 7.8 and 7.9. The problem in each channel is coupled with the four neighbouring channels. Treatment of the channels with fewer neighbours, which are present at the outer border of the filter, is discussed below.

The multi-channel model formulation is then completed through the following boundary conditions, which reflect the fact that: (i) the velocity at the entrance of each inlet channel is known, (ii) the velocity at the entrance of the outlet channels and at the end of the inlet channels is zero (as the plug blocks the flow), and (iii) the pressure at the exit of the outlet cell is known:

Inlet channels ($i+j=$ even)

$$u_{i,j}(x=0) = U_{i,j}, \quad (7.10)$$

$$u_{i,j}(x = L) = 0, \tag{7.11}$$

Outlet channels ($i + j =$ odd)

$$u_{i,j}(x = 0) = 0, \tag{7.12}$$

$$P_{i,j}(x = L) = P_{Outlet}, \tag{7.13}$$

where:

- $U_{i,j}$ is the mean cross-sectional axial velocity at the entrance of the inlet channel (i, j).
- $P_{i,j}$ is the mean cross-sectional pressure at the exit of the outlet channel (i, j).

In Eq. 7.10, the mean cross-sectional axial velocity at the entrance of the inlet channel can be assigned a priori by prescribing a velocity profile upstream the filter or, as in this study, it can be determined using CFD simulations. Although other authors used the former approach (e.g. [38]) to simplify the model solution, the determination of the velocity profile upstream the filter using CFD simulations is a more rigorous method.

The additional boundary conditions for the left, top, right and bottom impermeable walls of the channels at the border of the filter are respectively:

$$P_{i,j} - P_{i-1,j} = 0, \tag{7.14}$$

$$P_{i,j} - P_{i,j-1} = 0, \tag{7.15}$$

$$P_{i,j} - P_{i+1,j} = 0, \tag{7.16}$$

$$P_{i,j} - P_{i,j+1} = 0, \tag{7.17}$$

which reflect the fact that the through wall velocity ($v_{i,j}$, $w_{i,j}$, $v_{i+1,j}$ and $w_{i,j+1}$) is zero.

For a given geometry (e.g. the one shown in Figure 7.1), the resultant system of coupled differential equations can be solved numerically using a boundary value problem solver. In the present study, the multi-channel model has been implemented

in MATLAB and the boundary value problem solver bvp5c has been used to solve the system of coupled differential Eqs. 7.8 and 7.9 subject to boundary conditions 7.10 - 7.13 and extra algebraic Eqs. 7.14 - 7.17. The solver is a finite difference code that implements the four-stage Lobatto IIIa formula. This solver is not parallelised, which was not relevant for the cases simulated here, but parallel versions of the solver are also available. Once axial velocity and pressure distribution for each channel is known, the through wall velocities can also be calculated using Eqs. 7.3 – 7.6.

As for the new 1-D model, the losses due to contraction and expansion are added in series to the filter pressure drop. The pressure drop contribution due to contraction and expansion has been accounted for with the following approximations:

$$\Delta P_{Contr.} = \zeta_{Contr.} \frac{\sum_{n_{Inlet}} \left(\frac{\rho_{i,j-Inlet} u_{i,j-Inlet}^2}{2} \right)}{n_{Inlet}}, \tag{7.18}$$

$$\Delta P_{Exp.} = \zeta_{Exp.} \frac{\sum_{n_{Outlet}} \left(\frac{\rho_{i,j-Outlet} u_{i,j-Outlet}^2}{2} \right)}{n_{Outlet}}, \tag{7.19}$$

where:

- $u_{i,j-Inlet}$ and $u_{i,j-Outlet}$ are the mean cross-sectional axial velocity at the inlet and outlet of the (i, j) channel, respectively.
- $\rho_{i,j-Inlet}$ and $\rho_{i,j-Outlet}$ are the mean cross-sectional axial densities at the inlet and outlet of the (i, j) channel, respectively.
- n_{Inlet} and n_{Outlet} are the number of the inlet and outlet channels, respectively.
- $\zeta_{Contr.}$ and $\zeta_{Exp.}$ are the contraction and expansion coefficients, defined as in Eq. 1.14 and Eq. 1.15.

The total pressure drop across the filter can be calculated as the surface averaged absolute pressure at the entrance faces of the inlet open channels minus the surface averaged absolute pressure at the exit faces of the outlet channels, together with the irreversible losses from sudden contraction and expansion.

7.2.2 CFD methodology

In order to demonstrate how the multi-channel model can be coupled with computational fluid dynamics simulations, several simplified geometries representative of typical exhaust systems have been considered using Star-CCM+. The computational domain includes an inlet pipe with a sudden expansion downstream (Figure 7.3). The diameter of the filter was set as $50[mm]$, so that the results could be assessed with the experimental measurements reported in Chapter 5 and published in [14]. The other dimensions have been chosen arbitrary. A $30[g/s]$ mass flow rate is imposed at the inlet pipe entrance. Only the entrance faces of the filter inlet channels are included in the CFD computational domain and set up as pressure outlets (Figure 7.3), while the filter itself is not included. The value of the pressure for each filter channel is determined from the multi-channel model and is discussed in the next section. A no slip condition is prescribed for all other boundary surfaces.

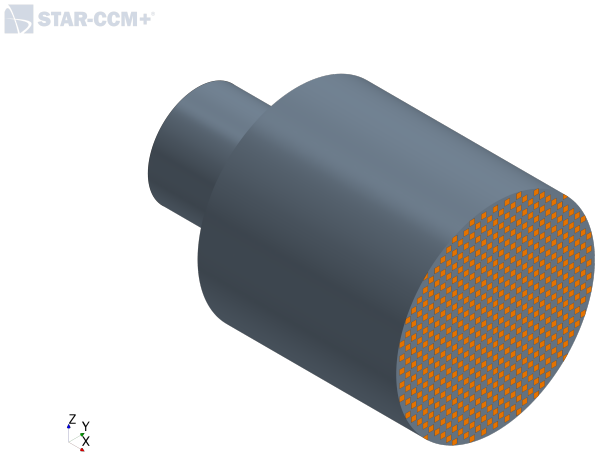

Fig. 7.3 Inlet section and expansion domain for the CFD simulations.

The other Star-CCM+ set-up parameters for the simulations are displayed in Table 7.1. The v^2f turbulence model has been selected among other turbulence models as it was shown to perform well in separated flows [113]. In order to compare the results of the present simulations with the experimental data published in [14], the flow temperature was set as $680[^{\circ}C]$.

Table 7.1 Star-CCM+ set-up parameters.

Parameter	Model
Geometry/Domain	3-D
Viscous Regime	Turbulent
Time	Steady State
Flow Solver	Segregated Flow
Solution Algorithm	SIMPLE
RANS Turbulent Model	v^2f
Convection Scheme	Second-Order
Temperature	$680[^{\circ}C]$
Equation of State	Idea Gas Law
Fluid Dynamic Viscosity	Sutherland's Law

7.2.3 Multi-channel model and CFD coupling methodology

The multi-channel model and CFD simulations are coupled through the front faces of the inlet channels (Figure 7.4), and an iterative procedure is used to obtain a converged solution in both domains. The following solution process has been used here:

1. Setup CFD simulation in Star-CCM+, with initial pressures at the inlet channel entrances estimated from the analytical solution of the one-dimensional model from [16].

2. Run the CFD simulation until convergence.

3. Extract the mass flow rate and density from each entrance face of the inlet channels and calculate the mean cross-sectional velocity entering each channel $\left(U_{i,j} = \frac{\dot{m}_{i,j}}{d_h^2 \rho_{i,j}}\right)$.

4. Use these velocities as inlet boundary conditions for the multi-channel model and solve the boundary value problem using MATLAB. The pressure at the exit of the outlet channels is set as ambient pressure here because the flow downstream

the filter is not considered, but would generally need to be coupled with the downstream solution.

5. Extract pressure at the entrance of each inlet channel from the model solution.

6. Update the outlet pressure boundary condition of each entrance face of the inlet channels in the CFD simulation with the newly calculated back-pressure.

7. Steps 2) to 6) are repeated n times, until the difference in back-pressure of each single channel between two successive iterations is lower that 0.1%, which is the criterion selected for the convergence here.

A pressure correction limiter between successive iterations has been implemented to improve convergence time and stability. If the absolute pressure value at the entrance to the inlet channels exceeded 1% difference from the value of the previous iteration, then only a 1% correction was used. The solution time for each case is around 10 hours. This is because the boundary value problem solver used here is not parallelised and as a consequence $2/3$ of the solution time is taken by the multi-channel model solution in MATLAB. In the multi-channel model, the 1-D solution from the model by Konstandopoulos [16] was used as the initial guess.

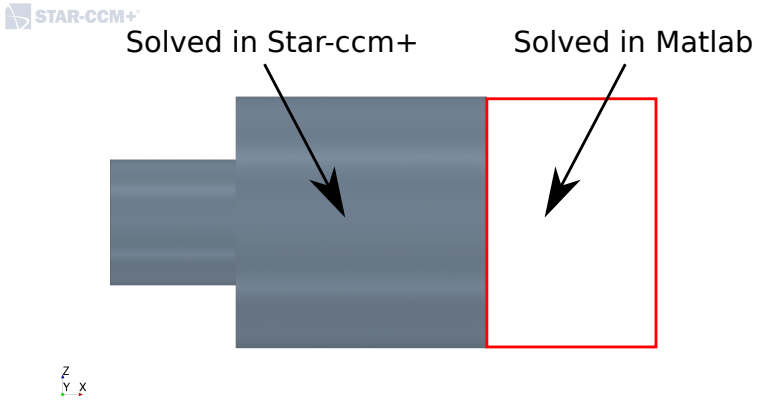

Fig. 7.4 Inlet section and expansion solved in Star-CCM+ (in gray) and multi-channel model solved in MATLAB (in white).

Thus, the multi-channel model and the CFD simulations are fully coupled and the velocity and pressure profile at the filter inlet are not assumed a priori but calculated.

This means that the velocity profile at the filter inlet is influenced both the non-uniform back-pressure from different channels and the upstream geometry configuration.

7.3 Results

7.3.1 Bare and coated filters

In this section the results from two cases, including a bare and a catalyst coated filter cores, are presented and compared with the experimental measurements reported in Chapter 5. This provided an initial assessment of the proposed modelling approach, as a more thorough validation of this approach, and in particular of the velocity redistribution upstream the filters solved in Star-CCM+, would require comparing the results with PIV measurements, which are not available. A simple upstream configuration with no sudden expansion (Figure 7.5) is considered here to replicate the geometry used in the experiments reported in Chapter 5 and published in [14]. Also, the filter properties used for the calculations are those reported in [14] (see Table 2.3 core #1 bare and core #2 coated), including the values of the permeability.

Note that the permeability estimated in [14] is based on the assumption that the filter permeability is homogeneous. Although for bare filters this is usually true, catalyst-coated filters might exhibit different coating penetration depth and thickness of the coating layer in different regions of the filter. As a consequence the local permeability of the filter might not be homogeneous.

For the two cases investigated in this section the permeability of the filters has been assumed homogeneous. The effect of non-homogeneous filter permeability is investigated and presented later in this chapter.

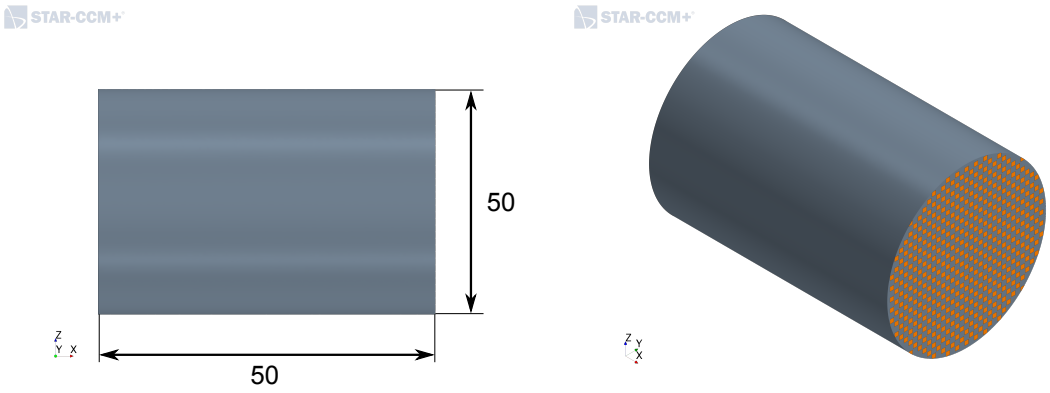

(a) (b)

Fig. 7.5 Computational domain: (a) side view and (b) isometric view. Dimensions in $[mm]$.

For both the bare and catalyst coated filter cores the multi-channel model computational domain includes 437 inlet channels and 448 outlet channels, for a total of 885 channels. This number is related to the selected filter diameter, cells density and wall thickness, and it would change if different filter parameters are considered.

The multi-channel model equations have been solved using the boundary value problem bvp5c. Since bvp5c is a finite difference code this requires a mesh of points to be created for of each single channel along its axial direction. Thus, several mesh densities have been investigated for the bare and coated filter in order to achieve mesh independent solutions. It was found that 31 mesh points for the bare filter and 11 mesh points for the coated one are sufficient to reach independence of the solutions. In both cases the mesh points are equally spaced along the channels axis. Note that the number of mesh points required to achieve mesh independent solutions might be different if a solver other than bvp5c is used. The different number of mesh points required by the bare and coated filters can be explained by looking at the difference in the channel velocity and pressure distribution for different permeability values. Two representative velocity and pressure distribution in filters with different permeability are shown in Figures 6.4 - 6.5 and Figures 6.7 - 6.8. In a coated filter the velocity profile in the axial direction is almost linear, while in bare filters a sharp velocity gradient is present near the end of inlet and outlet channels. These sharp velocity gradients require a denser mesh to be captured properly.

Figure 7.6 and Figure 7.7 show the results for the bare and coated filters, respectively. Figure 7.6 and Figure 7.7 (a) and (b) show that for both filters the velocity and pressure distribution are uniform up to a few millimetres away from the filter frontal face. This behaviour was expected as, for this configuration, the flow at the inlet was provided with a uniform velocity profile and the upstream configuration does not include any expansion which may cause flow separation. At the interface between the upstream section and the filter frontal face the flow accelerates rapidly to enter the open channels while it forms small stagnation regions where the plugs are present. The local flow acceleration is caused by the sudden change in cross-section which forces the flow into a smaller open frontal area. The pressure field reflects the velocity distribution, with a high stagnation pressure in the proximity of the plugs and a lower pressure at the entrance of the open channels, where the flow is allowed to pass.

Figure 7.6 and Figure 7.7 (c) and (d) show the mean channel velocity and pressure at the entrance of each inlet channel. Here it can be seen that the velocity entering in most of the channels does not vary considerably and that the pressure field is predominately uniform. This also means that the mass flow rate entering most of the channels is nearly identical. Only a few channels at the border of the filter present a different behaviour, with either higher velocity and lower pressure or a lower velocity and higher pressure. This result is not surprising as the outer channels are bounded by one or more impermeable walls and thus should not behave as the central channels. Looking at the 8 cells with the lowest velocity in Figure 7.6 (c) it can be seen that they also have the highest back-pressure from Figure 7.6 (d). These cells have two porous walls and two impermeable walls and, hence, are only coupled with two other cells each. Since all of the mass flow entering these cells is forced to pass through two porous walls only, instead of three or four as in other cells, the velocity through the porous wall will be higher and thus, in accordance with Darcy's law, the resulting pressure drop increases. The different behaviour of the outer cells affects also the adjacent channels and few lines of channels located next to them.

Comparing Figure 7.6 and Figure 7.7 (c), it can be notice that the velocity and pressure at the entrance of the channels are more uniform in the coated filter. This

behaviour can be explained by the fact that the lower permeability of coated filters, which provides greater resistance to the flow, discourage the cross-flow between channels.

Figure 7.6 and Figure 7.7 (e) show the mean channel velocity at the exit of each outlet channel. The outlet velocity shows the same qualitative trend of the inlet, but its magnitude is higher. The increased velocity reflects the fact that as the flow advances through the channels its local pressure decreases and so does the density. Thus, in accordance with the conservation of mass, the magnitude of the velocity increases towards the end of the filter. This effect, which is physical and not a numerical artefact, underline the importance of accounting for the density change along the filter channels. In fact, all models which assume the density as constant will not be able to predict the flow acceleration at the end of the exit channels.

As mentioned at the beginning of this section, the two cases simulated here replicate the same geometry and flow conditions of the experiments presented in Chapter 5. Thus, the multi-channel model results are now assessed against the experimental data. The total pressure drop of the bare filter is in good agreement with the experimental data (Figure 7.8 (a)), with a difference of about 7.5%, which is within the experimental uncertainty. Instead, the total pressure drop of the coated filter (Figure 7.8 (b)) is about 16% higher with respect the experimental data, which is slightly outside the experimental uncertainty. The fact that the coated filter shows a less accurate agreement with respect to the bare filter could be attributed to the non-uniform permeability in different filter channels in the experiments, caused by the non-uniform catalyst coating distribution.

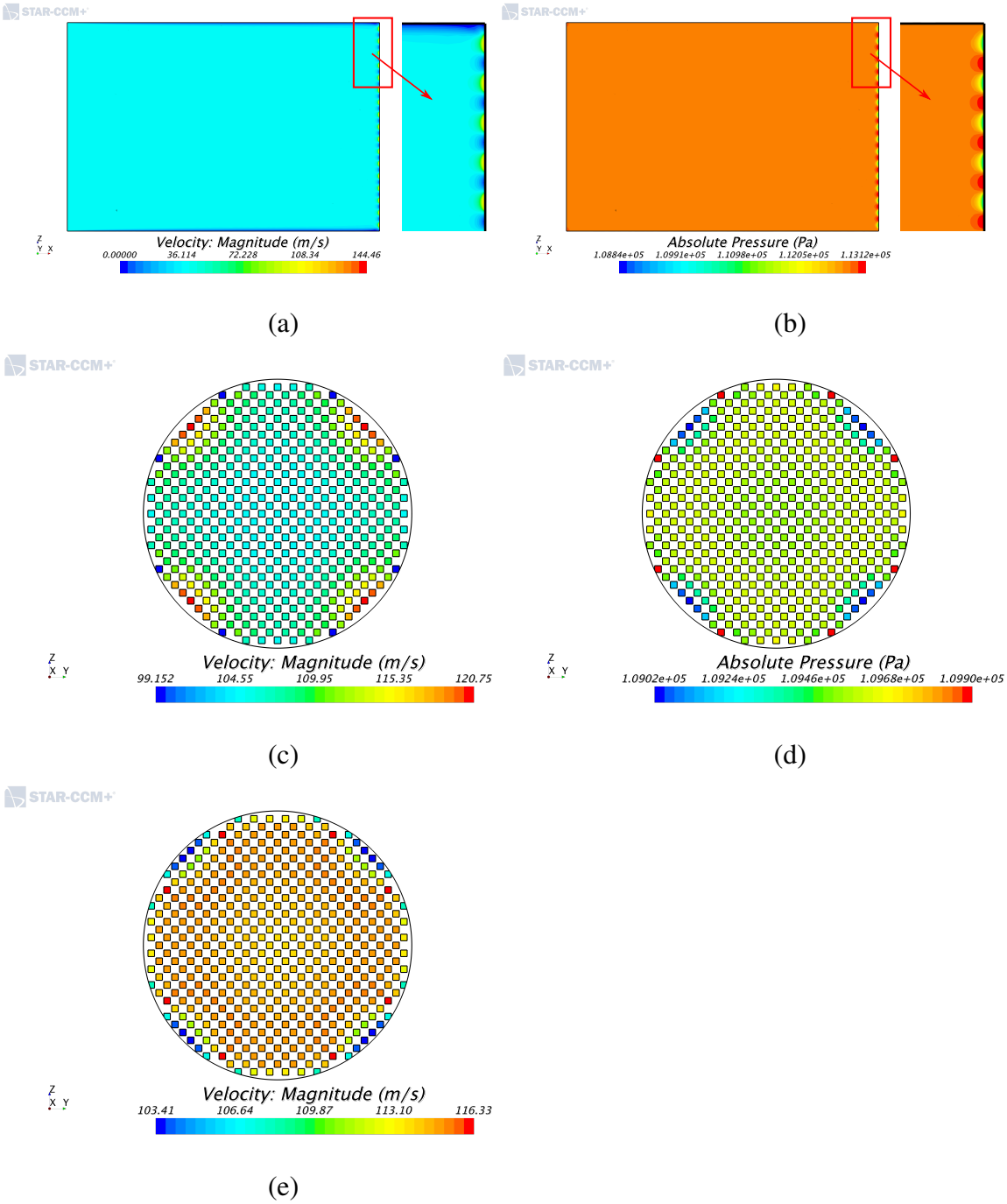

Fig. 7.6 300/8 bare filter: Velocity magnitude and absolute pressure in the mid-plane of the upstream domain and at the entrance or exit of each channel.

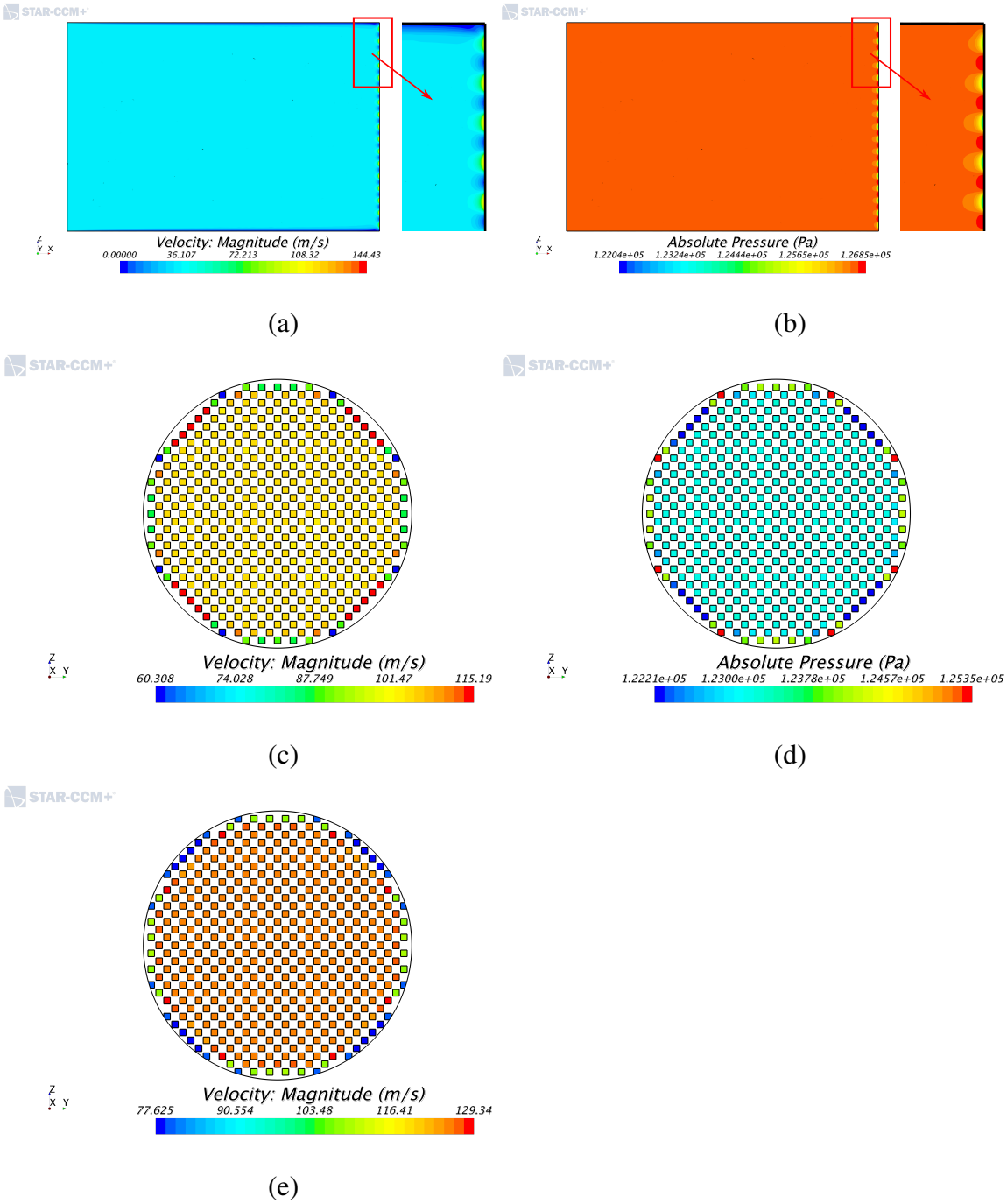

Fig. 7.7 300/8 coated filter: Velocity magnitude and absolute pressure in the mid-plane of the upstream domain and at the entrance or exit of each channel.

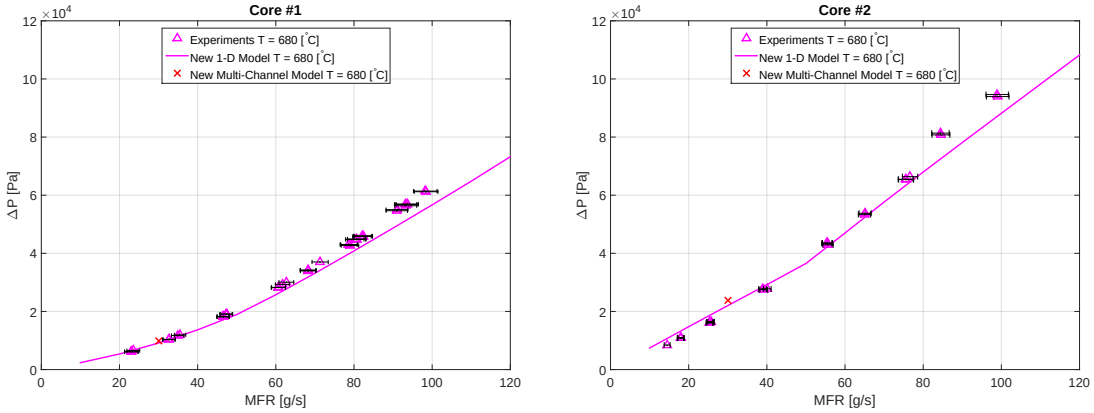

(a) (b)

Fig. 7.8 Pressure drop comparison between the new 1-D model, the multi-channel model and the experiments: (a) 300/8 bare filter and (b) 300/8 coated filter.

7.3.2 Coated filter with upstream concentric and eccentric expansion

Due to the different size of the filter diameter and the vehicle's exhaust pipeline and the placement of the particulate filter, which does not always allow to have the exhaust pipeline in alignment with the monolith axis, the flow profile approaching the filter is often non-uniform. Thus, two configurations are considered in this section, which include an upstream concentric and eccentric expansion upstream of the filter (Figure 7.9). For both cases, the filter geometry and permeability are the same as those reported in the previous section for the coated filter. In the case with the eccentric expansion the inlet section axis is shifted 6.25$[mm]$ away from the expansion axis.

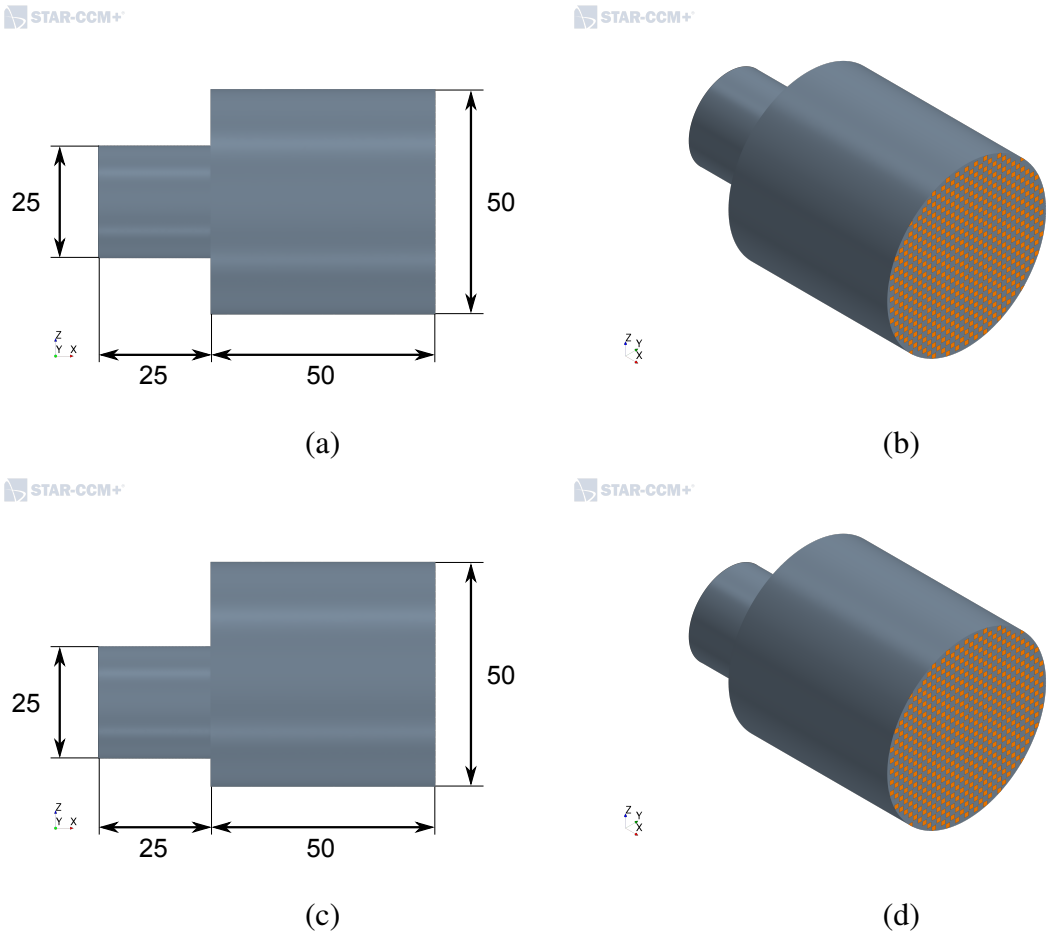

Fig. 7.9 Side and isometric views of the computational domains for concentric expansion case (a)-(b) and eccentric expansion case (c)-(d). Dimensions in $[mm]$.

Figure 7.10 and Figure 7.11 show the results of the concentric and eccentric expansion cases, respectively.

Figure 7.10 and Figure 7.11 (a) and (b) show that the flow profile upstream the filter is highly non-uniform in both configurations. This is caused by the "jet" that develops when the flow is discharged in the expansion section and hits the filter.

In the concentric expansion case (Figure 7.10 (a) and (b)), an adverse pressure gradient region is formed as the flow impinges the filter frontal face. This also causes the flow to spread towards the outer part of the filter and to enter the channels with an angle. Instead, in the central part of the filter the flow entering the filter channels is predominantly axial. As expected, due to the sudden expansion, the flow separates from the expansion walls, forming a shear layer region between the jet and the recirculation region.

Figure 7.10 (c) and (d) show the mean channel velocity and pressure at the entrance of each inlet channel. Here it can be seen that, as for the upstream section, the velocity at the entrance of the filter is non-uniform and that the velocity magnitude in the outer part of the filter is about 10% lower than in the central part. The pressure at the entrance of the filter is also non-uniform and the highest back-pressure is located in correspondence to the impinging region. The velocity non-uniformity is then preserved as the flow progresses through the channels towards the end of the filter, as shown by Figure 7.10 (e).

The eccentric expansion case (Figure 7.11) shows similar features to the concentric case. Thus only the differences between the two are highlighted below. Firstly, it can be observed that the recirculation region after the expansion is bigger above the jet core, as here the flow has more space to expand (Figure 7.11 (a)).

Secondly, the jet is slightly shifted towards the nearest wall and a smaller secondary pressure peak is generated next to the nearest wall just below the main impingement region, which is aligned with the inlet pipe axis (Figure 7.11 (b)). The secondary pressure peak is formed because in that location the flow is squashed on three sides by the filter frontal face, the lower wall and the main region with adverse pressure gradient.

The results of these two cases show that, although the high back-pressure from the filter tends to flatten the flow profile, a highly non-uniform flow profile upstream will result in non-uniform flow distribution between the filter channels. This means that a higher mass flow rate will be observed in some of the channels and thus will cause higher soot and ashes accumulation, changing the filter performance.

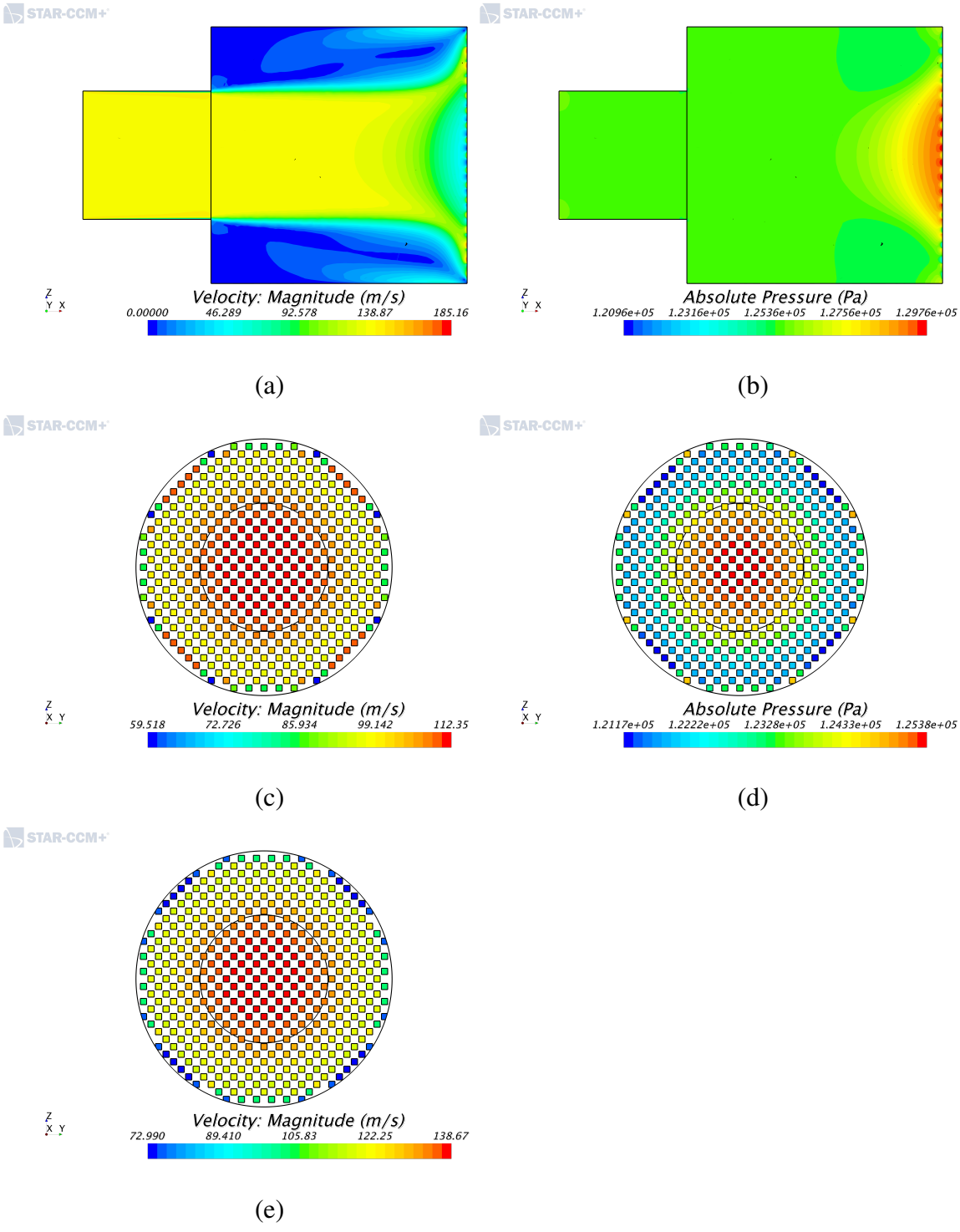

Fig. 7.10 300/8 coated filter with concentric expansion: Velocity magnitude and absolute pressure in the mid-plane of the upstream domain and at the entrance or exit of each channel.

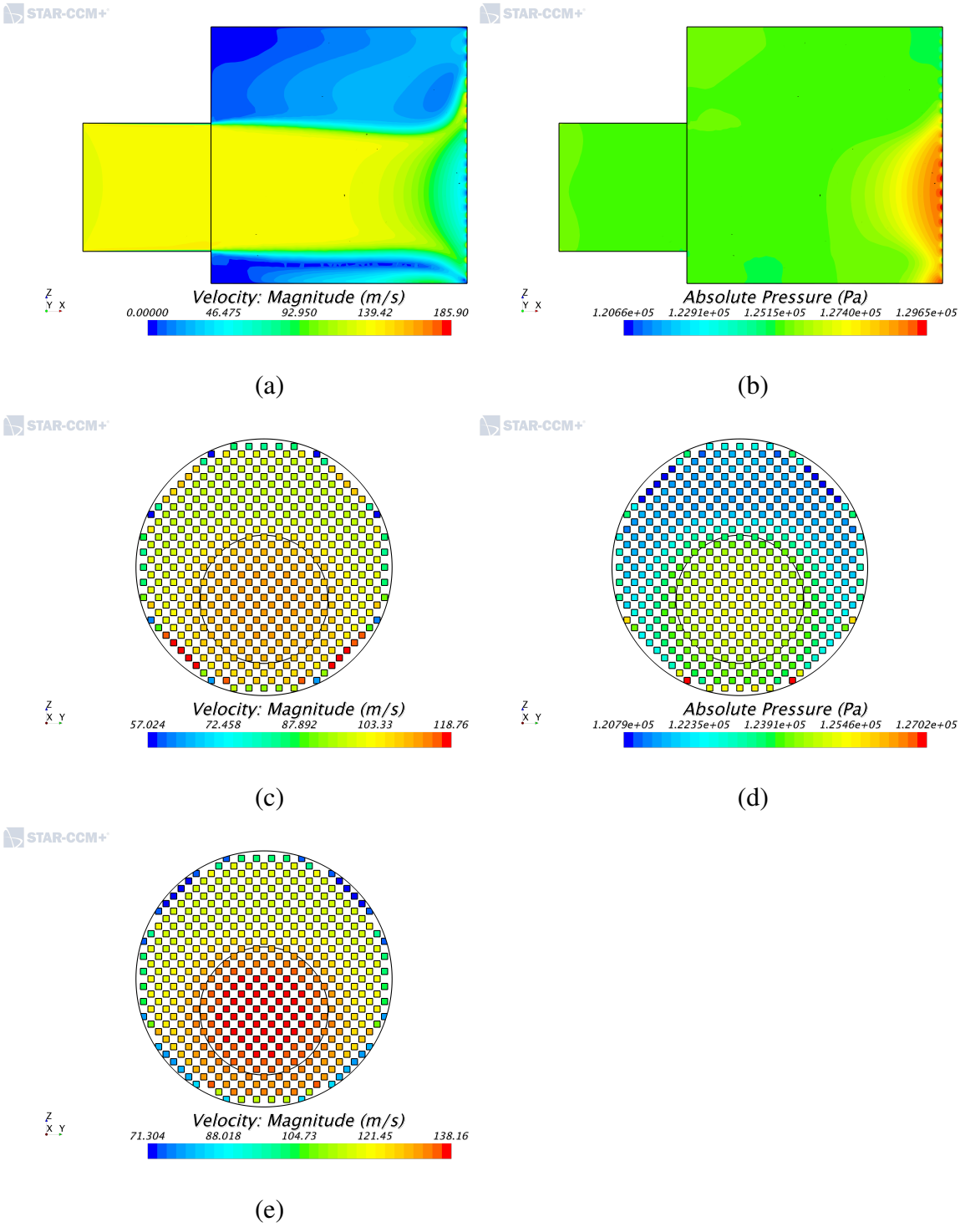

Fig. 7.11 300/8 coated filter with eccentric expansion: Velocity magnitude and absolute pressure in the mid-plane of the upstream domain and at the entrance or exit of each channel.

7.3.3 Coated filter with uneven permeability

In the two cases presented in previous section, the non-uniformity of the flow approaching the filter was caused primarily by the shape of the section upstream of the filter (i.e. the concentric or eccentric expansion). However, the geometry of the upstream section is not the only factor which may influence the flow distribution approaching the filter and its total pressure drop. The deposit of soot and ashes, a non-homogeneous catalyst coating, and thus wall permeability, in different channels, cracks and manufacturing defects can also play an important role. In fact these will change the local properties of the filter and consequently the back-pressure coming from individual channels.

Therefore, to demonstrate how the proposed modelling approach can be used to investigate non-uniform filter properties, two additional cases have been simulated in this section. The first case includes a filter with non-homogeneous permeability and an upstream pipe without changes in the cross-section (as in Figure 7.5), while the second case includes a filter with non-homogeneous permeability and an upstream pipe with a concentric expansion (as in Figure 7.9 (a) and (b)).

The filter geometry is the same as the one reported in Table 2.3 for the core #2, while a permeability of $k_{out} = 2.09 \times 10^{-13}[m^2]$ (10% higher than the value reported in section 6.4.1) has been assigned in the outer region of the filter and a permeability of $k_{in} = 1.71 \times 10^{-13}[m^2]$ (10% lower than the value reported in section 6.4.1) has been assigned in the inner region, as shown in Figure 7.12. The 10% difference in the permeability has been chosen arbitrarily and it is intended only for demonstration purposes. In a practical case, the lower value of the permeability in the central part of the filter might be caused by an uneven soot and ash accumulation or by an uneven application of the catalyst coating layer on the filter walls.

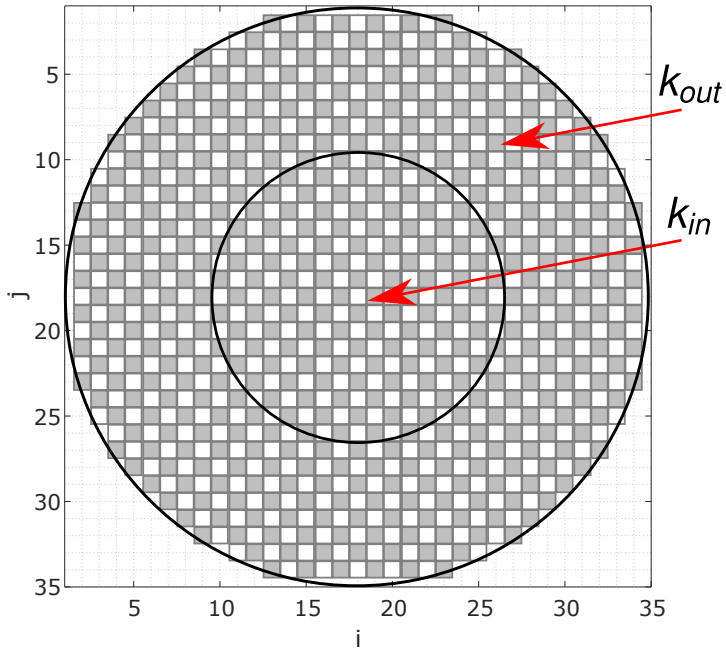

Fig. 7.12 Inner and outer region with different values of the permeability.

Figure 7.13 and Figure 7.14 show the results for the case without expansion upstream and the case with the concentric expansion, respectively. The flow field on the mid-plane of the upstream domain is not presented, as in both cases there is not a significant difference from the respective cases with homogeneous permeability, which have been already discussed.

In the case without expansion, Figure 7.13 (b) shows a marked uneven pressure distribution, with the channels in the center providing an higher back-pressure compared to the outer channels. This effect is caused by the lower permeability assigned to the channels located in the inner part of the filter, which provide a higher resistance to the flow. As a result of the uneven pressure distribution, the flow is diverted towards the outer part of the filter and the channels in this region are characterised by an higher inlet velocity, as shown in Figure 7.13 (a). Thus, the flow distribution becomes less uniform with respect to the case with homogeneous permeability.

Figure 7.14 shows the results for the case with the concentric expansion. As observed in the case without the upstream expansion, the lower permeability in the central part of the filter causes the flow to divert towards the outer region. However, since the lower permeability region coincides with the "jet" impingement region, the

higher resistance in the central part results in flow deceleration and thus helps the flow to become more uniform, as evident from a comparison between Figure 7.14 (b) and Figure 7.10 (c).

The present results show that non-homogeneous filter properties can have a non negligible impact on the filter performance. Depending on the shape of the upstream section and the location of the non-homogeneous permeability different flow behaviours can be observed. In the first case the non-homogeneous permeability causes an increase in flow non-uniformity, which is generally considered not beneficial. This is because the channels with higher inlet velocity will accumulate more soot and ashes (which are transported by the flow) compared to the channels with a lower inlet velocity, as the mass flow rate entering the former is higher. Thus, not all the channels are used efficiently. In the second case, instead, the non-homogeneous permeability helps the flow to become more uniform, thus producing a beneficial effect in terms of soot and ash accumulation.

The effect of the non-homogeneous permeability on the total pressure drop of the filter is discussed in the next section, where all the six cases investigated in the previous sections are compared.

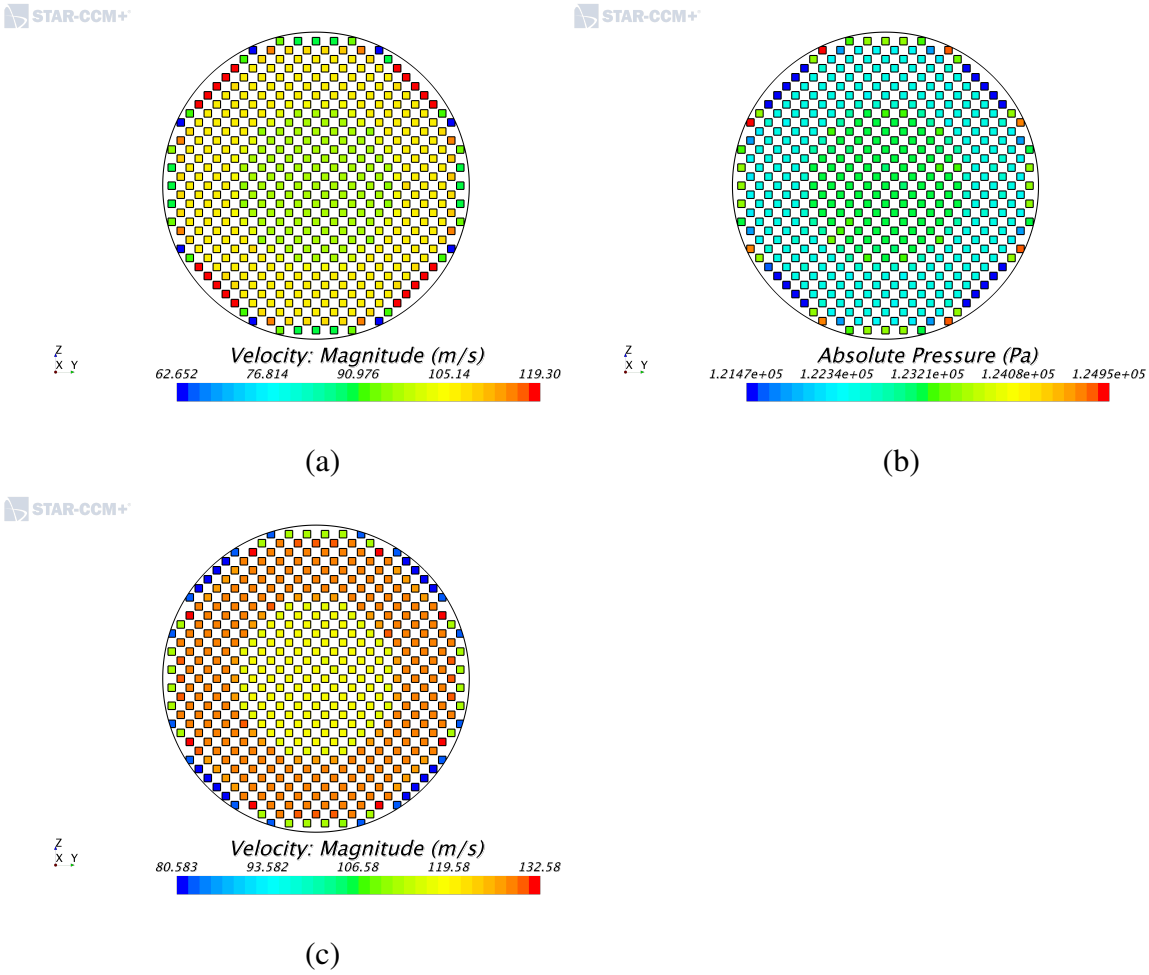

Fig. 7.13 300/8 coated filter without expansion in front of the filter and with non-homogeneous permeability: Velocity magnitude and absolute pressure at the entrance or exit of each channel.

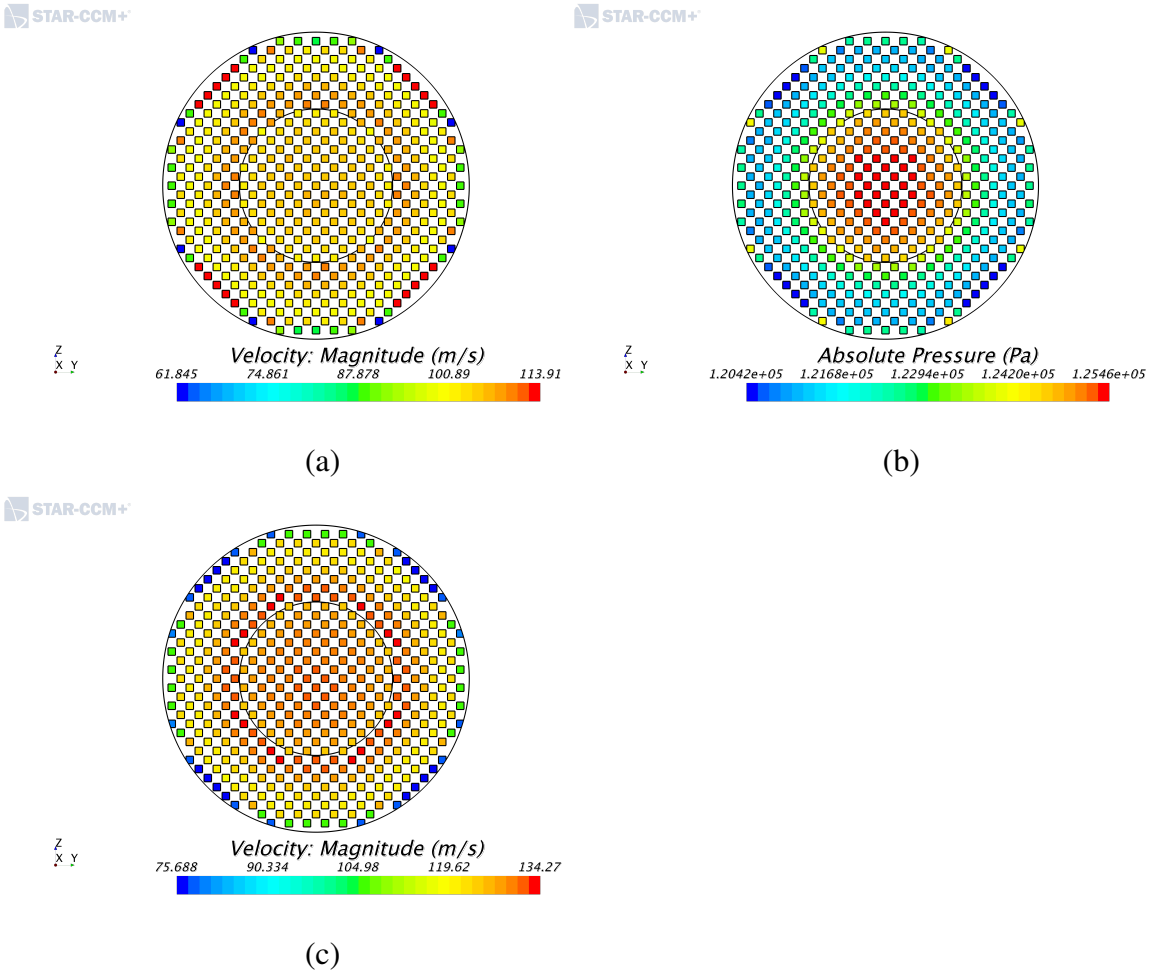

Fig. 7.14 300/8 coated filter with concentric expansion in front of the filter and non-homogeneous permeability: Velocity magnitude and absolute pressure at the entrance or exit of each channel.

7.3.4 Total pressure drop

In the previous sections six test cases have been simulated to show how the proposed modelling approach can be used to investigate the effect on the flow field of different upstream configurations and non-homogeneous filter properties. In this section the total pressure drop across the filter has been calculated for all cases, as discussed in section 7.2, and is presented in Table 7.2 for comparison purposes.

Table 7.2 Total pressure drop across the filter cores.

Filter	Upstream Configuration	Permeability	Total Pressure Drop
300/8 Bare	Without Expansion	Homogeneous	9.9[*kPa*]
300/8 Coated	Without Expansion	Homogeneous	23.8[*kPa*]
300/8 Coated	Concentric Expansion	Homogeneous	23.8[*kPa*]
300/8 Coated	Eccentric Expansion	Homogeneous	23.8[*kPa*]
300/8 Coated	Without Expansion	Non-Homogeneous	23.3[*kPa*]
300/8 Coated	Concentric Expansion	Non-Homogeneous	23.4[*kPa*]

Comparing the pressure drop of the three coated filters with homogeneous permeability and different upstream configuration it can be seen that, although they present different flow features (see Figure 7.7, Figure 7.10 and Figure 7.11), the non-uniform upstream flow seems to have little to none effect on the total pressure drop.

Looking instead at the two cases with non-homogeneous permeability it can be seen that the overall filter pressure drop for both these cases is about 2% lower than for the respective cases with uniform filter properties. This can be explained by the fact that there is a higher mass flow entering the channels with higher permeability, which provide a lower resistance to the flow. Note that, core #2, which properties have been used here for the simulations, is likely to have a non-uniform permeability due to the application of the catalyst coating layer on its channels walls. Thus, this finding might explain why the pressure drop for the coated filter predicted with the multi-channel approach and uniform permeability shows a higher value than the experimental results reported in Chapter 5.

It is important to underline that the results of the comparison presented above are valid only for the specific cases investigated here and cannot be generalised, as different upstream configurations or different distribution of the uneven permeability might change these results. It is also reasonable to assume that as the configurations investigated here provide different flow distributions, their respective soot and ash accumulation patterns, and hence filter local permeability, will be different. Consequently, it is likely that after a short period of loading, filters with different upstream configurations

will provide different total pressure drops. A modification of the present multi-channel model to account for transient flows would allow to properly investigate these effects.

7.3.5 Through wall velocity in individual channels

While 0-D and 1-D models can provide quick results for the total pressure drop of a filter, they cannot model or provide details about the axial flow and pressure distribution in all the filter channels. However, the proposed multi-channel modelling approach is able to provide these information, and in particular, it allows to analyse the distribution of the through wall velocity in different channels. This is very helpful in predicting the axial location of the soot accumulation and will be even more useful once the model is extended to account for transient flows.

Thus, an analysis of the through wall velocity distribution in two pairs of channels, one pair next to the outer filter wall (Ch1) and one pair at the centre of the filter (Ch2), is presented in this section to further show the potentiality of the multi-channel modelling approach. Two cases have been considered for this study.

Firstly, Figure 7.15 (a) compares the through wall velocities in the outer inlet channel (Ch 1) with the central one (Ch 2), for the case without expansion upstream of the filter and non-homogeneous permeability. Note here that the terms left, right, top and bottom through wall velocities used in the legend of both Figure 7.15 and Figure 7.16 refer to the velocity magnitude between the central cell and neighbouring cells according to the notation shown in Figure 7.2. The through wall velocities in the channel at the centre of the filter (Ch2) show the same magnitude and trend (in fact they are overlapping in Figure 7.15 (a)), as expected due to the channel particular location. However, the through wall velocities in the channel at the border of the filter (Ch1) show a slightly different trend from the previous ones, and a clear difference between the flow through different walls is also noticeable. In both channels the magnitude of the through wall velocities is higher towards the end of the filter, showing that a higher percentage of the flow passes from the inlet to the outlet channel in the second half of the filter. This means that a higher soot accumulation is expected towards the end of the filter. Note that this behaviour was also captured by the 1-D model, as shown in Figure 6.5. Figure 7.15 (b) compares the through wall velocities in the outlet channels near the wall (Ch 1)

and near the centre of the filter (Ch 2). Here the velocity trends are similar to the inlet channels, however the magnitudes are higher. This is caused by the density difference between the inlet and outlet channels, as discussed before.

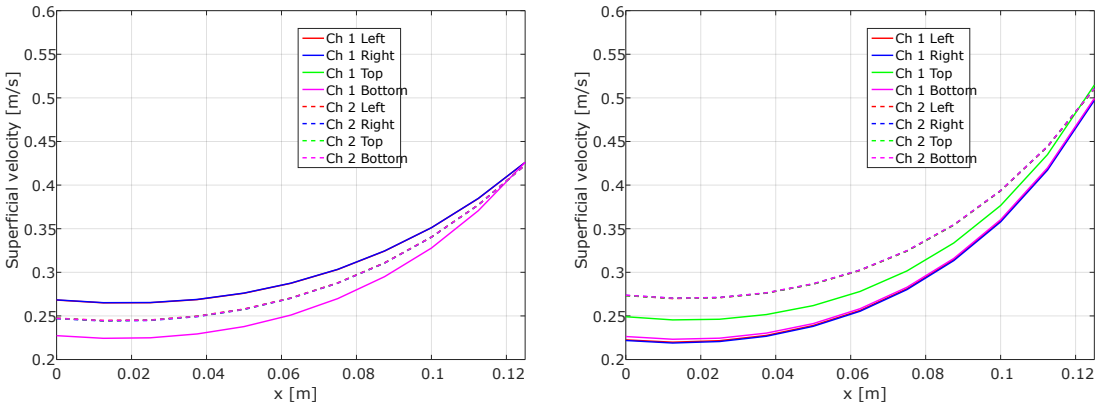

(a) (b)

Fig. 7.15 Through wall velocity magnitude along the filter axial direction for the 300/8 coated filter without expansion and with non-homogeneous permeability: (a) Inlet channel and (b) outlet channel.

Figure 7.16 (a) and (b) show the through wall velocities for the case with the concentric expansion upstream the filter and homogeneous permeability. The through wall velocities present the same trend as the previous case. However, here the difference in through wall velocities between the central and peripheral channel is bigger, which reflects the fact that the flow is much more non-uniform.

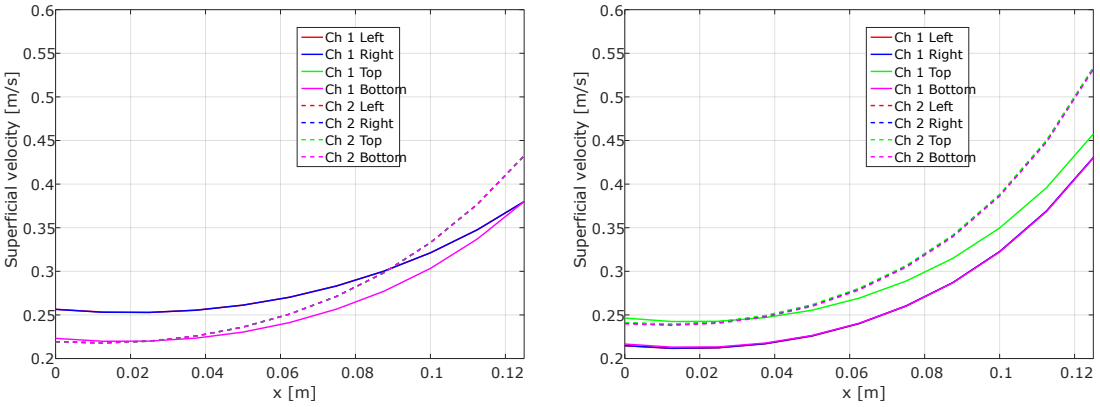

Fig. 7.16 Through wall velocity magnitude along the filter axial direction for the 300/8 coated filter with concentric expansion and homogeneous permeability: (a) Inlet channel and (b) outlet channel.

7.4 Chapter summary

This chapter presents a new multi-channel particulate filter model and coupling with CFD. This modelling approach overcomes the main limitations of the traditional 0-D and 1-D modelling approaches, which simulate only representative pair of channels. Although previous attempts to formulate and implement such model exist [38], this is the first multi-channel model which accounts for the full cross-flow between channels. Additionally, the formulation of the proposed model includes the density variation effect and allows to change individual channel properties, such as wall thickness, hydraulic diameter and wall permeability, which were not included in any of the previous formulations.

The coupling between a 3-D CFD simulations of the upstream flow and the multi-channel model has been demonstrated by using MATLAB and Star-CCM+. The coupling with the CFD simulations has also never been included in any of the previous multi-channel modelling approaches.

In order to demonstrate the potential of the new modelling approach, six different cases, which include three distinctive upstream geometries, homogeneous and non-homogeneous filter permeability or a combination of both, have been simulated. It has

been shown that the upstream geometry and the non-homogeneous filter permeability can affect the flow distribution approaching the filter frontal face and that the upstream flow non-uniformity persists through the filter.

The model provides not only global flow parameters such as the total pressure drop across the filter, but also offers insight into flow and pressure distribution along the channel axis. This has been demonstrated by analysing the through wall velocities in different channels, which are particularly important as these are used to predict the axial location of the soot accumulation.

The main limitation of this modelling approach and the current implementation is related to the computational time and resources required for the solution, which are much more demanding than for the solution of the single inlet/outlet models. These can be resolved by using a parallelised version of the boundary value problem solver.

The model formulation can be further extended to account for the heat transfer, which can be included by using the local temperature for density calculations and adding energy conservation equation, and to account for the turbulent regime by including the turbulent friction factor, as done for the 1-D model proposed in Chapter 6.

Finally, the flow downstream of the filter was not considered and ambient pressure conditions were assumed at the filter channel exit. However, the methodology for coupling the downstream flow model to the multi-channel model would be exactly the same as with the upstream flow, and thus this modification would be straightforward to implement.

Chapter 8

Conclusion

The aim of this project was to develop a fundamental understanding of the complex physics of the flow in wall-flow filters and to develop tools for modelling filter flows, with particular focus on Gasoline Particulate Filters (GPFs) and their operating conditions. In order to achieve this aim several objectives were set and addressed.

From an industrial/practical point of view and with regard to particulate filters, the main outcomes of this work include the collection of the pressure drop experimental data for several filter core samples in different flow regimes and temperatures and the development and assessment of two new physics-based particulate filter models. The results of the numerical investigations on the developing flow losses and contraction losses in laminar flow regime and of the experiments on unplugged filters provided useful informations in order to support the physical base of the new models, but they can also be used for the prediction/optimisation of the pressure drop in other applications (i.e. catalyst filters, multi-channel systems, wind tunnels and flow meters). Although the work was focussed more on the GPFs as a new technology with higher temperatures and flow rates, all results can be used to improve the predictions of flows within DPFs and their operation conditions.

8.1 Pressure losses in laminar flow

To the author knowledge this is the first study which uses an up to date RANS CFD analysis to investigate these losses in laminar flow regime.

A numerical investigation of **laminar developing flows** in circular and square cross-sectional ducts has been conducted in order to improve the existing correlations for developing flow losses, as shown in Chapter 3. The results clearly demonstrate that for different inlet configurations the pressure defect $K(x)$ can be Reynolds-independent, or change with the Reynolds number. This would explain the scatter in the experimental results found in the literature.

Several new correlations have been derived by fitting of the CFD solutions. Firstly, two new improved correlations for the pressure defect and hydrodynamic entrance length for Reynolds number independent developing flows in circular and square cross-sectional ducts have been proposed. Secondly, a new Reynolds number dependent pressure defect correlation for a bell-mouth contraction nozzle inlet geometry has been proposed. These correlations can be used to improve/optimise the design of components such as automotive catalysts and filters or compact heat exchangers, where the extra pressure loss will result in increased fuel and/or energy consumption, as well as for the design of flow meters and laminar flow wind tunnels.

Finally, a new correlation for the momentum correction factor and kinetic energy correction factor, as a function of the axial position from the duct entrance, have been proposed for the first time (to the author knowledge). These can be used for calculation of flow contraction and expansion losses in heat exchangers (e.g. [24]) and other applications such as particulate filters.

A new method has been proposed to derive the **contraction loss coefficient** and to separate the contribution of the contraction losses from the friction and developing flow losses upstream and downstream the contraction location. This means that the contraction loss coefficient derived through this method can be used to estimate the local losses due to the contraction regardless of the fact that the flow may or may not re-develop downstream the contraction (i.e. in a particulate filter).

For the single channel contraction with circular and square cross-section the results show that there isn't a significant difference between the two geometries investigated and that the Borda-Carnot equation for a sudden change in cross-section provides a good fit for the the contraction loss coefficient. For the multi-channel contraction with square cross-section the contraction loss coefficient results show a significant difference from

the values derived from the Borda-Carnot equation for a sudden change in cross-section. A new correlation, Eq. 4.7, has been proposed and provides a good fit for the the contraction loss coefficient in multi-channel systems with square cross-section.

Since all the reviewed studies on this topic do not provide enough or any information on the experimental set-up, range of Reynolds numbers and method used to calculate the contraction loss coefficients it was not possible to identify the source of the discrepancy between the present results and the correlations reported in the literature, and further experimental data is required for validation. For this reason Eq. 4.7 was not ultimately implemented in the particulate filter models developed in Chapter 6 and Chapter 7. Nevertheless, the study was still useful in order to determine that the inertial loss coefficients estimated by Konstandopoulos [28], ranging from 2.4 to 8.3, are too high (non-physical) and should not be used.

Finally, the CFD predictions presented and the method used to calculate the contraction loss coefficient can be exploited to design an experimental set-up to measure and estimate the contraction losses.

8.2 Experimental studies of filter pressure losses

A series of experiments have been carried out on plugged and unplugged cores in order to provide further insight into the origins and magnitude of different contributions to the total pressure loss, and to collect a robust set of data for the validation of the developed model.

An experimental study on unplugged filter cores has been conducted to investigate the friction factor in channels with porous walls, as shown in Chapter 5, as this was never charactered before for wall porosities typical of particulate filters.

The results show that the friction factor and the transitional regime in channels with porous walls, and porosity typical for particulate filters, are comparable to those in channels with solid walls. The measurements are in good agreement with Eq. 5.10, which is a modified version of Churchill's correlation, Eq. 5.8, with a correction factor to account for the square cross-section suggested by Jones [50].

Note that the experimental results presented in this study are limited to wall porosities typical of particulate filters and the validity of Eq. 5.10 for other porosities has not been assessed.

An experimental investigation of pressure losses in plugged filter cores has been conducted to fill the lack of experimental data for particulate filter pressure drop at high mass flow rates and temperatures, as shown in Chapter 5.

The data was collected by a team of researchers as part of a project with Jaguar Land Rover and published in [107] and [14] can be used to validate particulate filter predictive models in a wide range of flow conditions as well as filter properties.

The results have provided experimental evidence of laminar to turbulent transition regime in particulate filters. Also the data indicates that the flow is no longer fully laminar for Reynolds numbers above $Re > 1800$, which should be accounted for in particulate filter predictive models.

These results are limited to clean filters and steady state flow conditions, where the velocity profile entering the filter is flat.

8.3 New 1-D particulate filter model

Based on the insights gained from the numerical and experimental studies presented in Chapter 3, Chapter 4 and Chapter 5, a new 1-D particulate filter model has been proposed, which extends the Bissett-Kostandopoulos [16] model to the turbulent flow regime and to high temperatures, as shown in Chapter 6. As reported by Masoudi [13] and Prantoni et al. [14] turbulent flow regime within the filter channels can be present in certain operating conditions of both DPFs and GPFs and this is the first 1-D model which accounts for the turbulent friction losses.

The new model involves solving an ordinary differential equation. The equation is non-linear and does not have a closed solution, which is the case for most of the filter flow models based on the Bisset-Konstandopoulos model. However, it has been demonstrated how the model can be readily implemented in MATLAB. Other commercial and open source boundary value problem solvers can be used instead.

The model predictions agree well with experimental data for four different filter cores (with varying cell density, length and permeability), in both laminar and turbulent flow regimes. At high mass flow rates and temperatures the new model can improve the pressure drop predictions up to $30-40\%$ with respect to the Bissett-Kostandopoulos [16] model.

The main advantage of 1-D models over CFD and experimental studies is their computational efficiency and flexibility. This makes them an invaluable tool in choosing filter design parameters and optimisation of filter properties. In order to demonstrate this potential of the new model, a parametric study has been carried out looking at the effect of the filter geometry on the flow distribution and pressure losses. The results demonstrate that for most of the considered filter geometries there is a range of filter sizes providing minimum losses in the given mass flow rate range. Such insights would allow filter designers to select the best filter configuration within other constraints used in the development process.

Apart from inclusion of the turbulent flow regime, the new model uses more accurate values of the density inside the filter. Although for simplicity an average of the inlet and outlet density values has been included, it is possible to modify the model to account for the local value of the density. This is particularly important for Gasoline Particulate Filters where the back-pressure can reach very high values, therefore the density variation inside the filter channels is considerable.

Finally, the model is subject to the same limitations of the other single inlet/outlet models and can be used for the prediction of the pressure drop and flow of clean filters only.

8.4 New multi-channel particulate filter model

A new multi-channel particulate filter model and coupling with CFD have been proposed, which overcome the limitations of the traditional 0-D and 1-D modelling approaches, as shown in Chapter 7.

Although previous attempts to formulate and implement such model exist [38], this is the first multi-channel model which accounts for the full flow coupling between the

channels and that allows full flexibility in prescription of individual channel properties (wall thickness, hydraulic diameter and wall permeability).

The multi-channel framework developed here is based on the laminar Bisset-Konstandopoulos model. Similar to the 1-D model presented in Chapter 6, it requires solving a boundary value problem (now multi-dimensional). This is considerably more computationally expensive than its one channel counterpart, however can also be implemented using MATLAB or other boundary value problem solvers. The suggested solution methodology allows inclusion of the turbulent flow losses instead of the laminar flow model. One of the main challenges of using multi-channel filter models is prescribing the flow entering individual channels, as this depends on filter geometry, pressure losses in each channel and the flow configuration upstream and downstream of the filter. This has been tackled here by coupling the filter model with a full CFD solution of the flow upstream of the monolith. This is also the first time that a multi-channel model is successfully coupled with a 3-D CFD simulation of the domain upstream the filter. Although the flow downstream of the filter was not considered and ambient pressure conditions were assumed at the filter channel exit, the methodology for coupling downstream flow model to the multi-channel model would be exactly the same as with the upstream flow.

In order to demonstrate the potential of the new model, several representative geometries were considered, featuring non-uniform flow caused by the upstream geometry (such as a symmetric or asymmetric sudden expansion) and channel properties (different permeability in different areas of the filter). It has been shown that upstream flow non-uniformity may persist through the filter, which needs to be taken into account in filter design. This highlights the limitations of the traditional filter modelling where only one representative pair of channels is usually considered. The effect of different wall permeability between different channels has also been demonstrated.

The model provides not only global flow parameters such as the total pressure drop across the filter, but also offers insight into flow and pressure distribution along the channel axis, which is important for heat transfer, soot and ash accumulation studies. By varying wall thickness and/or permeability in the radial direction, the effect of the soot accumulation and uneven catalyst coating distribution can also be considered.

The main limitation of this modelling approach and the current implementation is related to the computational time and resources required for the solution, which are much more demanding than for the solution of the single inlet/outlet models. These can be resolved by using a parallelised version of the boundary value problem solver.

8.5 Recommendations for future work

The present work has successfully used experimental and modelling tools to improve the understanding of flow distribution and pressure losses in particulate filters and provide new methodologies for further studies. However, there are several areas which require further investigations and, thus, some recommendations for future work are proposed below.

Although the presented study of **contraction losses** in laminar duct flows provided correlations that can be used for filter modelling, it would be instructive to have a better insight into the discrepancies between the reviewed experimental studies discussed in section 1.2.2.2. A more thorough characterisation of the contraction loss coefficient may further help in improving the predictions of particulate filter models and strengthen theirs physical base. Therefore, an experimental study of the contraction losses using state-of-the-art instrumentation and analysis method would be useful not only for improvement of filter modelling tools, but also extending the derived correlations to other configurations.

The **new 1-D particulate filter model**, proposed here assumes that the density is constant along the filter channel. Although a better approximation of this density is used (an average between the inlet and outlet gas densities), this is a limitation which would cause loss of accuracy when the back pressure (and thus density variation) is high. The model can thus be improved by using the local gas density, as done for the new multi-channel model, instead of assuming it as spatially constant. This would be a natural extension of the model improving its accuracy. The model also readily allows using channel properties varying in the axial direction. Including transient effects and soot accumulation would be less straightforward but also possible.

The **new multi-channel particulate filter model** can be extended to the turbulent regime by including turbulent friction factor as done for the new 1-D particulate filter model. Although in the current formulation of the model different wall thickness and channel hydraulic diameter can be provided for different channels, better predictions could be achieved by modifying the Darcy losses equations to account for the cross-sectional area changes in the walls between channels of different hydraulic diameters. The new multi-channel model approach could also be extended by coupling the model with a downstream CFD solution, which should be reasonably straightforward and can be performed following an approach similar to that used for the upstream CFD coupling. Making the framework more computationally efficient by using a parallelised version of the boundary value problem solver would also be beneficial for making the model more accessible for industrial use.

Finally, **both the new models** could be complemented by including the heat transfer. This can be realised by using local temperature for density calculations and adding energy conservation equation. Both models could be extended to account for transient flows and a variable wall thickness, channel hydraulic diameter and permeability along the channels axis to model the effect of the soot accumulation. These would also require further experimental studies to obtain data for model assessment of loaded filters.

References

[1] https://www.who.int/sustainable-development/transport/health-risks/climate-impacts/en/.

[2] https://www.who.int/sustainable-development/transport/health-risks/air-pollution/en/.

[3] Niessner R. The many faces of soot: Characterization of soot nanoparticles produced by engines. *Angew. Chem. Int. Ed.*, 53(46), 2014.

[4] Reşitoğlu İ.A., Altinişik K., and Keskin A. The pollutant emissions from diesel-engine vehicles and exhaust aftertreatment systems. *Clean Techn. Environ. Policy*, 17, 2015.

[5] Tollefson J. Soot a major contributor to climate change. *Nature News*, 2013.

[6] Ito Y., Shimoda T., Aoki T., Shibagaki Y., Yuuki K., Sakamoto H., Vogt C., Matsumoto T., Heuss W., Kattouah P., Makino M., and Kato K. Advanced ceramic wall flow filter for reduction of particulate number emission of direct injection gasoline engines. *SAE Technical Paper*, (2013-01-0836), 2013.

[7] Piock W., Hoffmann G., Berndorfer A., Salemi P., and Fusshoeller B. Strategies towards meeting future particulate matter emission requirements in homogeneous gasoline direct injection engines. *SAE Int. J. Engines*, 4(1):1455–1468, 2011.

[8] Shimoda T., Ito Y., Saito C., Nakatani T., Shibagaki Y., Yuuki K., Sakamoto H., Vogt C., Matsumoto T., Furuta Y., Heuss W., Kattouah P., and Makino M. Potential of a low pressure drop filter concept for direct injection gasoline engines to reduce particulate number emission. *SAE Technical Paper*, (2012-01-1241), 2012.

[9] https://dieselnet.com/tech/diesel_exh_pres.php.

[10] Johnson T. V. Diesel emission control in review - the last 12 months. *SAE Technical Paper*, (2003-01-0039), 2003.

[11] Van Nieuwstadt M. and Ulrey J. Control strategies for gasoline particulate filters. *SAE Technical Paper*, (2017-01-0931), 2017.

[12] Lanzerath P., Wunsch R., and Schon C. The first series-production particulate filter for mercedes-benz gasoline engines. *17. Internationales Stuttgarter Symposium*, 2017.

[13] Masoudi M. Hydrodynamics of diesel perticulate filters. *SAE*, (2002-01-1016), 2002.

[14] Prantoni M., Aleksandrova S., Medina H., Saul J., Benjamin S., and Garcia Afonso O. Modelling pressure losses in gasoline particulate filters in high flow regimes and temperatures. *SAE Technical Paper*, (2019-01-2330), 2019.

[15] Bissett E. J. Mathematical model of the thermal regeneration of a wall-flow monolith diesel particulate filter. *Chemical Engineering Science*, 39(7/8):1233–1244, 1984.

[16] Konstandopoulos A. G. and Johnson J. H. Wall-flow diesel particulate filters - their pressure drop and collection efficiency. *SAE*, (890405), 1989.

[17] Mogaka Z. N., Wong V. W., and Shahed S. M. Performance and regeneration characteristics of a cellular ceramic diesel particulate trap. *SAE*, 1982.

[18] Miller P. R., Scholl J., Bagley S., Leddy D., and Johnson J. H. The effects of a porous ceramic particulate trap on the physical, chemical and biological character of diesel particulate emissions. *SAE*, 1983.

[19] Konstandopoulos A. G., Skaperdas E., Warren J., and Allansson R. Optimized filter design and selection criteria for continuously regenerating diesel particulate trap. *SAE*, (1999-01-0468), 1999.

[20] Masoudi M., Heibel A., and Then P. M. Predicting pressure drop of wall-flow diesel particulate filters – theory and experiments. *SAE*, (2000-01-0184), 2000.

[21] Konstandopoulos A. G., Kostoglou M., Skaperdas E., Papaioannou E., Zarvalis D., and Kladopoulou E. Fundamental studies of diesel particulate filters: Transient loading, regeneration and aging. *SAE*, (2000-01-1016), 2000.

[22] Kwetkus B. A. and Egli W. The monolithic ceramic filter module: Filtration properties and denox potential. *in High Temperature Gas Cleaning*, 1996.

[23] Konstandopoulos A. G., Skaperdas E., and Masoudi M. Inertial contributions to the pressure drop of diesel particulate filters. *SAE*, (2001-01-0909), 2001.

[24] Kays W. M. Loss coefficients for abrupt changes in flow cross section with low reynolds number flow in single and multiple tube system. *Transaction of the American Society of Mechanical Engineers*, 1950.

[25] Kolodzie P. A. and Van Winkle M. Discharge coefficients through perforated plates. *A.I.Ch.E. Journal*, 1957.

[26] Smith P. L. and Van Winkle M. Discharge coefficients through perforated plates at reynolds numbers of 400 to 3000. *A.I.Ch.E. Journal*, 1958.

[27] Hashimoto S., Miyairi Y., Hamanaka T., Matsubara R., Harada T., and Miwa S. Sic and cordierite diesel particulate filters designed for low pressure drop and catalyzed, uncatalyzed systems. *SAE*, (2002-01-0322), 2002.

[28] Konstandopoulos A. G. Flow resistance descriptors for diesel particulate filters: Definitions, measurements and testing. *SAE*, (2003-01-0846), 2003.

[29] Haralampous O. A., Kandylas I. P., Koltsakis G. C., and Samaras Z. C. Diesel particulate filter pressure drop part 1: modelling and experimental validation. *Int. J. Engine Res.*, 5(2), 2004.

[30] Watling T. C., Ravenscroft M. R., Cleeton J. P. E., Rees I. D., and Wilkins D. A. R. Development of a particulate filter model for the prediction of backpressure: Improved momentum balance and entrance and exit effects equations. *SAE*, 2017.

[31] Depcik C., Spickler B., and Gaire A. Revisiting the single equation pressure drop model for particulate filters. *SAE*, (2018-01-0952), 2018.

[32] Opris C. N. and Johnson J. H. A 2-d computational model describing the flow and filtration characteristics of a ceramic diesel particulate trap. *SAE Technical Paper*, (980545), 1998.

[33] Oxarango L., Schmitz P., and Quintard M. Laminar flow in channels with wall suction or injection: A new model to study multi-channels filtration systems. *Chemical Engineering Science*, 59, 2004.

[34] Basu S., Henrichsen M., Tandon P., He S., and Heibel A. Filtration efficiency and pressure drop performance of ceramic partial wall flow diesel particulate filters. *SAE*, 2013.

[35] Piscaglia F. and Ferrari G. A novel 1d approach for the simulation of unsteady reacting flows in diesel exhaust after-treatment systems. *Energy*, 34(12), 2009.

[36] Torregrosa A. J., Serrano J. R., Arnau F. J., and Piqueras P. A fluid dynamic model for unsteady compressible flow in wall-flow diesel particulate filters. *Energy*, 36, 2011.

[37] Yang S., Deng C., Gao Y., and He Y. Diesel particulate filter design simulation: A review. *Adv. Mech. Eng.*, 8(3), 2016.

[38] Konstandopoulos A. G., Kostogoul M, and Housiada P. Spatial non-uniformities in diesel particulate trap regeneration. *SAE Technical Paper*, (2001-01-0908), 2001.

[39] Haralampous O. C., Koltsakis G. C., and Samaras Z. C. Partial regenerations in diesel particulate filters. *SAE Technical Paper*, (2003-01-1881), 2003.

[40] Kostoglou M., Housiada P., and Konstandopoulos A. G. Multi-channel simulation of regeneration in honeycomb monolithic diesel particulate filters. *Chemical Engineering Science*, 58, 2013.

[41] Koltsakis G. C., Haralampous O. A., Margaritis N. K., Samaras Z. C., Vogt C. D., Ohara E., Watanbe Y., and Mizutani T. 3-dimensional modeling of the regeneration in sic particulate filters. *SAE Technical Paper*, (2003-01-0846), 2005.

[42] Pozzato G., Hoffman M. A., and Onori S. Multi-channel physics-based modeling and experimental validation of an uncoated gasoline particulate filter in clean operating conditions. *American Control Conference*, 2017.

[43] Cirstea R., Abo-Serie E. F., Bastien C., and Guo H. Modelling of a coupled catalyst and particulate filter for gasoline direct injection engines. *SAE Technical Paper*, (2018-01-0986), 2018.

[44] Munson B. R., Young D. F., Okiishi T. H., and Huebsch W. W. *Fundamentals of Fluid Mechanics*. Wiley, sixth edition, 2009.

[45] Cengel Y. and Cimbala J. *Fluid Mechanics Fundamentals and Applications*. McGraw-Hill, third edition, 2014.

[46] Nikuradse. Change. *CHANGE*, CHANGE.

[47] Colebrook C. K. Turbulent flow in pipes with particular reference to the transition region between the smooth and rough pipe laws. *Institution of Civil Engineers*, 1939.

[48] Brkić D. Review of explicit approximations to the colebrook relation for flow friction. *Journal of Petroleum Science and Engineering*, 77, 2011.

[49] Churchill S. W. Friction-factor equations spans all fluid regimes. *Chemical Engineering*, 84:91–102, 1977.

[50] Jones O. C. An improvement in the calculation of turbulent friction friction in rectangular ducts. *Journal of Fluid Engineering*, 98(2):173–180, 1976.

[51] Shah R. K. and London A. L. *Laminar flow forced convection in ducts - A source book for compact heat exchanger analytical data*. Elsevier Inc., 1978.

[52] Hagenbach E. Uber die bestimmung der zahigkeit einer flussigkeit durch den asfluss aus rohren. *Poggendorf's Annalen der Physik und Chemie*, 1860.

[53] Knibbs G. H. The history, theory and determination of the viscosity of water by the efflux method. *Royal Society of N. S. Wales*, 1895.

[54] Poiseuille J. L. M. Recherches experimentales sur le mouvement des liquides dans les tubes de tres-petits diametres. *In Memores presentes par divers savants a l'Academie Royale des Sciences de l'Institut de France*, 1846.

[55] Jacobson H. Beitrage zur haemodynamik. *Arch. Anat. Physiol*, 1860.

[56] Schiller L. Die entwicklung der laminarem geschwindigkeitsverteilung und ihre bedeuntung fur zahigkeitsmessungen. *Zeitscrft fur angewandte mathematik und mechanik*, 1922.

[57] Dorsey N. E. The flow of liquids through capillaries. *Physical Review*, 1926.

[58] Rieman W. The value of the hagenbach factor in the determination of the viscosity by the efflux method. *Journal of the American Chemica Society*, 1928.

[59] Weltmann R. N. and Keller T. A. Pressure losses of titania and magnesium slurries in pipes and pipeline transitions. *National Advisory Committee for Aeronautics*, 1957.

[60] Beavers G. S., Sparrow E. M., and Magnuson R. A. Experiments on hydrodynamically developing flow in rectangular ducts of arbitrary aspect ratio. *Int. J. Heat and Mass Transfer*, 13, 1970.

[61] Goldstein S. *Modern developments in fluid dynamics*. Oxford University Press, 1938.

[62] Langhaar H. L. Steady flow in the transition length of a straight tube. *Journal of Appliead Mechanics*, 9:55–58, 1942.

[63] Hornbeck R. W. Laminar flow in the entrance region of a pipe. *Applied Scientific Research*, 13:224–232, 1964.

[64] Schmidt F. W. and Zeldin B. Laminar flows in inlet sections of tubes and ducts. *AIChe Journal*, 15:612–614, 1969.

[65] Bender E. Druckverlust bei laminarer stromaung im rohreinlauf. *Chemic-Ingenicur-Technik*, 11:682–686, 1969.

[66] Shapiro A. H., Siegel R., and Kline S. J. Friction factor in the laminar entry region of a smooth tube. *Poroceedings of the the Second U. S. National Congress of Applied Mechanics*, pages 733–741, 1954.

[67] Kline S. J. and Shapiro A. H. Experimental investigation of the effects of cooling on friction and on boundary-layer transition for low-speed gas flow at the entry of a tube. *National Advisory Committee for Aeronautics*, 1953.

[68] Bender E. Differenzenverfahren zur berechnung der gekoppelten geschwindigkeits- und temperaturfelder bei laminarer rohrströmung mit temperaturabhängigen stoffwerten. *Wärme- und Stoffübertragung*, 1:72–79, 1968.

[69] Shah R. K. A correlation for laminar hydrodynamic enny length solutions for cicular and noncircular ducts. *Journal of Fluids Engineering*, 100:177–179, 1978.

[70] Liu J. Flow of a bingham fluid in the entrance region of an annular tube. M.S. thesis, University of Wisconsin-Milwaukee, 1974.

[71] Shah R. K. and Farnia K. Flow in the entrance of annular tubes. *Computer and Fluids*, 2:285–294, 1974.

[72] Su L., Duan Z., He B., Ma H., and Ding G. Laminar flow and heat transfer in the entrance region of elliptical minichannels. *Journal of Heat and Mass Transfer*, 2019.

[73] Yilmaz Y. General equations for pressure drop for laminar flow in ducts of arbitrary cross sections. *Journal of Energy Resources Technology*, 112:220–223, 1990.

[74] Muzychka Y. S. and Yovanovich M. M. Pressure drop in laminar developing flow in noncircular ducts: A scaling and modelling approach. *Journal of Fluids Engineering*, 131, 2009.

[75] Schetz J. A. and Fuhs A. E. *Handbook of fluid dynamics and fluid machinery*. John Wiley and Sons Inc., 1996.

[76] Suga K., Matsumura Y., Ashitaka Y., Tominaga S., and Kaneda M. Effects of wall permeability on turbulence. *International Journal of Heat and Fluid Flow*, 31, 2010.

[77] Jimenez J., Uhlmann M., Pinelli A., and Kawahara G. Turbulent shear flow over active and passive porous surfaces. *J. Fluid Mech.*, 2001.

[78] Breugem W. P. and Boersma B. J. The turbulent °ow over a permeable wall. *Center for Turbulence Research*, 2002.

[79] Hahn S., Je J., and Choi H. Direct numerical simulation of turbulent channel flow with permeable walls. *J. Fluid Mech.*, 450:259–285, 2002.

[80] Breugem W. P., Boersma B. J., and Uittenbogaard R. E. The influence of wall permeability on turbulent channel flow. *J. Fluid Mech.*, 2006.

[81] Rosti M. E., Cortelezzi L., and Quadrio M. Direct numerical simulation of turbulent channel flow over porous walls. *J. Fluid Mech.*, 784:396–442, 2015.

[82] Berman A. S. Laminar flow in channles with porous walls. *Journal of Applied Physics*, 24(9), 1953.

[83] Yuan S. W. and Finkelstein A. B. Laminar pipe flow with injection and suction through porous walls. *Unknown*, 1955.

[84] Yuan S. W. Further investigation of laminar flow in channels with porous walls. *Journal of Applied Physics*, 27(3), 1956.

[85] Kinney R. B. Fully developed frictional and heat-transfer characteristics of laminar flow in porous tubes. *International Journal of Heat and Mass Transfer*, 11, 1968.

[86] Raithby G. Laminar heat transfer in the thermal entrance region of circular tubes and two-dimensional rectangular ducts with wall suction and injection. *International Journal of Heat and Mass Transfer*, 14, 1970.

[87] Hwang G. J. and Cheng Y. C. Developing laminar flow and heat transfer in a square duct with one-walled injection and suction. *International Journal of Heat and Mass Transfer*, 36(9), 1992.

[88] Cheng Y. C. and Hwang G. J. Experimental studies of laminar flow and heat transfer in a one-porous-wall square duct with wall injection. *International Journal of Heat and Mass Transfer*, 38(18), 1995.

[89] Bissett E. J., Kostoglou M., and Konstandopoulos A. G. Frictional and heat transfer characteristics of flow in square porous tubes of wall-flow monoliths. *Chemical Engineering Science*, 84, 2012.

[90] Durst F. and Loy T. Investigations of the laminar flow in a pipe with sudden contraction of the cross sectional area. *Computers and Fluids*, 13(1):15–36, 1985.

[91] Brightmore A. W. Loss of pressure in water flowing through straight and curved pipes. *Institution of Civil Engineers reports*, 1907.

[92] Merriman M. *Treatise on Hydraulics*. Wiley, tenth edition, 1916.

[93] Oertel H., Prandtl L., Bohle M., and Mayes K. *Prandtl's Essentials of Fluid Mechanics*. Springer, second edition, 2004.

[94] Sullivan J. A. *Fluid Power: Theory and Applications*. Prentice-Hall, third edition, 1989.

[95] Crane Company. Flow of fluids through valves, fittings and pipe. *Technical Paper*, (410), 1976.

[96] Brater E. F., King H. W., and Lindell J. E. *Handbook of Hydraulics*. McGraw-Hill, seventh edition, 1996.

[97] Rouse H. *Elementary mechanics of fluids*. John Wiley and Sons, 1946.

[98] Aleksandrova S., Saul J., Prantoni M., Medina H., Garcia Afonso O., Bevan M., and Benjamin S. Turbulent flow pressure losses in gasoline particulate filters. *SAE Int. J. Engines*, (03-12-04-0030), 2019.

[99] Darcy H. Les fontaines publiques de la ville de dijon. *Victor Dalmont: Paris*, 1856.

[100] Dullien F. A. L. *Porous Media - Fluid Transport and Pore Structure*. Academic Press, second edition, 1991.

[101] Whitaker S. Flow in porous media i: A theoretical derivation of darcy's law. *Transport in Porous Media*, 1986.

[102] Whitaker S. The forchheimer equation: a theoretical development. *Transport in Porous Media*, 1996.

[103] Lage J. L. The fundamental theory of flow through permeable media from darcy to turbulence. *Transport Phenomena in Porous Media*, 1998.

[104] Forchheimer P. Wasserbewegung durch boden. *Zeitschrift des Vereines Deutscher Ingenieure*, 1901.

[105] Teng H. and Zhao T. S. An extension of darcy's law to non-stokes flow in porous media. *Chemical Engineering Science*, 1999.

[106] Zhang W. M., Meng G., and Wei X. A review on slip models for gas microflows. *Microfluid Nanofluid*, 2012.

[107] Aleksandrova S., Saul J., Medina H., Garcia Afonso O., Lin C., Herreros J. M., Bevan M., and Benjamin S. Gasoline particulate filter wall permeability testing. *SAE Int. J. Engines*, 11(5), 2018.

[108] Moghaddam R. N. and Jamiolahmady M. Slip flow in porous media. *Fuel*, 2016.

[109] Maxwell J. C. On stresses in rarified gases arising from inequalities of temperature. *Phil. Trans. R. Soc. Lond.*, 1879.

[110] Beskok A. and Karniadakis G. E. Report: A model for flows in channels, pipes, and ducts at micro and nano scales. *Microscale Thermophysical Engineering*, 1999.

[111] Moore Products. Pressure and temperature compensation of an orifice meter using the model 352 single-loop controller. *Moore Products*, 1994.

[112] Bin Rusli I. H. Experimental study of swirling flows in symmetric and asymmetric sudden expansion with downstream resistance. Ph.d. thesis, Coventry University, 2019.

[113] Padula G., Aleksandrova S., Medina H., and Benjamin S. A new take on the porous medium approach for modelling monoliths and other multiple channel devices. *SAE Technical Paper*, (2019-24-0049), 2019.

[114] https://uk.mathworks.com/discovery/what-is-matlab.html.

[115] https://uk.mathworks.com/help/optim/ug/lsqcurvefit.html.

[116] https://uk.mathworks.com/help/matlab/boundary-value-problems.html.

[117] Antony T. Rapid indirect trajectory optimization on highly parallel computing architectures. *Purdue Univeristy*, 2014.

[118] Sadri R. and Floryan J. M. Accurate evaluation of the loss coefficient and entrance length of the inlet region of a channel". *Journal of Fluids Engineering*, 124(3):685–693, 2002.

[119] Chalfi T. Y. and Ghiaasiaan S. M. Pressure drop caused by flow area changes in capillaries under low flow conditions". *International Journal of Multiphase Flow*, 34:2–12, 2008.

[120] Bell J. H. and Metha R. D. Contraction design for small low-speed wind tunnels. *NASA-CR-177488 Technical Report*, 1988.

[121] Benjamin S. F., Clarkson R. J., Haimad N., and Giris N. S. An experimental and predictive study of the flow field in axisymmetric automotive exhaust catalyst systems. *SAE Technical Paper*, 1996.

[122] Wojtkowiak J. and Popiel C. O. Inherently linear annular-duct-type laminar flowmeter. *J. Fluids Eng.*, 128(1):196–198, 2006.

[123] Pena F. L., Diaz A. D., Lema M. R., and Rodriguez S. V. A new approach to laminar flow meters. *Sensors*, 10(12):10560–10570, 2010.

[124] Ma D. D., Xia G.D., Li Y. F., and Jia Y. T. Effects of structural parameters on fluid flow and heat transfer characteristics in microchannel with offset zigzag grooves in sidewall". *Int. J. Heat and Mass Transfer*, 101:427–435, 2016.

[125] Prantoni M., Aleksandrova S., Medina H., and Benjamin S. Multi-channel modelling approach for particulate filters. *Results in Engineering*, 5(100077), 2020.

[126] Agami Reddy T. *Applied Data Analysis and Modeling for Energy Engineers and Scientists*. Springer, 2011.

Appendix A

Mass flow rate measurements and uncertainty estimation

Mass flow rate measurements

The mass flow rate provided for the rig was measured using a Viscous Flow Meter (VFM). The VFM was calibrated during another PhD project [112] at $1[bar]$ upstream absolute pressure and $20[^{\circ}C]$ upstream temperature. The calibration procedure involved correlating the differential pressure in the VFM to the mass flow rate calculated using the outlet velocities from a pipe measured with an hot wire anemometer. The formula correlating the differential pressure in the VFM to the mass flow rate is a follows:

$$MFR = C_1 \Delta P_{Exp.} + C_2 \Delta P_{Exp.}^2 + C_3 \Delta P_{Exp.}^3, \tag{A.1}$$

where $\Delta P_{Exp.}$ is the differential pressure through the VFM measured during the experiments (in $[Pa]$) and $C_1 = 1.13935 \times 10^{-1}$, $C_2 = -4.67864 \times 10^{-5}$ and $C_3 = 1.68481 \times 10^{-8}$ are fitting coefficients.

For high back pressures in the VFM, caused by the high resistance of the filter during testing, a pressure correction has to be applied in order to calculate the resulting mass flow rates through the line correctly [111]. A temperature correction is also applied for different VFM air temperatures, although the effect of temperature variation was

negligible. The back-pressure correction is applied using the following formula:

$$\Delta P_{Cal.} = \Delta P_{Exp.} \frac{\left(\frac{P_{Exp.}}{P_{Cal.}}\right)}{\left(\frac{T_{Exp.}}{T_{Cal.}}\right)}. \tag{A.2}$$

Here:

- $\Delta P_{Cal.}$ is the back-pressure corrected differential pressure through the VFM (in $[Pa]$).
- $\Delta P_{Exp.}$ is the differential pressure through the VFM measured during the experiments (in $[Pa]$).
- $P_{Cal.}$ is the absolute line pressure upstream of the VFM measured during the calibration (in $[Pa]$).
- $P_{Exp.}$ is the absolute line pressure upstream of the VFM measured during the experiments (in $[Pa]$).
- $T_{Cal.}$ is the temperature upstream of the VFM measured during the calibration (in $[^{\circ}C]$).
- $T_{Exp.}$ is the temperature upstream of the VFM measured during the experiments (in $[^{\circ}C]$).

Therefore, the back-pressure corrected formula for the mass flow rate estimation is:

$$MFR_{Corrected} = C_1 \Delta P_{Cal.} + C_2 \Delta P_{Cal.}^2 + C_3 \Delta P_{Cal.}^3. \tag{A.3}$$

Mass flow rate uncertainty estimation

Following the guidelines reported by Agami Reddy [126], the mass flow rate uncertainty has been estimated with the following method.

The experimental uncertainty of direct measurements can be estimated through the accuracy of the instrumentation (see Table 2.1). For example, a measured quantity A

can be estimated to be:

$$A = a \pm \delta a, \tag{A.4}$$

where a is the value that is measured/read by the instrumentation while $\pm\delta a$ is the uncertainty of the measurement (e.g. $\pm 0.25\%$ of the read).

When adding, subtracting, multiplying or dividing quantities from different measurements the propagation of the uncertainty has to be taken in to account. For example if C is a quantity measured as a sum or difference of two different quantities $A = a \pm \delta a$ and $B = b \pm \delta b$, then the uncertainty of C can be estimated as:

$$\delta c = \sqrt{(\delta a)^2 + (\delta b)^2}. \tag{A.5}$$

If $C = c \pm \delta c$ is a quantity measured by multiplying or dividing two different quantities $A = a \pm \delta a$ and $B = b \pm \delta b$, then the overall uncertainty can be estimated as:

$$\frac{\delta c}{c} = \sqrt{\left(\frac{\delta a}{a}\right)^2 + \left(\frac{\delta b}{b}\right)^2}. \tag{A.6}$$

Instead, when multiplying the same measurement by itself n times:

$$\frac{\delta c^n}{c^n} = |n| \frac{\delta c^{n-1}}{c^{n-1}}. \tag{A.7}$$

Therefore, as the mass flow rate has been calculated with Eq. A.3 and Eq. A.2, the resulting mass flow rate uncertainty δMFR estimated using Eqs. A.5 - A.7 is:

$$\delta MFR = \sqrt{(C_1 \delta P_{Cal.})^2 + (2C_2 P_{Cal.} \delta P_{Cal.})^2 + \left(3C_3 P_{Cal.}^2 \delta P_{Cal.}\right)^2}, \tag{A.8}$$

with

$$\frac{\delta P_{Cal.}}{P_{Cal.}} = \sqrt{\left(\frac{\delta \Delta P_{Exp.}}{\Delta P_{Exp.}}\right)^2 + \left(\frac{\delta P_{Exp.}}{P_{Exp.}}\right)^2 + \left(\frac{\delta P_{Cal.}}{P_{Cal.}}\right)^2 + \left(\frac{\delta T_{Exp.}}{T_{Exp.}}\right)^2 + \left(\frac{\delta T_{Cal.}}{T_{Cal.}}\right)^2}. \tag{A.9}$$